MANIPULATING CONJUGATION IN ELECTRONIC POLYMERS AND GRAPHITIC MATERIALS: CHEMOSENSORS, PRECURSOR ROUTES, AND SELF-ASSEMBLY

ARCHIVES
MASSACHUSETTS INSTITUTE OF TECHNOLOGY
JUN 24 2015
LIBRARIES

by

Jonathan G. Weis

B.S.E., B.A. *summa cum laude*
Polymer Science and Engineering, German
Case Western Reserve University, 2010

SUBMITTED TO THE DEPARTMENT OF CHEMISTRY
IN PARTIAL FULFILLMENT OF THE REQUIREMENTS FOR THE DEGREE OF

DOCTOR OF PHILOSOPHY IN CHEMISTRY

AT THE
MASSACHUSETTS INSTITUTE OF TECHNOLOGY

JUNE 2015

© 2015 Massachusetts Institute of Technology, 2015. All rights reserved.

Signature of Author: Signature redacted
Department of Chemistry
May 6, 2015

Certified by: Signature redacted
Timothy M. Swager
John D. MacArthur Professor of Chemistry
Thesis Supervisor

Accepted by: Signature redacted
Robert W. Field
Haslam and Dewey Professor of Chemistry
Chairman, Departmental Committee on Graduate Students

This doctoral thesis has been examined by a
Committee of the Department of Chemistry as follows

Signature redacted

Professor Rick L. Danheiser
Department of Chemistry
Thesis Committee Chairman

Signature redacted

Professor Timothy M. Swager
Department of Chemistry
Thesis Supervisor

Signature redacted

Professor Jeremiah A. Johnson
Department of Chemistry
Committee Member

for Sarah

MANIPULATING CONJUGATION IN ELECTRONIC POLYMERS AND GRAPHITIC MATERIALS: CHEMOSENSORS, PRECURSOR ROUTES, AND SELF-ASSEMBLY

BY

JONATHAN G. WEIS

SUBMITTED TO THE DEPARTMENT OF CHEMISTRY
ON MAY 6, 2015
IN PARTIAL FULFILLMENT OF THE REQUIREMENTS FOR THE DEGREE OF
DOCTOR OF PHILOSOPHY IN CHEMISTRY

ABSTRACT

In Chapter 1, we synthesize dithienobenzotropone-based conjugated alternating copolymers by direct arylation polycondensation. Post-polymerization hydride reduction furnishes cross-conjugated copolymeric hydrogels that undergo phosphorylation and subsequent ionization upon exposure to chemical warfare agent (CWA) mimics. The resulting conjugated, cationic copolymer is intensely colored and facilitates spectroscopic and colorimetric detection of CWA mimics in solution and as a thin film. Similarly, we report the incorporation of CWA-responsive units into random copolymers prepared by ring-opening metathesis polymerization (ROMP) to create highly modular, chromogenic thin films.

In Chapter 2, we explore homoconjugated polynorbornadienes possessing various electron-withdrawing groups as polymeric precursors to electron-accepting poly(cyclopentadienylene vinylene) derivatives. Tungsten oxo alkylidene catalysts were utilized to polymerize a variety of 7-isopropylidene- and 7-oxa-2,3-disubstituted norbornadienes in a *cis*-highly tactic fashion by ROMP. We further demonstrate the excellent scope of tungsten oxo complexes by polymerizing norbornadienes that are unreactive with traditional molybdenum-, tungsten-, and ruthenium-based catalysts.

In Chapter 3, we employ atomic force microscopy (AFM) and scanning tunneling microscopy (STM) to examine graphene oxide (GO) samples with gradations of (de)oxygenation. We analyze the roughness of the apparent height in STM topographic measurements — i.e. the "apparent roughness" — and report a correlation between increasing deoxygenation and decreasing surface roughness. The "apparent roughness" therefore serves as a supplemental technique for analyzing samples of GO. Furthermore, we report the first example of using an STM tip to locally reduce GO without local destruction of the graphene sample.

In Chapter 4, we exploit the extraordinary self-recognition properties of deoxyribonucleic acid (DNA) to assemble single-walled carbon nanotubes (SWCNTs) in a controllable manner. Networks of SWCNTs with three-way junctions could be constructed in solution or sequentially on a surface. We envision that more complex nanoscale architectures and circuits can be prepared in this bottom-up manner.

In Chapter 5, we introduce halogen bonding in SWCNT-based chemiresistive gas sensors. These chemiresistors were prepared by ball milling of SWCNTs and selectors, compression into a pellet, and mechanical abrasion between gold electrodes on paper. We demonstrate that sensing responses reflect halogen bonding trends, with some exceptions. The predominant signal transduction mechanism is likely attributed to swelling of the insulating haloarene matrix.

Thesis Supervisor: Timothy M. Swager
Title: John D. MacArthur Professor of Chemistry

RESPECTIVE CONTRIBUTIONS

CHAPTER 1

The author conducted all of the work presented in Chapter 1, with the exception of the synthesis of monomer **CM6**, which was synthesized by Dr. Christian Belger. The author thanks Dr. Christian Belger, Dr. Eilaf Ahmed, and Dr. Derek Schipper for helpful discussions.

CHAPTER 2

This chapter was the result of collaborative efforts between the author and members of the Schrock lab at MIT. The collaboration was initiated by the author with Jonathan Axtell. The author prepared all monomers, purified and characterized polymers, and performed all experiments with post-polymerization modification. Dr. William Forrest, Jonathan Axtell, and Dr. Jeremy John synthesized all Mo and W catalysts, set-up all Mo-based and W-based polymerizations, and purified and characterized polymers. The author thanks Lily Chen for assisting in the synthesis of monomers and polymers, Dr. Jeffrey Simpson and Dr. Benjamin Autenrieth for their assistance with NMR experiments, and Dr. Myles Herbert for helpful discussions.

CHAPTER 3

This chapter was a result of collaborative efforts between Dr. Duncan den Boer, the author, Dr. Carlos Zuniga, and Dr. Stefanie Sydlik. Dr. Duncan den Boer performed all STM measurements and local manipulation, designed experiments, and performed the majority of roughness analysis. The author performed all AFM measurements, designed experiments, and performed roughness analysis. Dr. Carlos Zuniga synthesized **GO**, **loGO**, **prGO**, and **rGO** samples, performed XPS measurements, and designed experiments. Dr. Stefanie Sydlik synthesized **GO** for initial results and provided helpful feedback. The author thanks Dr. Elizabeth Shaw of CMSE at MIT for useful discussions on XPS analysis.

CHAPTER 4

The author conducted all of the work presented in Chapter 4. The author thanks Dr. Yossi Weizmann for assisting with the design of preliminary experiments.

CHAPTER 5

The author conducted all of the work presented in Chapter 5. Preliminary experiments for this project were conducted by Dr. Jens Ravnsbæk and the author. The author thanks Dr. Katherine Mirica and Dr. Jan Schnorr for helpful discussions and John Fennell for XPS measurements.

TABLE OF CONTENTS

Title Page 1
Signature Page 3
Dedication 5
Abstract 7
Respective Contributions 9
Table of Contents 11
List of Figures 15
List of Schemes 21
List of Tables 23
List of Abbreviations 25

CHAPTER 1: THIOPHENE-FUSED TROPONES AS CHEMICAL WARFARE AGENT-RESPONSIVE BUILDING BLOCKS 27

1.1 Introduction 28
1.2 Results and Discussion 31
1.2.1 Synthesis of CWA Simulant-Reactive Monomers 31
1.2.2 Responses to CWA Mimic DCP 33
1.2.3 Polymer Synthesis by Direct Arylation Polycondensation 38
1.2.4 Polymer Response to DCP 43
1.2.5 Synthesis of TEG-Containing Monomer 44
1.2.6 Thin-Film Response of TEG-Containing Polymers to DCP 45
1.2.7 CWA-responsive Polymers Prepared by ROMP 49
1.3 Conclusions 54
1.4 Experimental Details 55
1.4.1 General 55
1.4.2 Synthesis of Monomers 56
1.4.3 Synthesis of Polymers 68
1.4.4 Sensing Experiments with DCP 72
1.5 References 73
1.6 Appendix for Chapter 1 77

CHAPTER 2: POLYNORBORNADIENES AS HOMOCONJUGATED PRECURSORS TO ELECTRONIC MATERIALS 99

2.1 Introduction 100

2.2 Results and Discussion 105

2.2.1 Ring-Opening Metathesis Polymerization of Norbornadienes 105

2.2.2 Stereoregular Polymerization of Norbornadienes 107

2.2.3 Expansion of Scope for Tungsten Oxo-based Catalysts 115

2.2.4 Post-Polymerization Conversion to Conjugated Polymers 117

2.3 Conclusions 122

2.4 Experimental Details 122

2.4.1 General 122

2.4.2 Synthesis of Monomers 123

2.4.3 Synthesis of Polymers 131

2.5 References 134

2.6 Appendix for Chapter 2 139

CHAPTER 3: APPARENT ROUGHNESS AS AN INDICATOR OF DEOXYGENATION OF GRAPHENE OXIDE 167

3.1 Introduction 168

3.2 Results and Discussion 173

3.2.1 Synthesis of Materials 173

3.2.2 AFM Studies 174

3.2.3 STM Studies and Apparent Roughness 176

3.2.4 Local Manipulation Induced by STM 182

3.3 Conclusions 185

3.4 Acknowledgements 186

3.5 Experimental Details 186

3.5.1 General 186

3.5.2 Synthesis of loGO, GO, prGO2h, prGO4h, and rGO 186

3.5.3 AFM and STM Measurements 187

3.5.4 Apparent Roughness Analysis 188

3.6 References 190

3.7 Appendix for Chapter 3 195

CHAPTER 4: DNA-MEDIATED SELF-ASSEMBLY OF CARBON NANOTUBES 199

4.1 Introduction 200

4.2 Results and Discussion 204

4.2.1 Solution-based Assembly Methods 204

4.2.2 Surface-based Assembly Methods 213

4.3 Conclusions 217

4.4 Experimental Details 218

4.4.1 General 218

4.4.2 Design of DNA Sequences 219

4.4.3 Oxidation, Shielding, and Length Separation of SWCNTs 220

4.4.4 Self-Assembly of CNT–DNA Conjugates 221

4.5 References 224

CHAPTER 5: HALOGEN BONDING IN CARBON NANOTUBE-BASED CHEMIRESISTIVE SENSORS 231

5.1 A Primer on CNT-based Chemiresistors 232

5.2 Introduction 238

5.3 Results and Discussion 240

5.3.1 Selection and Fabrication of Sensors 240

5.3.2 Sensing Responses to Pyridine 242

5.3.3 Fabrication of Covalently-functionalized CNT-based Sensors 250

5.4 Conclusions 254

5.5 Experimental Details 255

5.5.1 General 255

5.5.2 Fabrication of Sensors 255

5.5.3 Sensing Measurements 257

5.5.4 Characterization of Devices 258

5.5.5 Synthesis of Selectors 259

5.5.6 References 261

5.6 Appendix for Chapter 5 266

Curriculum Vitae 271
Acknowledgements 275

LIST OF FIGURES

Figure 1.1. a) G-type (German) and b) V- type (viscous, victory, or venomous) nerve agents along with the year in which they were discovered. c) CWA mimics dimethyl methylphosphonate (DMMP), diethyl chlorophosphate (DCP), and diisopropyl fluorophosphates (DFP).....29

Figure 1.2. (a) UV–Vis absorption spectra of 5 μM solutions of monomers **RM1a** (black) and **RM2a** (red) in CH_2Cl_2 before (solid) and after (dotted) exposure to 40 ppm DCP. Photographs of **RM1a** in CH_2Cl_2 before (b) and after (c) addition of DCP. 33

Figure 1.3. NMR spectra of **RM1a** (black) and the cation of **RM1a** [**RM1a**–OH]$^+$ (red) in $CDCl_3$ (δ 7.26). TFA was used for complete ionization of the compounds.....34

Figure 1.4. NMR spectra of **RM2a** (black) and the cation of **RM2a** [**RM2a**–OH]$^+$ (red) in $CDCl_3$ (δ 7.26). TFA was used for complete ionization of the compounds.....35

Figure 1.5. UV–Vis absorption spectra of monomers **RM1d** (a) and **RM1a** (b) as a 5 μM solution in CH_2Cl_2 and their response to 100 equivalents DCP (70 ppm) over time. The calculated pseudo-first-order rate constants showed >100-fold enhancement with **RM1a** over **RM1c–e**.....36

Figure 1.6. Optimized geometry (B3LYP/6–31G*) of the tropylium cation of monomer **RM1c**. The aryl ring attached at the 8-position is orthogonal to the aromatic tropylium ring. 37

Figure 1.7. Photograph of polymer **RM1a** in a 5 μM CH_2Cl_2 solution before (a) and after (b) addition of 100 equivalents DCP, after washing with water (c), and finally after washing with 1M NaOH (aq.) (d). In (c) and (d), the aqueous layer lies above the organic layer.....37

Figure 1.8. UV–Vis absorption spectra of monomers **RM1c** (a), **RM1e** (b), **RM1d** (c), and **RM1b** (d) upon exposure to 100 equivalents of TFA in 5 μM solution of CH_2Cl_2. TFA was used for complete ionization of the compounds.....38

Figure 1.9. UV–Vis absorption (solid) and fluorescence (dotted) spectra of polymers **P1c** (red) and **RP1c** (green).....41

Figure 1.10. UV–Vis absorption spectra of polymers **RP2** (a), **RP3** (b), **RP4** (c), and **RP5** (d) in 5 μg/mL solutions in CH_2Cl_2 and their response to 40 ppm DCP. 42

Figure 1.11. (a) UV–Vis absorption spectrum of a 5 μg/mL solution of polymer **RP1c** in CH_2Cl_2 (black, solid line) and after addition of DCP (blue, dashed line). Photographs of solution (b) before and (c) after addition of DCP.....43

Figure 1.12. Photograph of polymer **RP1c** in 5 μg/mL CH_2Cl_2 solution before (a) and after (b) addition of 100 equivalents DCP, after washing with water (c), and finally after washing with 1M NaOH (aq.) (d). In (c) and (d), the aqueous layer lies above the organic layer. 44

Figure 1.13. Photograph of polymer **RP1d** in 5 μg/mL CH_2Cl_2 solution before (a) and after (b) addition of 40 ppm DCP, after washing with water (c), and finally after washing with 1M NaOH (aq.) (d). In (c) and (d), the aqueous layer lies above the organic layer. 46

Figure 1.14. Response of polymer **RP1d** (5 μg/mL) to different concentrations of DCP in CH_2Cl_2. The calculated limit of detection is 6 ppm. 47

Figure 1.15. Response of polymer **RP1d** (5 μg/mL) in CH_2Cl_2 to 100 μM analyte. Dimethyl methylphosphonate (DMMP), pinacolyl methylphosphonate (PMP), and acetic acid (AcOH) were tested as interferents. Diethyl chlorophosphate (DCP) and diisopropyl fluorophosphates (DFP) were tested as agent simulants.....47

Figure 1.16. UV–Vis absorption spectrum of polymer **RP1d** as a thin film (a) before (black, solid line) and after exposure to saturated vapor of (b) DCP (blue, dotted line) and (c) TFA (green, dashed line). 48

Figure 1.17. Photographs of thin films of polymer **RP1d** before (a) and after (b) exposure to saturated DCP vapor. The response is further intensified by exposure to TFA (c), and the active material can be regenerated by exposure to ammonium hydroxide vapor (d). 49

Figure 1.18. Response of **RCP1** to DCP in CH_2Cl_2 at varying concentrations and calculation for limit of detection (3.3 ppm). 52

Figure 1.19. Response of **RCP2** to DCP in CH_2Cl_2 at varying concentrations and calculation for limit of detection (1.2 ppm). 53

Figure 1.20. Response of polymers a) **RCP1** and b) **RCP2** to concentration vapors of DCP and TFA and resulting regeneration with exposure to NH_4OH vapor. 54

Figure 2.1. Norbornadiene monomers explored in this study. 105

Figure 2.2. Catalysts employed in this study.....107

Figure 2.3. Olefinic protons H_a and H_b in *cis, syndiotactic* and *cis, isotactic* polymers where R* = CO_2Menth and Y = O (poly(**2c**)) or Y = C=CMe_2 (poly(**3c**)). 110

Figure 2.4. ATR–FTIR spectra of a) model compound before and after treatment with 3 equiv. DDQ and b) poly(**2b**) before and after treatment with 3 equiv. DDQ. 118

Figure 2.5. a) NMR spectra of poly(**2b**) before and after treatment with 3 equiv. DDQ. b) UV–Vis spectra of poly(**2b**) before and after treatment with DDQ.....119

Figure 2.6. Benzoxanorbornadiene-based monomers **17–19** and resulting polymers poly(**17**)–poly(**19**). Naphthol **20** results from the ring-opening of **19** rather than polymerization at room temperature. 121

Figure 2.7. UV–Vis absorption spectra for dialkoxy-substituted poly(**19**) and after treatment with Br_2 and I_2. 121

Figure 3.1. Modified Lerf–Klinowski model of GO.[13,14] 169

Figure 3.2. AFM images of graphene oxide flakes at varying degrees of (de)oxygenation at the HOPG / air interface after dropcasting. Top: AFM topographic images; center: AFM phase images; bottom: line profiles of the corresponding phase image. a) Less oxidized graphene oxide (**loGO**) deposited from H_2O. b) Graphene oxide (**GO**) deposited from H_2O. c) Partially reduced graphene oxide, after 2 h of reduction (**prGO2h**), deposited from H_2O. d) Partially reduced graphene oxide, after 4 h of reduction (**prGO4h**), deposited from H_2O. e) Fully reduced graphene oxide (**rGO**) deposited from NMP. 175

Figure 3.3. STM topographic images of graphene oxide flakes at varying degrees of (de)oxygenation at the HOPG / air interface. The depicted z scale bars are in nm. V_{bias} = +1 V, I_{set} = 2–5 pA. a) **loGO** deposited from H_2O. b) **GO** deposited from H_2O. c) **prGO2h** deposited from H_2O. d) **prGO4h** deposited from H_2O. e) **rGO** deposited from NMP. 178

Figure 3.4. Apparent RMS roughness, R_q, of graphene oxide flakes at different degrees of oxygenation and deoxygenation on HOPG, as determined by topographic STM measurements. For every bar, n = 9–11 flakes, and error bars represent the standard deviation. All measurements were obtained with at least 2 different STM tips. V_{bias} = +1 V, I_{set} = 2–5 pA. Indicated on the right is the apparent roughness that was found for experiments with local manipulation (see Figure 3.5), in which areas of the surface of **loGO** were scanned at the indicated voltage. 181

Figure 3.5. Local manipulation of **loGO** at the HOPG / air interface by STM. V_{bias} = +1 V, I_{set} = 2 pA. a–e) The yellow squares indicate the area that is scanned twice (once up and once down) at the specified negative voltage, with each scan taking ~ 4 min, for a total of ~ 8 min between the STM images that are shown. The yellow, dotted line in the lower right in images a–e is drawn as a guide for the edge of the flake, displaying the flake degrades during the local manipulation. f) The resulting flake after the local manipulation, with the yellow squares indicating the different voltages applied. g) Line profile corresponding to the dotted white line displayed in (f). 183

Figure 3.6. Local manipulation of **GO** by STM at the HOPG / air interface. V_{bias} = +1 V, I_{set} = 2 pA. The yellow squares indicate the area that has been scanned twice (up and down) at a V_{bias} = −2 V. Δt ~ 12 minutes. The yellow circle indicates a high feature that was used as a reference point. STM measurements are taken before (a) and after (b) the local manipulation. 184

Figure 3.7. a–e) X-ray photoelectron spectra of **loGO**, **GO**, **prGO2h**, **prGO4h**, and **rGO**, respectively. 195

Figure 3.8. Additional AFM topographic images of graphene oxide flakes at varying degrees of (de)oxygenation at the HOPG / air interface after deposition from solution. Depicted x,y scale bars are in μm. 196

Figure 3.9. a–c) Apparent roughness graphs, determined from the same STM topography measurements as in Figure 3.4. a) Apparent average roughness, R_a, showing the same trend that more deoxygenation corresponds to lower apparent roughness. b) Apparent R_q determined with all areas ~2500 nm^2. c) Same as (b) but for the apparent R_a. d) R_q obtained from AFM measurements. For every bar, n = 9–11 flakes. 197

Figure 3.10. An additional example of local manipulation of **loGO** by STM at the HOPG / air interface. V_{bias} = +1 V, I_{set} = 2 pA. The yellow squares indicate the areas that have been scanned at a V_{bias} = −2 V between the shown images. Δt ~ 9 minutes. 197

Figure 4.1. Chiral vectors in CNTs. $na_1+ma_2 \equiv (n,m)$. n and m are integers where $0 \leq |m| \leq n$. For $n - m = 3k$, CNTs are metallic if k is an integer and semiconducting if not. 200

Figure 4.2. Schematic of an ideal DNA–CNT network deposited between gold electrodes. 203

Figure 4.3. Structure of 5′-6-aminohexyl terminus of DNA that allows bioconjugation to oxidized SWCNTs. 204

Figure 4.4. a) UV–Vis absorption spectrum of shielded SWCNTs dispersed in H_2O. To calculate the concentration of SWCNTs, an extinction coefficient of 0.0078 L mg^{-1} cm^{-1} at 808 nm was used. b) Transmission electron micrograph of shielded SWCNTs. 206

Figure 4.5. Length separation of carbon nanotubes by SEC with 1000Å controlled pore glass. Histograms and corresponding TEM image of fractions 1–3. 207

Figure 4.6. Characterization of 3WJs formed by solution assembly method A (Scheme 4.2). a, b) AFM images. The x and y scale bars are in μm. c) Line profiles indicating shielded CNTs and DNA as marked in (d). d, e) TEM images. The red arrows indicate the locations of 3WJs. 209

Figure 4.7. Characterization by TEM of 3WJs formed by Solution Assembly Method B. .210

Figure 4.8. a) Structure of fluorous amine used to cause aggregation b,c) TEM images displaying aggregates. d) Scheme for formation of linear DNA–CNT nanowires. e–g) TEM images of linear DNA–CNT nanowires. 211

Figure 4.9. a) AFM topographic image of aggregates formed during DNA–CNT network construction in PBS buffer. The x- and y-axes are in μm. b) TEM image of DNA hybridization-induced aggregation. c) Zoom in on region labeled in (b). 212

Figure 4.10. AFM topographic measurements of DNA–CNT networks assembled by surface method A. The x- and y- axes are in μm. 214

Figure 4.11. AFM amplitude images of control measurements (a) with and (b) without the presence of DNA anchors. The x- and y- axes are in μm.....214

Figure 4.12. AFM topographic measurements of CNT–DNA 3WJs prepared by Solution Method B with DNA:CNT bioconjugation ratios of a) 3:1, b) 4:1, and c) 5:1. 217

Figure 5.1. Schematic of a chemiresistor based on a randomly oriented network of CNTs deposited between two gold electrodes. 233

Figure 5.2. "Selectors" employed in this study. 242

Figure 5.3. Sensing response of *p*-dihalobenzene series to varying concentrations of pyridine in N_2 carrier gas at room temperature. Each type of sensor was examined in triplicate. The three traces for each type of sensor are overlaid to show reproducibility. 243

Figure 5.4. Sensing response of halodurene series to varying concentrations of pyridine. A composite with unsubstituted durene and pristine CNTs were used as controls. Each type of sensor was examined in triplicate. The three traces for each type of sensor are overlaid to show reproducibility. 244

Figure 5.5. Sensing response of durene-based selectors to varying concentrations of pyridine. 245

Figure 5.6. Electronic effects on sensing response to varying concentrations of pyridine. Sensing responses ($-\Delta G/G_0$, %) of sensors to varying concentrations of pyridine. Each type of sensor was examined in triplicate. The three traces for each type of sensor are overlaid to show reproducibility. 246

Figure 5.7. Effect on alkyl chain length on enhancement by dialkyldiiodobenzenes. 247

Figure 5.8. Screening for XB-specific signal enhancement. Pyridine was tested as an analyte in comparison to hexanes, benzene, isopropanol, and acetonitrile.....248

Figure 5.9. Sensing response ($-\Delta G/G_0$, %) of alkynyl aryl iodides to varying concentrations of pyridine. 249

Figure 5.10. Other selectors employed for the selective enhancement of signal upon exposure to pyridine vapor.....249

Figure 5.11. Sensing response of covalently functionalized CNTs to pyridine vapor at 1, 4, and 25 ppm. 254

Figure 5.12. Structure of device used for drop-casting covalently functionalized CNTs between electrodes.....256

Figure 5.13. Layout of sensing device a) with and b) without the PTFE enclosure.....257

Figure 5.14. Sensing response ($-\Delta G/G_0$, %) of CNT-based to 25 ppm pyridine on copy paper (high roughness) and weighing paper (low roughness). Each type of sensor was examined in triplicate. The three traces for each type of sensor are overlaid to show reproducibility.....266

Figure 5.15. Sensing response of electron-deficient selector / SWCNT composites to benzene, ethanol, and pyridine. 266

Figure 5.16. X-ray photoelectron spectra of covalently functionalized CNTS. a) Cl, 0.1 equiv.; b) Cl, 0.2 equiv.; c) Br, 0.1 equiv.; d) Br, 0.2 equiv.; e) I, 0.1 equiv.; f) I, 0.2 equiv. 267

LIST OF SCHEMES

Scheme 1.1. Synthesis of CWA-reactive **RM1a** and ionization with CWA mimic diethyl chlorophosphate.....30

Scheme 1.2. Synthesis of monomers **M1a**, **M1b**, and **M1c**: i) R–Br (3 equiv.), K_2CO_3 (3 equiv.) in DMF at 80°C, ii) Br_2 (2.2 equiv.) in DCM at 0°C, iii) 3-thienylboronic (2.2 equiv.) acid, Na_2CO_3 (8 equiv.), $Pd(PPh_3)_4$ in toluene/ethanol/water (4:1:1) at 90°C, iv) *N*-bromosuccinimide (2.0 equiv.) in $CHCl_3$/AcOH (1:1) at 0°C, v) *n*-butyllithium (2.1 equiv.) then dimethylcarbamyl chloride in Et_2O at −78°C.....31

Scheme 1.3. Synthesis of reduced monomer **RM2a**: i) *N*-bromosuccinimide in $CHCl_3$/AcOH at 0°C, ii) *n*-BuLi then TMS–Cl in Et_2O at −78°C, iii) *n*-BuLi then dimethylcarbamyl chloride in Et_2O at −78°C, iv) KF in refluxing MeOH, v) $NaBH_4$ in THF/MeOH at 0°C.....32

Scheme 1.4. Synthesis of reduced monomers **RM1a–e**.....35

Scheme 1.5. Direct arylation polycondensation of monomers **M1a–c** and 9,9-dioctyl-2,7-dibromofluorene (**CM1**) to alternating copolymers **P1a–c** and their subsequent reduction to **RP1a–c**.....40

Scheme 1.6. Synthesis of polymers **P1c–5** and **RP1c–5**.....42

Scheme 1.7. Synthesis of tetra(ethylene glycol) monomethyl ether-substituted monomer **M1d** from monomer **M1a**.....45

Scheme 1.8. Synthesis of polymer **P1d** by direct arylation polycondensation and subsequent reduction to CWA-responsive polymer **RP1d**.....46

Scheme 1.9. Synthesis of CWA-responsive monomer **M3** from dithienobenzotropone **M1c**. Norbornene **10** was synthesized by Pd-catalyzed hydroarylation of norbornadiene according to literature procedure.[58].....50

Scheme 1.10. Synthesis of random copolymers **RCP1** and **RCP2** by ROMP initiated with Grubbs' 3rd generation catalyst **G3**.....51

Scheme 2.1. Examples of conjugated polymers prepared by metathesis.....102

Scheme 2.2. a) General scheme for ROMP of norbornadienes and subsequent oxidation to poly(cyclopentadienylene vinylene) derivatives. b) Special case of poly(fulvenylene vinylene)s that can isomerize to a conducting isopropyl-substituted poly(cyclopentadienylene vinylene). EWG = electron-withdrawing group.....104

Scheme 2.3. Synthesis of dicyanoacetylene. i) NH_4OH (94% yield); ii) P_4O_{10}, sulfolane, 110°C, 2 Torr (49% yield). CAUTION: Dicyanoacetylene (**7**) is known to decompose explosively and likely releases hydrogen cyanide under ambient conditions. 105

Scheme 2.4. Synthesis of 7-oxanorbornadienes **2b** and **2c** and 7-isopropylidenenorbornadienes **3b** and **3c**. 109

Scheme 2.5. Synthesis of monomers **11** and **12**: i) vinylene carbonate, toluene, 180 °C, 3 days (58% yield); ii) 6M KOH (85% yield); iii) DMSO, $(CF_3CO)_2O$, CH_2Cl_2, −78 °C, 3 h; Et_3N, r.t., 12 h (90% yield); iv) diaminomaleonitrile, THF, reflux, 16 h (77% yield) 116

Scheme 2.6. Synthesis and polymerization of Ru complex **14** by catalyst **A** (Figure 2.2)... 117

Scheme 2.7. Oxidation of test monomer with DDQ. 118

Scheme 4.1. Oxidation and subsequent shielding of SWCNTs. 205

Scheme 4.2. Assembly method A for forming CNT–DNA 3WJs in solution. 208

Scheme 4.3. Assembly method B for formation of CNT–DNA 3WJs in solution. 210

Scheme 4.4. Surface assembly method A for the bottom-up construction of CNT–DNA 3WJs on silicon surfaces. 213

Scheme 4.5. Surface assembly method B. Alternative functionalization of silicon surfaces with NHS esters by sonochemical hydrosilation. 215

Scheme 5.1. Covalent functionalization of carbon nanotubes with aryl iodides through diazonium chemistry. 251

LIST OF TABLES

Table 2.1. Polymerization attempts with 7-isopropylidenenorbornadienes **3a–e**, **4a**. a) reference 49. b) reference 58. c) reference 37. 112

Table 2.2. Polymerization attempts with 7-oxanorbornadienes **2a–c**, **4b**. a) reference 49. b) reference 58. c) reference 37. 114

Table 3.1. Relative atomic percentages of O 1s and C 1s, determined by X-ray photoelectron spectroscopy (XPS). Spectra are displayed in Figure 3.7 in the appendix of this chapter. ... 173

Table 5.1. Characterization of covalently functionalized CNTs. [1]1 equiv. = 6 CNT carbons. [2]Sufficiently low resistance ($R < 500$ kΩ) determined by dropcasting 20 drops of concentrated CNT solution in DMF between 1 mm gold electrodes on glass. [3]X:C ratio, as determined by X-ray photoelectron spectroscopy (XPS). 252

LIST OF ABBREVIATIONS

AFM	atomic force microscopy
ATR–FTIR	attenuated total reflectance – Fourier transform infrared (spectroscopy)
CNT	carbon nanotube
COSY	correlation spectroscopy
DART–MS	direct analysis in real time – mass spectrometry
DMAD	dimethyl acetylenedicarboxylate
DMF	*N*,*N*-dimethylformamide
DMSO	dimethyl sulfoxide
EDX	energy-dispersive X-ray spectroscopy
ESI	electrospray ionization
EtOH	ethanol
FT–ICR–MS	Fourier transform – ion cyclotron resonance mass spectrometry
GC–MS	gas chromatography – mass spectrometry
gCOSY	gradient-selected correlation spectroscopy
GPC	gel permeation chromatography
HOMO	highest occupied molecular orbital
HRMS	high-resolution mass spectrometry
HSQC	heteronuclear single quantum coherence
hν	light
LED	light-emitting diode
LUMO	lowest unoccupied molecular orbital
MAP	monoaryloxide pyrrolide
MeOH	methanol
mp	melting point
MWCNT	multi-walled carbon nanotube
M_n	number-average molecular weight
NMR	nuclear magnetic resonance
ROMP	ring-opening metathesis polymerization
PDI	polydispersity index
PPE	poly(*para*-phenylene ethynylene)
PPV	poly(*para*-phenylene vinylene)
r.t.	room temperature
SEM	scanning electron microscopy
SWCNT	single-walled carbon nanotube
TEM	transmission electron microscopy
TGA	thermogravimetric analysis

THF	tetrahydrofuran
UV–Vis	ultraviolet–visible
wt	weight
XPS	X-ray photoelectron spectroscopy

CHAPTER 1

Thiophene-Fused Tropones as Chemical Warfare Agent-Responsive Building Blocks

Adapted and reprinted with permission from Weis, J. G.; Swager, T. M.* "Thiophene-Fused Tropones as Chemical Warfare Agent-Responsive Building Blocks" *ACS Macro Lett.* **2015**, *4*, 138–142.

Parts of this chapter were reprinted from Belger, C.; Weis, J. G.; Ahmed, E.; Swager, T. M.* "Colorimetric Stimuli-Responsive Hydrogel Polymers for the Detection of Nerve Agents." *in preparation.*

This work was supported by the Chemical and Biological Technologies Department at the Defense Threat Reduction Agency (DTRA–CB) via Grant BA12PHM123 in the "Dynamic Multifunctional Materials for a Second Skin D[MS]^2" program.

1.1 Introduction

Electrophilic organophosphates are the basis of many chemical warfare agents (CWAs) and pesticides. They derive their high toxicity from their capacity to inhibit acetylcholinesterase (AChE) by phosphorylating a serine residue at the active site of the enzyme.[1] The ensuing buildup of acetylcholine (ACh) in the body leads to an initial overstimulation and subsequent paralysis of neurotransmission in the victim.[2,3] The resulting threat of CWAs against military and civilian targets necessitates materials for detection and protection schemes that are operationally simple, sensitive, portable, and cost-effective.[4]

Reported techniques used to detect organophosphorus CWAs and their mimics (see Figure 1.1) include mass spectroscopy,[5–7] infrared spectroscopy,[8] electrochemical sensors,[9,10] microelectromechanical systems,[11,12] chemiresistors,[13–17] and luminescent indicators.[18–22] Colorimetric sensors are attractive as a result of their excellent operational simplicity, portability, and ability to integrate functionality that reacts with CWAs. Colorimetric schemes have been reported with reactive aldehydes,[23] ketones,[24] alcohols,[25–34] oximes,[35–39] pyridines,[40] and amines.[20,41,42]

Although many solution-based colorimetric detection schemes have been reported, there are far fewer examples of colorimetric responses in thin films, which are necessary for the real-time detection of organophosphates. Most previous approaches to CWA colorimetric thin-film sensing involve embedding chromogenic small molecules into a polymer matrix.[27,42] An attractive alternative is the covalent attachment or direct incorporation of chromophores into polymers.[35] This strategy can greatly increase the robustness and versatility of these materials by preventing dissolution or separation of the CWA-responsive unit over time. By incorporating the responsive unit into the polymer backbone, we envision stimuli-responsive

materials that undergo simultaneous bulk electronic and mechanical changes in response to CWAs to both detect and protect against CWAs.

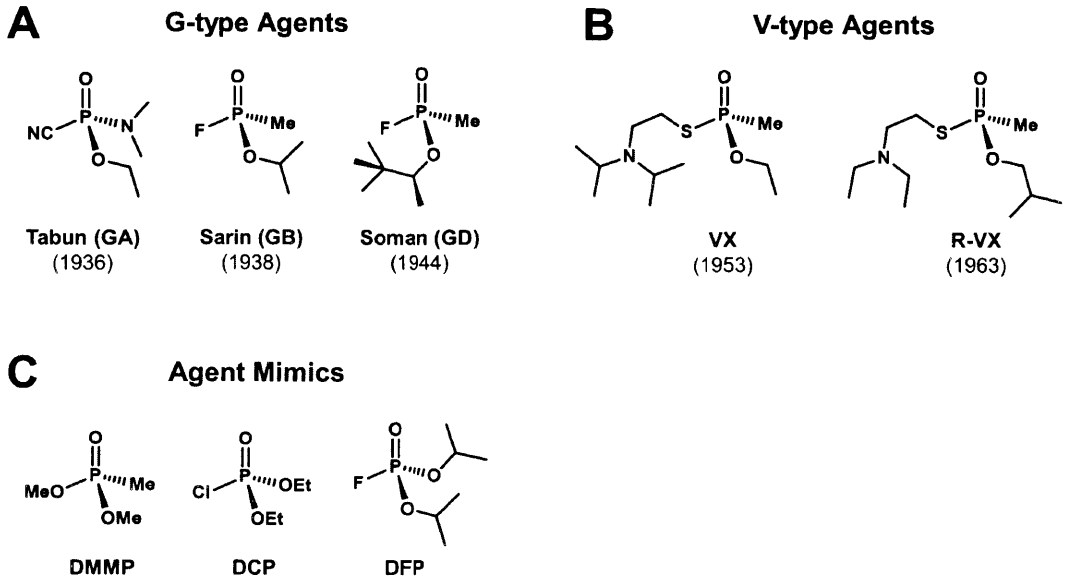

Figure 1.1. a) G-type (German) and b) V- type (viscous, victory, or venomous) nerve agents along with the year in which they were discovered. c) CWA mimics dimethyl methylphosphonate (DMMP), diethyl chlorophosphate (DCP), and diisopropyl fluorophosphates (DFP).

Inspired by the triarylmethanol-containing chromophores reported by Gotor et al.,[27] and our group's successful synthesis of dithienobenzotropone **M1a**,[43] we postulated that reduction of a dithienobenzotropone-containing polymer would result in reactive alcohols that function as CWA indicators. As a result of the fused, electron-donating thiophene and dialkoxybenzene rings, the phosphorylated alcohol will readily ionize to form a highly resonance-stabilized and colored tropylium cation, realizing colorimetric and spectroscopic detection (Scheme 1.1).

In addition to serving as a probe for CWAs, the molecule undergoes a concomitant change in conformation from a bowl-shaped alcohol (**RM1a**) to a planar tropylium cation. The

resulting ionization and increased surface area for π–π interactions could induce a mechanical response that limits the breathability of a hydrogel, for instance, ultimately realizing a dynamic protective material.

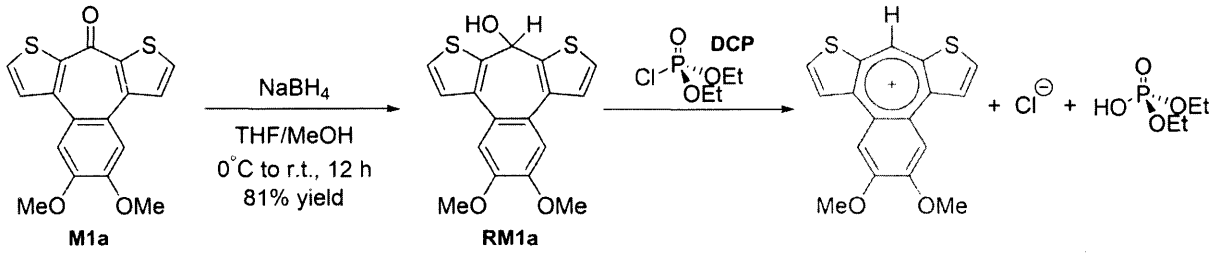

Scheme 1.1. Synthesis of CWA-reactive **RM1a** and ionization with CWA mimic diethyl chlorophosphate.

To incorporate the dithienobenzotropone moiety into a polymer, we chose direct arylation polycondensation, which circumvents the need to prefunctionalize one of the monomers and avoids the stoichiometric formation of toxic, organotin byproducts.[44,45] The consequent ease of purification of the polymers results in materials with enhanced optical and electronic properties.[46] Direct arylation polymerization has been demonstrated to be an excellent tool for the polymerization of thiophene-containing compounds.[47–51] This method relies on C–H activation at the α position on the thiophene to couple the thiophene with aryl halides, and the mechanism of the reaction is reported to proceed through a concerted metalation deprotonation pathway.[52,53]

In addition to synthesizing these polymeric compounds by direct arylation, we report the reduction of these polymers to CWA simulant-reactive alcohols. Upon exposure to nerve agent simulant diethyl chlorophosphate (DCP), these polymers undergo drastic spectroscopic and colorimetric changes in solution and thin-film measurements. Furthermore, we demonstrate that ring-opening metathesis polymerization can be used as a modular method to

synthesize nonconjugated polymers that possess pendant CWA-responsive dithienobenzotropone-derived moieties. For both systems, the inclusion of plasticizing side chains significantly enhances the response of these polymers to DCP in thin films.

1.2 Results and Discussion

1.2.1 Synthesis of CWA Simulant-Reactive Monomers

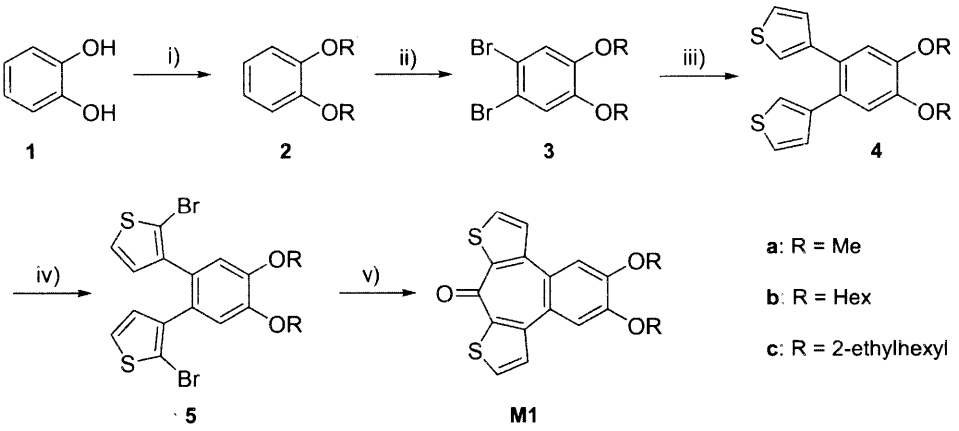

Scheme 1.2. Synthesis of monomers **M1a**, **M1b**, and **M1c**: i) R–Br (3 equiv.), K_2CO_3 (3 equiv.) in DMF at 80°C, ii) Br_2 (2.2 equiv.) in DCM at 0°C, iii) 3-thienylboronic (2.2 equiv.) acid, Na_2CO_3 (8 equiv.), $Pd(PPh_3)_4$ in toluene/ethanol/water (4:1:1) at 90°C, iv) *N*-bromosuccinimide (2.0 equiv.) in $CHCl_3$/AcOH (1:1) at 0°C, v) *n*-butyllithium (2.1 equiv.) then dimethylcarbamyl chloride in Et_2O at −78°C.

To examine the reactivity of the 8*H*-benzo[6,7]cyclohepta[2,1-*b*:4,5-*b*']dithiophen-8-ol unit (**RM1a** in Scheme 1.1), we first synthesized reduced derivatives of our tropone-containing monomers for direct arylation. Dimethoxy-substituted dithienobenzotropone **M1a** (Scheme 1.2) was synthesized from veratrole according to a procedure reported by our group,[43] and tropones **M1b** and **M1c** were synthesized from catechol in five steps using an analogous synthesis, as displayed in Scheme 1.2. *o*-Dialkoxybenzenes were prepared by the alkylation of catechol with *n*-alkyl bromides. Subsequent bromination and Suzuki coupling with 3-thienyl

boronic acid afforded the desired 3,3′-(4,5-bis(alkoxy)-1,2-phenylene)dithiophene. Regioselective bromination at the 2-position on the thiophene was achieved by reaction with *N*-bromosuccinimide. The final dithienobenzotropone was obtained by lithium–halogen exchange with *n*-butyllithium followed by quenching with dimethylcarbamyl chloride.

We synthesized the reactive alcohol by reducing tropone **M1a** to alcohol **RM1a** using sodium borohydride in a tetrahydrofuran/methanol (4:1) solution at room temperature in 81% yield, as shown in Scheme 1.1. We also synthesized its regioisomer **RM2a** using a similar synthetic route starting from 4,5-di-(2-thienyl)-veratrole,[54] as shown in Scheme 1.3. It should be noted that because these thiophenes preferentially undergo bromination and lithium–halogen exchange at the 2- and 5-positions, it was necessary to protect the α-positions with trimethylsilyl groups for the ring-forming step. Final deprotection with potassium fluoride in refluxing methanol furnished tropone **M2a**.

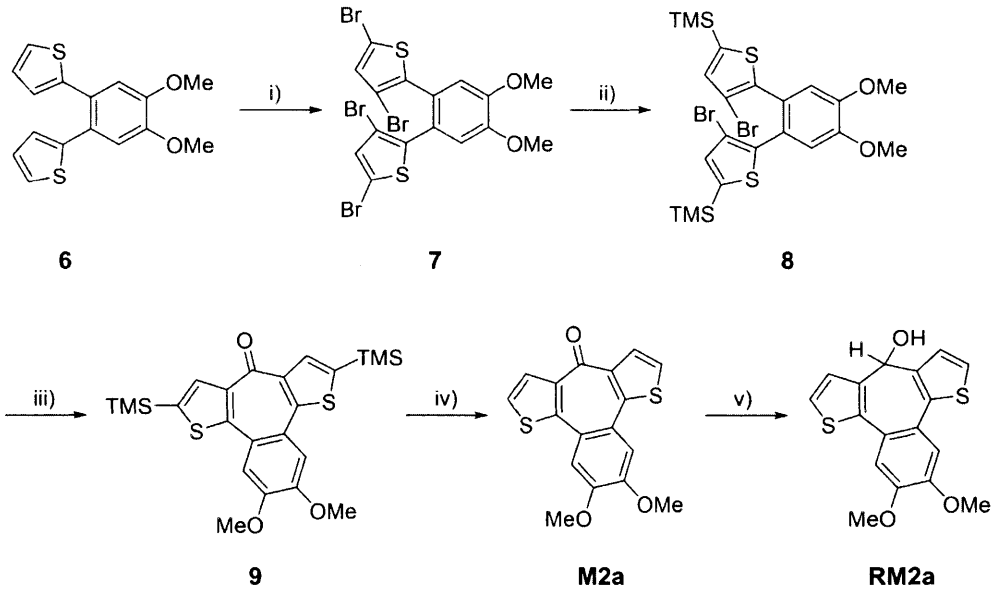

Scheme 1.3. Synthesis of reduced monomer **RM2a**: i) *N*-bromosuccinimide in $CHCl_3$/AcOH at 0°C, ii) *n*-BuLi then TMS–Cl in Et_2O at −78°C, iii) *n*-BuLi then dimethylcarbamyl chloride in Et_2O at −78°C, iv) KF in refluxing MeOH, v) $NaBH_4$ in THF/MeOH at 0°C.

1.2.2 Responses to CWA Mimic DCP

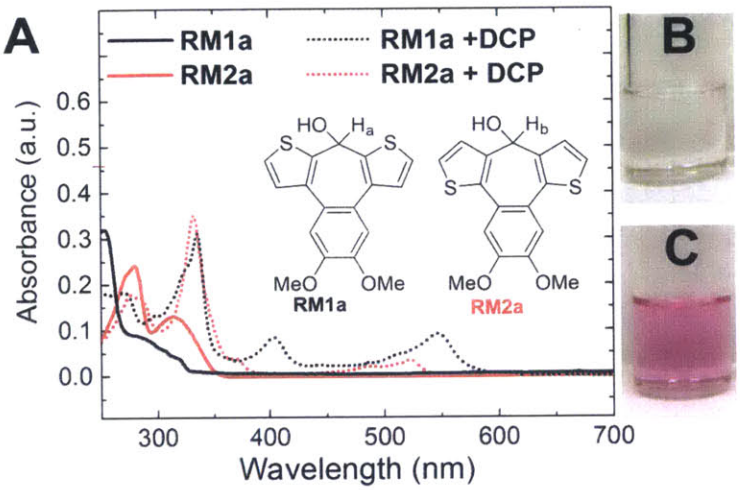

Figure 1.2. (a) UV–Vis absorption spectra of 5 μM solutions of monomers **RM1a** (black) and **RM2a** (red) in CH_2Cl_2 before (solid) and after (dotted) exposure to 40 ppm DCP. Photographs of **RM1a** in CH_2Cl_2 before (b) and after (c) addition of DCP.

Diethyl chlorophosphate (DCP) is often used as a nerve agent simulant in the development of CWA detection schemes as a result of its similar electrophilic reactivity and lower relative toxicity than actual nerve agents (e.g., Sarin, Soman, Tabun).[24,26,29,32] These organophosphorus CWA simulants are known to degrade to acidic products over time.[28] To prevent interference (false positives) from strong acids, we passed a 1 M DCP solution in dichloromethane through a pad of dry potassium carbonate before each sensing experiment. To evaluate the response of alcohol **RM1a** to DCP, we exposed a 5 μM solution of **RM1a** in dry dichloromethane to DCP at a concentration of 40 ppm. The UV–Vis absorption spectrum exhibited a strong bathochromic shift of λ_{onset} from 330 nm to 580 nm (Figure 1.2a), and comparison of the proton NMR spectra of alcohol **RM1a** and the resulting cation reveals a downfield shift of the proton labeled H_a in Figure 1.2 from δ 5.87 to δ 9.65, as a result of aromatic ring currents and deshielding caused by ionization (Figure 1.3). Both of these

observations and the change in color from colorless to bright pink (Figure 1.2b and Figure 1.2c) are consistent with the formation of the aromatic dithienobenzotropylium cation.

Spectroscopic and colorimetric comparison of monomers **RM1a** and **RM2a** led us to pursue polymers containing the 3-thienyl-derived regiomeric structure of **RM1a** that provides a more intense color change and greater bathochromic shift as compared to the 2-thienyl-derived **RM2a** (Figure 1.2a). Nonetheless, alcohol **RM2a** undergoes phosphorylation and ionization to yield the resulting tropylium cation, exhibiting a bathochromic shift in the absorption spectra (Figure 1.2a) and a downfield shift in the NMR spectra of the proton labeled H_b in Figure 1.2 from δ 5.39 to δ 9.65 (Figure 1.4).

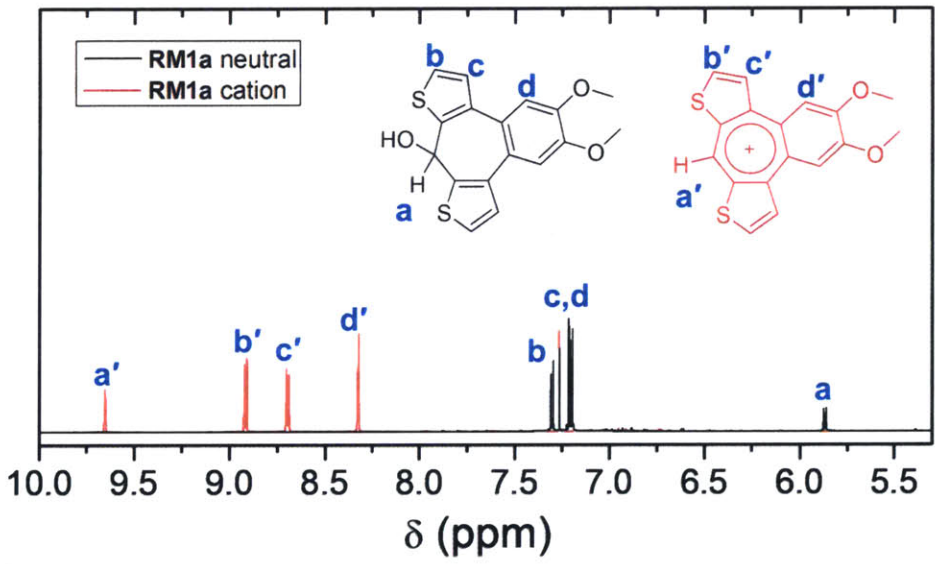

Figure 1.3. NMR spectra of **RM1a** (black) and the cation of **RM1a** [**RM1a**−OH]$^+$ (red) in $CDCl_3$ (δ 7.26). TFA was used for complete ionization of the compounds.

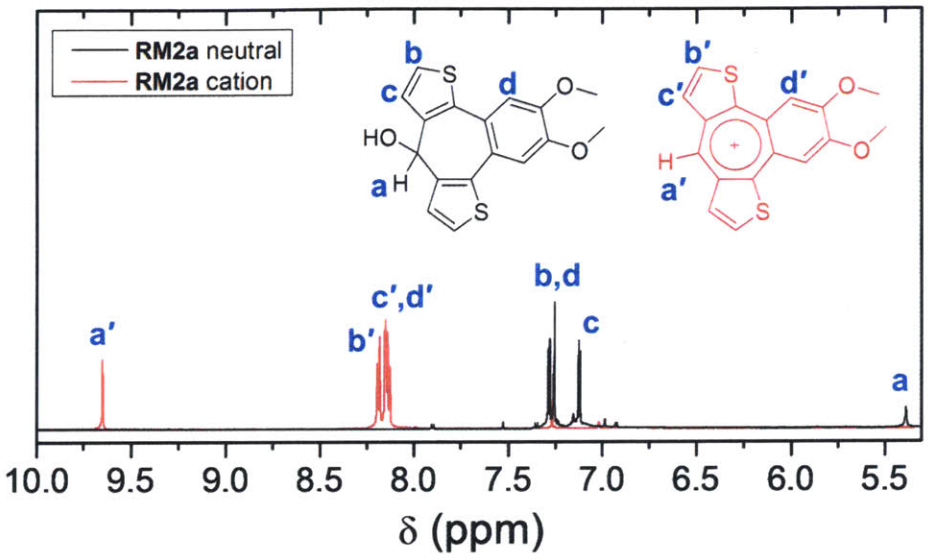

Figure 1.4. NMR spectra of **RM2a** (black) and the cation of **RM2a** [**RM2a**–OH]$^+$ (red) in $CDCl_3$ (δ 7.26). TFA was used for complete ionization of the compounds.

In addition to the reduction with sodium borohydride, the tropone can be converted into a reactive alcohol by addition of an alkyl- or aryllithium to create a readily ionizable compound (Scheme 1.4).

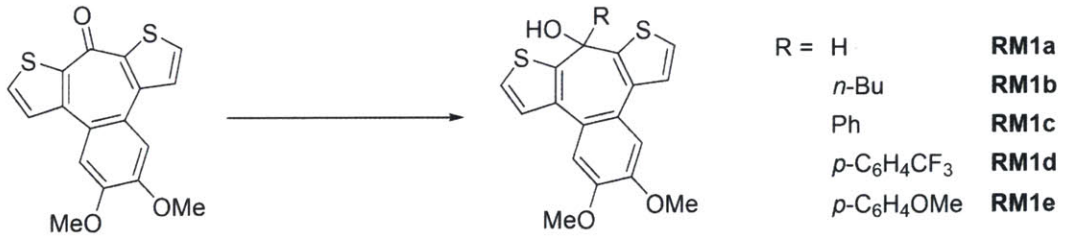

Scheme 1.4. Synthesis of reduced monomers **RM1a–e**.

To evaluate these different constructs, we performed comparative kinetics for the reaction of the respective tertiary and secondary alcohols with DCP, as determined by UV–Vis spectroscopy (Figure 1.5). The addition of a phenyl group resulted in a 100-fold decrease in the pseudo-first-order rate constant compared to that of the secondary alcohol

created by hydride reduction. We attribute this decrease to the increased steric demand of the phenyl adduct in the phosphorylation step. It is important to note that the addition of an aromatic ring does not significantly alter the electronic transitions or chromaticity of the tropylium cation formed upon reacting with the nerve agent simulant.

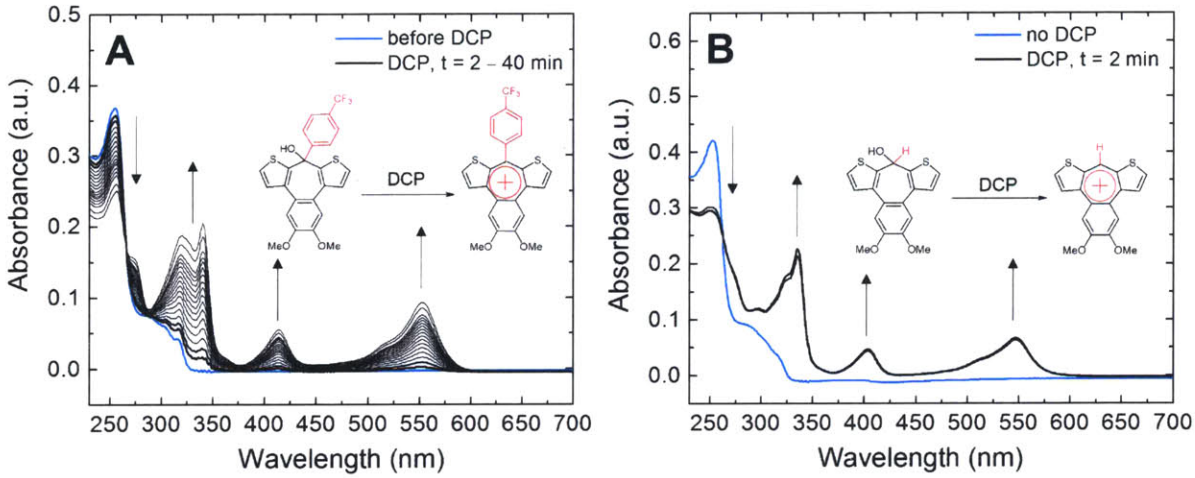

Figure 1.5. UV–Vis absorption spectra of monomers **RM1d** (a) and **RM1a** (b) as a 5 μM solution in CH_2Cl_2 and their response to 100 equivalents DCP (70 ppm) over time. The calculated pseudo-first-order rate constants showed >100-fold enhancement with **RM1a** over **RM1c–e**.

Density functional theory (DFT) calculations (B3LYP/6–31G*) of the tropylium cations suggest that the aromatic ring is oriented nearly perpendicular to the tropylium ring (Figure 1.6). This calculation is in agreement with the observation that there is no significant change in the absorption spectra for different phenyl adducts having *para* electron-donating and -withdrawing groups (Figure 1.8a–c). Similarly, we evaluated the butyl adduct and find no significant alteration of the absorption spectrum or color of the resulting cation, in comparison to that of hydride adduct **RM1a** (Figure 1.8d).

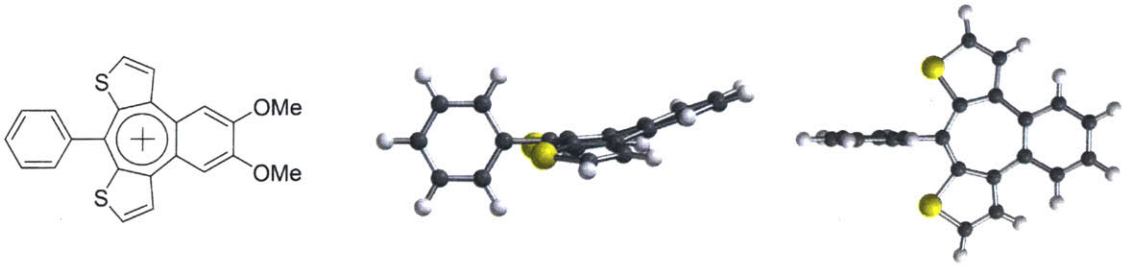

Figure 1.6. Optimized geometry (B3LYP/6–31G*) of the tropylium cation of monomer **RM1c**. The aryl ring attached at the 8-position is orthogonal to the aromatic tropylium ring.

The fully substituted tropylium cations have indefinite stability in ambient conditions; however, those generated from the secondary alcohols began to generate traces of tropones (**M1a** or **M2a**) after a few hours in solution. In this case, we expect that the carbocations, along with secondary alcohols undergo hydrogen atom abstraction reactions that generate the tropones.

We demonstrated that the CWA-responsive monomer can be regenerated from the tropylium cation by washing the cation with a 1M aqueous solution of sodium hydroxide. A change in color from fuchsia to colorless was observed (Figure 1.7), and UV–Vis absorption measurements confirm the regeneration of alcohol **RM1a**.

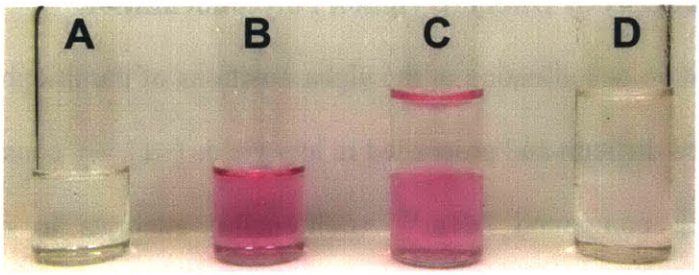

Figure 1.7. Photograph of polymer **RM1a** in a 5 μM CH_2Cl_2 solution before (a) and after (b) addition of 100 equivalents DCP, after washing with water (c), and finally after washing with 1M NaOH (aq.) (d). In (c) and (d), the aqueous layer lies above the organic layer.

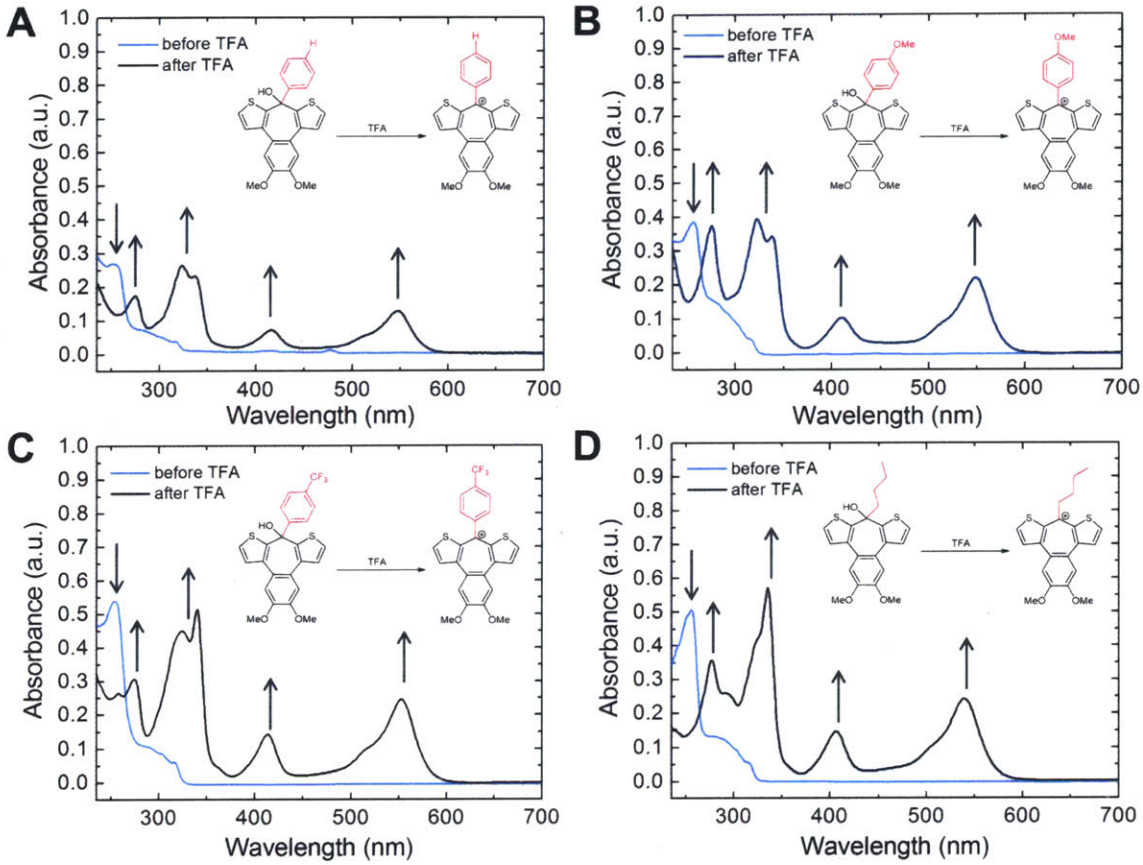

Figure 1.8. UV–Vis absorption spectra of monomers **RM1c** (a), **RM1e** (b), **RM1d** (c), and **RM1b** (d) upon exposure to 100 equivalents of TFA in 5 μM solution of CH_2Cl_2. TFA was used for complete ionization of the compounds.

1.2.3 Polymer Synthesis by Direct Arylation Polycondensation

The bromination or iodination at the alpha positions of the thiophenes in compounds **M1b** and **M1c** proved difficult and proceeded in low yields (<17 %), consistent with previous efforts in iodinating compound **M1a**.[43] Additionally, attempts to copolymerize these compounds by Stille coupling with 5,5′-bis(tributylstannyl)-2,2′-bithiophene yielded only oligomers, although it should be noted that these results may be limited by solubility with methoxy-substituted **M1a**.

Consequently, we chose an alternative, direct arylation polycondensation, in order to circumvent the current limitations in chemical reactivity imposed by **M1a–c**. This strategy — a step-growth polymerization that relies on C–H activation — also eliminates the toxic byproducts associated with Stille couplings and is fundamentally more atom economical. Our initial investigations with Herrmann's catalyst,[47] tris(*o*-anisyl)phosphine, and cesium carbonate in tetrahydrofuran at 120°C resulted in the successful polymerization of regioisomers **M1a** and **M2a** with comonomer 2,7-dibromo-9,9-dioctylfluorene (**CM1**). Although the alternating copolymers were isolated in high yields (>90%), the molecular weights obtained by gel permeation chromatography (GPC) were low for the THF-soluble fractions (< 2.50 kDa), which suggests that the polymerization may be limited by solubility.

To create higher molecular weight materials, we synthesized monomers **M1b** and **M1c**, with solubilizing hexyloxy and 2-ethylhexyloxy groups, respectively, for increased solubility in order to enable the screening of additional conditions for direct arylation polycondensation. We ultimately found the previously reported conditions[55,56] of $Pd(OAc)_2$, $PCy_3 \cdot HBF_4$, pivalic acid, and K_2CO_3 in *N*,*N*-dimethylacetamide at 100°C for 12 hours to be the optimized reaction conditions. Higher molecular weights were obtained, although polymers **P1b** (M_n = 6.20 kDa, Đ = 1.98) and **P1c** (M_n = 7.60 kDa, Đ = 2.61) exhibited only moderate solubility in organic solvents, despite the inclusion of two solubilizing 2-ethylhexyl chains in polymer **P1c**.

To obtain CWA-responsive polymers, we reduced polymers **P1b** and **P1c** to polymers **RP1b** and **RP1c**, respectively, by post-polymerization modification using sodium borohydride at 40°C in tetrahydrofuran/methanol (4:1) (Scheme 1.5).

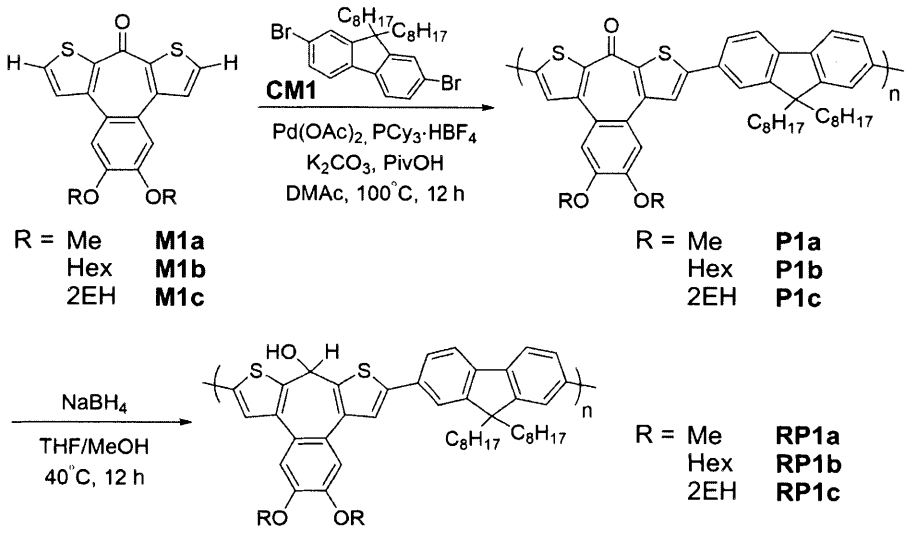

Scheme 1.5. Direct arylation polycondensation of monomers **M1a–c** and 9,9-dioctyl-2,7-dibromofluorene (**CM1**) to alternating copolymers **P1a–c** and their subsequent reduction to **RP1a–c**.

The resulting alcohol-containing polymers exhibited markedly improved solubility in organic solvents, and the UV–Vis and fluorescence spectra (Figure 1.9) reveal hypsochromic shifts upon reduction, which is expected considering the conversion from the highly delocalized dithienobenzotropone-containing polymer **P1c** to the reduced, cross-conjugated polymer **RP1c**.

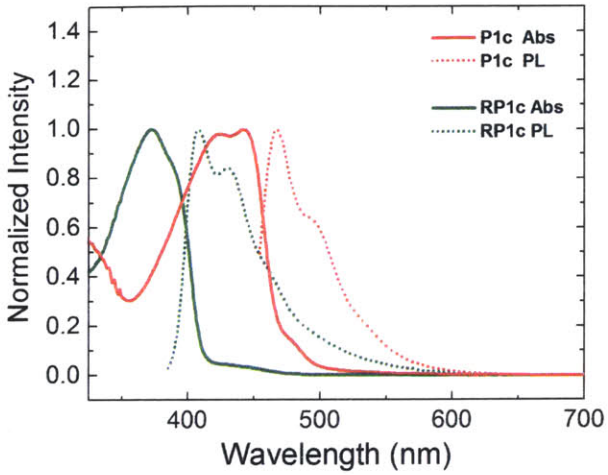

Figure 1.9. UV–Vis absorption (solid) and fluorescence (dotted) spectra of polymers **P1c** (red) and **RP1c** (green).

Various other copolymers were targeted from **P1c**, specifically those replacing the fluorene comonomer unit with a thiophene or bithiophene (Scheme 1.6). The increased donor–acceptor character between the tropylium cation and electron-rich bithiophenes in particular resulted in large bathochromic shifts of greater than 50 nm in the absorption spectra (Figure 1.10) in comparison to the resulting polymer with the fluorene-based comonomer (Figure 1.11). Unfortunately, limited solubility for both the parent and reduced bithiophene-containing polymers prevented further characterization. It is important to note that the strong bathochromic shift in the bithiophene-containing polymer **RP3** relative to thiophene-containing polymer **RP4** could be attributed to either increased donor–acceptor character or increased solubility during the polymerization resulting in higher molecular weights and consequently conjugation lengths. Polymer **RP3**'s red shift relative to bithiophene-containing **RP2**, however, is likely due to the increased conjugation lengths caused by increased solubility during the polymerization. A similar effect is observed in alkyl-containing thiophene **RP4** in comparison to thiophene **RP5**.

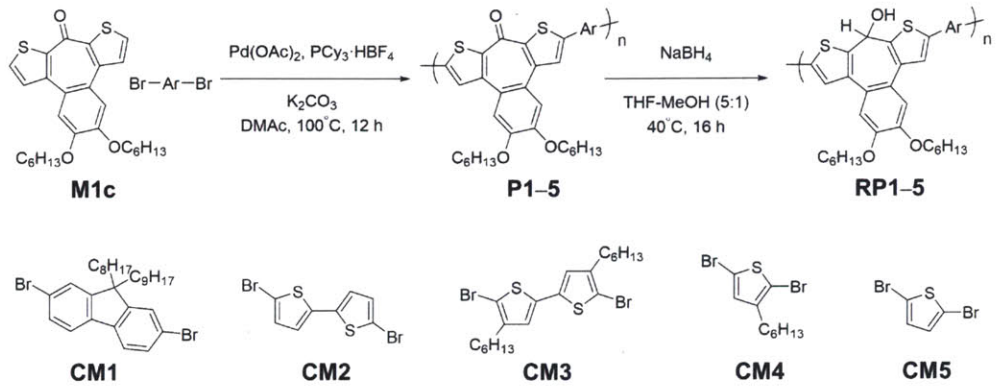

Scheme 1.6. Synthesis of polymers **P1c–5** and **RP1c–5**.

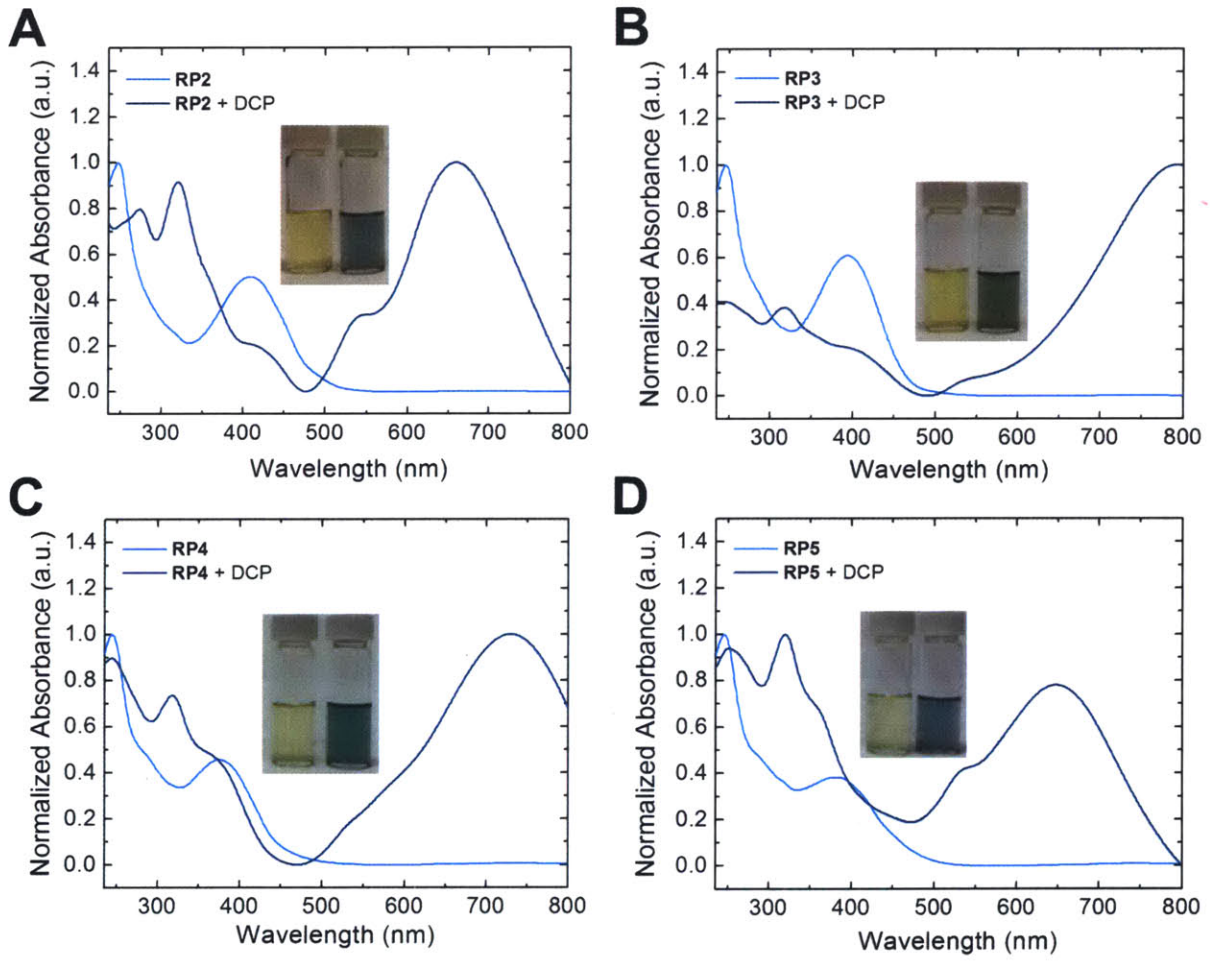

Figure 1.10. UV–Vis absorption spectra of polymers **RP2** (a), **RP3** (b), **RP4** (c), and **RP5** (d) in 5 μg/mL solutions in CH_2Cl_2 and their response to 40 ppm DCP.

1.2.4 Polymer Response to DCP

To examine the polymers' response to DCP in solution, we exposed a 5 μg/mL solution of **RP1c** (Scheme 1.5) in dichloromethane to 40 ppm DCP. We chose **RP1c** as a result of its increased solubility in comparison to **RP1a**, **RP1b**, and **RP2–5**. The UV–Vis absorption spectrum displayed a strong, bathochromic shift upon exposure to DCP, shifting the absorption onset from 480 nm in **RP1c** to 784 nm (Figure 1.11). This process functions well as a colorimetric detection scheme, with an immediate change in color from colorless to bright blue (Figure 1.11b, c). We also successfully regenerated the parent reduced material by washing the organic layer with 1M sodium hydroxide (Figure 1.12).

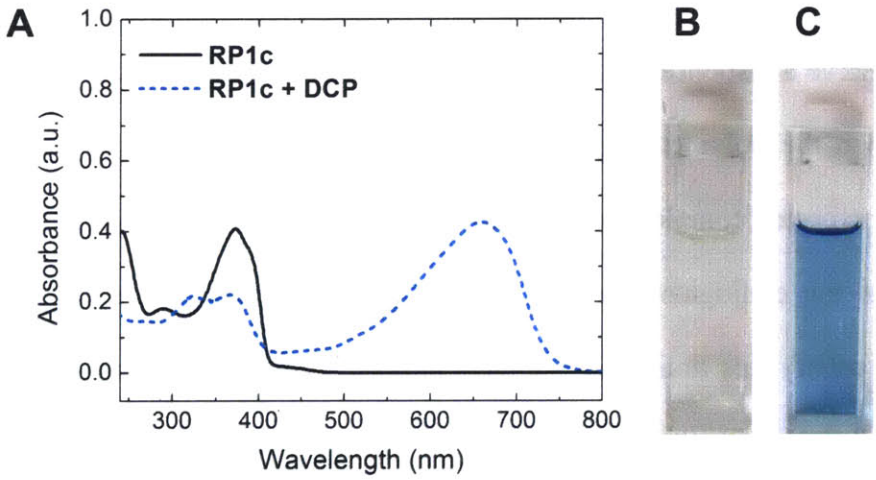

Figure 1.11. (a) UV–Vis absorption spectrum of a 5 μg/mL solution of polymer **RP1c** in CH_2Cl_2 (black, solid line) and after addition of DCP (blue, dashed line). Photographs of solution (b) before and (c) after addition of DCP.

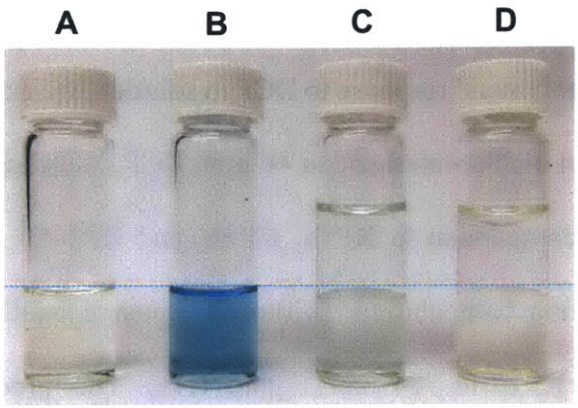

Figure 1.12. Photograph of polymer **RP1c** in 5 μg/mL CH_2Cl_2 solution before (a) and after (b) addition of 100 equivalents DCP, after washing with water (c), and finally after washing with 1M NaOH (aq.) (d). In (c) and (d), the aqueous layer lies above the organic layer.

To investigate thin-film responses of **RP1b** and **RP1c**, we spin-coated the polymers onto glass microscope cover slides. This initial approach was unsuccessful, and we were unable to observe a response with saturated DCP vapor. A small spectroscopic response was observed when the polymer film was exposed to concentrated trifluoroacetic acid vapor, although we expected complete conversion under such extreme conditions. Consequently, we reasoned that the conjugated polymer thin film exhibits low permeability to the desired analytes. To rectify this limitation, we have targeted conjugated polymers with plasticizing tetra(ethylene glycol) monomethyl ether side chains to promote a more breathable material. This property was expected to facilitate percolation of the analyte into the membrane, giving rise to enhanced colorimetric and spectroscopic responses in the thin film.[57]

1.2.5 Synthesis of TEG-Containing Monomer

The high polarity and diverse solubility of tetra(ethylene glycol)-containing dithienylbenzene precursors can present difficulties in the purification of the various intermediates. To best prepare monomer **M1d**, we opted to add the polar groups at a late stage

in the synthesis by modifying **M1a** through deprotection of the methoxy groups with boron tribromide and subsequent dialkylation with tetra(ethylene glycol) monomethyl ether tosylate with an overall yield of 78%, as shown in Scheme 1.7. It is important to note that the intermediate catechol is air-sensitive and insoluble in common organic solvents, and appropriate synthetic measures must be followed to avoid its decomposition, as discussed in the experimental details.

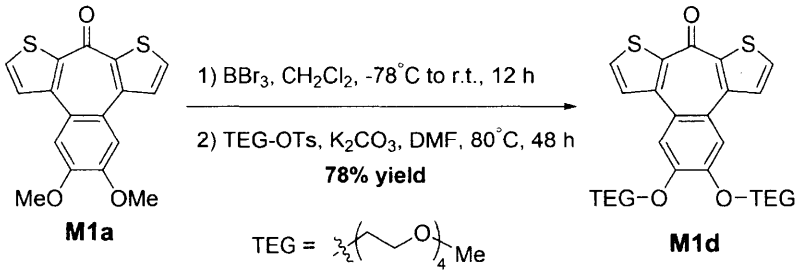

Scheme 1.7. Synthesis of tetra(ethylene glycol) monomethyl ether-substituted monomer **M1d** from monomer **M1a**.

1.2.6 Thin-Film Response of TEG-Containing Polymers to DCP

Direct arylation polycondensation of monomer **M1d** with dibromofluorene **CP1** yielded polymer **P1d** (Scheme 1.8) with an improved number-average molecular weight of 12.2 kDa (Đ = 1.90) determined by GPC, as compared to polymers **P1b** and **P1c**. We ascribe this increased molecular weight to the favorable solubilizing effect of the tetra(ethylene glycol) monomethyl ether side chains. Polymer **P1d** was subsequently reduced to polymer **RP1d** (M_n = 16.6 kDa, Đ = 1.91) with sodium borohydride (Scheme 1.8). The discrepancy in the molecular weight can be attributed to a conformational change upon reduction and an increased affinity for the tetrahydrofuran solvent. The nearly identical Đ values and unimodal distributions by GPC suggest that no degradation to the polymer backbone occurred.

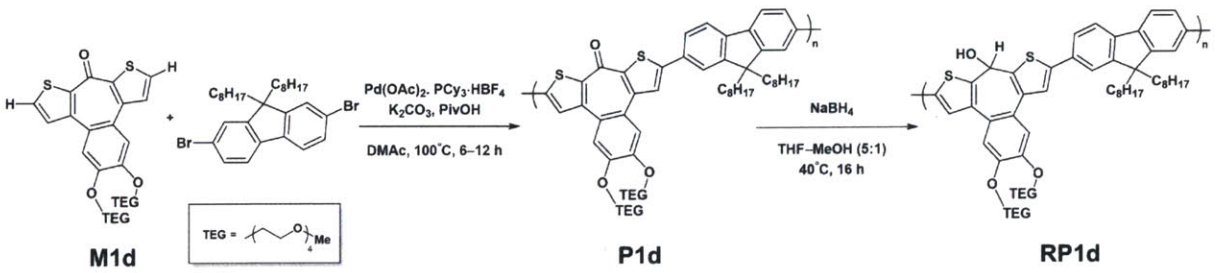

Scheme 1.8. Synthesis of polymer **P1d** by direct arylation polycondensation and subsequent reduction to CWA-responsive polymer **RP1d**.

Tetra(ethylene glycol) monomethyl ether-containing polymer **RP1d** behaves similarly to 2-ethylhexyl-containing polymer **RP1c** in its response to CWA simulants DCP and diisopropyl fluorophosphate (DFP) in a solution of dichloromethane (Figure 1.13 and Figure 1.15), undergoing a colorimetric change from faint yellow to bright blue and exhibiting a strong bathochromic shift in the absorption spectrum. Polymer **RP1d** has a detection limit of 6 ppm for DCP (Figure 1.14) and exhibits no response to possible interferents dimethyl methylphosphonate, pinacolyl methylphosphonate, and acetic acid (Figure 1.15).

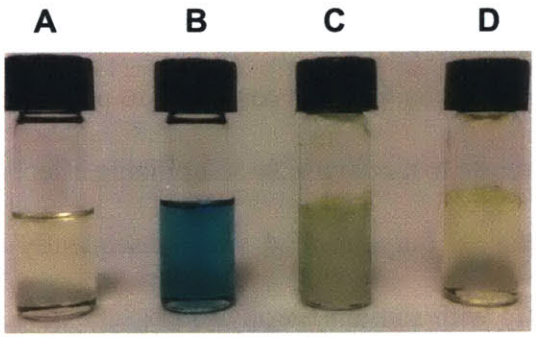

Figure 1.13. Photograph of polymer **RP1d** in 5 μg/mL CH_2Cl_2 solution before (a) and after (b) addition of 40 ppm DCP, after washing with water (c), and finally after washing with 1M NaOH (aq.) (d). In (c) and (d), the aqueous layer lies above the organic layer.

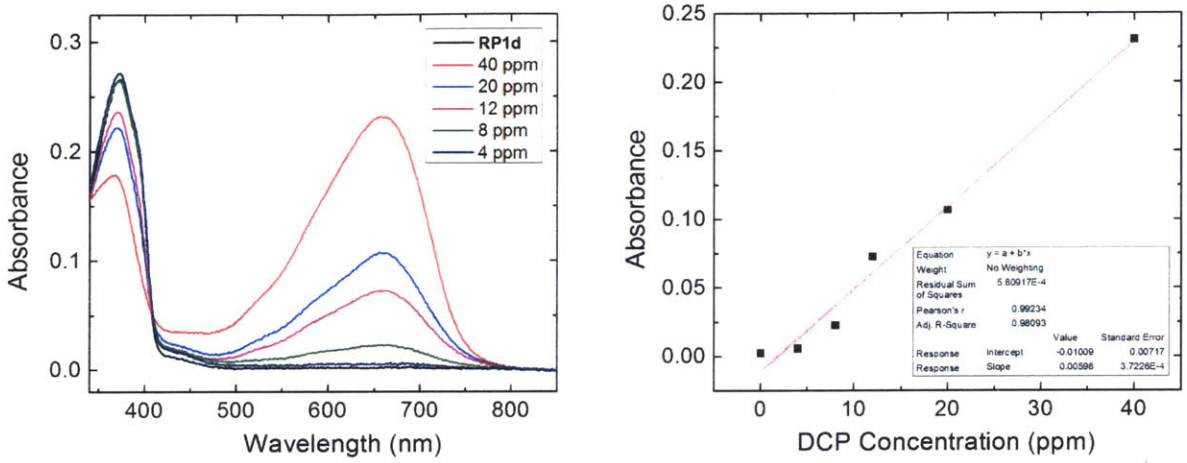

Figure 1.14. Response of polymer **RP1d** (5 μg/mL) to different concentrations of DCP in CH_2Cl_2. The calculated limit of detection is 6 ppm.

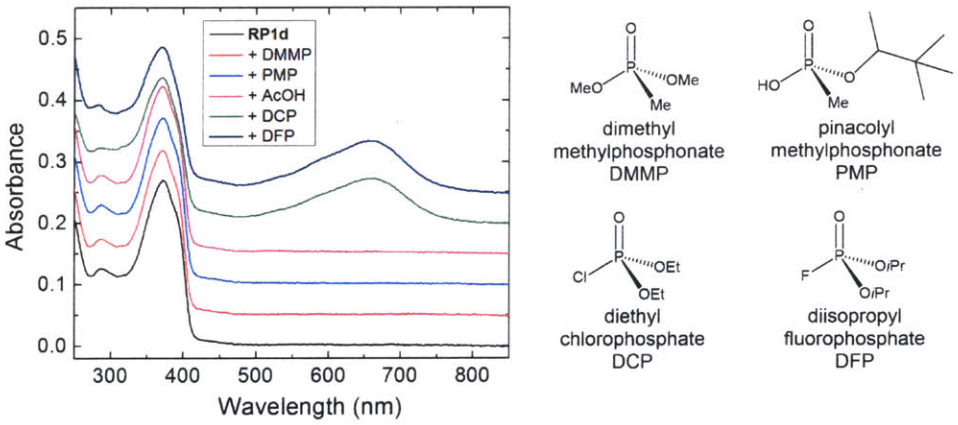

Figure 1.15. Response of polymer **RP1d** (5 μg/mL) in CH_2Cl_2 to 100 μM analyte. Dimethyl methylphosphonate (DMMP), pinacolyl methylphosphonate (PMP), and acetic acid (AcOH) were tested as interferents. Diethyl chlorophosphate (DCP) and diisopropyl fluorophosphates (DFP) were tested as agent simulants.

Gratifyingly, thin films of polymer **RP1d** also gave strong colorimetric and spectroscopic responses to DCP vapor, as shown in Figure 1.16. This response is consistent with the increased breathability of the TEG-containing thin film facilitating permeation of the analyte into the film, as compared to the nonresponsive 2-ethylhexyl-containing polymer. The

thin-film response of polymer **RP1d** to trifluoroacetic acid vapor is also significantly enhanced (>200% of the response of **RP1c**). The thickness of the films of **RP1c** were approximately 50 nm, as measured by profilometry, and thinner films could enhance the response. However, it is also likely that the mechanical properties of the film are critical for diffusion. Polymer **RP1d**, possessing plasticizing components, is sufficiently soft that thickness could not be measured by profilometry. The polymer dynamics in this case likely enhance diffusion into the polymer films.

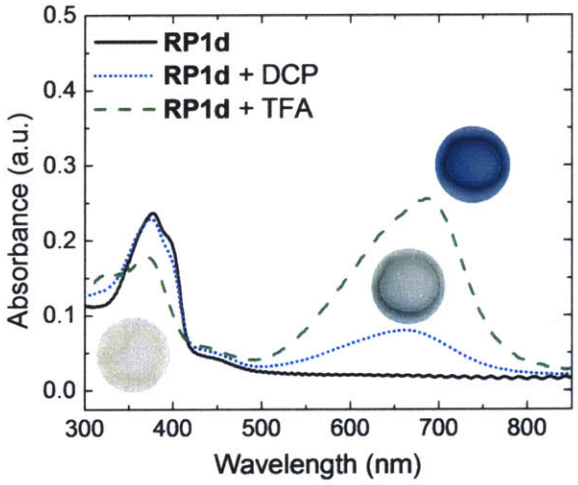

Figure 1.16. UV–Vis absorption spectrum of polymer **RP1d** as a thin film (a) before (black, solid line) and after exposure to saturated vapor of (b) DCP (blue, dotted line) and (c) TFA (green, dashed line).

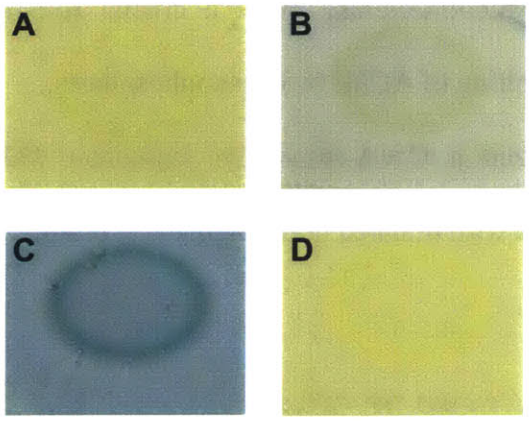

Figure 1.17. Photographs of thin films of polymer **RP1d** before (a) and after (b) exposure to saturated DCP vapor. The response is further intensified by exposure to TFA (c), and the active material can be regenerated by exposure to ammonium hydroxide vapor (d).

Although we were able to successfully regenerate the active alcohol-containing polymers in solution by washing with basic aqueous solution, a vapor-phase regeneration is ideal for thin-films. With the improved breathability of the tetra(ethylene glycol)-containing polymer, we were able to successfully convert the cationic polymer back to the reactive cross-conjugated polymer by exposure to ammonium hydroxide vapor (Figure 1.17).

1.2.7 CWA-responsive Polymers Prepared by ROMP

In addition to polymers prepared by direct arylation polycondensation, we sought CWA-responsive materials prepared by ring-opening metathesis polymerization (ROMP). The key advantages of materials prepared by ROMP are that their properties and functionality are highly modular, and higher molecular weights are more easily obtained in comparison to direct arylation polymerization. By tuning monomer structure and feed ratios, an optimal balance of sensitivity and breathability can be obtained. Furthermore, monomer units that incorporate phosphorylation catalysts and acid suppressants could be incorporated to increase reaction kinetics and mitigate false positives, respectively. For example, the imidazole moiety of a

histidine residue in acetylcholinesterase plays a crucial role in both the hydrolysis of acetylcholine and the inhibition of AChE by organophosphates.[3]

We first synthesized a CWA-responsive monomer **M3** for ROMP by reacting dithienobenzotropone **M1c** with lithiated norbornenyl aryl bromide **10** in 72% yield, as shown in Scheme 1.9.

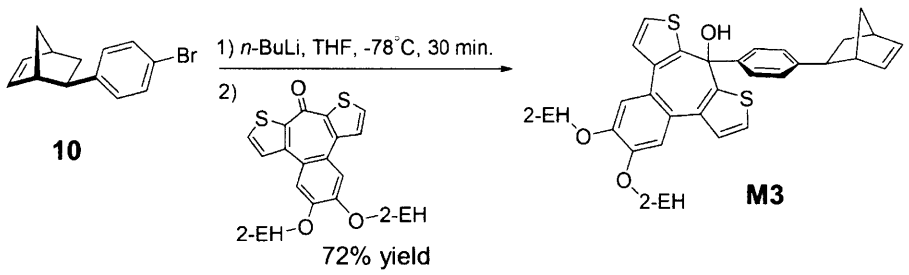

Scheme 1.9. Synthesis of CWA-responsive monomer **M3** from dithienobenzotropone **M1c**. Norbornene **10** was synthesized by Pd-catalyzed hydroarylation of norbornadiene according to literature procedure.[58]

We then prepared two random copolymers of **M3** by ROMP with Grubbs' third generation catalyst **G3**, as shown in Scheme 1.10. Random copolymer **RCP1** was synthesized with 15% CWA-responsive monomer **M3**, 30% alkyl-containing comonomer **CM6**, and 55% hydrogel-promoting monomer **CM7** to yield a colorless, sticky solid with M_n = 68.5 kDa and a Đ of 1.19, as measured by GPC. The hydrogel-free analogue **RCP2** was prepared similarly with 10% monomer **M3** and 90% comonomer **RCP2** to afford a colorless, sticky solid with M_n = 63.1 kDa and a Đ of 1.25, as measured by GPC. The inclusion of the alkyl component in both polymers was necessary to promote uniform thin films prepared by dropcasting or spin-coating.

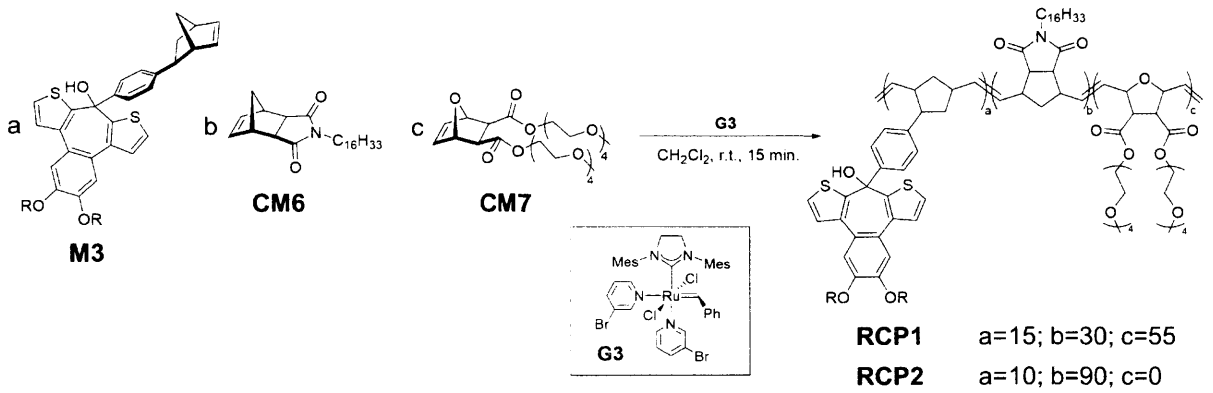

Scheme 1.10. Synthesis of random copolymers **RCP1** and **RCP2** by ROMP initiated with Grubbs' 3rd generation catalyst **G3**.

In order to examine the reactivity of copolymers **RCP1** and **RCP2**, we exposed the polymers to varying concentrations of the CWA simulant DCP and measured their behavior by UV–Vis spectroscopy. Both polymers produce an identical pink color, consistent with the formation of the dithienobenzotropylium cation. It is important to note that this color is consistent with the expected monomeric chromophore rather than the conjugated chromogenic polymers **RP1–5** examined in the previous section. We do not expect the inclusion of comonomers **CM6** or **CM7** into the copolymer to influence the colorimetric or spectroscopic signatures of the material.

$$LoD = \frac{3}{m}\sqrt{\frac{SS}{n-1}} \quad (1)$$

The limits of detection (LoD) for polymers **RCP1** and **RCP2** were determined by plotting the absorbance at 554 nm vs. DCP concentration obtained from the data shown in the insets in Figure 1.18c and Figure 1.19c. The resulting plots are shown in Figure 1.18d for **RCP1** and Figure 1.19d for **RCP2**. Assuming that $A_{554nm} = 0$, the LoD can then be determined with Equation 1, where *m* is the slope of the linear regression for the measured absorbance at

554 nm vs. DCP concentration (ppm), *SS* is the residual sum of squares for the linear regression, and *n* is the number of data points.

The limit of detection for **RCP1** was determined to be 3.3 ppm, whereas the limit of detection for **RCP2** was calculated at 1.2 ppm. These comparable values are expected for the solution detection scheme using the same chromogenic monomer unit, and the lower LoD for **RCP2** can be attributed to the less accurate fit of the regression line.

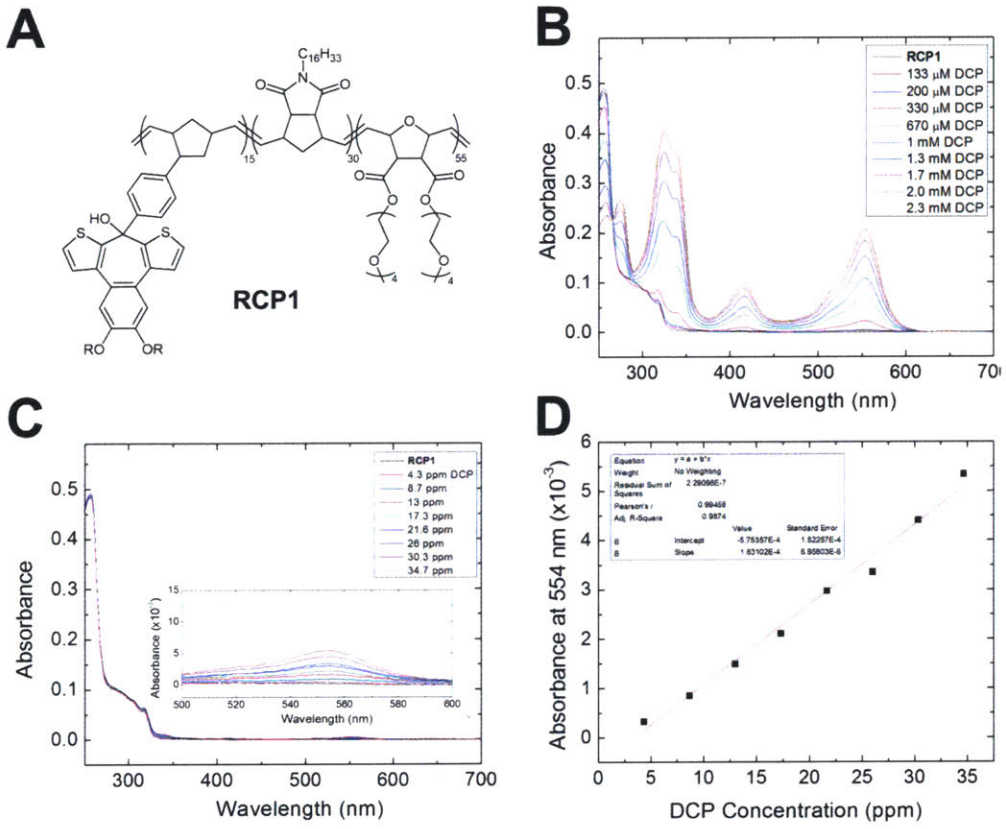

Figure 1.18. Response of **RCP1** to DCP in CH_2Cl_2 at varying concentrations and calculation for limit of detection (3.3 ppm).

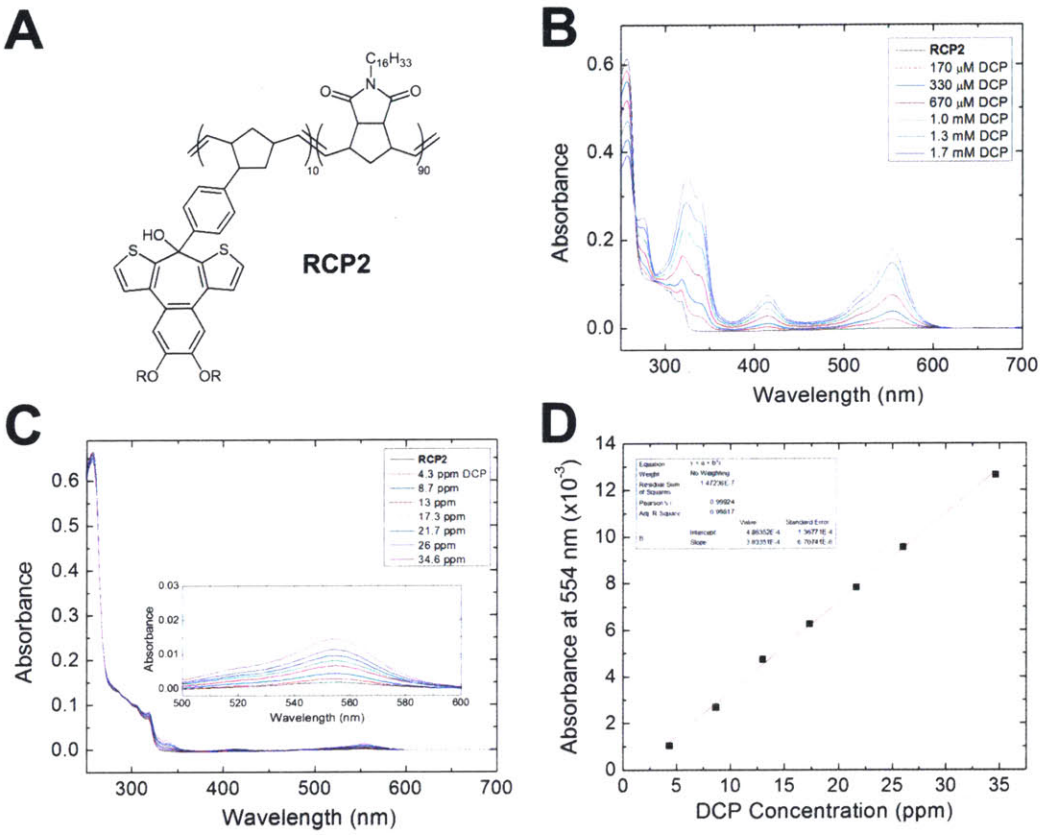

Figure 1.19. Response of **RCP2** to DCP in CH_2Cl_2 at varying concentrations and calculation for limit of detection (1.2 ppm).

Although measurements in solution are excellent for initial screening of reactivity, practical applications demand a chromogenic thin film. We spincoated 10 mg/mL solutions of **RCP1** and **RCP2** in chloroform onto glass slides and monitored their color and UV–Vis absorption spectra, as shown in Figure 1.20. The films turn bright pink upon exposure to DCP or TFA for 30 seconds and can be regenerated upon exposure to ammonium hydroxide vapor. It is interesting to note that copolymer **RCP1** responds similarly to DCP and TFA, whereas copolymer **RCP2** exhibits a significantly stronger response to TFA than DCP. This observation is consistent with the proposal that the incorporated hydrogel-promoting

monomers facilitate greater percolation of the DCP into the film in comparison to their strictly alkyl analogues.

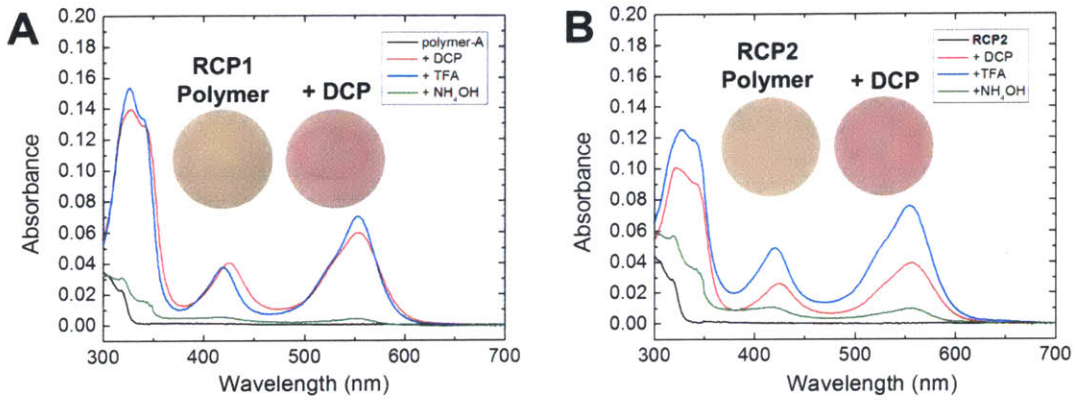

Figure 1.20. Response of polymers a) **RCP1** and b) **RCP2** to concentration vapors of DCP and TFA and resulting regeneration with exposure to NH_4OH vapor.

1.3 Conclusions

In conclusion, we have synthesized a cross-conjugated polymer that undergoes rapid phosphorylation and ionization to form an aromatic, conjugated polymer upon exposure to the CWA simulant DCP in solution and thin films. The resulting cationic copolymer is highly colored and enables the colorimetric and spectroscopic detection of the nerve agent simulant diethyl chlorophosphate. Direct arylation polycondensation was essential to achieve sufficiently high molecular weights (>10 kDa), and the inclusion of plasticizing tetra(ethylene glycol) monomethyl ether side chains was critical to increasing the molecular weight and thin-film permeability of the polymer to the analyte. Furthermore, we have demonstrated that ROMP can be used to create CWA-responsive polymers whose properties are highly modular. With the inclusion of these moieties that undergo electronic and conformational changes upon exposure to CWAs, we envision a class of stimuli-responsive materials that not only detect the

presence of chemical threats, but also functionally respond by undergoing conformational changes that affect their physical properties.

1.4 Experimental Details

1.4.1 General

All air- and water-sensitive syntheses were performed in flame-dried flasks under an inert atmosphere with dry argon using standard Schlenk techniques. Diethyl ether, tetrahydrofuran, dichloromethane, and toluene were taken from an Innovative Technologies solvent purification system containing activated alumina columns and stored under argon over 3Å or 4Å molecular sieves. The progress of reactions was monitored by thin layer chromatography (Merck silica gel 60 F254 plates), and column chromatography was performed using silica gel (60Å pore size, 230–500 mesh, Aldrich). ^{1}H (and ^{13}C) NMR spectra were recorded at 400 MHz (100 MHz) or 500 MHz (125 MHz) using Bruker AVANCE-400 or Varian Inova-500 NMR spectrometers, respectively. Chemical shifts are reported in ppm and referenced to residual NMR solvent peaks ($CDCl_3$: δ 7.26 for ^{1}H and δ 77.16 for ^{13}C). High resolution mass spectra were determined with a Bruker Daltonics APEXIV 4.7 Tesla FT–ICR–MS using ESI or DART ionization. UV–Vis absorption spectra were measured using an Agilent Cary 4000 Series UV–Vis spectrophotometer. Fluorescence measurements were taken using a Horiba Jobin Yvon SPEX Fluorolog-τ3 fluorometer (model FL-321, 450 W Xenon lamp) using right-angle detection. Gel permeation chromatography (GPC) measurements were performed in tetrahydrofuran using an Agilent 1260 Infinity system and calibrated with a polystyrene standard. ATR–FTIR spectra were acquired using a Thermo Scientific Nicolet 6700 FT–IR with a Ge crystal for ATR and subjected to the 'atmospheric suppression' correction in OMNIC™ Specta software.

1,2-dibromo-4,5-bis(hexyloxy)benzene (**3b**),[59] 3,3′-(4,5-bis((2-ethylhexyl)oxy)-1,2-phenylene)bis(2-bromothiophene) (**5c**),[60,61] 2,3-dimethoxy-8*H*-benzo[6,7]cyclohepta[2,1-*b*:4,5-*b*′]dithiophen-8-one (**M1a**),[43] 2,2′-(4,5-dimethoxy-1,2-phenylene)dithiophene (**6**),[54] tetraethylene glycol monomethyl ether tosylate,[62] and catalyst **G3**[63] were prepared according to literature procedures. 9,9-dioctyl-2,7-dibromofluorene (**CM1**) was purchased and recrystallized before use. All other chemicals were commercially available and used as received.

1.4.2 Synthesis of Monomers

4b. 3,3′-(4,5-Bis(hexyloxy)-1,2-phenylene)dithiophene. Compound **3b** (6.50 g, 14.9 mmol), 3-thienylboronic acid (4.39 g, 34.3 mmol, 2.3 equiv.), and sodium carbonate (12.63 g, 119.2 mmol, 8.0 equiv.) were added to a mixture of 260 mL toluene, 60 mL ethanol, and 60 mL water. The mixture was then sparged with argon for 30 minutes before adding tetrakis(triphenylphosphine) palladium(0) (860 mg, 0.75 mmol, 0.05 equiv.). The reaction mixture was stirred and heated at 90°C for 48 hours. After cooling to room temperature, the reaction mixture was diluted with diethyl ether, washed twice with 1M NaOH (aq.) and once with brine. The organic phase was dried over sodium sulfate, and the solvent was removed under reduced pressure. The product was purified by column chromatography (SiO_2, 35% CH_2Cl_2 in hexanes) to afford a white solid (6.59 g, 99% yield). mp 68–70°C. ^{1}H NMR (400 MHz, $CDCl_3$) δ 7.19 (dd, 2H), 7.04 (dd, 2H), 6.99 (s, 2H), 6.80 (dd, 2H), 4.08 (t, 4H), 1.87 (m, 4H), 1.51 (m, 4H), 1.38 (m, 8H), 0.94 (t, 6H). ^{13}C NMR (100 MHz, $CDCl_3$) δ 148.4, 142.1, 129.1, 128.0, 124.5, 122.3, 115.8, 69.5, 31.6, 29.3, 25.7, 22.6, 14.0. HRMS (ESI) calc for $C_{26}H_{34}O_2S_2$ $[M+H]^+$ 443.2073, found 443.2064. FT–IR (ATR, ν/cm^{-1}): 3096 (w), 2954 (m),

2931 (m), 2859 (m), 1601 (w), 1536 (w), 1504 (m), 1466 (m), 1427 (w), 1385 (m), 1339 (w), 1307 (w), 1259 (m), 1229 (w), 1211 (w), 1202 (w), 1163 (m), 1078 (w), 1056 (w), 1046 (w), 1015 (w), 1002 (w), 927 (w), 850 (m), 798 (w), 780 (s), 728 (w).

5b. 3,3′-(4,5-Bis(hexyloxy)-1,2-phenylene)bis(2-bromothiophene). Compound **4b** (5.00 g, 11.3 mmol) was dissolved in 250 mL of $CHCl_3$/AcOH (1:1) and cooled in an ice bath. *N*-bromosuccinimide (4.02 g, 22.7 mmol, 2 equiv.) was added in portions before allowing the reaction mixture to slowly warm to room temperature overnight. The reaction mixture was then washed twice with water, twice with saturated sodium bicarbonate, and once with brine before drying over sodium sulfate and removing the solvent under reduced pressure. The clear, light brown oil (6.60 g, 97% yield) was used without further purification. ^{1}H NMR (400 MHz, $CDCl_3$) δ 7.10 (d, 2H), 6.99 (s, 2H), 6.55 (d, 2H), 4.09 (t, 4H), 1.87 (m, 4H), 1.50 (m, 4H), 1.38 (m, 8H), 0.93 (t, 6H).

M1b. 2,3-Bis(hexyloxy)-8*H*-benzo[6,7]cyclohepta[2,1-*b*:4,5-*b*′]dithiophen-8-one. Compound **5b** (6.60 g, 11.0 mmol) was dissolved in 400 mL of diethyl ether and cooled to −78°C. *n*-Butyllithium (2.5 M, 9.7 mL, 24.2 mmol, 2.2 equiv.) was then added, and the reaction mixture was stirred at 0°C for 3 hours. The reaction mixture was cooled again to −78°C, and dimethylcarbamyl chloride (1.18 g, 1.01 mL, 11.0 mmol, 1.0 equiv.) was added in one portion. The reaction mixture was allowed to slowly warm to room temperature overnight. The solvent was removed under reduced pressure, and the crude material was redissolved in dichloromethane and washed once with water and once with brine. The organic layer was dried over sodium sulfate, and the solvent was removed under reduced pressure. The product was purified by column chromatography (SiO_2, CH_2Cl_2) to afford a bright yellow solid (3.78 g, 74% yield). mp 99–101°C. ^{1}H NMR (400 MHz, $CDCl_3$) δ 7.84 (d, 2H), 7.78 (d, 2H), 7.63 (s,

2H), 4.18 (t, 4H), 1.93 (m, 4H), 1.55 (m, 4H), 1.40 (m, 8H), 0.97 (t, 6H). ^{13}C NMR (100 MHz, $CDCl_3$) δ 175.5, 149.5, 141.0, 140.9, 132.5, 129.0, 125.8, 114.0, 69.4, 31.6, 29.2, 25.7, 22.6, 14.0. HRMS (ESI) calc for $C_{27}H_{32}O_3S_2$ $[M+H]^+$ 469.1866, found 469.1870. FT–IR (ATR, ν/cm^{-1}): 3094 (w), 2954 (m), 2927 (m), 2855 (m), 1607 (w), 1576 (w), 1557 (s), 1529 (w), 1504 (w), 1447 (s), 1418 (w), 1389 (m), 1332 (w), 1275 (s), 1250 (w), 1178 (m), 1139 (m), 1099 (m), 1073 (w), 1048 (w), 996 (w), 930 (w), 854 (m), 801 (m), 768 (s), 724 (w), 706 (w).

M1c. 2,3-Bis((2-ethylhexyl)oxy)-8*H*-benzo[6,7]cyclohepta[2,1-*b*:4,5-*b*']dithiophen-8-one. was prepared from **5c** using the same procedure for monomer **M1b**. The product was purified by column chromatography (SiO_2, 30% hexanes in CH_2Cl_2) to give a bright yellow solid (68% yield). mp 82–84°C. ^{1}H NMR (400 MHz, $CDCl_3$) δ 7.88(d, 2H), 7.80 (d, 2H), 7.65 (s, 2H), 4.08 (t, 4H), 1.87 (m, 2H), 1.65–1.35 (m, 16H), 1.01 (t, 6H), 0.95 (t, 6H). ^{13}C NMR (100 MHz, $CDCl_3$) δ 175.5, 149.8, 141.0, 140.9, 132.6, 129.1, 125.7, 113.5, 71.6, 39.6, 30.7, 29.2, 24.0, 23.1, 14.1, 11.3. HRMS (ESI) calc for $C_{31}H_{40}O_3S_2$ $[M+H]^+$ 525.2492, found 525.2491. FT–IR (ATR, ν/cm^{-1}): 3088 (w), 2955 (m), 2927 (m), 2871 (m), 1607 (w), 1569 (w), 1548 (s), 1527 (w), 1503 (w), 1448 (s), 1422 (w), 1387 (m), 1336 (w), 1271 (s), 1183(m), 1145 (m), 1097 (m), 1046 (m), 1006 (w), 923 (w), 852 (m), 800 (m), 772 (s), 731 (w), 708 (w).

7. 5,5′-(4,5-Dimethoxy-1,2-phenylene)bis(2,4-dibromothiophene). To a mixture of 2,2′-(4,5-dimethoxy-1,2-phenylene)dithiophene (**6**) (1.5 g, 5.0 mmol) in 100 mL $CHCl_3$/AcOH (1:1) was added *N*-bromosuccinimide (3.62 g, 20.3 mmol, 4.1 equiv.) in portions at 0°C. The reaction mixture was allowed to stir and slowly warm to room temperature overnight. The reaction mixture was diluted with $CHCl_3$, washed twice with water, twice with 1M NaOH (aq.), and once with brine before drying over sodium sulfate and removing the solvent under reduced pressure. The product was purified by column chromatography (SiO_2, 1:1

hexanes:CH_2Cl_2) as a white solid (2.41 g, 79% yield). mp 163–165°C. ^{1}H NMR (400 MHz, $CDCl_3$) δ 6.98 (s, 2H), 6.96 (s, 2H), 3.96 (s, 6H). ^{13}C NMR (100 MHz, $CDCl_3$) δ 149.3, 138.2, 132.4, 124.6, 114.3, 112.9, 110.0, 56.1. HRMS (ESI) calc for $C_{16}H_{10}Br_4O_2S_2$ M^+ 617.6815, found 617.6805. FT–IR (ATR, ν/cm^{-1}): 3087 (w), 3005 (w), 2953 (w), 2904 (w), 2833 (w), 1600 (m), 1537 (m), 1495 (s), 1464 (m), 1448 (m), 1430 (m), 1377 (w), 1338 (m), 1296 (w), 1263 (s), 1225 (s), 1149 (m), 1124 (m), 1040 (w), 1015 (m), 973 (m), 867 (s), 822 (s), 812 (s), 779 (m).

8. ((4,5-Dimethoxy-1,2-phenylene)bis(4-bromothiophene-5,2-diyl)) bis(trimethyl silane). To a solution of compound **7** (500 mg, 0.81 mmol) in 15 mL diethyl ether was added dropwise *n*-butyllithium (2.4M, 0.69 mL, 1.66 mmol, 2.05 equiv.) at −78°C. After stirring for one hour, trimethylsilyl chloride (352 mg, 0.41 μL, 3.24 mmol, 4.00 equiv.) was added, and the reaction was allowed to slowly warm to room temperature overnight. Water was added to quench the reaction, and the solvent was then removed under reduced pressure. The product was extracted with CH_2Cl_2 and washed once with water and once with brine. The organic layer was then dried over sodium sulfate, and the solvent was removed under reduced pressure. The product was passed through a plug of silica gel and used without additional purification (350 mg, 71% yield). ^{1}H NMR (400 MHz, $CDCl_3$) δ 7.08 (s, 2H), 7.04 (s, 2H), 3.97 (s, 6H), 0.28 (s, 18H). ^{13}C NMR (100 MHz, $CDCl_3$) δ 148.7, 141.9, 141.4, 136.2, 125.6, 114.0, 111.8, 56.1, −0.4.

9. 2,3-Dimethoxy-6,10-bis(trimethylsilyl)-8*H*-benzo[6,7]cyclohepta[1,2-*b*:5,4-*b*′] dithiophen-8-one. To a solution of compound **8** (350 mg, 580 μmol) in 100 mL dry diethyl ether was added *n*-butyllithium (2.4M, 530 μL, 1.3 mmol, 2.2 equiv.) at −78°C. The reaction mixture was warmed to 0°C and then stirred for an hour before cooling to −78°C.

Dimethylaminocarbamoyl chloride (62 mg, 53 μL, 580 μmol, 1.0 equiv.) was then added in one portion, and the reaction mixture was allowed to slowly warm to room temperature overnight. The reaction was quenched with water before removing the solvent under reduced pressure, and the crude material was redissolved in dichloromethane and washed once with water and once with brine. The organic layer was dried over sodium sulfate, and the solvent was removed under reduced pressure. The product was purified by column chromatography (SiO_2, $CHCl_3$) (175 mg, 64% yield). dec. pt. 235–237°C. ^{1}H NMR (400 MHz, $CDCl_3$) δ 8.01 (s, 2H), 7.57 (s, 2H), 4.09 (s, 6H), 0.42 (s, 18H). ^{13}C NMR (100 MHz, $CDCl_3$) δ 151.5, 149.8, 140.8, 139.4, 137.8, 123.4, 111.5, 56.1, 0.3. HRMS (ESI) calc for $C_{23}H_{28}O_3S_2Si_2$ $[M+H]^+$ 473.1091, found 473.1102. FT–IR (ATR, ν/cm^{-1}): 2956 (w), 2896 (w), 2839 (w), 1602 (m), 1562 (w), 1527 (m), 1466 (w), 1439 (w), 1408 (w), 1367 (w), 1303 (w), 1265 (m), 1259 (m), 1248 (m), 1210, (m), 1157 (w), 1050 (w), 1105 (m), 997 (m), 882 (w), 837 (s), 794 (w), 773 (w), 755 (m).

M2a. 2,3-Dimethoxy-8*H*-benzo[6,7]cyclohepta[1,2:-*b*:5,4-*b*']dithiophen-8-one. To a solution of compound **S9** (100 mg, 211 μmol) in 5 mL methanol was added potassium fluoride (54 mg, 930 μmol), and the reaction mixture was refluxed overnight before adding water. The product was extracted with CH_2Cl_2 and washed once with water and once with brine. The organic layer was dried over sodium sulfate, and the solvent was removed under reduced pressure. The product was purified by preparatory thin layer chromatography (SiO_2, 4:1 dichloromethane:hexanes) (49 mg, 71% yield). ^{1}H NMR (400 MHz, $CDCl_3$) δ 7.88 (d, 2H), 7.42 (s, 2H), 7.31 (d, 2H), 4.01 (s, 6H). ^{13}C NMR (100 MHz, $CDCl_3$) δ 178.3, 149.7, 147.2, 139.5, 131.0, 123.7, 123.4, 111.1, 56.0. HRMS (ESI) calc for $C_{17}H_{12}O_3S_2$ $[M+H]^+$ 329.0301, found 329.0287. FT–IR (ATR, ν/cm^{-1}): 3085 (w), 2958 (w), 2931 (w), 2839 (w), 1613 (w),

1584 (s), 1560 (w), 1533 (m), 1517 (m), 1474 (w), 1438 (w), 1422 (w), 1375 (w), 1347 (m), 1280 (m), 1264 (s), 1232 (m), 1198 (w), 1158 (m), 1083 (m), 1024 (m), 883 (w), 850 (m), 830 (m), 791 (w), 712 (s).

RM2a. 2,3-Dimethoxy-8*H*-benzo[6,7]cyclohepta[1,2:-*b*:5,4-*b*']dithiophen-8-ol. To a solution of monomer **M2a** (49 mg, 0.15 mmol) in 3 mL dry tetrahydrofuran/MeOH (2:1) at 0°C was added sodium borohydride (17 mg, 0.45 mmol, 3.0 equiv.). The solution was slowly allowed to warm to room temperature over 3 hours. An aqueous solution of 1M hydrochloric acid was added until the pH was 6. The product was then extracted in dichloromethane and washed once with saturated sodium bicarbonate and once with brine. The organic layer was dried over sodium sulfate, and the organic layer was removed under reduced pressure. The compound was purified by preparatory thin layer chromatography (neutralized SiO_2, CH_2Cl_2) to obtain a light yellow solid (40 mg, 82% yield). ^1H NMR (500 MHz, $CDCl_3$) δ 7.30 (d, 2H), 7.28 (s, 2H), 7.14 (d, 2H), 5.40 (s, 1H), 4.02 (s, 6H). ^{13}C NMR (125 MHz, $CDCl_3$) δ 149.4, 141.4, 138.0, 128.6, 125.5, 124.2, 112.3, 67.4, 56.8. HRMS (ESI) calc for $C_{17}H_{14}O_3S_2$ $[M-OH]^+$ 313.0357, found 313.0345. FT–IR (ATR, ν/cm^{-1}): 3491 (br, w), 3105 (w), 2999 (w), 2932 (w), 2837 (w), 1606 (m), 1514 (s), 1462 (m), 1434 (m), 1353 (m), 1257 (s), 1229 (w), 1208 (m), 1147 (m), 1108 (w), 1095 (w), 1018 (s), 981 (w), 884 (w), 858 (m), 840 (s), 787 (w), 778 (w), 743 (m), 706 (m).

RM1a. 2,3-Dimethoxy-8*H*-benzo[6,7]cyclohepta[2,1-*b*:4,5-*b*']dithiophen-8-ol. To a solution of compound **M1a** (100 mg, 0.30 mmol) dissolved in 4 mL THF/dry MeOH (3:1) at room temperature was added sodium borohydride (23 mg, 0.61 mmol, 2.0 equiv.). The reaction mixture was allowed to stir at room temperature for 12 hours. The solution was acidified to pH=6 using 1M HCl and then diluted with CH_2Cl_2. The organic layer was washed with

saturated $NaHCO_3$ and brine before drying over sodium sulfate. The solvent was removed under reduced pressure, and the product was purified by column chromatography (neutralized SiO_2, CH_2Cl_2) as a slightly yellow solid (81 mg, 81% yield). ^1H NMR (500 MHz, $CDCl_3$) δ 7.30 (d, 2H), 7.21 (d, 2H), 7.20 (s, 2H) 5.87 (d, 1H), 3.98 (s, 6H), 2.94 (br, s, 1H). ^{13}C NMR (125 MHz, $CDCl_3$) δ 148.7, 140.5, 135.5, 129.8, 126.5, 123.2, 112.0, 68.7, 56.7. HRMS (ESI) calc for $C_{17}H_{14}O_3S_2$ $[M–OH]^+$ 313.0351, found 313.0356. FT–IR (ATR, ν/cm^{-1}): .3475 (br, w), 3104 (w), 2996 (w), 2955 (w), 2933 (w), 2843 (w), 1609 (m), 1515 (s), 1462 (m), 1449 (m), 1389 (m), 1323 (w), 1257 (s), 1241 (w), 1206 (m), 1167 (s), 1096 (w), 1049 (s), 993 (w), 915 (w), 865 (m), 852 (m), 836 (w), 791 (w), 769 (m), 738 (m).

RM1b. 8-Butyl-1,2-dimethoxy-8*H*-benzo[6,7]cyclohepta[2,1-*b*:4,5-*b*′]dithiophen-8-ol. Compound **M1a** (100 mg, 0.30 mmol) was dissolved in 20 mL dry tetrahydrofuran and cooled to −78°C. A solution of *n*-butyllithium (2.15 M, 170 μL, 1.2 equiv.) was added dropwise, and the reaction mixture was allowed to slowly warm to room temperature overnight. After quenching with water, the product was extracted in dichloromethane and washed once with water and once with brine. The organic layer was dried over sodium sulfate, and the solvent was removed under reduced pressure. The product was purified by column chromatography (neutralized SiO_2, 1:1 CH_2Cl_2/hexanes) and obtained as a light yellow solid (66 mg, 56% yield). ^1H NMR (400 MHz, $CDCl_3$) δ 7.31 (d, 2H), 7.21 (d, 2H), 7.17 (s, 2H), 4.01 (s, 6H), 3.07 (s, 1H), 1.73 (t, 2H), 1.22 (m, 2H), 1.09 (m, 2H), 0.72 (t, 3H). ^{13}C NMR (100 MHz, $CDCl_3$) δ 147.7, 145.4, 132.9, 129.2, 125.9, 121.5, 111.2, 77.2, 56.0, 38.2, 25.4, 22.4, 13.8. HRMS (ESI) calc for $C_{21}H_{22}O_3S_2$ $[M–OH]^+$ 369.0977, found 369.0965. FT–IR (ATR, ν/cm^{-1}): 3520 (m), 3108 (w), 3002 (w), 2954 (m), 2929 (w), 2868 (w), 1651 (w), 1608

(w), 1513 (s), 1461 (m), 1447 (m), 1388 (m), 1252 (s), 1236 (m), 1203 (m), 1164 (s), 1158 (s), 1137 (w), 1094 (m), 1046 (s), 991 (s), 863 (m), 841 (w), 770 (m), 736 (s).

RM1c. 1,2-Dimethoxy-8-phenyl-8*H*-benzo[6,7]cyclohepta[2,1-*b*:4,5-*b*']dithiophen-8-ol. Compound **M1a** (200 mg, 0.61 mmol) was dissolved in 40 mL dry THF and cooled to −78°C. A solution of phenyllithium (1.8 M, 0.41 mL, 0.74 mmol, 1.2 equiv.) was added dropwise, and the reaction mixture was allowed to slowly warm to room temperature overnight. A few drops of water were added before extracting with CH_2Cl_2. The organic layer was washed once with water and once with brine and dried over sodium sulfate. The solvent was then removed under reduced pressure. The product was purified by column chromatography (SiO_2, 2% Et_3N in CH_2Cl_2) and obtained as a light yellow solid (227 mg, 92% yield). dec. pt. 108°C. ^{1}H NMR (400 MHz, $CDCl_3$) δ 7.31 (d, 2H), 7.26 (d, 2H), 7.07 (m, 5H), 6.99 (s, 2H), 4.81 (s, 1H), 3.87 (s, 6H). ^{13}C NMR (100 MHz, $CDCl_3$) δ 147.7, 144.4, 143.1, 134.5, 129.4, 128.6, 128.3, 126.7, 126.2, 122.3, 110.8, 77.6, 56.1. HRMS (ESI) calc for $C_{23}H_{18}O_3S_2$ $[M–OH]^+$ 389.0664, found 389.0657. FT–IR (ATR, ν/cm^{-1}): 3469 (w), 3102 (w), 2933 (w), 2842 (w), 1609 (w), 1515 (s), 1462 (w), 1450 (w), 1389 (m), 1361 (w), 1322 (w), 1256 (s), 1241 (w), 1213 (m), 1167 (m), 1142 (m), 1097 (w), 1048 (s), 992 (w), 910 (m), 865 (m), 833 (w), 819 (w), 773 (m), 730 (s).

RM1d. 2,3-Dimethoxy-8-(4-(trifluoromethyl)phenyl)-8*H*-benzo[6,7]cyclohepta[2,1-*b*:4,5-*b*']dithiophen-8-ol. To a solution of 1-iodo-4-(trifluoromethyl)benzene (137 mg, 74 μL, 0.50 mmol, 1.1 equiv.) in 5 mL dry tetrahydrofuran at −78°C was added *n*-butyllithium (2.15 M, 260 μL, 0.55 mmol, 1.2 equiv.) dropwise. The solution was allowed to stir at −78°C for 30 minutes. A solution of compound **M1a** (150 mg, 0.46 mmol) in 5 mL dry tetrahydrofuran was added dropwise, and the reaction mixture was allowed to slowly warm to

room temperature over three hours. The product was extracted with CH_2Cl_2, washed once with water and once with brine, and finally purified by column chromatography (neutralized SiO_2, 4:1 CH_2Cl_2/hexanes) to obtain a light yellow solid (171 mg, 79% yield). dec. pt. 142°C. ^{1}H NMR (400 MHz, $CDCl_3$) δ 7.34 (d, 2H), 7.33(d, 2H), 7.30 (d, 2H), 7.22 (d, 2H), 7.00 (s, 2H), 3.90 (s, 6H), 3.56 (s, 1H). ^{13}C NMR (100 MHz, $CDCl_3$) δ 148.5, 147.2, 143.9, 135.4, 130.8, 127.7, 127.1, 125.9, 125.8, 123.2, 111.4, 77.7, 56.6. HRMS (ESI) calc for $C_{24}H_{17}F_3O_3S_2$ [M–OH]$^+$ 457.0538, found 457.0526. FT–IR (ATR, ν/cm^{-1}): 3466 (m), 3017, (w), 2956 (w), 2936 (w), 2850 (w), 1611 (w), 1515 (s), 1467 (w), 1454 (w), 1411 (w), 1391 (m), 1325 (s), 1275 (w), 1255 (m), 1241 (w), 1215 (m), 1188 (w), 1165 (m), 1146 (m), 1111 (m), 1122 (s), 1068 (m), 1049 (m), 1016 (w), 994, (w), 918 (w), 881 (w), 867 (m), 844 (m), 834 (w), 821 (w), 773 (m), 729 (m).

RM1e. 2,3-Dimethoxy-8-(4-methoxyphenyl)-8*H*-benzo[6,7]cyclohepta[2,1-*b*:4,5-*b*']dithiophen-8-ol. To a solution of 1-iodo-4-methoxybenzene (118 mg, 0.50 mmol, 1.1 equiv.) in 5 mL dry tetrahydrofuran at −78°C was added *n*-butyllithium (2.15 M, 260 μL, 0.55 mmol, 1.2 equiv.) dropwise. The solution was allowed to stir at −78°C for 30 minutes. A solution of compound **M1a** (150 mg, 0.46 mmol) in 5 mL dry tetrahydrofuran was added dropwise, and the reaction mixture was allowed to slowly warm to room temperature over three hours. The product was extracted with CH_2Cl_2, washed twice with water and once with brine, and finally purified by column chromatography (neutralized SiO_2, 1:1 CH_2Cl_2/hexanes) to obtain a light yellow solid (145 mg, 73% yield). dec. pt. 102°C. ^{1}H NMR (500 MHz, $CDCl_3$) δ 7.33 (d, 2H), 7.28 (d, 2H), 7.02 (s, 2H), 7.01 (d, 2H), 6.59 (d, 2H), 3.92 (s, 6H), 3.68 (s, 3H), 3.23 (br, s, 1H). ^{13}C NMR (125 MHz, $CDCl_3$) δ 160.0, 148.2, 145.2, 136.0, 134.9, 129.8, 128.6, 126.8, 122.6, 114.0, 111.3, 77.9, 56.6, 55.8. HRMS (ESI) calc for $C_{24}H_{20}O_4S_2$ [M–OH]$^+$

419.0770, found 419.0754. FT–IR (ATR, ν/cm^{-1}): 3462 (br, w), 3102 (w), 3002 (w), 2958 (w), 2934 (w), 2909 (w), 2838 (w), 1607 (m), 1582 (w), 1513 (s), 1462 (m), 1451 (m), 1389 (m), 1361 (w), 1305 (w), 1255 (s), 1214 (m), 1172 (m), 1141 (m), 1114 (w), 1098 (w), 1049 (s), 1032 (m), 992 (w), 910 (m), 877 (w), 865 (m), 835 (m), 816 (w), 772 (w), 733 (s), 724 (s).

M1d. 2,3-Bis((2,5,8,11-tetraoxatridecan-13-yl)oxy)-8*H*-benzo[6,7]cyclohepta[2,1-*b*:4,5-*b*']dithiophen-8-one. Compound **M1a** (500 mg, 1.5 mmol) was suspended in dry dichloromethane and cooled to −78°C. Boron tribromide (1.0 M in CH_2Cl_2, 5.3 mL, 5.3 mmol, 3.5 equiv.) was then added dropwise, and the reaction mixture was allowed to stir and slowly warm to room temperature overnight. The mixture was washed with saturated aqueous sodium dithionite (sparged with Ar) and filtered under nitrogen. The product was extracted with *N*,*N*-dimethylformamide (DMF, sparged with Ar), and the solvent was removed by distillation. The intermediate catechol was redissolved in 3 mL dry DMF, and this solution was added to a flask charged with potassium carbonate (168 mg, 1.2 mmol, 4.0 equiv.) and tetra(ethylene glycol) monomethyl ether tosylate (331 mg, 0.91 mmol, 3.0 equiv.). The reaction mixture was then allowed to stir for 48 h at 80°C under Ar. The solvent was removed by distillation, and the product was purified by column chromatography (SiO_2, 0 to 10% MeOH in CH_2Cl_2) and obtained as a yellow oil (0.82 g, 79% yield). ^{1}H NMR (400 MHz, $CDCl_3$) δ 7.87 (d, 2H), 7.81 (d, 2H), 7.79 (s, 2H), 4.38 (t, 4H), 3.97 (t, 4H), 3.78 (m, 4H), 3.74–3.60 (16H), 3.54 (m, 4H), 3.38 (s, 6H). ^{13}C NMR (100 MHz, $CDCl_3$) δ 175.3, 149.1, 140.8, 140.7, 132.7, 129.2, 126.0, 114.9, 71.8, 70.8, 70.6, 70.5, 70.4, 69.8, 69.0, 58.9. HRMS (ESI) calc for $C_{33}H_{44}O_{11}S_2$ $[M+H]^+$ 681.2398, found 681.2413. FT–IR (ATR, ν/cm^{-1}): 3083 (w), 2921 (m), 2872 (m), 1710 (m), 1604 (w), 1576 (w), 1526 (w), 1504 (w), 1443 (m), 1394 (w), 1349 (w), 1331 (w), 1269 (s), 1182 (m), 1100 (s), 1057 (m), 946 (w), 851 (m), 799 (m), 772 (m), 731 (w), 706 (w).

M3. 8-(4-(Bicyclo[2.2.1]hept-5-en-2-yl)phenyl)-8*H*-benzo[6,7]cyclohepta[2,1-*b*:4,5-*b*']dithiophen-8-ol. To a solution of 5-(4-bromophenyl)bicyclo[2.2.1]hept-2-ene (500 mg, 2.00 mmol, 1.4 equiv.) in 15 mL dry tetrahydrofuran at −78°C was added *n*-butyllithium (2.50 M, 800 μL, 2.00 mmol, 1.4 equiv.) dropwise. The solution was allowed to stir at −78°C for one hour. A solution of tropone **M1a** (750 mg, 1.43 mmol) in 15 mL dry tetrahydrofuran was added dropwise, and the reaction mixture was allowed to slowly warm to room temperature over three hours. The product was extracted with CH_2Cl_2, washed twice with water and once with brine, and finally purified by column chromatography (neutralized SiO_2, 2% Et_3N, 48% CH_2Cl_2 in hexanes) to afford a light yellow oil (710 mg, 72% yield). ^{1}H NMR (500 MHz, $CDCl_3$) δ 7.33 (2H), 7.26 (2H), 7.03 (2H), 7.01 (2H), 6.97 (2H), 6.18 (1H), 6.12 (1H), 3.90 (4H), 3.27 (br, 1H), 2.90 (1H), 2.76 (1H), 2.54 (1H), 1.77 (2H), 1.60–1.25 (20H), 1.00–0.85 (12H). ^{13}C NMR (125 MHz, $CDCl_3$) δ 148.2, 146.5, 144.3, 140.5, 137.6, 137.4, 134.7, 129.5, 127.6, 126.6, 126.3, 122.1, 113.2, 77.5, 71.8, 71.8, 48.2, 45.9, 43.5, 42.5, 39.8, 33.8, 30.8, 29.5, 24.2, 23.3, 14.4, 11.5. HRMS (ESI) calc for $C_{44}H_{54}O_3S_2$ $[M–OH]^+$ 677.3481, found 677.3466. FT–IR (ATR, ν/cm^{-1}): 3503 (br, w), 3056 (w), 2958 (m), 2929 (m), 2871 (m), 1606 (w), 1514 (s), 1463 (m), 1380 (m), 1331 (w), 1255 (s), 1174 (w), 1140 (m), 1096 (w), 1045 (s), 861 (w), 843 (w), 775 (w), 726 (m), 707 (m).

CM6. 2-Hexadecyl-3a,4,7,7a-tetrahydro-1*H*-4,7-methanoisoindole-1,3(2*H*)-dione. Monomer **CM6** was prepared according to an analogous literature procedure.[64] Bicyclo[2.2.1]hept-5-ene-2,3-dicarboxylic anhydride (500 mg, 3.05 mmol), hexadecylamine (1.10 g, 4.57 mmol, 1.5 equiv.), and triethylamine (1.27 mL, 924 mg, 9.14 mmol, 3 equiv.) were dissolved in toluene (25 mL), and the reaction mixture was refluxed for 16 hours. The solvents were removed under reduced pressure, and the product was purified by column

chromatography (1:5 EtOAc in hexanes to yield a white solid (1.12 g, 95% yield). mp 43–44 °C. ^{1}H NMR (500 MHz, $CDCl_3$) δ 6.26 (m, 2H), 3.42 (t, 2H), 3.24 (m, 2H), 2.64 (m, 2H), 1.55–1.45 (3H), 1.30–1.15 (27H), 0.85 (t, 3H). ^{13}C NMR (125 MHz, $CDCl_3$) δ 178.3, 138.1, 48.1, 45.4, 43.0, 39.0, 32.2, 30.0 (x5), 29.9, 29.8, 29.8, 29.7, 29.4, 28.1, 27.3, 23.0, 14.4. HRMS (ESI) calc for $C_{25}H_{41}NO_2$ $[M+NH_4]^+$ 405.3476, found 405.3476. FT–IR (ATR, ν/cm^{-1}): 2916 (s), 2849 (m), 1770 (w), 1698 (s), 1472 (w), 1464 (w), 1400 (m), 1370 (w), 1334 (w), 1285 (w), 1244 (w), 1227 (w), 1208 (w), 1188 (w), 1143 (m), 1104 (w), 1032 (w), 1011 (w), 976 (w), 888 (w), 825 (w), 796 (w), 779 (m), 725 (m), 666 (m), 648 (m).

CM7. Di(2,5,8,11-tetraoxatrdecan-13-yl)-*exo*-7-oxabicyclo[2.2.1]hept-5-ene-2,3-dicarboxylate. Monomer **CM7** was prepared according to an analogous literature procedure.[65] *exo*-7-Oxabicyclo[2.2.1]hept-5-ene-2,3-dicarboxylic anhydride (1.60 g, 9.63 mmol), tetra(ethylene glycol) monomethyl ether (4.22 mL, 4.41 g, 21.2 mmol, 2.2 equiv.), 4-(dimethylamino)pyridine (470 mg, 3.85 mmol, 0.4 equiv.), and 2-chloro-1-methyl-pyridinium chloride (Mukaiyama's reagent, 2.96 g, 11.6 mmol, 1.2 equiv.) were dissolved in dichloromethane (25 mL) and triethylamine (7 mL), and the reaction mixture was refluxed for 48 hours. After cooling to room temperature, the reaction mixture was diluted with dichloromethane and washed once with 1M aqueous HCl and brine. The product was purified by column chromatography (0→6% MeOH in CH_2Cl_2 to yield a colorless oil (4.48 g, 83% yield). ^{1}H NMR (500 MHz, $CDCl_3$) δ 6.37 (2H), 5.16 (2H), 4.20 (2H), 4.09 (2H), 3.60 (4H), 3.58–3.50 (20H), 3.45 (4H), 3.28 (6H), 2.75 (2H). ^{13}C NMR (125 MHz, $CDCl_3$) δ 171.3, 136.5, 80.5, 71.7, 70.4, 70.4, 70.4, 70.3, 70.3, 68.8, 64.0, 58.9, 46.6. HRMS (ESI) calc for $C_{26}H_{44}O_{13}$ $[M+Na]^+$ 587.2674, found 587.2685. FT–IR (ATR, ν/cm^{-1}): 2940 (w), 2874 (m), 1744 (s),

1453 (m), 1348 (w), 1305 (w), 1243 (m), 1105 (s), 1057 (m), 1030 (w), 997 (w), 919 (m), 858 (m), 816 (w), 751 (m).

1.4.3 Synthesis of Polymers

Polymers **P1a–c** and **P2–5** were prepared by direct arylation polycondensation. Generally, a vial was charged with monomer **M1** (0.21 mmol), dibromoarene (0.21 mmol, 1.0 equiv.), potassium carbonate (74 mg, 0.53 mmol, 2.5 equiv.), palladium acetate (1.9 mg, 8.5 μmol, 0.04 equiv.), tricyclohexylphosphine tetrafluoroborate (6.3 mg, 17 μmol, 0.08 equiv.), and pivalic acid (6.5 mg, 64 μmol, 0.3 equiv.). The system was evacuated and backfilled with argon three times before adding 4 mL dry *N*,*N*-dimethylacetamide and heating the reaction mixture to 100°C for 12 hours. After allowing the reaction mixture to cool to room temperature, the product was precipitated by adding the polymerization solution dropwise to vigorously stirring methanol and collected by filtration.

Preparation of polymers **RP1–5**. Generally, the polymer (50 mg) was dispersed in 5 mL solvent (4:1 THF/MeOH), and sodium borohydride (25 mg, ~10 equiv.) was then added. The reaction mixture was heated to 40°C and allowed to stir for 16 hours. The product was then precipitated by dropwise addition to vigorously stirred methanol and collection by filtration. Characterization of polymers **RP2–5** is limited by solubility.

Preparation of polymers **RCP1** and **RCP2**. To a solution of monomers (100 equiv. total) dissolved in dry CH_2Cl_2 (1.5 mL) under Ar was added catalyst **G3** (2.2 mg, 2.6 μmol) dissolved in dry CH_2Cl_2 (0.5 mL). The polymerization was allowed to stir at room temperature for 15 minutes before quenching with ethyl vinyl ether. The reaction mixture was then precipitated into a vigorously stirring solution of hexanes (**RCP1**) or methanol (**RCP2**). The polymers were collected by centrifugation and used without additional purification.

P1b. (159 mg, 87% yield). ^{1}H NMR (500 MHz, $CHCl_3$): δ 8.20–8.05 (2H), 7.95–7.70 (8H), 4.35–4.17 (4H), 2.12 (4H), 1.98 (4H), 1.61 (4H), 1.43 (8 H), 1.12 (24 H), 0.96 (6H), 0.80 (6H). GPC (THF-soluble fraction): M_n = 6.20 kDa, Đ = 1.98. FT–IR (ATR, ν/cm^{-1}): 2952 (w), 2927 (s), 2855 (m), 1641 (w), 1606 (w), 1551 (m), 1521 (m), 1451 (s), 1417 (m), 1387 (w), 1266 (s), 1180 (m), 1136 (w), 1098 (m), 1011 (w), 814 (s), 764 (w), 723 (w).

P1c. (190 mg, 99% yield). ^{1}H NMR (400 MHz, $CHCl_3$). δ 8.20–8.10 (2H), 7.95–7.65 (8H), 4.25–4.07 (4H), 2.14 (4H), 1.93 (2H), 1.75–1.50 (8H), 1.50–1.35 (8H), 1.25–1.10 (24H), 0.96 (6H), 0.80 (12H). GPC (THF-soluble fraction): M_n = 7.60 kDa, Đ = 2.61. FT–IR (ATR, ν/cm^{-1}): 2955 (m), 2926 (s), 2855 (m), 1605 (w), 1552 (w), 1520 (m), 1452 (s), 1416 (m), 1379 (w), 1264 (s), 1179 (m), 1134 (w), 1098 (w), 1012 (w), 814 (s), 765 (w), 748 (w), 730 (w), 720 (w).

P1d. (237 mg, 94% yield). ^{1}H NMR (500 MHz, $CHCl_3$): δ 8.14 (2H), 7.95–7.70 (8H), 4.44 (4H), 3.99 (4H), 3.82 (4H), 3.73 (4H), 3.68–3.58 (12H), 3.52 (4H), 3.35 (6H), 2.14 (4H), 1.30–0.95 (24H), 0.80–0.65 (6H). GPC: M_n = 12.2 kDa, Đ = 1.90. FT–IR (ATR, ν/cm^{-1}): 2926 (m), 2856 (m), 1630 (w), 1606 (w), 1533 (m), 1524 (w), 1451 (s), 1418 (s), 1268 (s), 1182 (w), 1101 (s), 1009 (w), 951 (w), 885 (w), 850 (w), 830 (m), 818 (m), 704 (m).

P2. Sparingly soluble, dark red powder (122 mg, 91% yield). GPC (THF-soluble fraction): M_n = 1.04 kDa, Đ = 1.73. FT–IR (ATR, ν/cm^{-1}): 3071 (w), 2951 (m), 2929 (m), 2857 (w), 1605 (w), 1577 (w), 1553 (m), 1522 (m), 1458 (s), 1409 (m), 1379 (m), 1267 (s), 1176 (m), 1137 (w), 1096 (m), 1054 (w), 1012 (w), 801 (s), 763 (m), 725 (w).

P3. Sparingly soluble, bright red powder (168 mg, 98% yield). GPC (THF-soluble fraction): M_n = 5.60 kDa, Đ = 1.71. FT–IR (ATR, ν/cm^{-1}): 2954 (w), 2928 (m), 2857 (m),

1607 (w), 1553 (m), 1524 (m), 1457 (s), 1406 (m), 1379 (w), 1268 (s), 1180 (m), 1140 (w), 1097 (m), 1008 (w), 827 (m), 806 (m), 762 (w), 746 (w), 725 (w).

P4. Sparingly soluble, bright red powder (118 mg, 89% yield). GPC (THF-soluble fraction): M_n = 3.92 kDa, Đ = 2.02. FT–IR (ATR, ν/cm^{-1}): 3087 (w), 2953 (m), 2928 (m), 2858 (m), 1606 (w), 1578 (w), 1554 (m), 1524 (m), 1454 (s), 1412 (m), 1381 (w), 1268 (s), 1179 (m), 1138 (w), 1097 (m), 1058 (w), 1011 (w), 925 (w), 832 (w), 805 (m), 764 (m), 747 (w), 725 (w).

P5. Insoluble, dark red powder. (86 mg, 74% yield). FT–IR (ATR, ν/cm^{-1}): 3085 (w), 2952 (m), 2929 (m), 2857 (w), 1605 (w), 1577 (w), 1553 (m), 1523 (m), 1451 (s), 1411 (m), 1385 (m), 1267 (s), 1177 (m), 1138 (w), 1096 (m), 1055 (w), 1013 (w), 923 (w), 803 (s), 764 (m), 726 (w), 708 (w).

RP1b. (44 mg, 87% yield). ^{1}H NMR (500 MHz, $CHCl_3$): δ 7.80–7.50 (6H), 7.35–7.15 (4H), 5.92 (1H), 4.16 (4H), 2.20–1.75 (8H), 1.55 (4H), 1.38 (8H), 1.25–0.80 (24H), 0.75–0.50 (12H). GPC: M_n = 7.8 kDa, Đ = 2.0. FT–IR (ATR, ν/cm^{-1}): 3388 (br, w), 2927 (s), 2855 (m), 1604 (w), 1515 (m), 1455 (s), 1418 (m), 1377 (m), 1377 (m), 1260 (s), 1174 (m), 1098 (w), 1008 (w), 886 (w), 817 (s), 764 (w), 723 (w).

RP1c. (50 mg, 99% yield). ^{1}H NMR (500 MHz, $CHCl_3$): δ 7.80–7.50 (6H), 7.35–7.15 (4H), 5.92 (1H), 4.04 (4H), 2.02 (4H), 1.85 (2H), 1.70–1.25 (16H), 1.25–0.80 (32H), 0.75–0.50 (10H). GPC: M_n = 9.7, Đ = 2.5. FT–IR (ATR, ν/cm^{-1}): 3320 (br, w), 2955 (m), 2926 (s), 2855 (m), 1606 (w), 1514 (s), 1458 (s), 1418 (w), 1378 (m), 1257 (s), 1213 (w), 1168 (w), 1034 (w), 1009 (w), 981 (w), 834 (w), 816 (s), 766 (w), 755 (w), 743 (w), 728 (w).

RP1d. (44 mg, 87% yield). ^{1}H NMR (500 MHz, $CHCl_3$): δ 7.80–7.30 (10H), 5.92 (1H), 4.36 (4H), 3.92 (4H), 3.80–3.45 (24H), 3.36 (6H), 2.04 (4H), 1.25–0.85 (20H), 0.80–0.50

(10H). GPC: M_n = 16.6 kDa, Đ = 1.91. FT–IR (ATR, ν/cm^{-1}): 3358 (br, w), 2927 (s), 2856 (s), 1607 (w), 1518 (m), 1455 (m), 1377 (w), 1256 (s), 1198 (w), 1105 (s), 1070 (w), 947 (w), 850 (w), 821 (m), 767 (w), 721 (w).

RP2. (47 mg, 94% yield). GPC (THF-soluble fraction): M_n = 3.94 kDa, Đ = 4.08. FT–IR (ATR, ν/cm^{-1}): 3067 (w), 2952 (m), 2928 (m), 2858 (m), 1605 (w), 1512 (s), 1465 (s), 1378 (s), 1256 (s), 1167 (m), 1096 (w), 1054 (m), 1015 (w), 921 (w), 829 (w), 794 (s), 765 (w), 722 (w),709 (w).

RP3. (46 mg, 91% yield). GPC (THF-soluble fraction): M_n = 7.89 kDa, Đ = 2.42. FT–IR (ATR, ν/cm^{-1}): 3356 (br, w), 2953 (m), 2928 (s), 2857 (m), 1605 (w), 1513 (m), 1465 (m), 1377 (m), 1256 (s), 1222 (w), 1167 (m), 1063 (w), 1015 (w), 927 (w), 831 (s), 764 (w), 728 (w).

RP4. (43 mg, 87% yield). GPC (THF-soluble fraction): M_n = 6.90 kDa, Đ = 2.69. FT–IR (ATR, ν/cm^{-1}): 3333 (br, w), 2953 (m), 2929 (m), 2858 (m), 1656 (w), 1605 (w), 1515 (s), 1464 (s), 1427 (m), 1378 (s), 1259 (s), 1176 (s), 1095 (w), 1058 (w), 1015 (w), 925 (w), 832 (m), 806 (w), 765 (w), 725 (w).

RP5. (49 mg, 97% yield). GPC (THF-soluble fraction): M_n = 5.37 kDa, Đ = 2.71. FT–IR (ATR, ν/cm^{-1}): 3354 (br, w), 3086 (w), 2952 (m), 2929 (m), 2857 (w), 1655 (w), 1605 (w), 1515 (s), 1454 (s), 1378 (s), 1257 (s), 1171 (s), 1096 (w), 1060 (w), 1013 (w), 924 (w), 842 (m), 803 (m), 765 (w), 733 (w).

RCP1. 27 mg, 15 equiv. **M3**; 30 mg, 30 equiv. **CM6**; 80 mg, 55 equiv. **CM7** (120 mg, 88% yield). GPC (THF): M_n = 68.5 kDa, Đ = 1.19.

RPC2. 17 mg, 10 equiv. **M3**; 85 mg, 90 equiv. **CM6**. (80 mg, 78% yield). GPC (THF): M_n = 63.1 kDa, Đ = 1.25.

1.4.4 Sensing Experiments with DCP

Diethyl chlorophosphate (DCP) was passed through a pad of potassium carbonate in a syringe filer (~ 2 cm^3 K_2CO_3 in a 5 mL syringe with a 0.45 μm PTFE filter) on each new day of experiments. Stock solutions of 0.1 M or 0.01 M in dry CH_2Cl_2 were prepared.

For sensing experiments with DCP for monomers **RM1a–e** and **RM2a**, the appropriate stock solution of DCP (typically 1–20 μL) was added to 3 mL of a 50 μM solution of monomer in dry CH_2Cl_2 to achieve the desired concentration of DCP. Unless stated otherwise, UV–Vis absorption measurements were taken two minutes after addition of DCP. For polymers **RP1–RP5**, a 5 μg/mL solution was used. For polymers **RCP1** and **RCP2**, a 50 μg/mL solution was used.

1.5 References

(1) Benschop, H. P.; De Jong, L. P. A. *Acc. Chem. Res.* **1988**, *21*, 368–374.

(2) Sidell, F. R.; Borak, J. *Ann. Emerg. Med.* **1992**, *21*, 865–871.

(3) Delfino, R. T.; Ribeiro, T. S.; Figueroa-Villar, J. D. *J. Braz. Chem. Soc.* **2009**, *20*, 407–428.

(4) Kim, K.; Tsay, O. G.; Atwood, D. A.; Churchill, D. G. *Chem. Rev.* **2011**, *111*, 5345–5403.

(5) John, H.; Worek, F.; Thiermann, H. *Anal. Bioanal. Chem.* **2008**, *391*, 97–116.

(6) Francis, G. J.; Milligan, D. B.; McEwan, M. J. *Anal. Chem.* **2009**, *81*, 8892–8899.

(7) Steiner, W. E.; Klopsch, S. J.; English, W. A.; Clowers, B. H.; Hill, H. H. *Anal Chem* **2005**, *77*, 4792–4799.

(8) Kanan, S. M.; Tripp, C. P. *Langmuir* **2002**, *18*, 722–728.

(9) Diakowski, P. M.; Xiao, Y.; Petryk, M. W. P.; Kraatz, H.-B. *Anal. Chem.* **2010**, *82*, 3191–3197.

(10) Khan, M. A. K.; Kerman, K.; Petryk, M.; Kraatz, H.-B. *Anal. Chem.* **2008**, *80*, 2574–2582.

(11) Mlsna, T. E.; Cemalovic, S.; Warburton, M.; Hobson, S. T.; Mlsna, D. A ; Patel, S. V. *Sensors Actuators B Chem.* **2006**, *116*, 192–201.

(12) Meier, D. C.; Taylor, C. J.; Cavicchi, R. E.; V, E. W.; Ellzy, M. W.; Sumpter, K. B.; Semancik, S. *IEEE Sens. J.* **2005**, *5*, 712–725.

(13) Wang, F.; Gu, H.; Swager, T. M. *J. Am. Chem. Soc.* **2008**, *130*, 5392–5393.

(14) Kim, Y.; Lee, S.; Choi, H. H.; Noh, J.-S.; Lee, W. *Nanotechnology* **2010**, *21*, 5501.

(15) Kong, L.; Wang, J.; Luo, T.; Meng, F.; Chen, X.; Li, M.; Liu, J. *Analyst* **2010**, *135*, 368–374.

(16) Kwon, O. S.; Park, S. J.; Lee, J. S.; Park, E.; Kim, T.; Park, H.-W.; You, S. A.; Yoon, H.; Jang, J. *Nano Lett.* **2012**, *12*, 2797–2802.

(17) Wei, L.; Shi, D.; Ye, P.; Dai, Z.; Chen, H.; Chen, C.; Wang, J.; Zhang, L.; Xu, D.; Wang, Z.; Zhang, Y. *Nanotechnology* **2011**, *22*, 425501.

(18) Van Houten, K. A.; Heath, D. C.; Pilato, R. S. *J. Am. Chem. Soc.* **1998**, *120*, 12359–12360.

(19) Burnworth, M.; Rowan, S. J.; Weder, C. *Chem. Eur. J.* **2007**, *13*, 7828–7836.

(20) Bencic-Nagale, S.; Sternfeld, T.; Walt, D. R. *J. Am. Chem. Soc.* **2006**, *128*, 5041–5048.

(21) Knapton, D.; Burnworth, M.; Rowan, S. J.; Weder, C. *Angew. Chem. Int. Ed.* **2006**, *45*, 5825–5829.

(22) Obare, S. O.; De, C.; Guo, W.; Haywood, T. L.; Samuels, T. A.; Adams, C. P.; Masika, N. O.; Murray, D. H.; Anderson, G. A.; Campbell, K.; Fletcher, K. *Sensors* **2010**, *10*, 7018–7043.

(23) Lei, Z.; Yang, Y. *J. Am. Chem. Soc.* **2014**, *136*, 6594–6597.

(24) Xuan, W.; Cao, Y.; Zhou, J.; Wang, W. *Chem. Commun.* **2013**, *49*, 10474–10476.

(25) Zhang, S.-W.; Swager, T. M. *J. Am. Chem. Soc.* **2003**, *125*, 3420–3421.

(26) Dale, T. J.; Rebek, J. *J. Am. Chem. Soc.* **2006**, *128*, 4500–4501.

(27) Gotor, R.; Costero, A. M.; Gil, S.; Parra, M.; Martínez-Máñez, R.; Sancenón, F. *Chem. Eur. J.* **2011**, *17*, 11994–11997.

(28) Costero, A. M.; Parra, M.; Gil, S.; Gotor, R.; Martínez-Mañez, R.; Sancenón, F.; Royo, S. *Eur. J. Org. Chem.* **2012**, *2012*, 4937–4946.

(29) Wu, X.; Wu, Z.; Han, S. *Chem. Commun.* **2011**, *47*, 11468–11470.

(30) Pardasani, D.; Tak, V.; Purohit, A. K.; Dubey, D. K. *Analyst* **2012**, *137*, 5648–5653.

(31) Wu, W.; Dong, J.; Wang, X.; Li, J.; Sui, S.; Chen, G.; Liu, J.; Zhang, M. *Analyst* **2012**, *137*, 3224–3226.

(32) Costero, A. M.; Gil, S.; Parra, M.; Mancini, P. M. E.; Martínez-Máñez, R.; Sancenón, F.; Royo, S. *Chem. Commun.* **2008**, 6002–6004.

(33) Costero, A. M.; Parra, M.; Gil, S.; Gotor, R.; Mancini, P. M. E.; Martínez-Máñez, R.; Sancenón, F.; Royo, S. *Chem. Asian J.* **2010**, *5*, 1573–1585.

(34) Wu, Z.; Wu, X.; Yang, Y.; Wen, T.; Han, S. *Bioorg. Med. Chem. Lett.* **2012**, *22*, 6358–6361.

(35) Pangeni, D.; Nesterov, E. E. *Macromolecules* **2013**, *46*, 7266–7273.

(36) Walton, I.; Davis, M.; Munro, L.; Catalano, V. J.; Cragg, P. J.; Huggins, M. T.; Wallace, K. J. *Org. Lett.* **2012**, *14*, 2686–2689.

(37) Dale, T. J.; Rebek, J. *Angew. Chem. Int. Ed.* **2009**, *48*, 7850–7852.

(38) Wallace, K. J.; Fagbemi, R. I.; Folmer-Andersen, F. J.; Morey, J.; Lynth, V. M.; Anslyn, E. V. *Chem. Commun.* **2006**, 3886–3888.

(39) Bharathi, S.; Wong, P. T.; Desai, A.; Lykhytska, O.; Choe, V.; Kim, H.; Thomas, T. P.; Baker, J. R.; Choi, S. K. *J. Mater. Chem. B* **2014**, *2*, 1068.

(40) Sarkar, S.; Shunmugam, R. *Chem. Commun.* **2014**, *50*, 8511–8513.

(41) Borja, D.; Gren, D.; Moreno, D.; Berg, A.; Gunnars, J.; Nilsson, T.; Nyman, R.; Persson, M.; Pettersson, J.; Eklind, I.; Díaz de Greñu, B.; Torroba, T.; Wästerby, P. *J Am. Chem. Soc.* **2014**, *136*, 4125–4128.

(42) Royo, S.; Costero, A. M.; Parra, M.; Gil, S.; Martínez-Máñez, R.; Sancenõn, F. *Chem. Eur. J.* **2011**, *17*, 6931–6934.

(43) Sugiyasu, K.; Song, C.; Swager, T. M. *Macromolecules* **2006**, *39*, 5598–5600.

(44) Facchetti, A.; Vaccaro, L.; Marrocchi, A. *Angew. Chem. Int. Ed.* **2012**, *51*, 3520–3523.

(45) Mercier, L. G.; Leclerc, M. *Acc. Chem. Res.* **2013**, *46*, 1597–1605.

(46) Kuwabara, J.; Yasuda, T.; Choi, S. J.; Lu, W.; Yamazaki, K.; Kagaya, S.; Han, L.; Kanbara, T. *Adv. Funct. Mater.* **2014**, *24*, 3226–3233.

(47) Wang, Q.; Takita, R.; Kikuzaki, Y.; Ozawa, F. *J. Am. Chem. Soc.* **2010**, *132*, 11420–11421.

(48) Fujinami, Y.; Kuwabara, J.; Lu, W.; Hayashi, H.; Kanbara, T. *ACS Macro Lett.* **2011**, *1*, 67–70.

(49) Chang, S.-W.; Waters, H.; Kettle, J.; Kuo, Z.-R.; Li, C.-H.; Yu, C.-Y.; Horie, M. *Macromol. Rapid Commun.* **2012**, *33*, 1927–1932.

(50) Kuwabara, J.; Nohara, Y.; Choi, S. J.; Fujinami, Y.; Lu, W.; Yoshimura, K.; Oguma, J.; Suenobu, K.; Kanbara, T. *Polym. Chem.* **2013**, *4*, 947.

(51) Berrouard, P.; Najari, A.; Pron, A.; Gendron, D.; Morin, P.-O.; Pouliot, J.-R.; Veilleux, J.; Leclerc, M. *Angew. Chem. Int. Ed.* **2012**, *51*, 2068–2071.

(52) Sun, H.-Y.; Gorelsky, S. I.; Stuart, D. R.; Campeau, L.-C.; Fagnou, K. *J. Org. Chem.* **2010**, *75*, 8180–8189.

(53) Gorelsky, S. I.; Lapointe, D.; Fagnou, K. *J. Org. Chem.* **2012**, *77*, 658–668.

(54) Tovar, J. D.; Swager, T. M. *Adv. Mater.* **2001**, *13*, 1775–1780.

(55) Schipper, D. J.; Fagnou, K. *Chem. Mater.* **2011**, *23*, 1594–1600.

(56) Kowalski, S.; Allard, S.; Zilberberg, K.; Riedl, T.; Scherf, U. *Prog. Polym. Sci.* **2013**, *38*, 1805–1814.

(57) Shim, E. *Smart Textiles for Protection*; Elsevier, 2013.

(58) Harned, A. M.; He, H. S.; Toy, P. H.; Flynn, D. L.; Hanson, P. R. *J. Am. Chem. Soc.* **2005**, *127*, 52–53.

(59) Cammidge, A. N.; Gopee, H. *J. Mater. Chem.* **2001**, *11*, 2773–2783.

(60) Song, C.; Swager, T. M. *J. Org. Chem.* **2010**, *75*, 999–1005.

(61) Tovar, J. D.; Rose, A.; Swager, T. M. *J. Am. Chem. Soc.* **2002**, *124*, 7762–7769.

(62) Wendeln, C.; Rinnen, S.; Schulz, C.; Kaufmann, T.; Arlinghaus, H. F.; Ravoo, B. J. *Chem. Eur. J.* **2012**, *18*, 5880–5888.

(63) Love, J. A.; Morgan, J. P.; Trnka, T. M.; Grubbs, R. H. *Angew. Chem. Int. Ed.* **2002**, *41*, 4035–4037.

(64) Foster, E. J.; Berda, E. B.; Meijer, E. W. *J. Polym. Sci. Part A Polym. Chem.* **2011**, *49*, 118–126.

(65) Sankaran, N. B.; Rys, A. Z.; Nassif, R.; Nayak, M. K.; Metera, K.; Chen, B.; Bazzi, H. S.; Sleiman, H. F. *Macromolecules* **2010**, *43*, 5530–5537.

1.6 Appendix for Chapter 1

NMR Spectra of Monomers

4b. 3,3′-(4,5-Bis(hexyloxy)-1,2-phenylene)dithiophene.

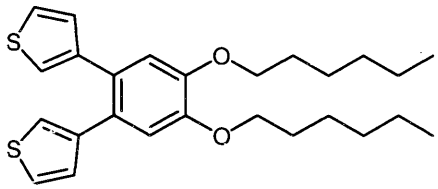

^{1}H NMR, $CDCl_3$, 400 MHz

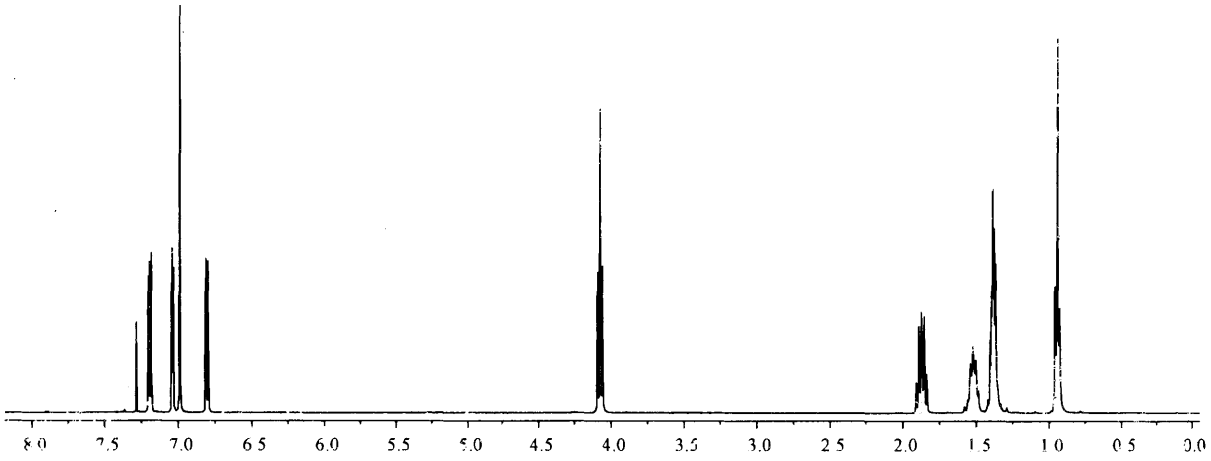

δ (ppm)

^{13}C NMR, $CDCl_3$, 100 MHz

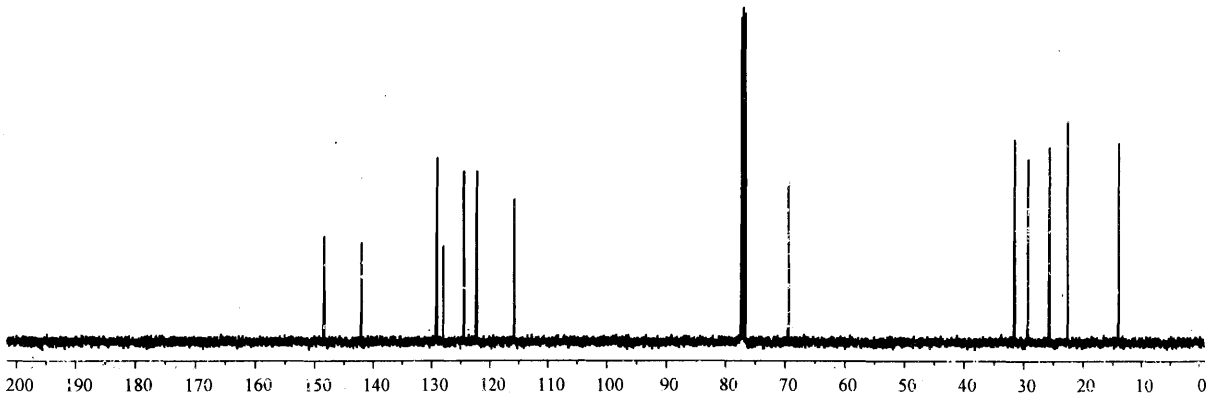

δ (ppm)

5b. 3,3′-(4,5-Bis(hexyloxy)-1,2-phenylene)bis(2-bromothiophene).

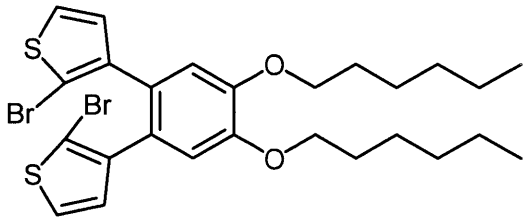

^{1}H NMR, $CDCl_3$, 400 MHz

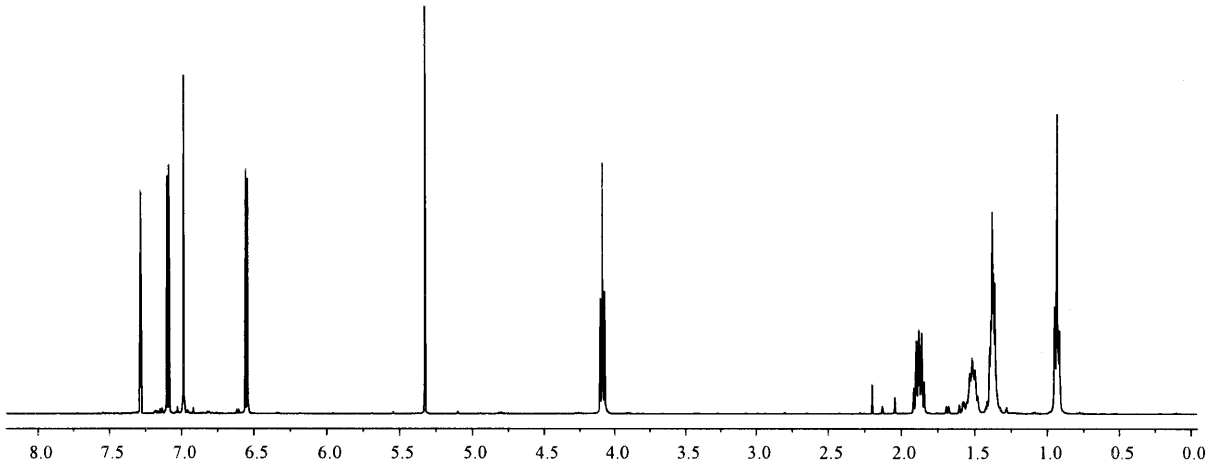

δ (ppm)

M1b. 2,3-Bis(hexyloxy)-8*H*-benzo[6,7]cyclohepta[2,1-*b*:4,5-*b'*]dithiophen-8-one.

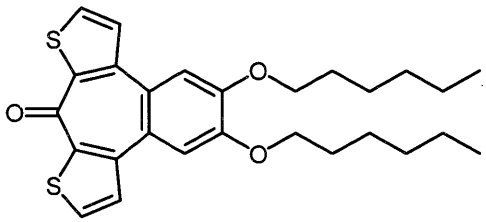

^{1}H NMR, $CDCl_3$, 400 MHz

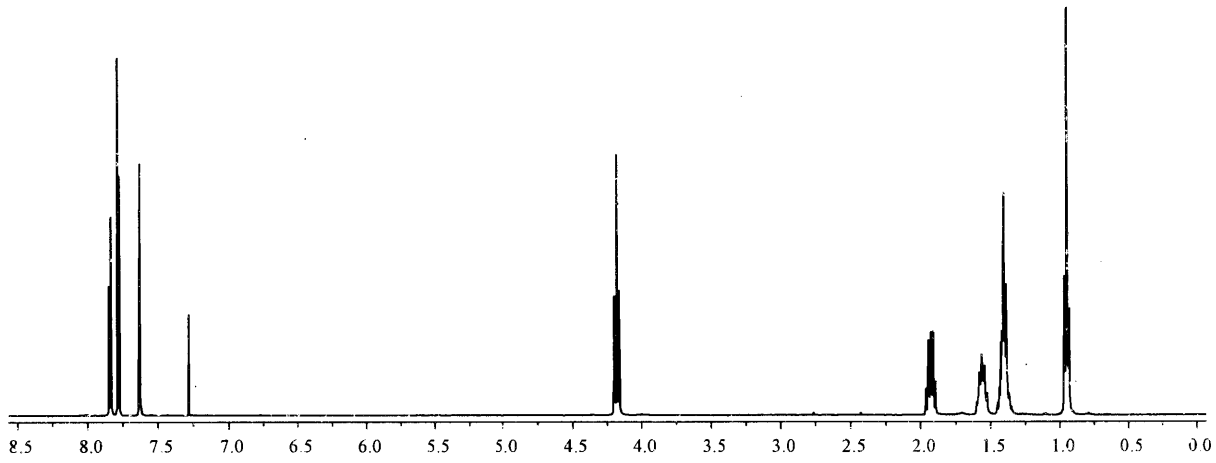

δ (ppm)

^{13}C NMR, $CDCl_3$, 100 MHz

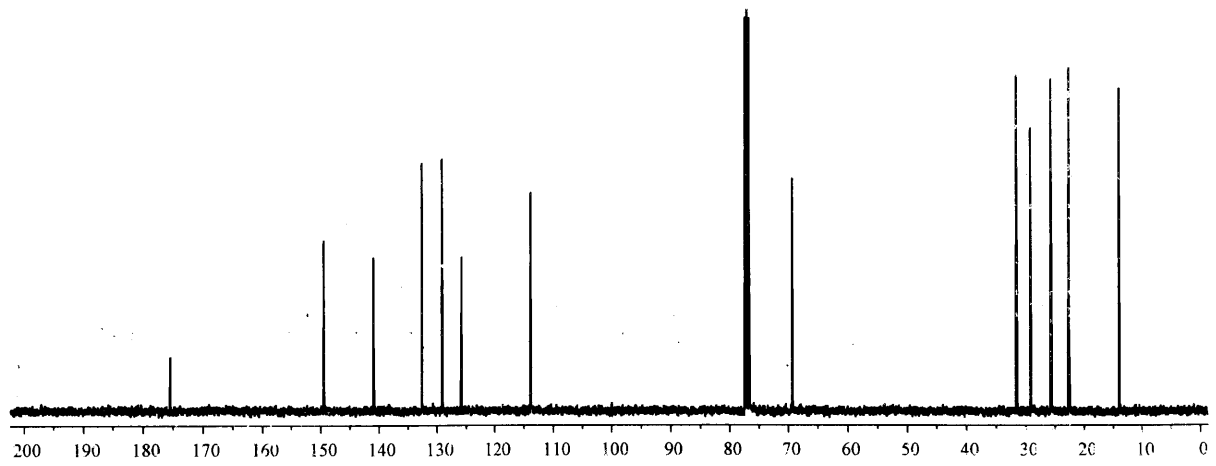

δ (ppm)

M1c. 2,3-Bis((2-ethylhexyl)oxy)-8*H*-benzo[6,7]cyclohepta[2,1-*b*:4,5-*b'*]dithiophen-8-one.

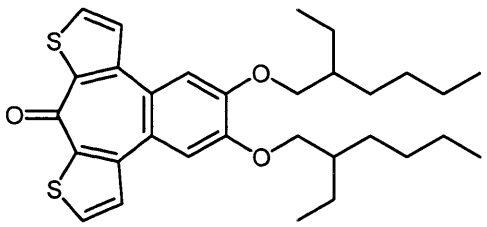

^{1}H NMR, $CDCl_3$, 400 MHz

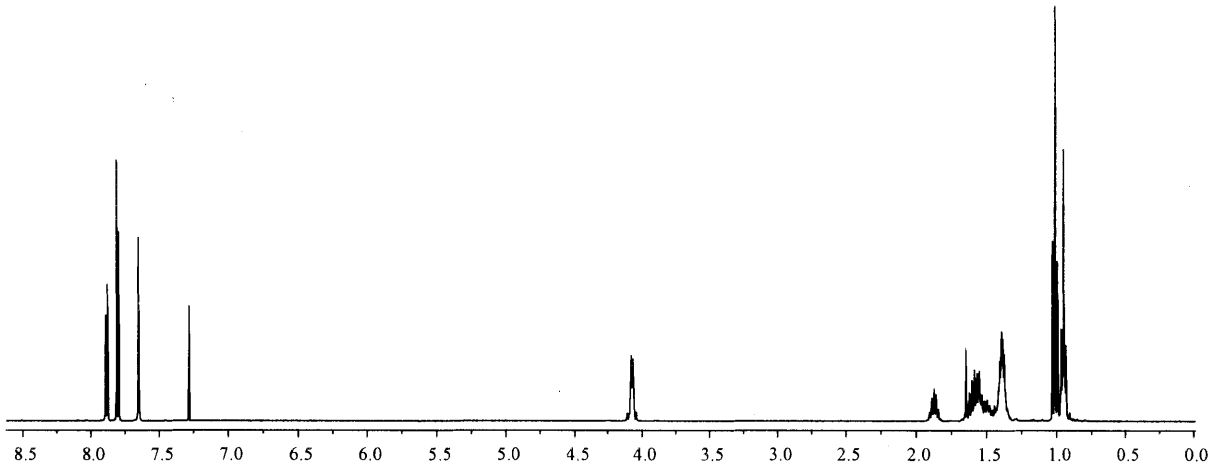

δ (ppm)

^{13}C NMR, $CDCl_3$, 100 MHz

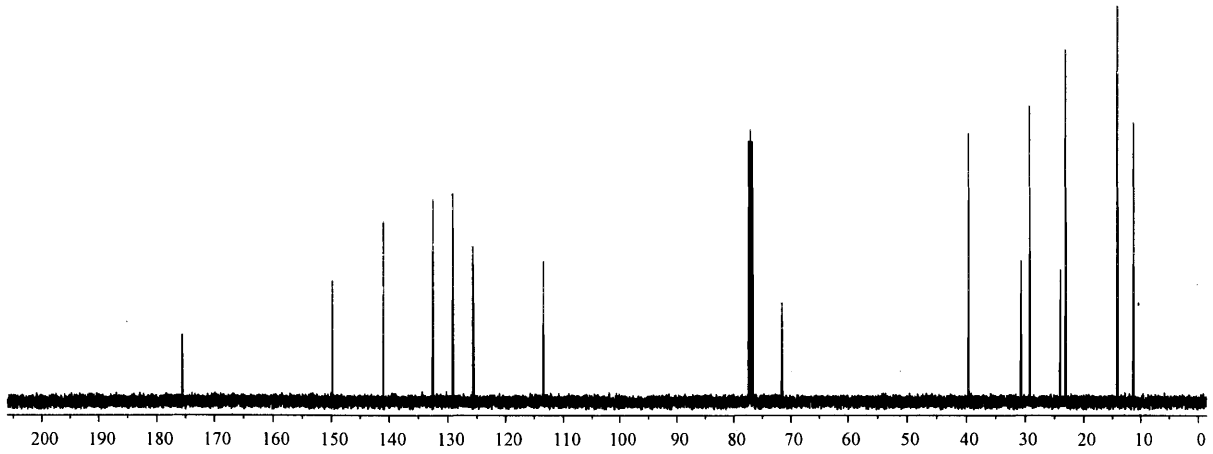

δ (ppm)

7. 5,5′-(4,5-Dimethoxy-1,2-phenylene)bis(2,4-dibromothiophene).

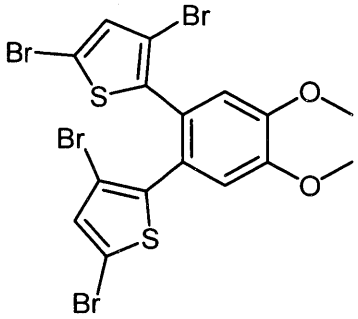

^{1}H NMR, $CDCl_3$, 400 MHz

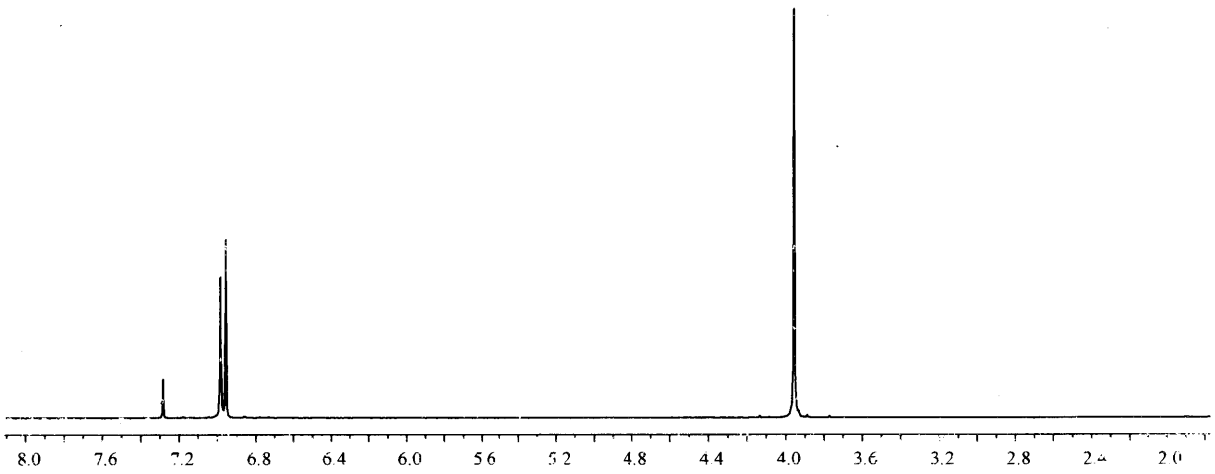

^{13}C NMR, $CDCl_3$, 100 MHz

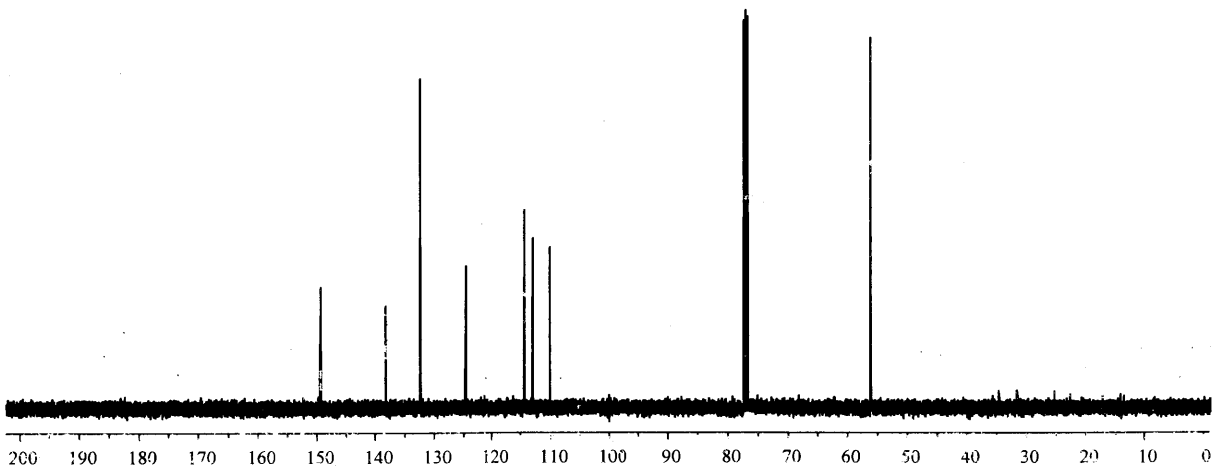

8. ((4,5-Dimethoxy-1,2-phenylene)bis(4-bromothiophene-5,2-diyl))bis(trimethylsilane).

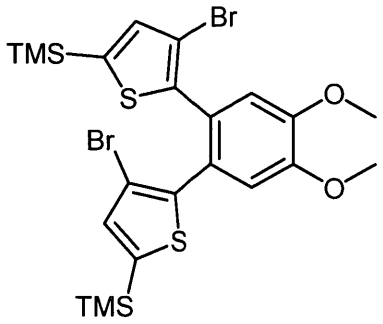

^{1}H NMR, $CDCl_3$, 400 MHz

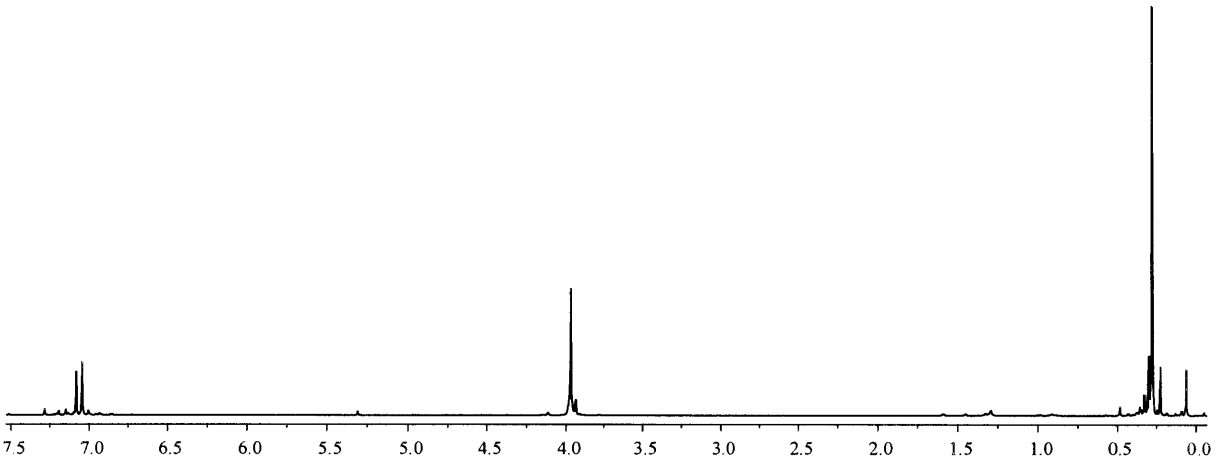

δ (ppm)

^{13}C NMR, $CDCl_3$, 100 MHz

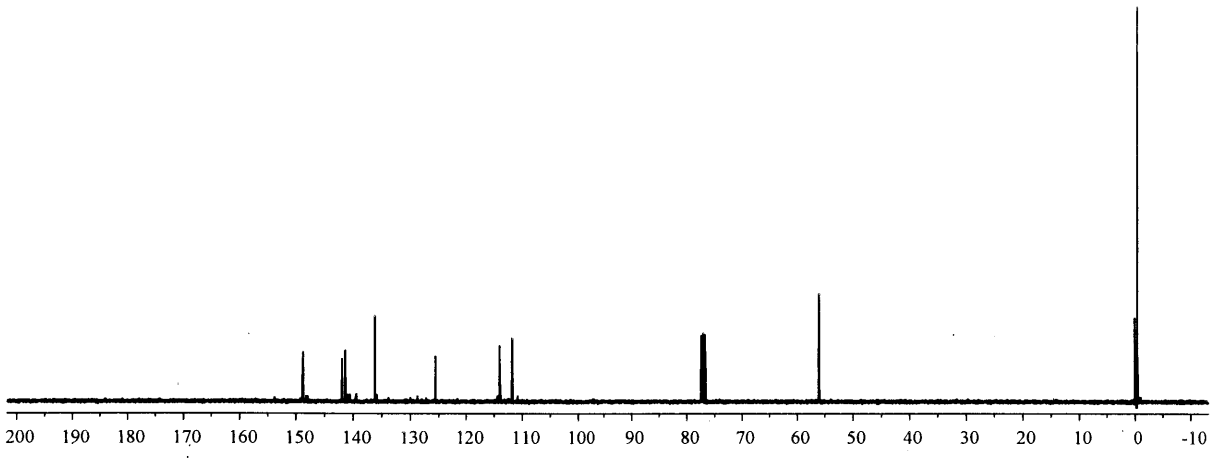

δ (ppm)

9. 2,3-Dimethoxy-6,10-bis(trimethylsilyl)-8*H*-benzo[6,7]cyclohepta[1,2-*b*:5,4-*b'*] dithiophen-8-one.

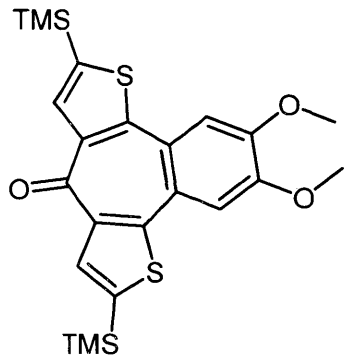

^{1}H NMR, $CDCl_3$, 400 MHz

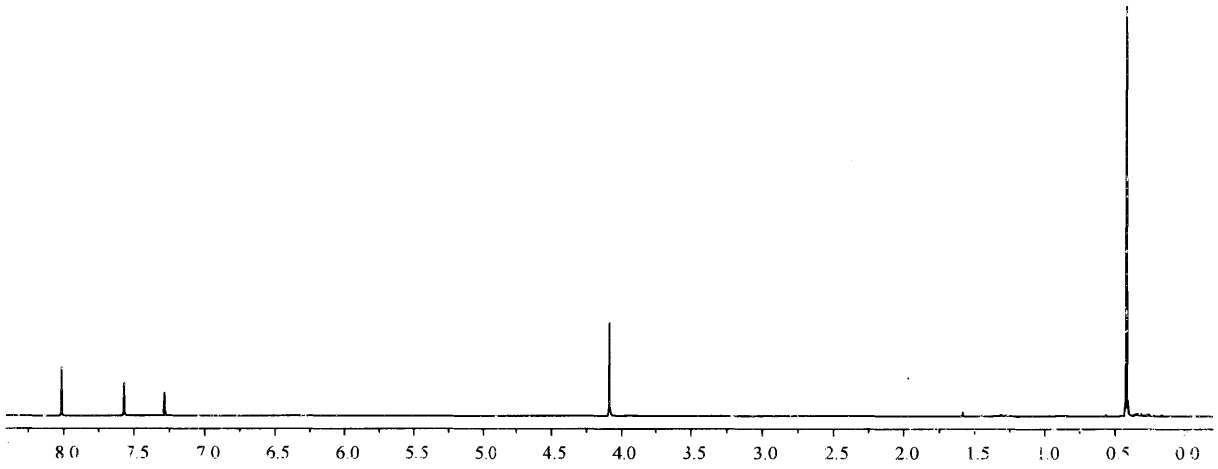

δ (ppm)

^{13}C NMR, $CDCl_3$, 100 MHz

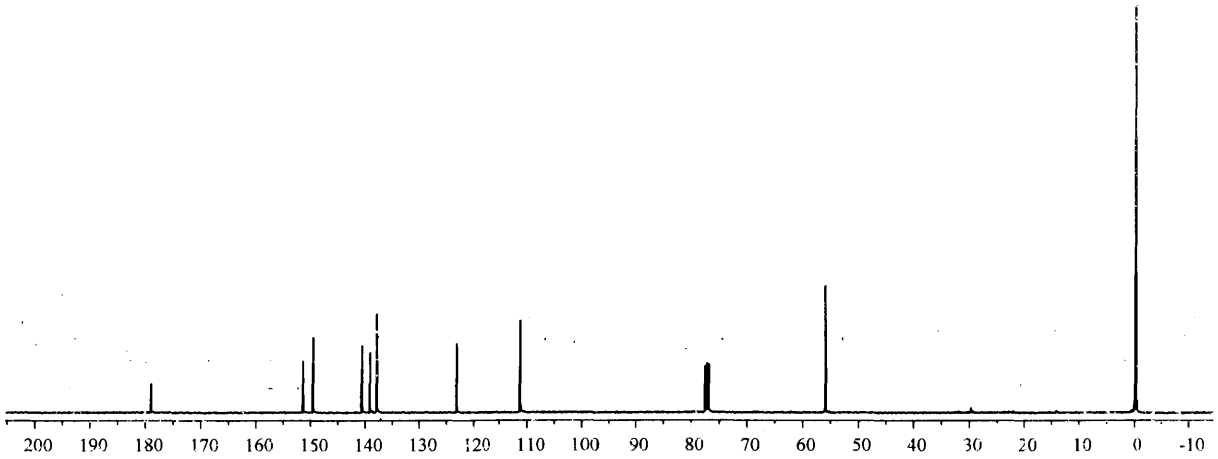

δ (ppm)

M2a. 2,3-Dimethoxy-8*H*-benzo[6,7]cyclohepta[1,2:-*b*:5,4-*b'*]dithiophen-8-one.

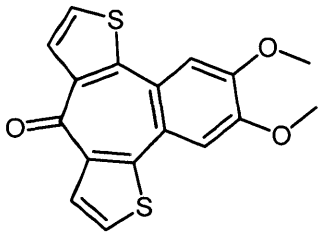

^{1}H NMR, $CDCl_3$, 400 MHz

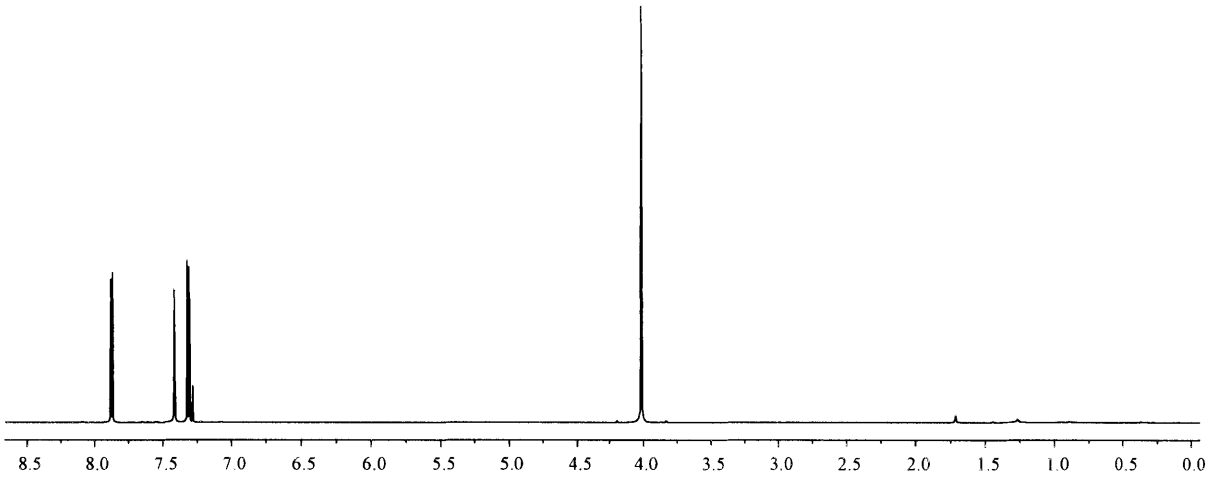

δ (ppm)

^{13}C NMR, $CDCl_3$, 100 MHz

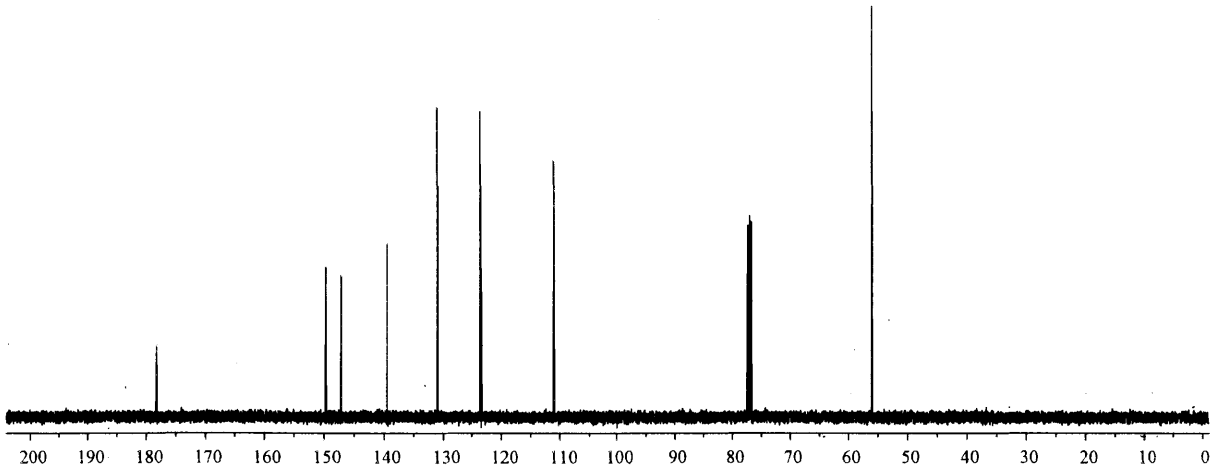

δ (ppm)

RM2a. 2,3-Dimethoxy-8*H*-benzo[6,7]cyclohepta[1,2:-*b*:5,4-*b'*]dithiophen-8-ol.

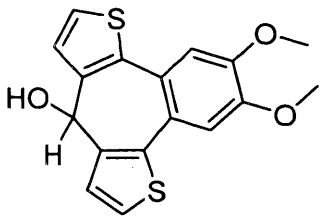

^{1}H NMR, $CDCl_3$, 500 MHz

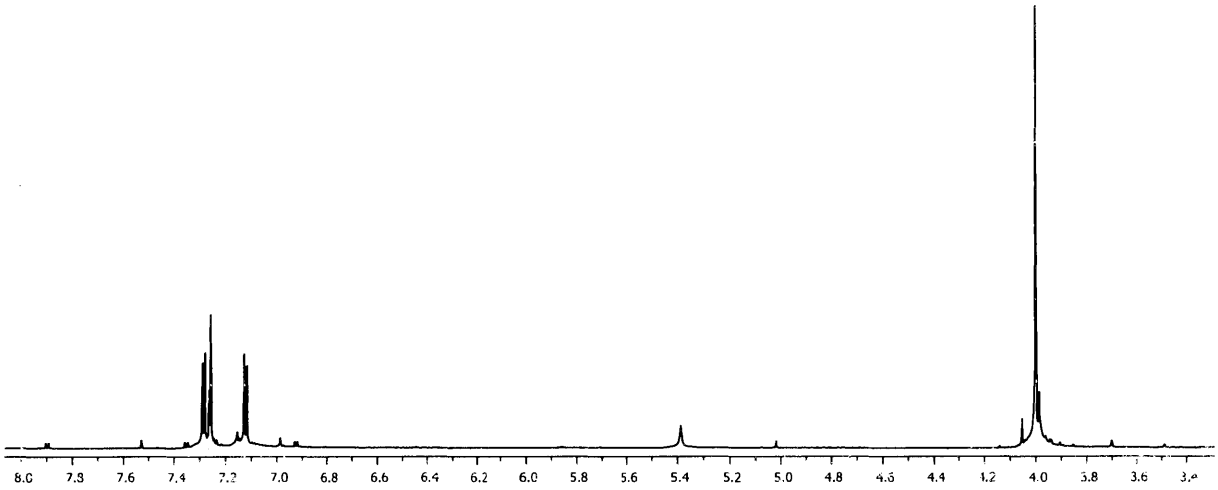

δ (ppm)

^{13}C NMR, $CDCl_3$, 125 MHz

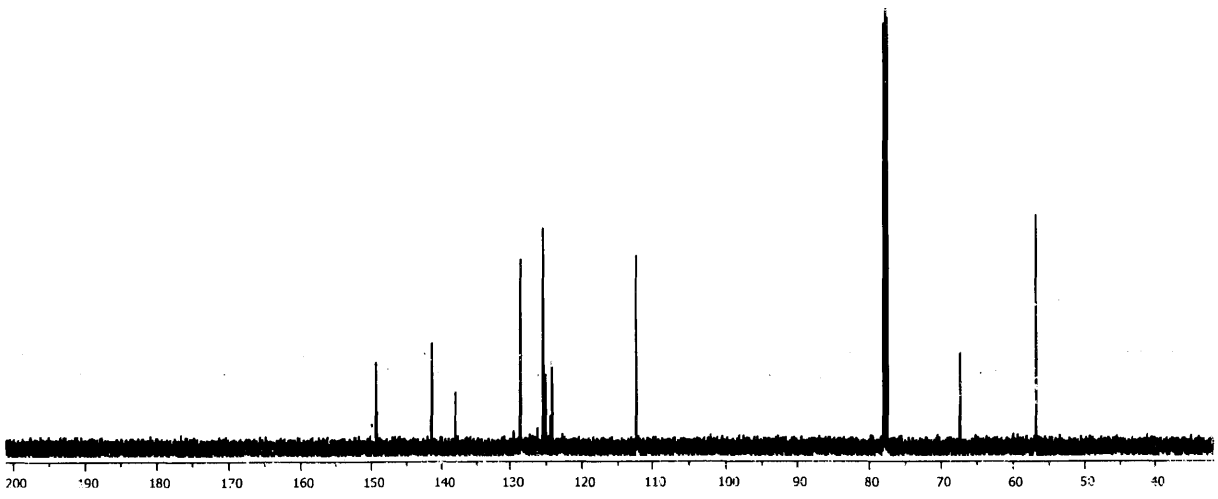

δ (ppm)

RM1a. 2,3-Dimethoxy-8*H*-benzo[6,7]cyclohepta[2,1-*b*:4,5-*b*']dithiophen-8-ol.

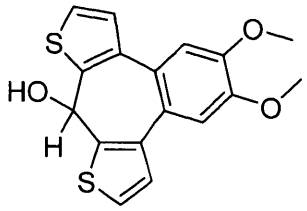

^{1}H NMR, $CDCl_3$, 500 MHz

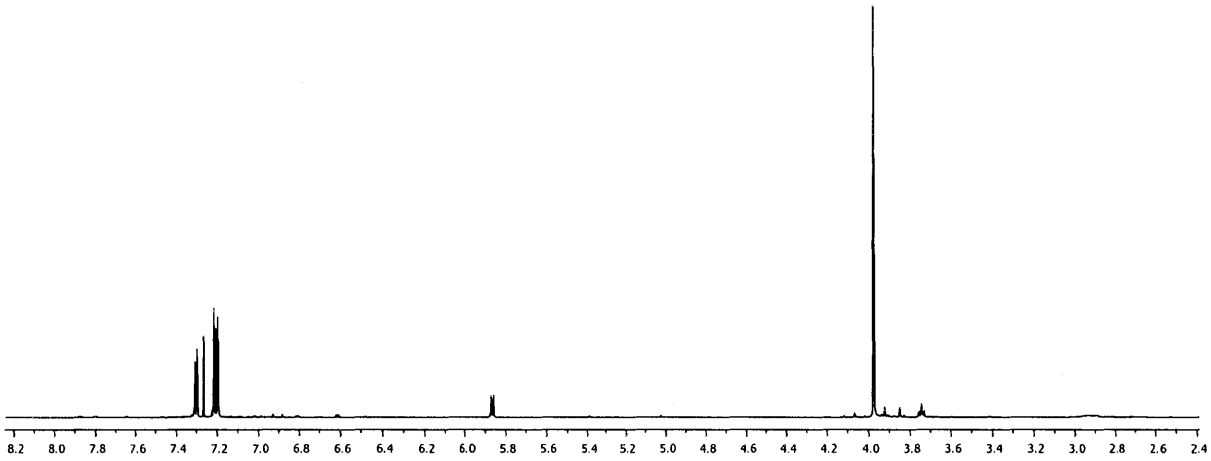

δ (ppm)

^{13}C NMR, $CDCl_3$, 125 MHz

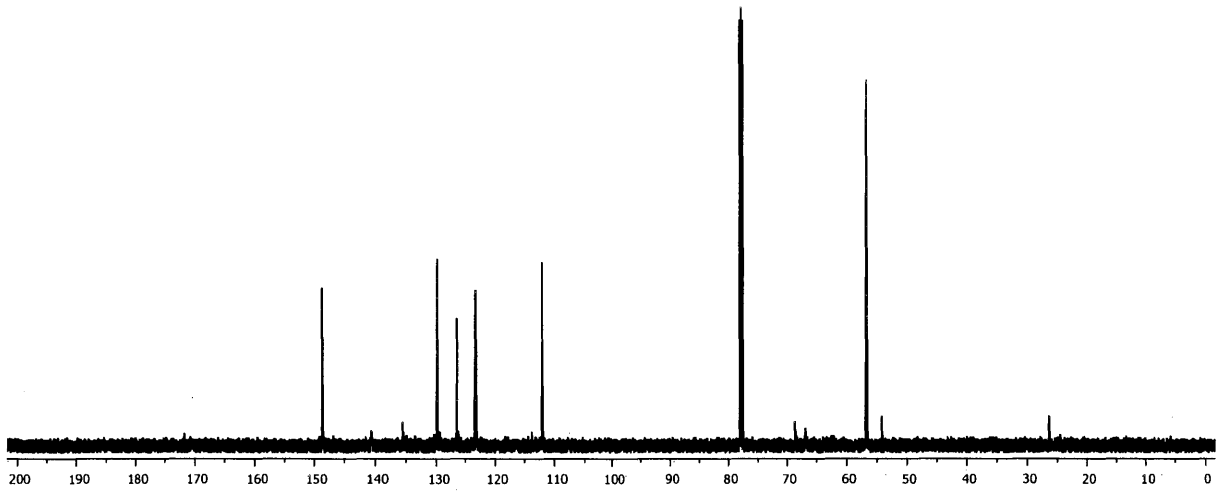

δ (ppm)

RM1b. 8-Butyl-1,2-dimethoxy-8*H*-benzo[6,7]cyclohepta[2,1-*b*:4,5-*b*']dithiophen-8-ol.

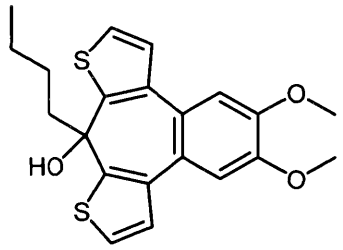

^{1}H NMR, $CDCl_3$, 400 MHz

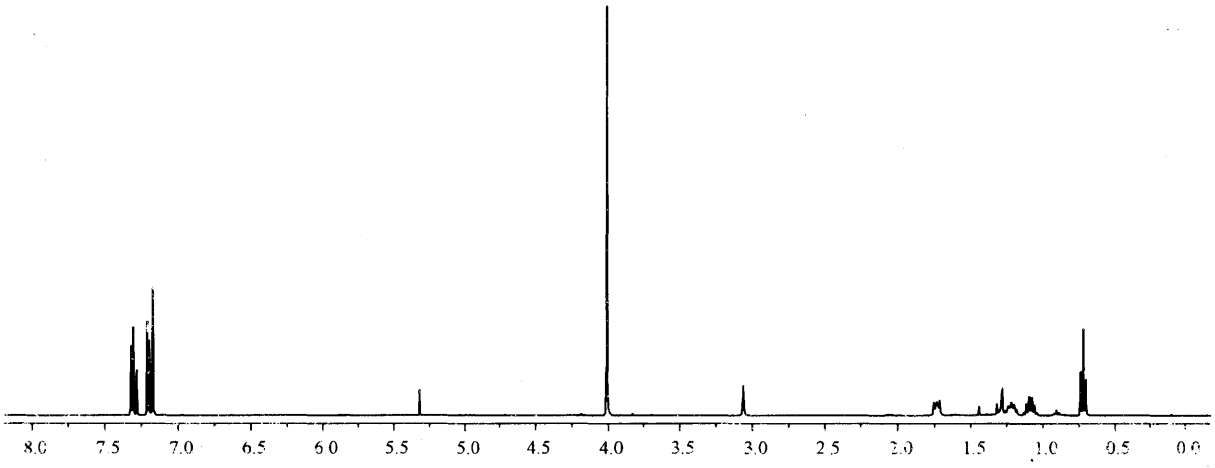

δ (ppm)

^{13}C NMR, $CDCl_3$, 100 MHz

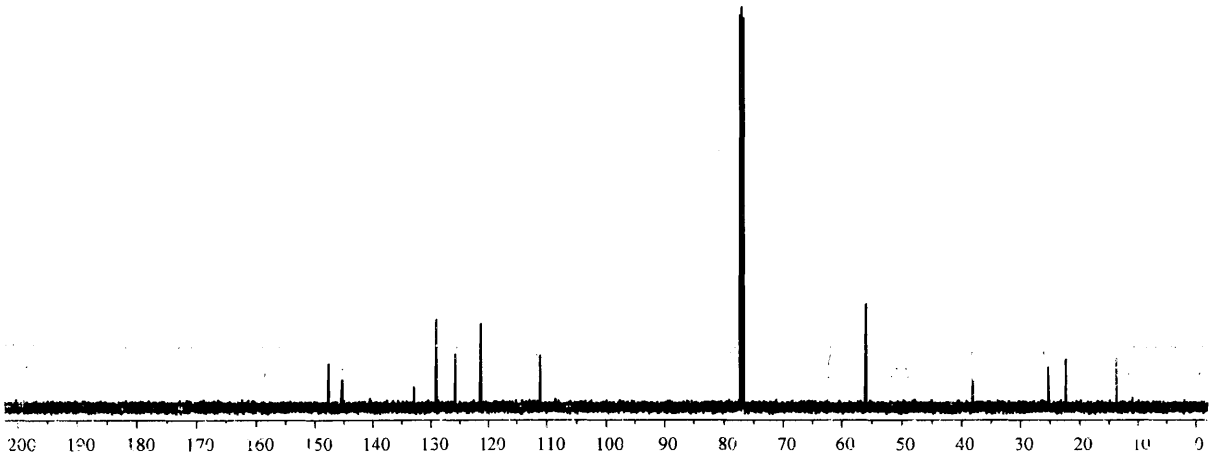

δ (ppm)

RM1c. 1,2-Dimethoxy-8-phenyl-8*H*-benzo[6,7]cyclohepta[2,1-*b*:4,5-*b'*]dithiophen-8-ol.

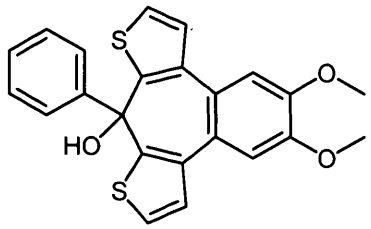

^{1}H NMR, $CDCl_3$, 400 MHz

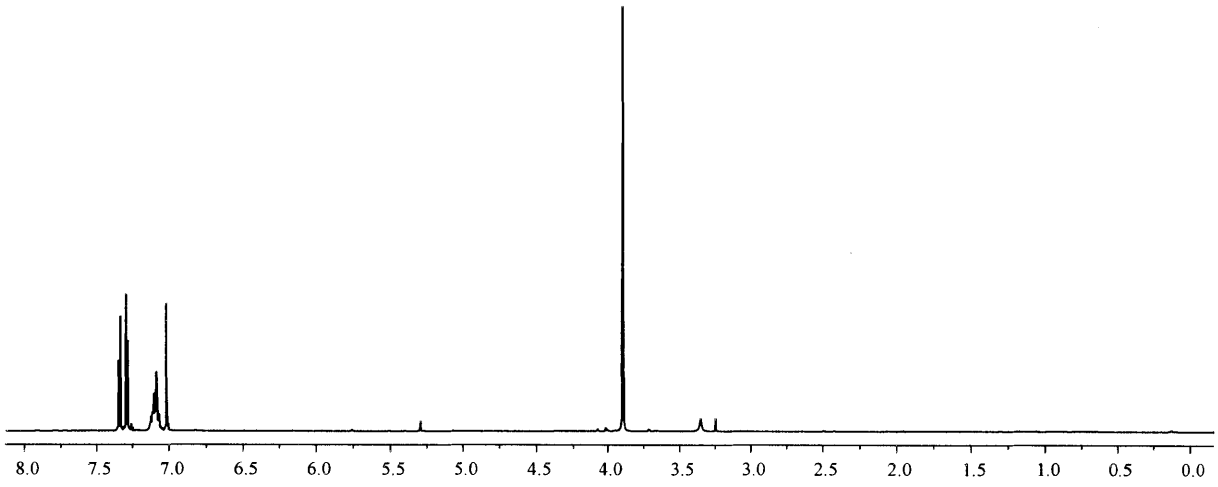

δ (ppm)

^{13}C NMR, $CDCl_3$, 100 MHz

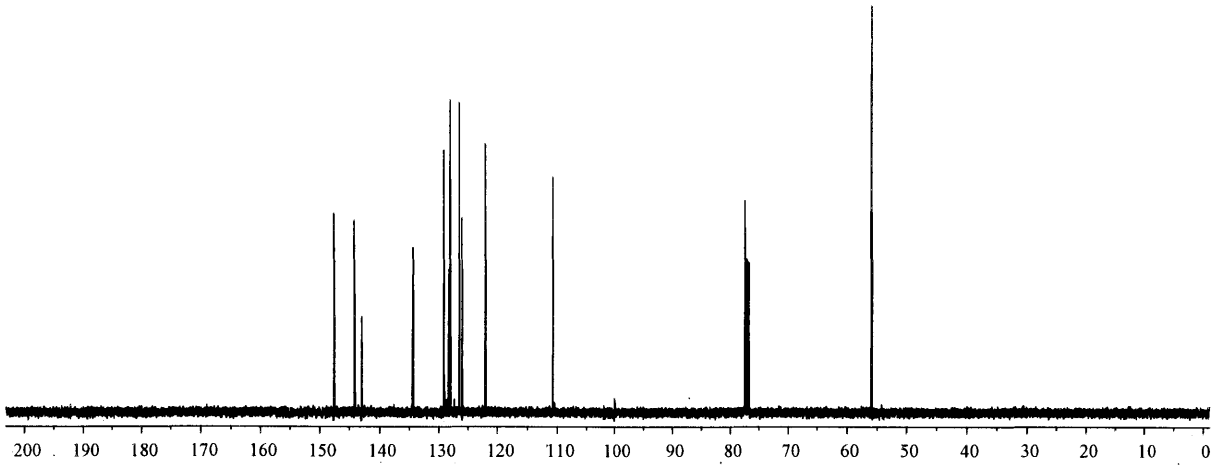

δ (ppm)

RM1d. 2,3-Dimethoxy-8-(4-(trifluoromethyl)phenyl)-8*H*-benzo[6,7]cyclohepta[2,1-*b*:4,5-*b'*]dithiophen-8-ol.

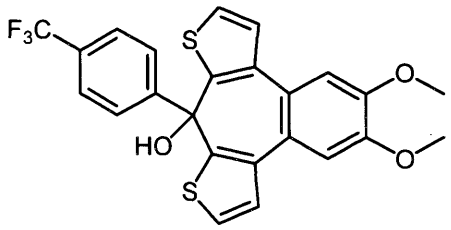

^{1}H NMR, $CDCl_3$, 400 MHz

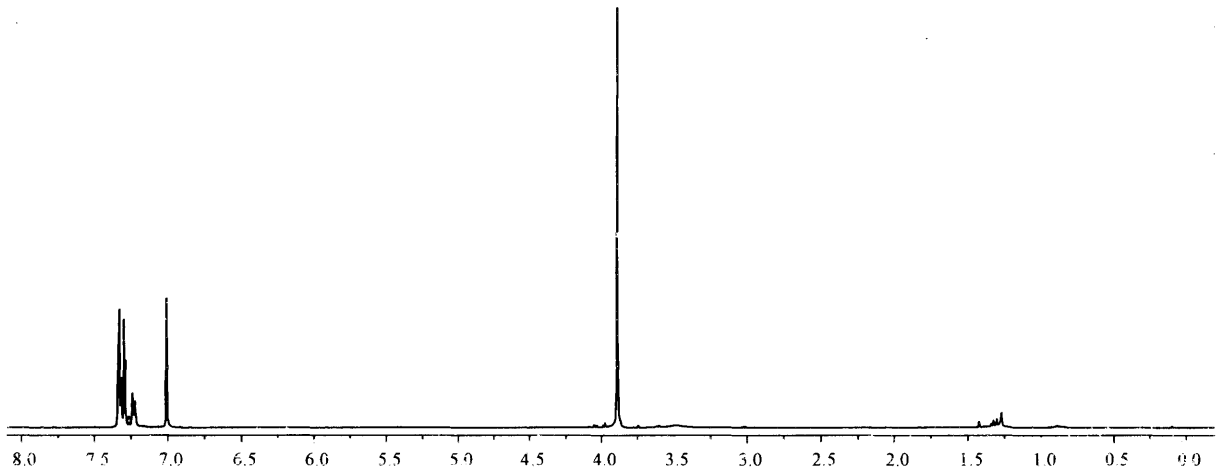

δ (ppm)

^{13}C NMR, $CDCl_3$, 100 MHz

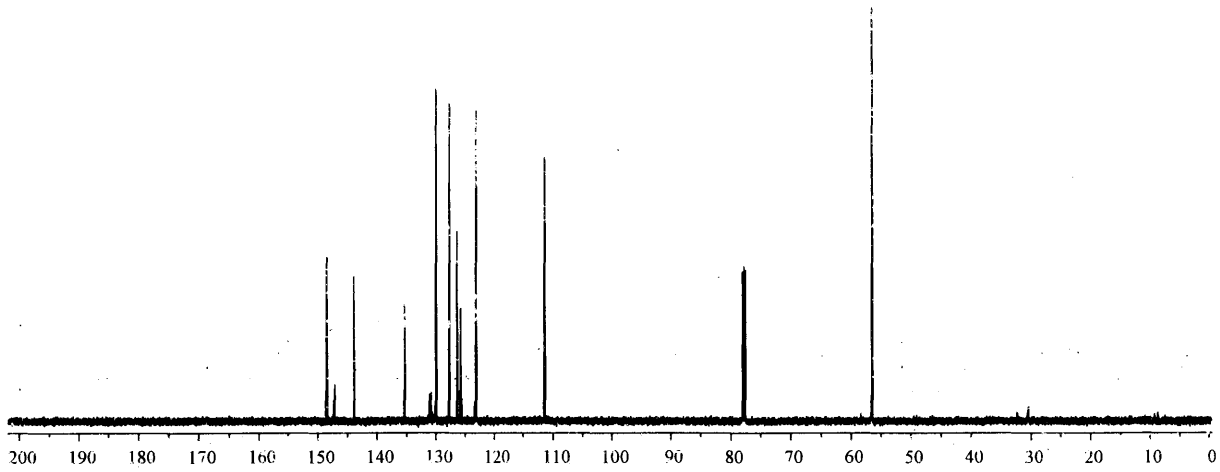

δ (ppm)

RM1e. 2,3-Dimethoxy-8-(4-methoxyphenyl)-8*H*-benzo[6,7]cyclohepta[2,1-*b*:4,5-*b'*]dithiophen-8-ol.

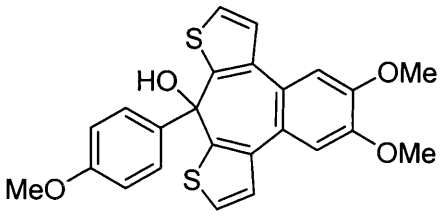

^{1}H NMR, $CDCl_3$, 400 MHz

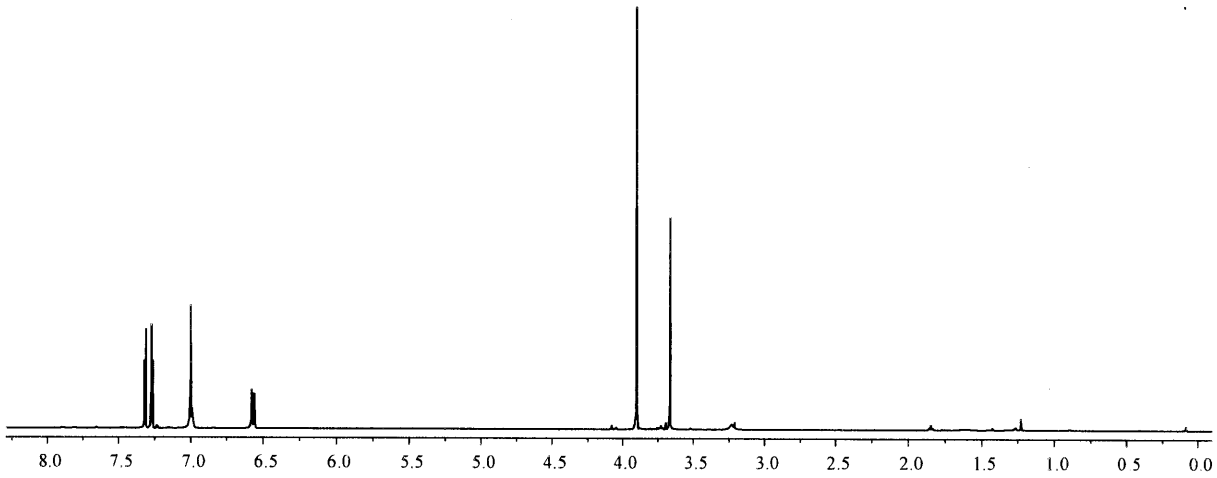

δ (ppm)

^{13}C NMR, $CDCl_3$, 100 MHz

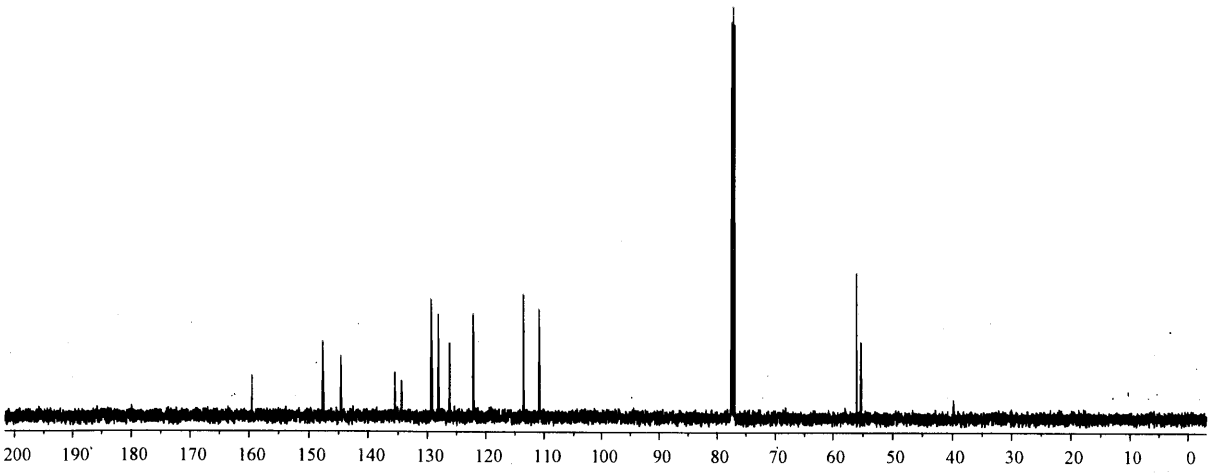

δ (ppm)

M1d. 2,3-Bis((2,5,8,11-tetraoxatridecan-13-yl)oxy)-8*H*-benzo[6,7]cyclohepta[2,1-*b*:4,5-*b'*]dithiophen-8-one.

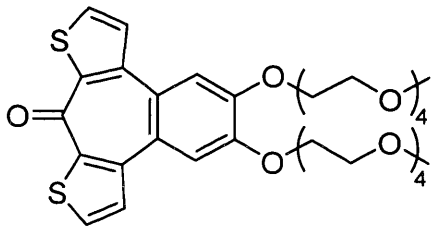

^{1}H NMR, $CDCl_3$, 400 MHz

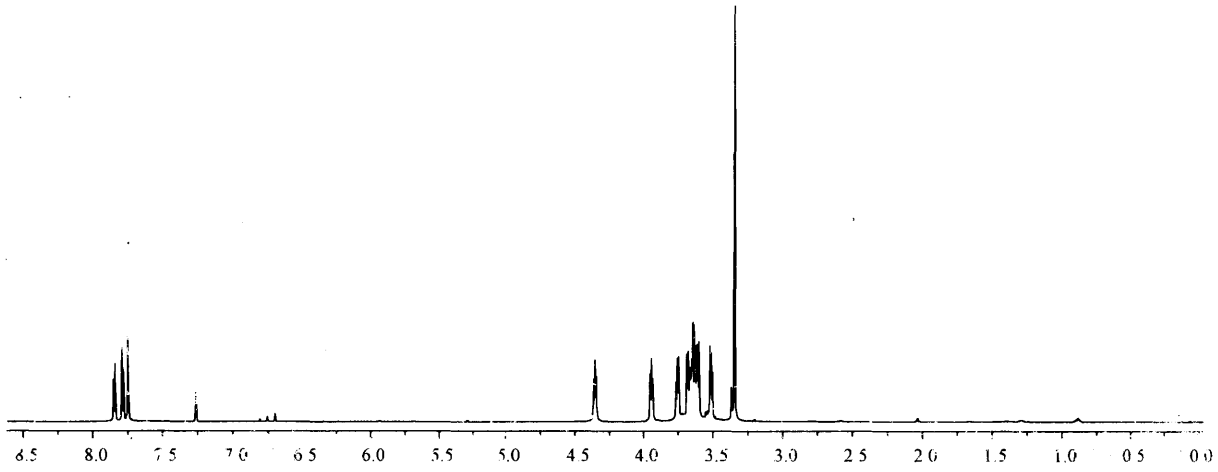

δ (ppm)

^{13}C NMR, $CDCl_3$, 100 MHz

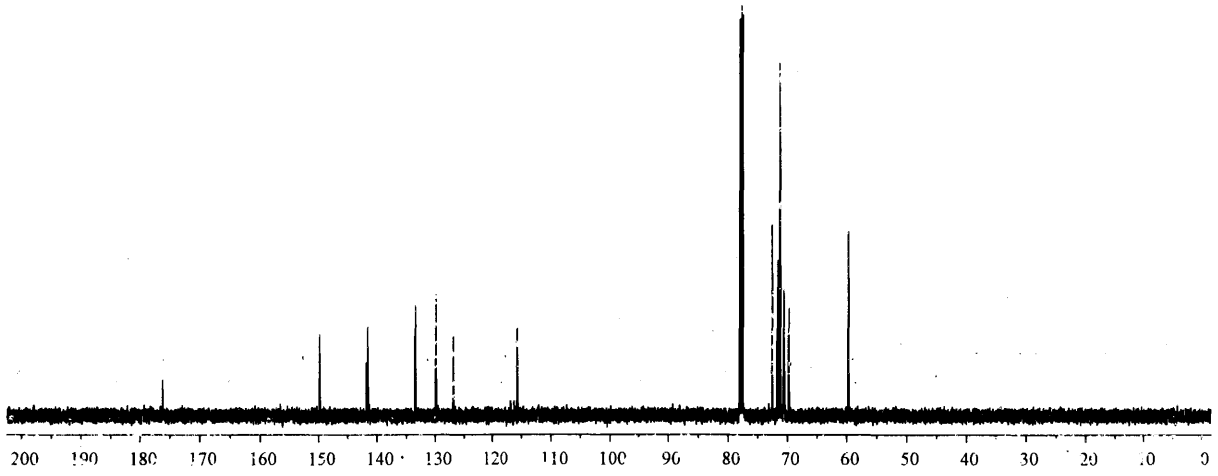

δ (ppm)

M3. 8-(4-(Bicyclo[2.2.1]hept-5-en-2-yl)phenyl)-8*H*-benzo[6,7]cyclohepta[2,1-*b*:4,5-*b'*]dithiophen-8-ol.

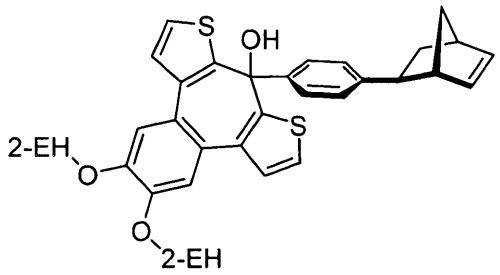

^{1}H NMR, $CDCl_3$, 500 MHz

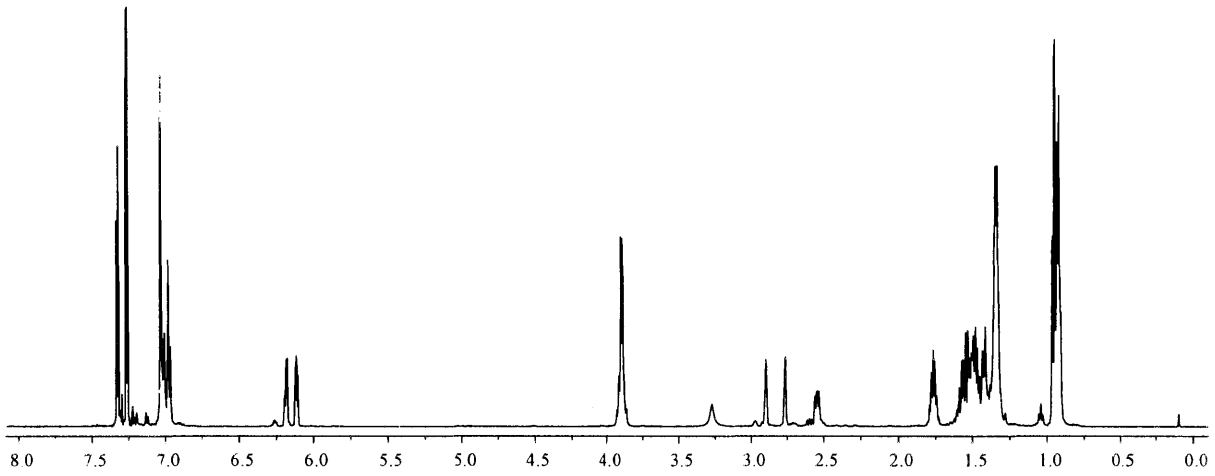

δ (ppm)

^{13}C NMR, $CDCl_3$, 125 MHz

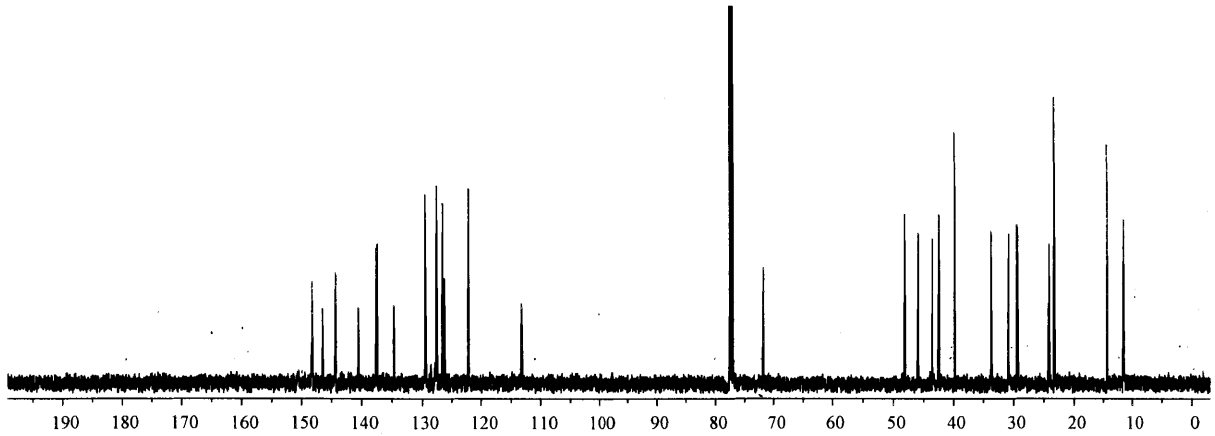

δ (ppm)

CM6. 2-Hexadecyl-3a,4,7,7a-tetrahydro-1*H*-4,7-methanoisoindole-1,3(2*H*)-dione.

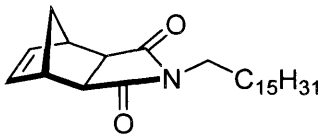

^{1}H NMR, $CDCl_3$, 500 MHz

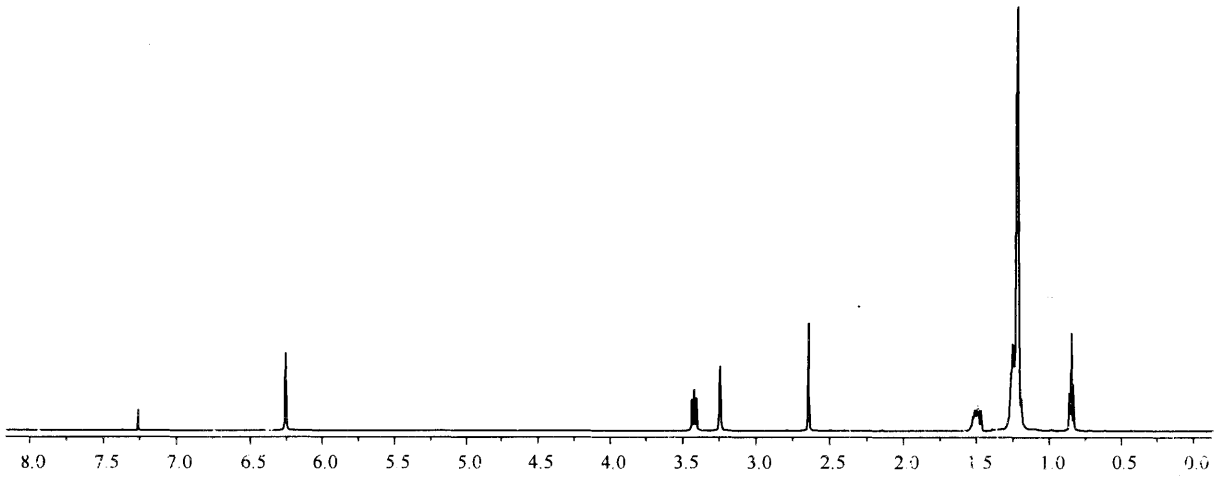

δ (ppm)

^{13}C NMR, $CDCl_3$, 125 MHz

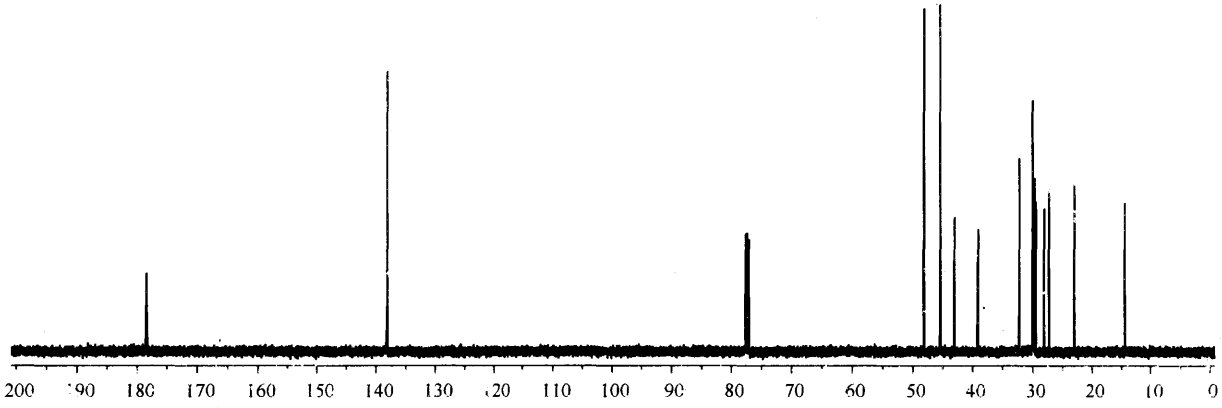

δ (ppm)

CM7. Di(2,5,8,11-tetraoxatrdecan-13-yl)-*exo*-7-oxabicyclo[2.2.1]hept-5-ene-2,3-dicarboxylate.

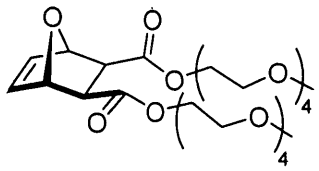

^{1}H NMR, $CDCl_3$, 500 MHz

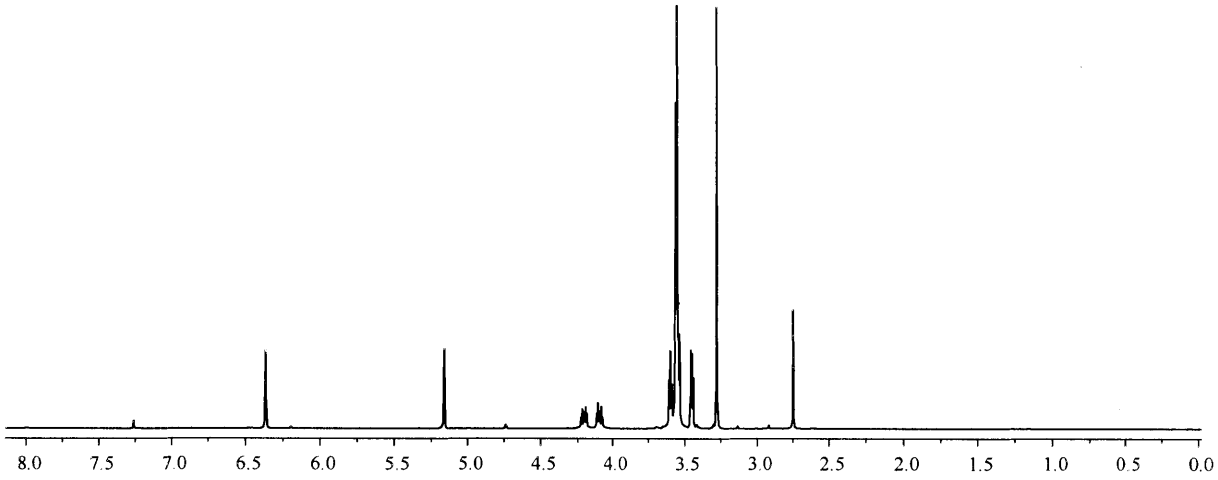

δ (ppm)

^{13}C NMR, $CDCl_3$, 125 MHz

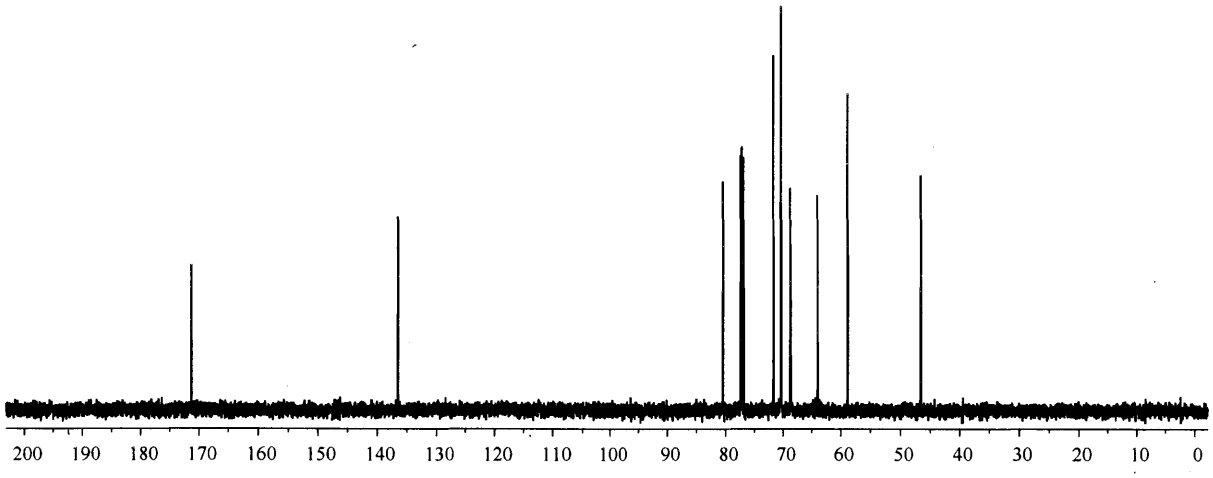

δ (ppm)

NMR Spectra of Polymers

P1b.

^{1}H NMR, $CDCl_3$, 500 MHz

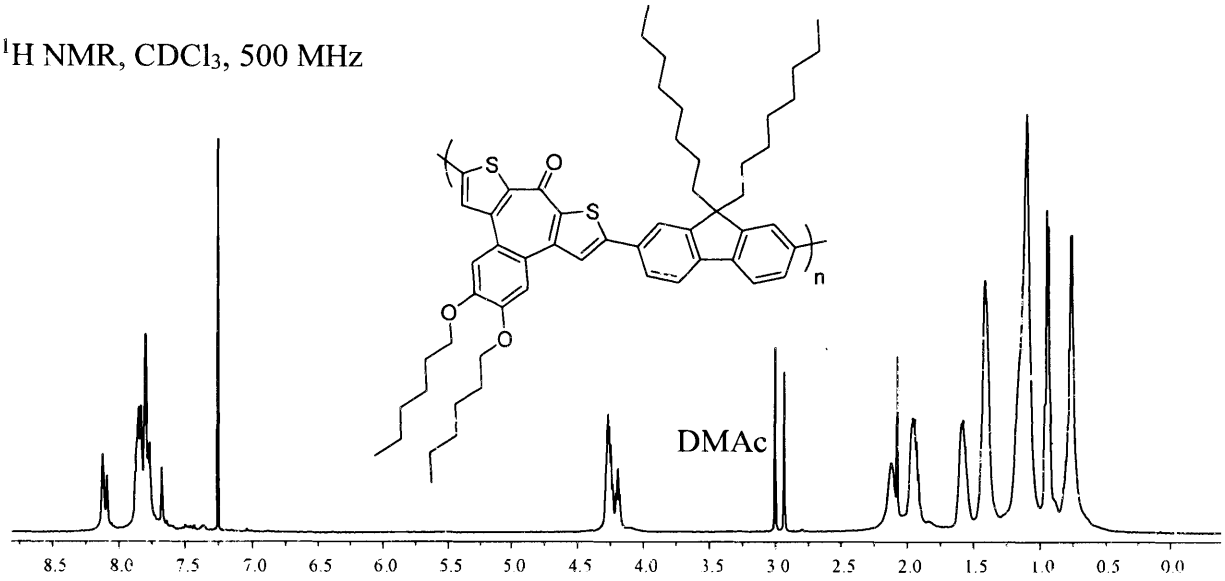

δ (ppm)

P1c.

^{1}H NMR, $CDCl_3$, 500 MHz

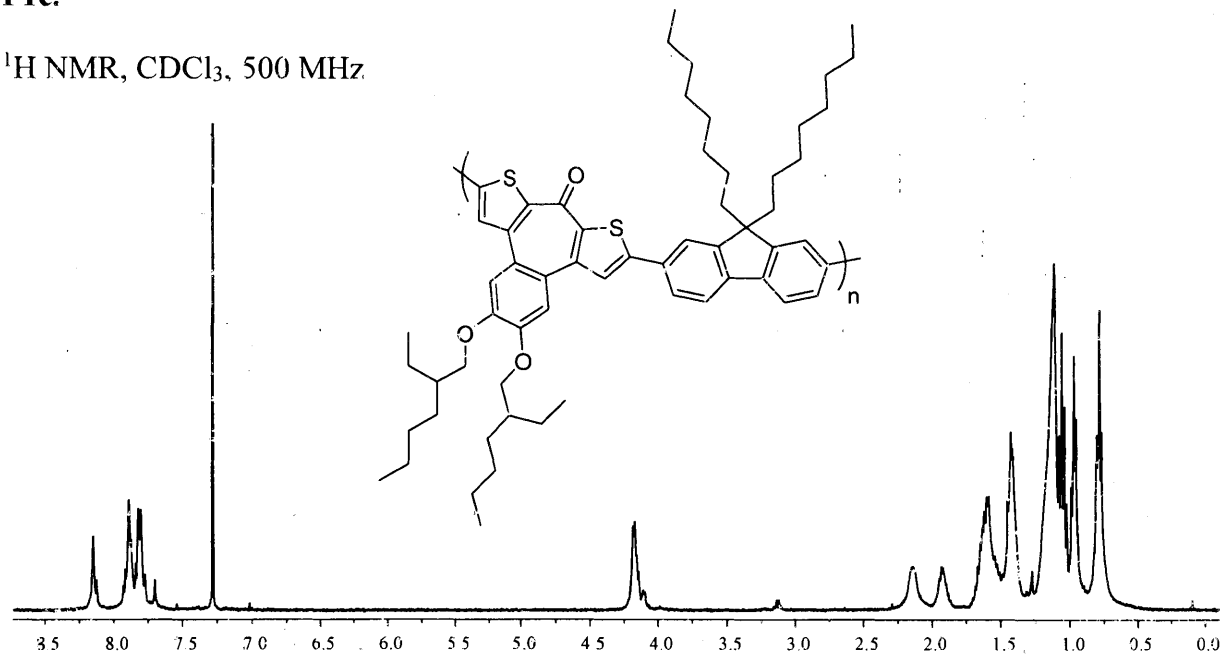

δ (ppm)

P1d.

^{1}H NMR, $CDCl_3$, 500 MHz

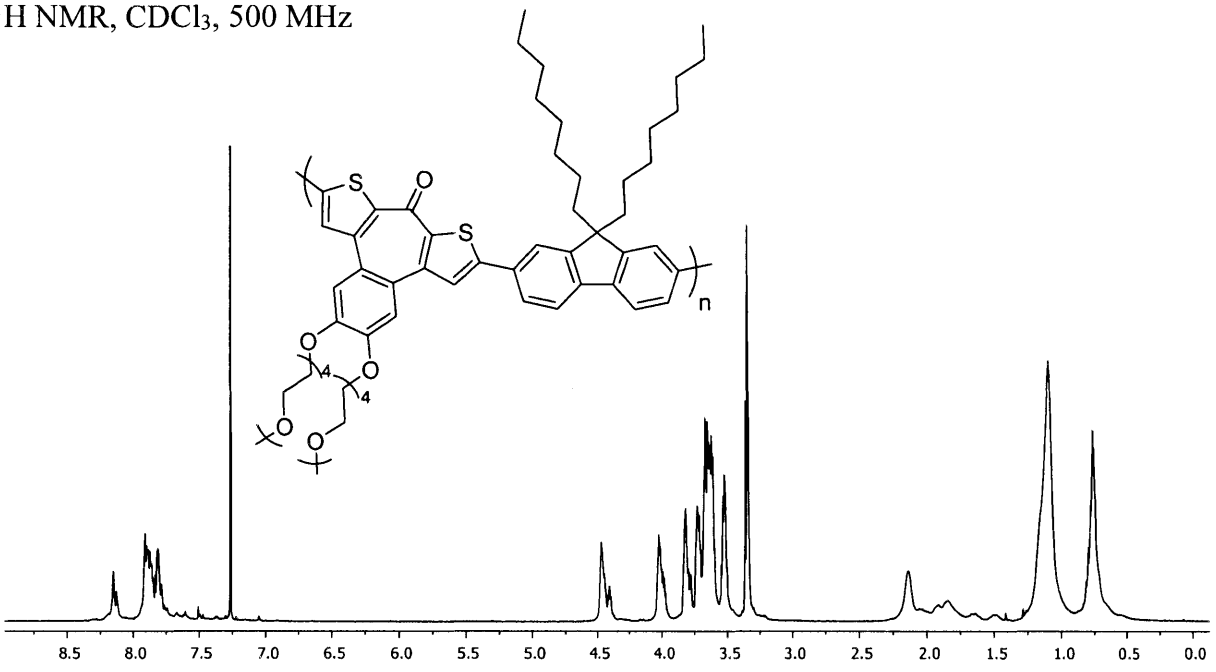

δ (ppm)

RP1b.

^{1}H NMR, $CDCl_3$, 500 MHz

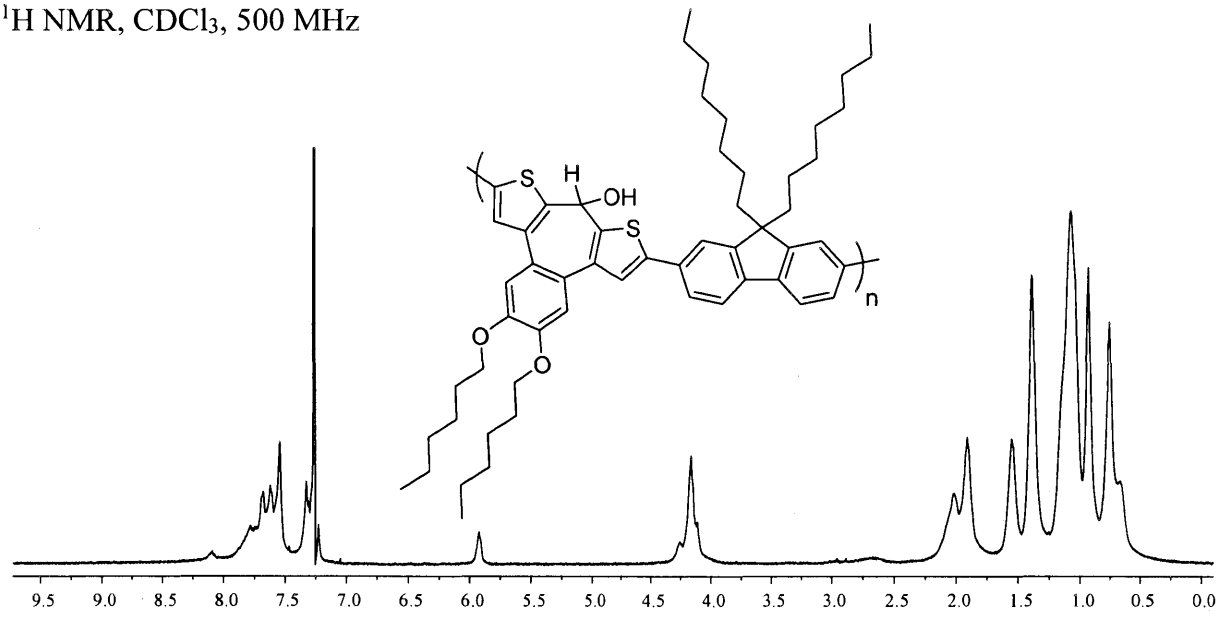

δ (ppm)

RP1c.

^{1}H NMR, $CDCl_3$, 500 MHz

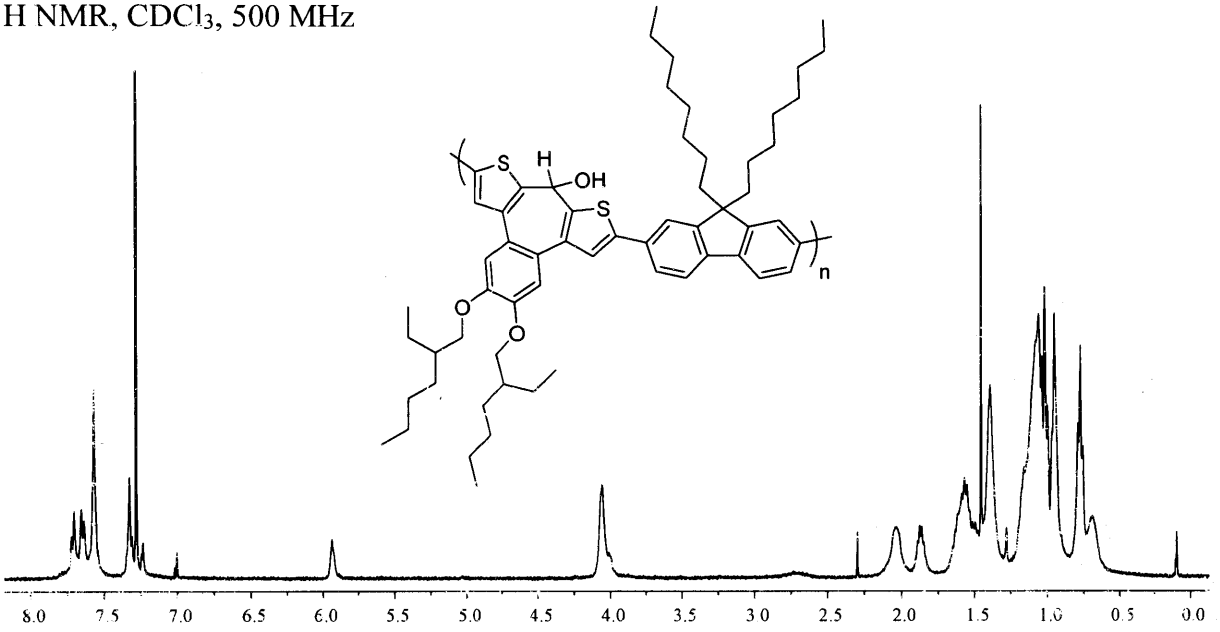

δ (ppm)

RP1d.

^{1}H NMR, $CDCl_3$, 500 MHz

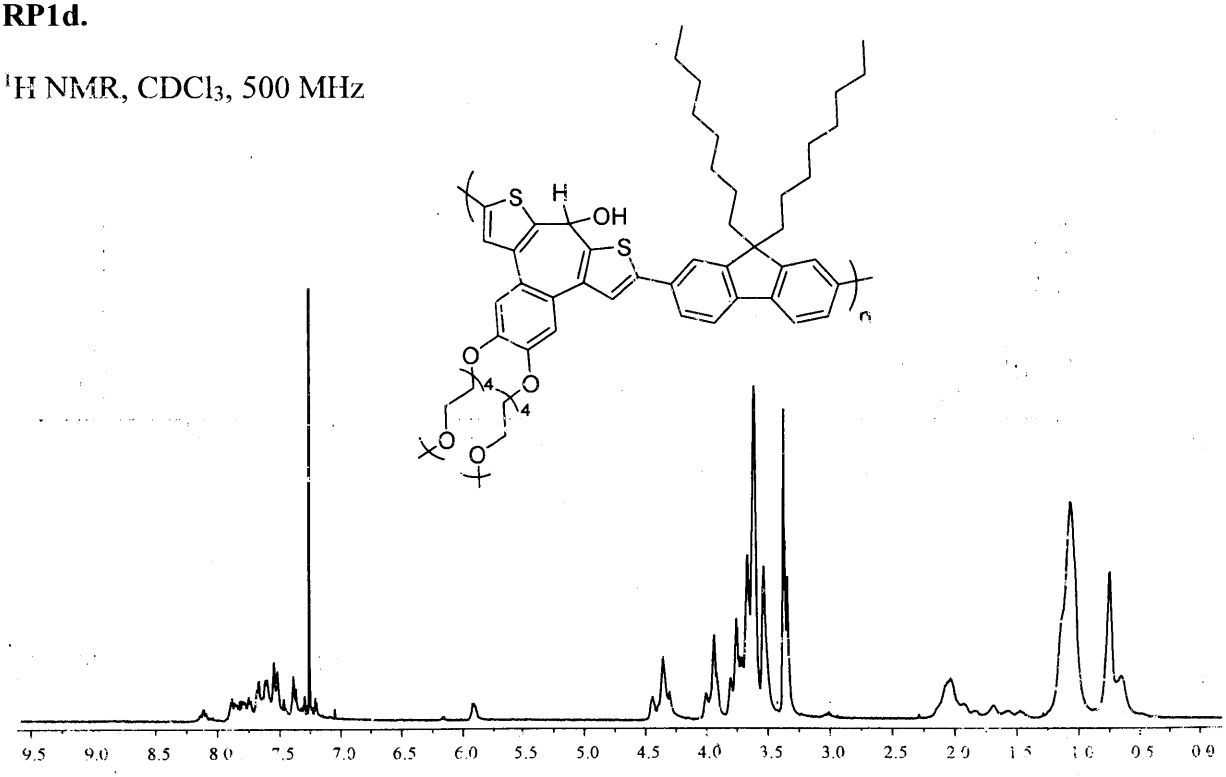

δ (ppm)

RCP1.

^{1}H NMR, $CDCl_3$, 500 MHz

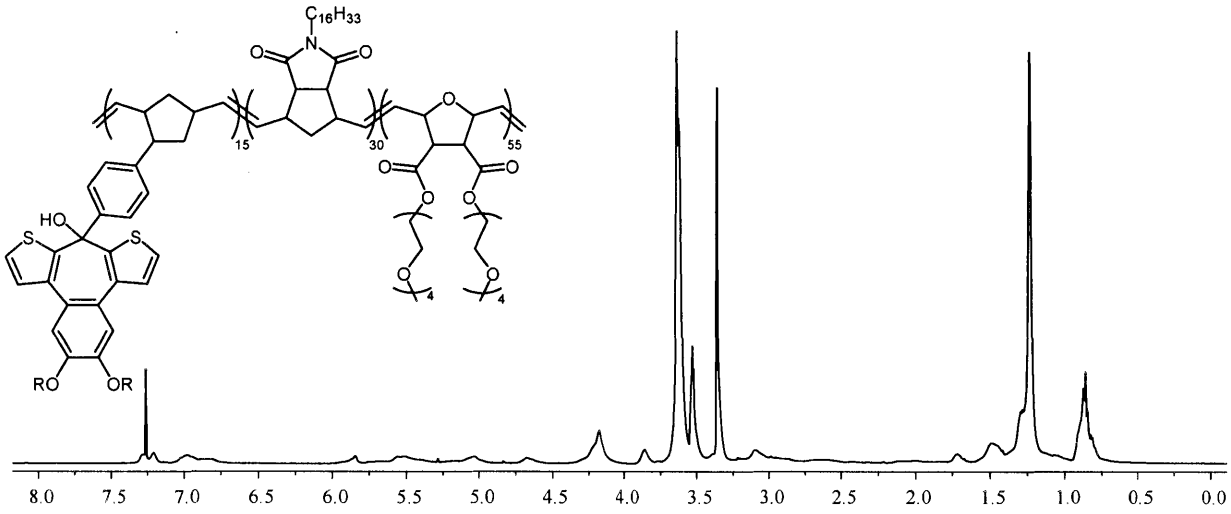

δ (ppm)

RCP2.

^{1}H NMR, $CDCl_3$, 500 MHz

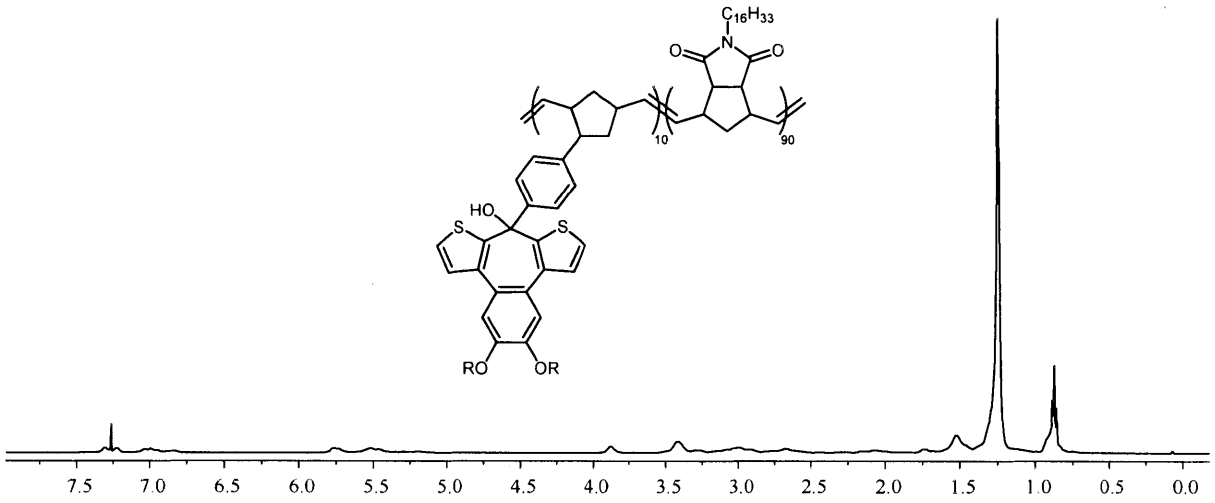

δ (ppm)

CHAPTER 2

Polynorbornadienes as Homoconjugated Precursors to Electronic Materials

Parts of this chapter were adapted and reprinted with permission from Forrest, W. P.; Weis, J. G.; John, J. M.; Axtell, J. C.; Simpson, J. H.; Swager, T. M.; Schrock, R. R.* "Stereospecific Ring-Opening Metathesis Polymerization of Norbornadienes Employing Tungsten Oxo Alkylidene Initiators" *J. Am. Chem. Soc.* **2014**, *136*, 10910–10913.

2.1 Introduction

Although desirable p-type organic materials are ubiquitous, there is a distinct paucity of high-performing n-type materials as a result of typically high-lying LUMO energies that render them unstable in ambient conditions. By lowering the LUMO energy level, the reductive power of the radical anion is mitigated and electron injection is facilitated. Common n-type organic semiconductors include functionalized fullerenes, rylene diimides, and heavily fluorinated acenes.[1] Our group has explored n-type polymers including poly(pyridinium phenylene)s,[2,3,4] poly(phenylene dicyanovinylene)s,[5] benzisoxazole-containing polyfluorenes,[6] fluorinated PPVs[7] and PPEs,[8,9,10] and fluorinated polythiophenes.[11,12]

The vast majority of syntheses for electronic polymers utilize polymerization techniques that are step-growth in nature. Consequently, there is little control over molecular weight and the synthesis of block copolymers is complicated by the difficulty in precisely defining each end group or the demand for orthogonal polymerization chemistry. Alternatively, ring-opening metathesis polymerization (ROMP), a living chain-growth polymerization technique, provides excellent control over molecular weight and allows the facile synthesis of multiblock copolymers. In the case of random copolymers, the polymerization is highly modular, and macroscopic properties can be tuned by controlling the monomer structures and relative stoichiometry. For the synthesis of electronic polymers, ROMP of norbornadienes and its derivatives produces excellent polymeric precursors for electronic polymers.

The discovery and exploitation of metathesis reactions have transformed organic synthesis and polymer chemistry along with it. Consequently, Chauvin, Grubbs, and Schrock were awarded the Nobel Prize in Chemistry in 2005. There are a number of metathesis polymerizations that are known to directly yield conjugated polymers. Attempting ring-

opening metathesis polymerization with unsubstituted cyclooctatetraene (COT) yields benzene due to back-biting.[13] Monosubstituted COTs, however, have successfully been polymerized to polyacetylenes that are substituted every fourth double bond.[14] Strained cyclophanedienes can undergo ROMP to yield poly(phenylene vinylene)s (PPVs).[15,16] A poly(thienylene vinylene) has been similarly synthesized.[17] Acyclic diene metathesis (ADMET) of divinyl arenes also leads to poly(arylene vinylene)s,[16,18,19] although this route is less atom-economical as a result of the loss of ethylene. Alkynes can also be directly polymerized to substituted polyacetylenes. Conjugated poly(arylene ethynylene)s can be prepared by alkyne metathesis.[20,21] The cyclopolymerization of 1,6-heptadiyne[22,23] or 1,7-octadiyne[24] derivatives is also known to give conjugated polymers.

The difficult synthetic route to some of these monomers hinders their widespread application, as other polymerization techniques create structurally similar polymers with high fidelity more easily. Oftentimes, precursor polymers provide more accessible synthetic routes and are well-known in conducting polymer literature. A classic in conjugated polymers, Feast and Edwards synthesized polyacetylene by polymerizing the Diels–Alder adduct of COT and hexafluoro-2-butyne by ROMP and subsequently performing a thermal retro-Diels–Alder to remove *o*-hexafluoroxylene (Scheme 2.1a).[25,26] Later, Grubbs and Swager reported a more atom-economical synthesis of polyacetylene (Scheme 2.1b).[27] Ring-opening metathesis polymerization of benzvalene yielded an elastomeric bicyclobutane-containing polymer. Interestingly, this polymer decomposed explosively upon stretching or heating. Subsequent treatment with mercury (II) chloride isomerizes the polybenzvalene to polyacetylene. The same group also synthesized cross-conjugated poly(bis(*exo*methylene(cyclobutene))),[28] as shown in Scheme 2.1c.

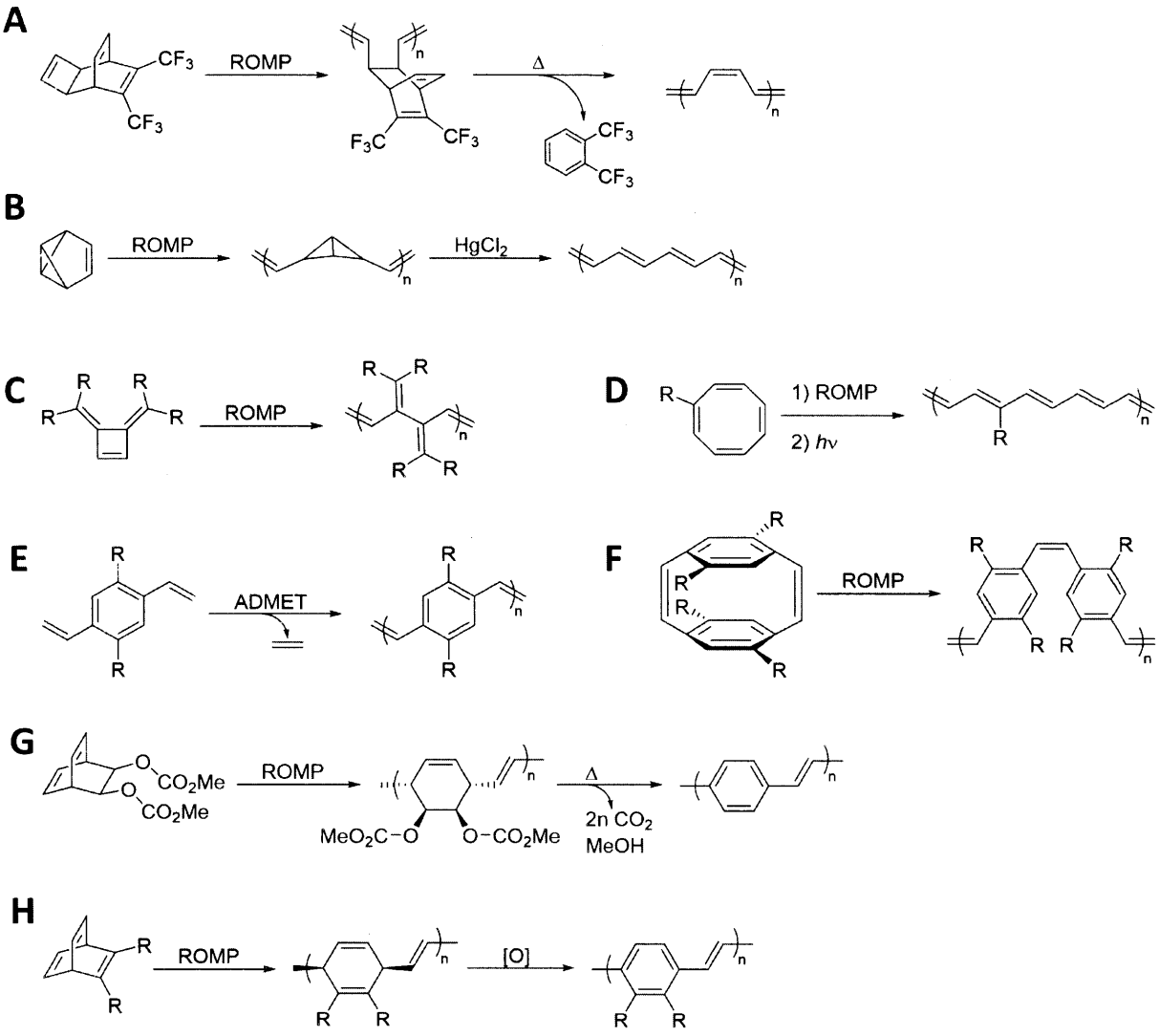

Scheme 2.1. Examples of conjugated polymers prepared by metathesis.

The Grubbs group has reported a number of transformations of substituted polybarrelenes,[29] which upon treatment with oxidizing agents furnish poly(phenylene vinylene)s, as shown in Scheme 2.1h. Similar sequences from benzobarrelenes can be used to reach poly(naphthalene vinylene)s.[30,31]

Poly(cyclopentadienylene vinylene)s and poly(furanylene vinylene)s are also desirable targets, as they are predicted to possess highly quinoidal character in their ground states.[32]

These electronic polymers are typically prepared by the thermal or base-induced elimination reactions of a dichlorocarbonate,[33] acetate,[34] carbonates[35] or xanthates[35,36] Ideally, oxygen can be used to convert the precursor poly(norbornadiene) to a poly(cyclopentadienylene vinylene) derivative;[37] however, chemical oxidants including DDQ have also been used.[38]

When considering monomers for ROMP, we wanted to exploit the nitrile group to develop stable n-type materials. The nitrile group is strongly electron-withdrawing, thus invoking desirable LUMO level-lowering properties. Additionally, nitriles exhibit intermolecular C≡N···H contacts, promoting closer packing. This trait is desirable in electronic materials, as it can lead to improved carrier mobilities. Nitrile-containing conjugated polymers, such as poly(phenylene cyanovinylene)s[39] and α,ω-dicyanooligothiophenes,[40] have been demonstrated to exhibit favorable n-type properties, and our group has previously reported the synthesis and application of poly(phenylene dicyanovinylene)s[5] and 6,6-dicyanofulvenes.[41] In efforts to further explore nitrile-containing materials, we looked to employ dicyanoacetylene (DCA) as a starting material as a result of its excellent dienophilicity. Uniquely, DCA undergoes Diels–Alder reactions with difficult dienes such as durene[42] and thiophene.[43]

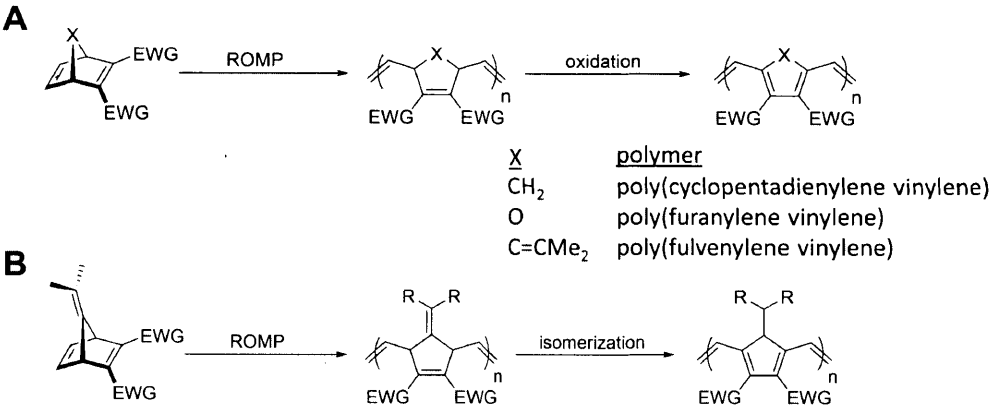

Scheme 2.2. a) General scheme for ROMP of norbornadienes and subsequent oxidation to poly(cyclopentadienylene vinylene) derivatives. b) Special case of poly(fulvenylene vinylene)s that can isomerize to a conducting isopropyl-substituted poly(cyclopentadienylene vinylene). EWG = electron-withdrawing group.

We hypothesized that the introduction of DCA's nitrile groups to poly(cyclopentadienylene vinylene) could enable an electron-transporting polymer. Polymerization of dicyano-substituted norbornadienes by ROMP produces polymer precursors that could be converted to electron-transporting conducting polymers upon post-polymerization modification. As shown in Scheme 2.2, oxidation — or isomerization in the case of alkylidenenorbornadienes — of the homoconjugated precursor polymers leads to the corresponding electronic polymers.

2.2 Results and Discussion

2.2.1 Ring-Opening Metathesis Polymerization of Norbornadienes

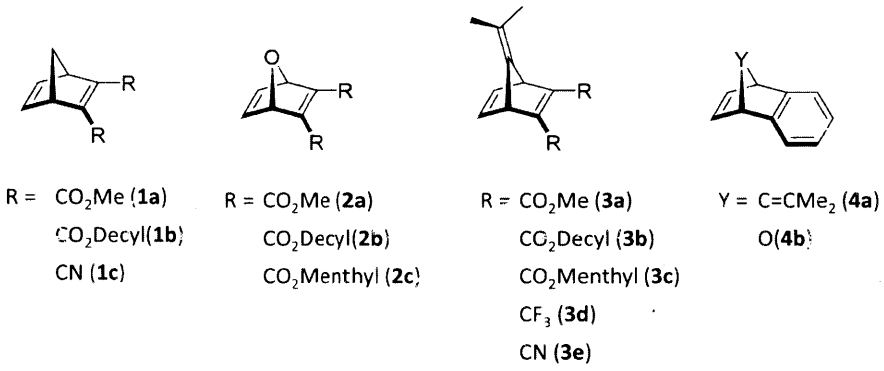

Figure 2.1. Norbornadiene monomers explored in this study.

Dicyanoacetylene (**7**) was synthesized from dimethyl acetylenedicarboxylate (**5**) according to a modified literature procedure,[44–46] as shown in Scheme 2.3. Diels–Alder adducts 2,3-dicyanonorbornadiene (**1c**) and 7-isopropylidene-2,3-dicyanonorbornadiene (**3e**) (Figure 2.1) could then be constructed with freshly cracked cyclopentadiene[47] and 6,6-dimethylfulvene,[48] respectively.

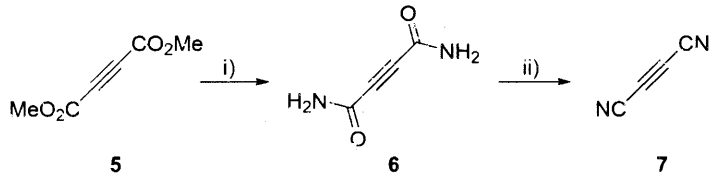

Scheme 2.3. Synthesis of dicyanoacetylene. i) NH_4OH (94% yield); ii) P_4O_{10}, sulfolane, 110°C, 2 Torr (49% yield). CAUTION: Dicyanoacetylene (**7**) is known to decompose explosively and likely releases hydrogen cyanide under ambient conditions.

We were interested in 7-oxanorbornadienes and 7-isopropylidenenorbornadienes because their polymers require only oxidation or isomerization, respectively, to attain poly(cyclopentadienylene vinylene)s. Due to the dearth of available n-type conducting

polymers and the strong electron-withdrawing properties of nitriles, we were interested in poly(2,3-dicyano-7-isopropylidenenorbornadiene) (poly(**3e**)). Initial attempts at polymerization with Grubbs' 2nd and 3rd generation catalysts, **G2** and **G3**, respectively, at 0°, 22°C, and 45°C in dichloromethane were unsuccessful. A number of other ruthenium-, molybdenum-, and tungsten-based catalysts were attempted (Table 2.1); however these polymerizations were all unsuccessful. 2,3-Dicyanonorbornadiene (**1c**) also failed to polymerize in the presence of catalysts **G2** or **G3**, suggesting that the nitriles may poison the catalyst; however, stoichiometric addition of monomer **3e** and catalyst **G2** displayed no changes in the chemical shifts in the ^{1}H NMR spectra, suggesting that the possible first insertion product or poisoning of the catalyst had not occurred. Furthermore, addition of norbornene resulted in the formation of polynorbornene homopolymer, dismissing the poisoning of the catalyst. Control experiments with 2,3-dicarbomethoxynorbornadiene (**1a**) and 2,3-dicarbomethoxy-7-isopropylidenenorbornadiene (**3a**) suggest that the isopropylidene may also be culpable for the lack of reactivity of monomer **3e**. Norbornadiene **1a** is polymerized by all ruthenium, molybdenum, and tungsten catalysts shown in Figure 2.2, but the isopropylidene-containing monomer **3a** is not polymerized by catalysts **G2** or **G3**. Furthermore, Schrock and coworkers demonstrated as early as 1990 that monomer **3a** cannot be polymerized by first generation catalyst **C1a**, even at temperatures of 45–55 °C. Only the monoinsertion product could be observed and even isolated.[49]

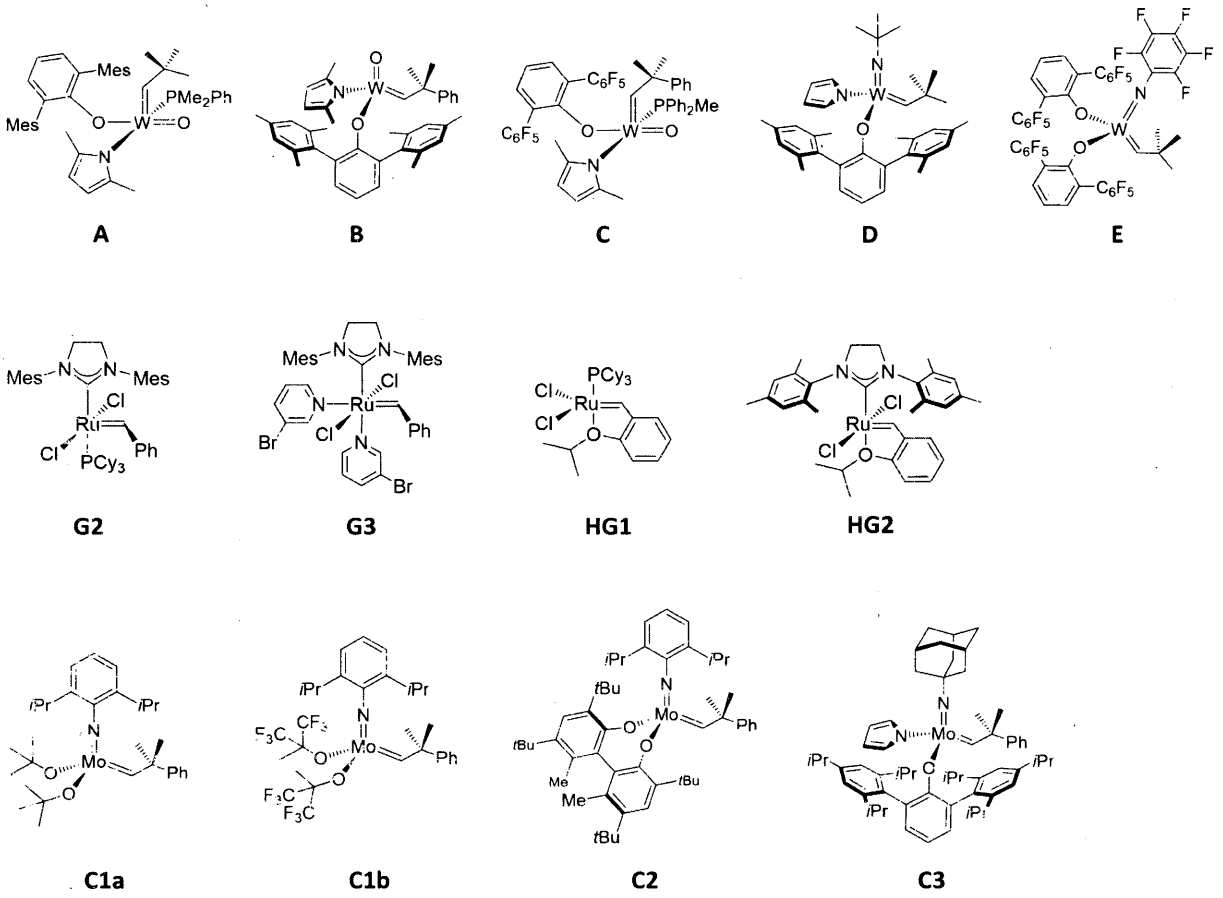

Figure 2.2. Catalysts employed in this study.

Ultimately, in collaboration with the Schrock lab, we determined that tungsten oxo catalysts **A**–**C** polymerized **3a** and **3e** quantitatively. Encouragingly, monomer **3a** is not only quantitatively polymerized, but catalysts **A**–**C** polymerize it in a highly stereoregular fashion. With these results, we sought to explore the scope of these catalysts in the stereoregular -- or even stereoirregular for previously unreactive monomers — polymerization of norbornadiene-based monomers.

2.2.2 Stereoregular Polymerization of Norbornadienes

Schrock and coworkers have recently demonstrated that molybdenum[50–53] catalysts based on monoaryloxide pyrrolide (MAP) polymerize 2,3-dicarbomethoxynorbornadiene (**1a**)

to give *cis*, *syndiotactic* poly(**1a**). The high degree of stereoregularity is attributed to the stereogenic metal control of the resulting polymer's structure. The high steric demands of the catalyst force each monomer to approach one side of the alkylidene bond and then the other with inversion of the configuration at the metal. Tungsten oxo MAP complexes have more recently been demonstrated to promote *Z*-selective metathesis reactions[54–56] and to polymerize monomer **1a** to furnish highly *cis*, *syndiotactic* poly(**1a**), particularly in the presence of $B(C_6F_5)_3$.[57] Tris(pentafluorophenyl)borane greatly accelerates the rate of polymerization as a result of its reversible binding to the oxo ligand, consequently enhancing the electrophilicity of the metal. We now demonstrate that these tungsten oxo alkylidene MAP complexes can polymerize norbornadienes that are more demanding than monomer **1a**, including norbornadienes that have not been reported, or if they have, did not undergo polymerization in a stereoregular fashion.

Tungsten oxo catalyst **A** readily polymerizes monomer **3a** to give *cis*, highly tactic poly(**3a**) quantitatively. In the ATR FT–IR spectrum, the relatively intense absorption band near 980 cm^{-1} that is characteristic of *trans* double bonds is absent; therefore, the poly(**3a**) formed with catalyst **A** contains *cis* vinylene linkages. The stereoregularity is further confirmed in the ^1H NMR spectrum, which exhibits sharp olefinic (δ 5.23) and methine (δ 4.63) proton resonances. The simple and sharp ^1H and ^{13}C resonances in the NMR spectra are consistent with poly(**3a**) possessing a single tacticity. Polymerization of monomer **3a** with catalyst **B** resulted in a polymer with identical ^1H and ^{13}C NMR spectra as the polymer formed with catalyst **A**. This finding is unsurprising, as catalyst **A** is known to lose the relatively labile phosphine to give catalyst **B**, resulting in a propagating four-coordinate, 14-electron species.[57]

Although we are able to assign the *cis* stereochemistry to the vinylene linkages, it is necessary to synthesize an analogous monomer possessing chiral groups in order to prove the tacticity of the stereoregular polymer. For this reason, we synthesized 2,3-dicarbo*menthoxy*-7-isopropylidenenorbornadiene (**3c**) from dimenthyl acetylene diester **9**, as shown in Scheme 2.4. The tacticity of the resulting poly(**3c**) can be assigned if two separate olefinic proton resonances are observed in the polymer's ^{1}H NMR spectrum. For a *cis*, *isotactic* structure, the two olefinic protons should be strongly coupled with a coupling constant of $J_{HH} \approx 11$ Hz; for a *cis*, *syndiotactic* structure, the two olefinic protons should not be strongly coupled.

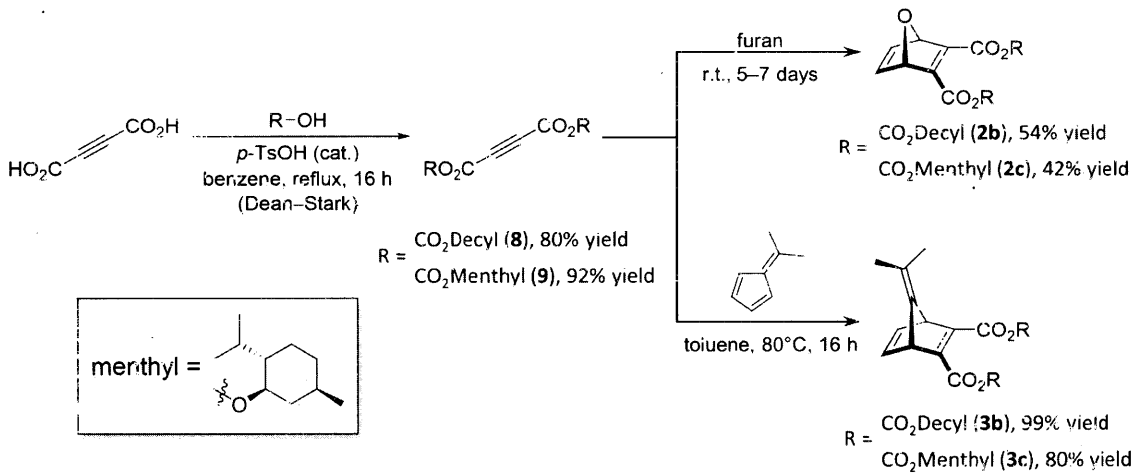

Scheme 2.4. Synthesis of 7-oxanorbornadienes **2b** and **2c** and 7-isopropylidenenorbornadienes **3b** and **3c**.

Menthyl-containing monomer **3c** possesses greater steric bulk than the methyl-containing monomer **3a**. Neither catalyst **A** nor **B** initiates the homopolymerization of monomer **3c** at room temperature; however, the polymerization is completed within three hours at 22 °C in $CDCl_3$ when tris(pentafluorophenyl)borane (1 equiv. with respect to the catalyst), is added. The resulting polymer is *cis* and highly tactic, according to the ATR–FTIR and ^{1}H and ^{13}C NMR spectra. The ^{1}H NMR spectrum contains overlapping resonances in the

olefinic region for the two OCH protons, two methine protons, and two olefinic protons. The olefinic protons are separated from each other and appear to have a pseudo triplet structure. This suggests that H_a and H_b (see Figure 2.3) are strongly coupled, which can be confirmed by strong cross peaks in $^1H/^1H$ COSY NMR spectroscopy. This strong coupling indicates that the structure of poly(**3c**) is *cis*, *isotactic* rather than the *cis*, *syndiotactic* structure expected on the basis of the MAP catalysts to yield *cis*, *syndiotactic* polymers. The sharp acceleration of the polymerization upon binding of $B(C_6F_5)_3$ can be ascribed to the resulting increase in the electrophilicity of the tungsten.

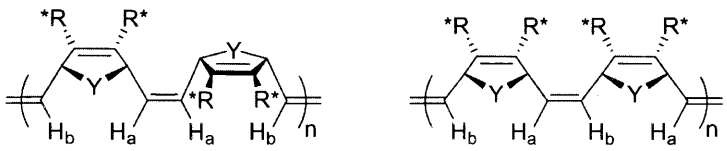

Figure 2.3. Olefinic protons H_a and H_b in *cis*, *syndiotactic* and *cis*, *isotactic* polymers where R* = CO_2Menth and Y = O (poly(**2c**)) or Y = C=CMe_2 (poly(**3c**)).

It is also important to determine if the presence of the $B(C_6F_5)_3$ affects the polymer structure in addition to the rate of polymerization. For this reason, we prepared poly(**3c**) in the absence of $B(C_6F_5)_3$. Fortunately, monomer **3c** can be polymerized completely by catalyst **B** at 55 °C in 16 hours, and the ^1H NMR spectrum is identical to the spectrum observed for poly(**3c**) prepared in the presence of $B(C_6F_5)_3$. Therefore, the presence of $B(C_6F_5)_3$ does not alter the structure of the resulting polymer.

In addition to the ester-containing monomers **3a–3c,** we were interested in exploring other strong electron-withdrawing groups, particularly trifluoromethyl and cyano groups. For

this reason, we synthesized 2,3-bis(trifluoromethyl)-7-isopropylidenenorbornadiene (**3d**) according to literature procedure.[48] The corresponding polymer, poly(**3d**), was previously synthesized by Feast and Millichamp using the classical "black box" catalyst $MoCl_5/SnMe_4$, although the degree of *cis* selectivity and tacticity was not discussed.[58] Monomer **3d** was polymerized by catalyst **A** in 16 hours at room temperature to yield a polymer whose ^1H NMR spectrum in the olefinic and methine region was unexpectedly complex. The same is true when catalyst **C** is employed. Investigation with ATR–FTIR spectroscopy suggests that the polymer contains no *trans* vinylene linkages, so the *cis/trans* isomerism is not the cause of the relatively complex set of olefinic resonances at δ 5.4. In contrast, monomer **3d** is polymerized within three hours at room temperature with catalyst **A** in the presence of two equivalents of $B(C_6F_5)_3$ (with respect to the catalyst) to give a *cis*, highly tactic polymer whose ^1H and ^{13}C NMR spectra are simple in comparison to the polymer prepared without $B(C_6F_5)_3$. The ^1H NMR spectrum reveals sharp olefinic (δ 5.4) and methine (δ 5.4) proton resonances, suggesting a highly regular structure. We propose that the poly(**3d**) formed with **A** in the absence of $B(C_6F_5)_3$ contains isotactic (*r*) and syndiotactic (*m*) dyads, but also longer range variations in tetrads (i.e., *mrm*, *mrr/rrm*, *mmr/rmm*, and *rmr*) that introduce other olefinic and methine proton resonances. With the coordination of $B(C_6F_5)_3$ to the oxo ligand, the formation of either an *rrr* (*syndiotactic*) or an *mmm* (*isotactic*) structure is comparatively faster than the mixed tacticities.

monomer	catalyst	solvent	temp (°C)	time	result
3a	**G2** or **G3**	CH_2Cl_2	22 °C, 45 °C	2 hr	no polymerization
	C1a	toluene	45–55 °C	3 hr	only monoinsertion product observed[a]
	A	$CDCl_3$	22 °C	5 min	polymerization; *cis, syndiotactic*
	B	$CDCl_3$	22 °C	5 min	polymerization; 68% *cis, syndiotactic*
	C	$CDCl_3$	22 °C	5 min	polymerization; ~10% *trans*
3b	**G2** or **G3**	CH_2Cl_2	22 °C, 45 °C	2 hr	no polymerization
	A	$CDCl_3$	22 °C	3 hr	polymerization; *cis, tactic*
3c	**A** or **B**	$CDCl_3$	22 °C	3 hr	no polymerization
	B	$CDCl_3$	55 °C	16 hr	polymerization; *cis, tactic*
	B, $B(C_6F_5)_3$	$CDCl_3$	22 °C	3 hr	polymerization; *cis, tactic*
3d	$MoCl_5$, $SnMe_4$	C_6H_5Cl	70 °C	30 min	polymerization; no stereoregularity[b]
	G2 or **G3**	CH_2Cl_2	22 °C, 45 °C	2 hr	no polymerization
	A	$CDCl_3$	22 °C	16 hr	polymerization; no stereoregularity
	A	$CDCl_3$	45 °C	1 hr	polymerization; no stereoregularity
	A, $B(C_6F_5)_3$	$CDCl_3$	22 °C	3 hr	polymerization; *cis, tactic*
	C	$CDCl_3$	22 °C	16 hr	polymerization; no stereoregularity
	C, $B(C_6F_5)_3$	$CDCl_3$	2 2°C	3 hr	polymerization; no stereoregularity
	D	$CDCl_3$	45 °C	48 hr	no polymerization
3e	**G2** or **G3**	CH_2Cl_2	22 °C, 45 °C	2 hr	no polymerization
	HG1 or **HG2**	CH_2Cl_2	22 °C, 45 °C	2 hr	no polymerization
	A	$CDCl_3$	22 °C	16 hr	polymerization; no stereoregularity
	A	$CDCl_3$	45 °C	1 hr	polymerization; no stereoregularity
	A, $B(C_6F_5)_3$	$CDCl_3$	22 °C	3 hr	polymerization; no stereoregularity
	E	$CDCl_3$	80 °C	12 hr	complete initiation; no polymerization
	C1a or **C1b**	toluene	22 °C	12 hr	no polymerization
	C2	toluene	22 °C	12 hr	no polymerization
	C3	toluene	22 °C	12 hr	no polymerization
4a	**G2** or **G3**	CH_2Cl_2	22 °C	5 min	polymerization; no stereoregularity
	A, **B**, or **C**	$CDCl_3$	22 °C	5 min	polymerization; *cis, tactic*
	C1a or **C1b**	toluene	22 °C	48 hr	polymerization; ~80% *trans*[c]
	D	$CDCl_3$	22 °C	3 days	no polymerization

Table 2.1. Polymerization attempts with 7-isopropylidenenorbornadienes **3a–e**, **4a**. a) reference 49. b) reference 58. c) reference 37.

Bis(nitrile)-containing poly(**3e**) was formed within 16 hours at 22 °C or within 1 hour at 45 °C to give a relatively insoluble polymer whose ^{1}H NMR spectrum in the olefinic region was similar to poly (**3d**) prepared without $B(C_6F_5)_3$. As a result of the absence of an IR absorption at 980 cm^{-1}, we propose that poly(**3e**) also has *cis* vinylene linkages with little to no tacticity. In contrast to monomer **3d**, the polymerization of monomer **3e** did not yield stereoregular polymer when $B(C_6F_5)_3$ was added. Acceleration of the stereoregular pathway is likely subdued by the exclusive binding of the tris(pentafluorophenyl)borane by the cyano groups, rather than the tungsten oxo group. Although no stereospecific polymers were able to be obtained, it is worth emphasizing that monomer **3d** was unable to be polymerized by many other molybdenum-, tungsten-, and ruthenium-based catalysts initially attempted.

In addition to 7-isopropylidenenorbornadienes, we wanted to explore the scope for the stereospecific ROMP of norbornadienes. We chose to investigate 7-oxanorbornadiene monomers 2,3-dicarbomethoxy-7-oxanorbornadiene (**2a**), 2,3-dicarbodecyloxy-7-oxanorbornadiene (**2b**), and 2,3-dicarbomenthoxy-7-oxanorbornadiene (**2c**), as shown in Figure 2.1. Monomer **2a** has been polymerized previously using **C1a** as the initiator to give poly(**2a**) that possesses *cis* and *trans* vinylene linkages[59] and can be polymerized by catalyst **A** in $CDCl_3$ within 5 minutes at 22 °C. The resulting poly(**2a**) is insoluble in common organic solvents at room temperature; however, the ^{1}H and ^{13}C NMR spectra could be acquired in CD_2Cl_4 at 80 °C. To overcome this lack of solubility, we synthesized monomer **2b**, which is substituted with solubilizing decyl groups, as shown in Scheme 2.4. Monomer **2b** is polymerized within five minutes with catalyst **A** in $CDCl_3$ at room temperature. As with poly(**2a**), poly(**2b**) contains *cis* vinylene linkages as shown by ATR–FTIR spectroscopy, and the ^{1}H and ^{13}C NMR spectra indicate that it is also highly tactic.

To identify the tacticity of the poly(7-oxanorbornadienes), we synthesized the menthyl-containing derivative **2c** in an analogous fashion to the determination of tacticity in the 7-isopropylidenenorbornadiene-derived polymers, as shown in Scheme 2.4. Monomer **2c** was polymerized within 10 minutes at room temperature in $CDCl_3$ to yield a white polymer with high solubility in chlorinated solvents. ATR–FTIR spectroscopy confirmed that this polymer contains all *cis*-vinylene linkages. Proton and ^{13}C NMR spectroscopy revealed two methine resonances at δ 5.85 and two vinyl resonances at δ 5.50, identified by an HSQC experiment. The absence of olefinic cross-peaks between the H_a and H_b resonances (see Figure 2.3) in the gCOSY ^1H NMR spectrum of poly(**2c**) confirms that H_a and H_b are not coupled. Therefore, poly(**2c**) has a *cis*, *syndiotactic* structure.

monomer	catalyst	solvent	temp (°C)	time	result
2a	**G2**	CH_2Cl_2	22 °C	60 min	polymerization; no stereoregularity
	G3	CH_2Cl_2	22 °C	60 min	polymerization; no stereoregularity
	A	$CDCl_3$	22 °C	5 min	polymerization; *cis, syndiotactic*
	B	$CDCl_3$	22 °C	5 min	polymerization; 68% *cis, syndiotactic*
	C1a	THF-d^8	22 °C	30 min	only oligomers obtained[a]
	C1b	$CDCl_3$	22 °C	30 min	polymerization; no stereoregularity
2b	**G2**	CH_2Cl_2	22 °C, 45 °C	2 hr	no polymerization
	G3	CH_2Cl_2	22 °C, 45 °C	2 hr	no polymerization
	A	$CDCl_3$	22 °C	5 min	polymerization; *cis, syndiotactic*
2c	**A**	$CDCl_3$	22 °C	10 min	polymerization; *cis, syndiotactic*
4b	**G2**	CH_2Cl_2	22 °C	5 min	polymerization; no stereoregularity
	C1a	$CDCl_3$	22 °C	45 min	polymerization; no stereoregularity
	A	$CDCl_3$	22 °C	5 min	polymerization; *cis, tactic*
	B	$CDCl_3$	22 °C	10 min	polymerization; little stereoregularity

Table 2.2. Polymerization attempts with 7-oxanorbornadienes **2a–c**, **4b**. a) reference 49. b) reference 58. c) reference 37.

11-Isopropylidenebenzonorbornadiene (**4a**) has been previously polymerized by Stelzer and coworkers in 48 hours at room temperature with catalysts **C1a** and **C1b**,[60] although the resulting poly(**4a**) possessed approximately 80% *trans* vinylene linkages with no tacticity. In contrast, monomer **4a** can be polymerized by catalyst **A** in less than five minutes to give a highly *cis* and tactic polymer.

Similarly, 11-oxabenzonorbornadiene (**4b**) can be polymerized by catalyst **A** to yield a polymer that is insoluble in organic solvents at room temperature. It was possible to obtain both ^{1}H and ^{13}C spectra of poly(**4b**) at 120 °C in 1,1,2,2-tetrachloroethane-d_2. From the ATR–FTIR and NMR spectra, we could again confirm that the polymer was highly *cis* and tactic.

2.2.3 Expansion of Scope for Tungsten Oxo-based Catalysts

With these results, we sought to further expand the scope of tungsten oxo-based catalysts for the polymerization of norbornadienes that cannot be polymerized by traditional ROMP catalysts. We designed isopropylidene norbornadiene **12** to exploit the strong electron-withdrawing effect of the dicyanopyrazine moiety. Monomer **12** was synthesized in four steps from 6,6-dimethylfulvene, as shown in Scheme 2.5. Briefly, Diels–Alder reaction of vinylene carbonate with 6,6-dimethylfulvene and subsequent decarbonylation with potassium hydroxide yielded diol **10**. A double Swern oxidation furnished α-diketone **11**, which could be condensed with diaminomaleonitrile to afford dicyanopyrazine **12**. Attempts to polymerize diketone **11** and dicyanopyrazine **12** with **G2**, **G3**, **HG1**, and **HG2** were unsuccessful; however, 20 equivalents of compound **12** could be polymerized with catalyst **A** to give poly(**12**). The limited solubility of poly(**12**) prevented successful characterization and post-polymerization manipulation.

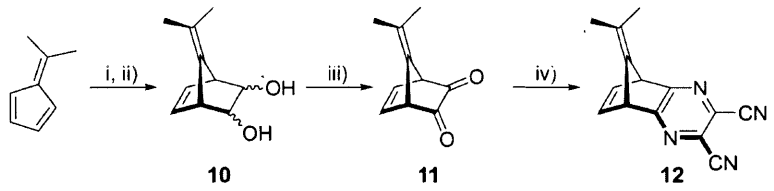

10 11 12

Scheme 2.5. Synthesis of monomers **11** and **12**: i) vinylene carbonate, toluene, 180 °C, 3 days (58% yield); ii) 6M KOH (85% yield); iii) DMSO, $(CF_3CO)_2O$, CH_2Cl_2, −78 °C, 3 h; Et_3N, r.t., 12 h (90% yield); iv) diaminomaleonitrile, THF, reflux, 16 h (77% yield).

Furthermore, we were interested in the synthesis of metallopolymers prepared by ROMP, which have applications as redox-active polymers in sensors, catalysis, and media storage.[61] $[(\eta^5\text{-}C_5(CH_3)_5)Ru(CH_3CN)_3]PF_6$ (**13**) is known to form $[(\eta^5\text{-}C_5(CH_3)_5)Ru(\eta^6\text{-arene})]^+$ complexes.[62,63] We synthesized Ru complex **14** from isopropylidenebenzonorbornadiene **4a** in 92 % yield, as a mixture of isomers, as shown through ^1H and ^{13}C NMR, 1D NOE experiments, ^1H gCOSY, and ESI–MS. The predominant isomer (4:1) expectedly has the isopropylidene facing away from the Cp* ligand, as confirmed with 1D NOE experiments. Attempts with ruthenium-based catalysts **G2** and **G3** were unsuccessful; however, monomer **14** was polymerized with catalyst **A** in CD_2Cl_2 at 45 °C in a sealed vial in 6 hours to yield a tan, insoluble polymer.

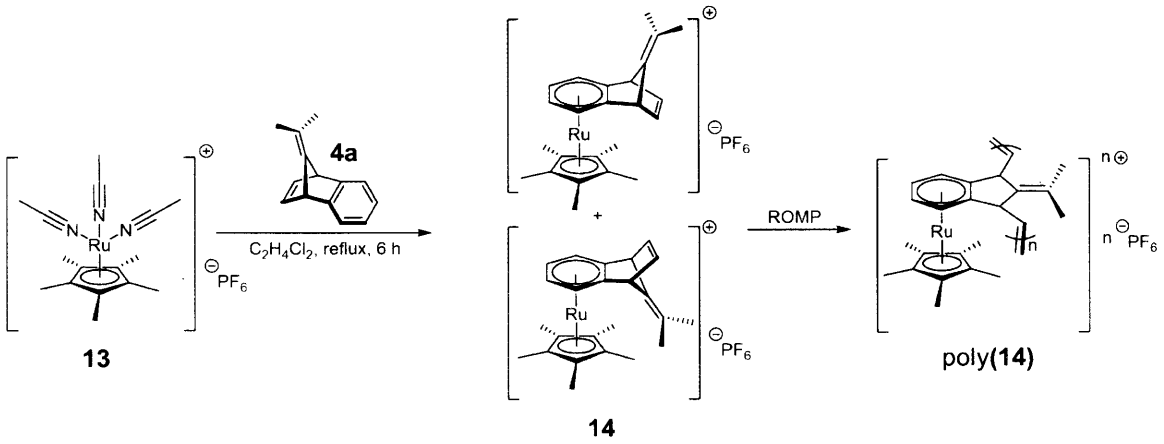

Scheme 2.6. Synthesis and polymerization of Ru complex **14** by catalyst **A** (Figure 2.2).

2.2.4 Post-Polymerization Conversion to Conjugated Polymers

We first sought the post-polymerization modification of poly(**2**) to yield poly(furanylene vinylene)s. In order to test oxidative conditions from the dihydrofuran to the furan unit, we synthesized model compound **15** by the photochemical reaction of *trans*-stilbene oxide and dimethyl acetylene dicarboxylate using naphthalene-1,4-dicarbonitrile as a photosensitizer, according to literature procedure.[64] A mixture of separable *cis* and *trans* isomers were obtained in 31% and 52% yield, respectively. Upon treatment with one equivalent of 2,3-dichloro-5,6-dicyano-1,4-benzoquinone (DDQ), oxidation of dihydrofuran **15** to furan **16** proceeded in quantitative conversion with the *trans* isomers but in only 27% conversion in the case of the *cis* isomer. Increases in temperature up to 60 °C did not result in a significantly increased yield; however, treatment with three equivalents of DDQ afforded the furan **16** quantitatively, as measured by NMR spectroscopy.

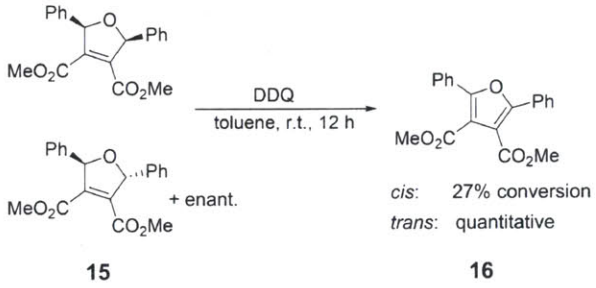

Scheme 2.7. Oxidation of test monomer with DDQ.

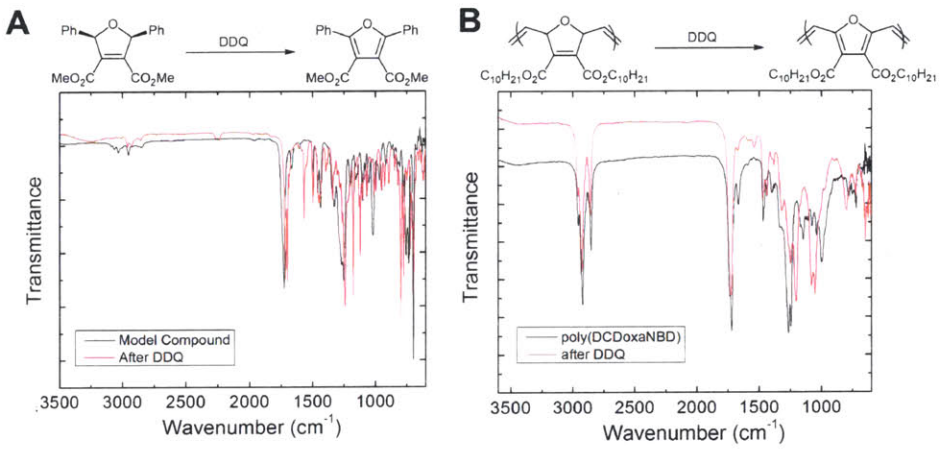

Figure 2.4. ATR–FTIR spectra of a) model compound before and after treatment with 3 equiv. DDQ and b) poly(**2b**) before and after treatment with 3 equiv. DDQ.

As a result of the insolubility the methyl ester-containing poly(**2a**), we synthesized the decyl ester-containing poly(**2b**) to enable characterization by techniques that demand solubility. Initial characterization by attenuated total reflectance – Fourier transform infrared spectroscopy (ATR–FTIR) reflected similar spectral signatures as the model compound, specifically in the C=O stretching bands, as indicated in gray in Figure 2.4. NMR spectroscopy reveals significant broadening of the esteric α- and β-methylene proton resonances, as shown in Figure 2.5a. As a result of the loss of tacticity in the precursor polymers, the vinylic proton resonances of the product were significantly broadened and shifted downfield to δ 6.5.

Although ATR–FTIR and NMR spectra were consistent with the poly(furanylene vinylene) product, UV–Vis spectroscopy revealed that only oligomeric regions of the dihydrofuran backbone were oxidized to the furan (Figure 2.5b). Further analysis by matrix-assisted laser desorption ionization time of flight (MALDI–TOF) spectrometry was unsuccessful as a result of the difficulty in ionization for the relatively nonpolar polymer. Further attempts with more equivalents, higher reaction temperatures, and other oxidizing agents (e.g., *o*- and *p*-chloranil) also failed to furnish a more fully conjugated polymer.

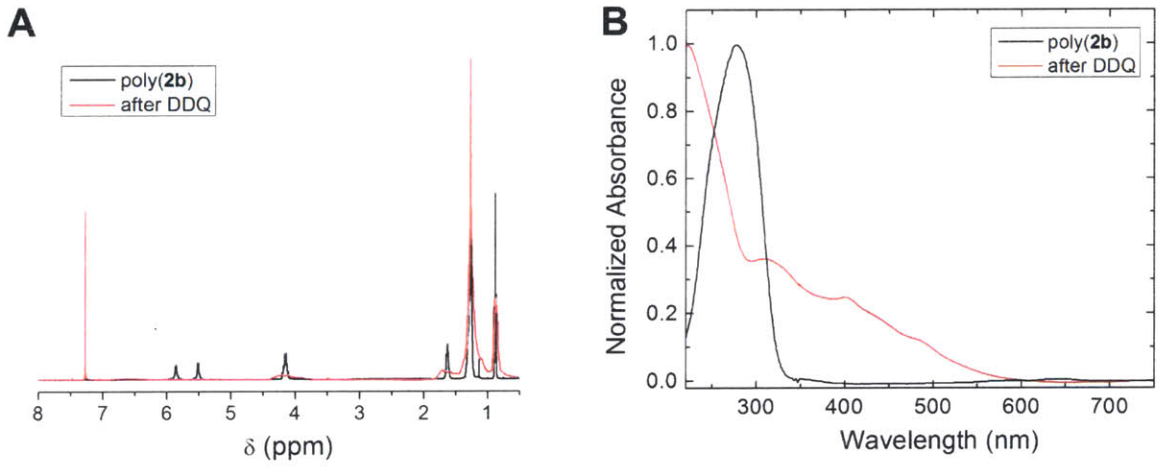

Figure 2.5. a) NMR spectra of poly(**2b**) before and after treatment with 3 equiv. DDQ. b) UV–Vis spectra of poly(**2b**) before and after treatment with DDQ.

In the case of poly(7-isopropylidenenorbornadiene)s poly(**3b**,**d**,**e**) and poly (**12**), we hypothesized that treatment with base and subsequent neutralization could result in isomerization to the fully conjugated poly(isopropylcyclopentadienylene vinylene), facilitated by the increased acidity of the triply allylic methine protons. Upon exposure to increasing equivalents of potassium *tert*-butoxide, a bathochromic shift is observed in the UV–Vis absorption spectrum, consistent with formation of the resulting anion; however, dropwise neutralization with acetic acid did not indicate the formation of a fully conjugated polymer.

Alternatively, post-deposition treatment of a soluble precursor thin film with different oxidizing agent could serve as a better device fabrication method than handling the semiconducting polymers in solution. An ideal agent for the post-polymerization modification of poly(norbornadienes) to yield conjugated polymers is atmospheric oxygen, as previously reported with poly(**4a**).[37] Stepwise heating of poly(oxanorbornadiene) poly(**2b**) and poly(isopropylidenenorbornadiene) poly(**3b**) under ambient conditions were monitored by UV–Vis spectroscopy. Oxidation resulted in a bathochromic shift, but there was no indication of a fully conjugated polymer. We screened poly(oxanorbornadiene) poly(**2b**), poly(isopropylidenenorbornadiene)s poly(**3b**) and poly(**3d**), and poly(benzonorbornadiene)s poly(**4a**) and poly(**4b**) by exposing them to harsher oxidizing agents Br_2 and I_2 vapors. Interestingly, only derivatives of benzoxanorbornadiene-containing poly(**4b**) were converted to higher conjugation lengths upon exposure to bromine and iodine vapors.

We synthesized poly(benzoxanorbornadiene)s by reacting furan with benzynes formed from the lithium–halogen exchange of *o*-aryldibromides, as shown in Figure 2.6. Monomers **17** and **18** could be polymerized with **G2** in CH_2Cl_2 at room temperature; however, treatment of dialkoxyepoxynaphthalene **19** with **G2** resulted in in the quantitative conversion to dialkoxynaphthol **20** at room temperature. Cooling to −50 °C and allowing the polymerization to proceed with slow warming resulted in quantitative polymerization.

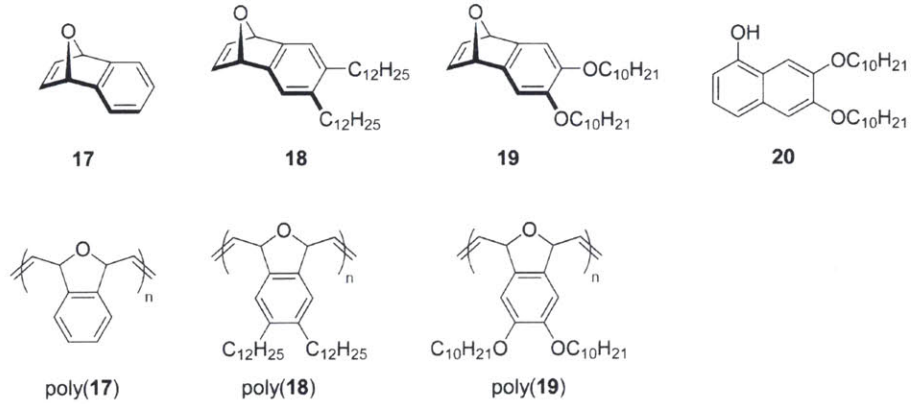

Figure 2.6. Benzoxanorbornadiene-based monomers **17**–**19** and resulting polymers poly(**17**)–poly(**19**). Naphthol **20** results from the ring-opening of **19** rather than polymerization at room temperature.

We exposed spincasted thin films of these polymers to saturated vapors of bromine and iodine and monitored their absorbance by UV–Vis spectroscopy. Polymers poly(**17**) and poly(**18**) turned a pale green upon exposure to bromine and iodine vapors, but poly(**19**) turned bright emerald green and developed a broad peak at 650 nm in the absorption spectrum, as shown in Figure 2.7. Crude conductance measurements with a multimeter did not indicate the formation of doped, conductive polymers, likely a result of incomplete conversion.

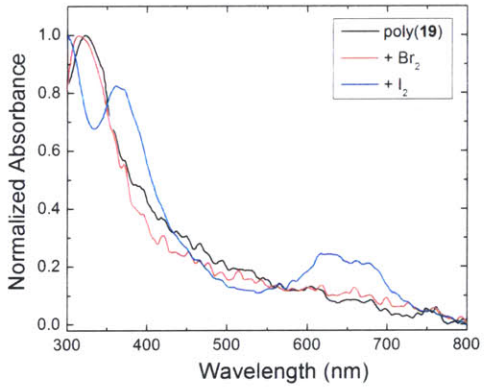

Figure 2.7. UV–Vis absorption spectra for dialkoxy-substituted poly(**19**) and after treatment with Br_2 and I_2.

2.3 Conclusions

We report the first polymerization of a number of monomers demonstrated to be incompatible with polymerization by traditional molybdenum-, tungsten-, and ruthenium-based ROMP catalysts. Many of the monomers were proven to exhibit high stereoregularity. With monomers containing nitrile groups, the monomers are readily polymerized by tungsten oxo complexes **A**–**C**, but the resulting polymers are not stereoregular. Although initial investigations with ATR–FTIR and NMR spectroscopy were promising, attempts at the post-polymerization oxidation or isomerization to the fully conjugated poly(cyclopentadienylene vinylene) derivatives were unsuccessful as a result of only partial oxidation and the difficulty of characterization, caused by decreased solubility upon oxidation.

Further optimization of oxidative conditions may generate fully conjugated polymers with many promising applications. The incorporation of fully fluorous side chains into norbornadienes can introduce strong electron-withdrawing character to the resulting polymers and impart the polymers with fluorous solubility for orthogonal solution processing that is critical in the fabrication of organic electronic devices.[65] The formation of block copolymers with significantly different side chains and electronic properties can lead to the formation of a precisely defined size and microstructure in bulk heterojunctions. Finally, the development of catalysts for alternating copolymers by ring-opening metathesis polymerization[66–73] opens possibilities in low band gap donor–acceptor polymers from alternating polymer precursors.

2.4 Experimental Details

2.4.1 General

Dimethyl bicyclo[2.2.1]hepta-2,5-diene-2,3-dicarboxylate (**1a**),[74] bicyclo[2.2.1]hepta-2,5-diene-2,3-dicarbonitrile (**1c**),[47] dimethyl 7-oxabicyclo[2.2.1]hepta-2,5-diene-2,3-

dicarboxylate (**2a**),[75] dimethyl 7-(propan-2-ylidene)bicyclo[2.2.1]hepta-2,5-diene-2,3-dicarboxylate (**3a**),[76] 7-(propan-2-ylidene)-2,3-bis(trifluoromethyl)bicyclo[2.2.1]hepta-2,5-diene (**3d**),[48] 11-isopropylidenebenzonorbornadiene (**4a**), 1,4-dihydro-1,4-epoxynaphthalene (**4b**),[77] and 6,6-dimethylfulvene[78] were synthesized according to published literature procedures. Diol **10** was synthesized according to literature procedure.[79] Catalysts **G3**,[80] **A**, **B**, and **C**[57] were prepared according to literature procedure. All other reagents were used as received unless noted otherwise.

All polymerizations with molybdenum- or tungsten-based catalysts were performed in a glove box with nitrogen atmosphere. Polymerizations with ruthenium-based catalysts were carried out using standard Schlenk air-free techniques. All solvents were stored over 3Å molecular sieves and sparged with argon. High-temperature NMR spectra were recorded using a Bruker Avance III spectrometer at 400 (^{1}H) and 100.6 (^{13}C) MHz and were referenced to the residual ^{1}H ($CDCl_3$: δ 7.26, CD_2Cl_2: δ 5.32) and ^{13}C ($CDCl_3$: 77.16, CD_2Cl_2: 53.84) solvent signals: $CDCl_3$: (ATR–FTIR spectra were acquired using a Thermo Scientific Nicolet 6700 FT–IR with a Ge crystal for ATR. High-resolution mass spectra (HRMS) were determined with a Bruker Daltonics APEXIV 4.7 Tesla FT–ICR–MS using ESI or DART ionization.

2.4.2 Synthesis of Monomers

2b. Didecyl 7-oxabicyclo[2.2.1]hepta-2,5-diene-2,3-dicarboxylate. Didecyl but-2-ynedioate (1.00 g, 2.5 mmol) was dissolved in 5 mL furan and allowed to stir at room temperature under nitrogen for seven days. The solvent was removed under reduced pressure, and the product was purified by column chromatography (SiO_2, 2% Et_3N and 0→5% EtOAc in hexanes) to afford a colorless oil (0.66 g, 54 % yield). ^{1}H NMR ($CDCl_3$) δ 7.23 (dd, 2H), 5.68 (dd, 2H), 4.21 (td, 4H), 1.69 (p, 4H), 1.45–1.24 (28H), 0.90 (6H). ^{13}C NMR ($CDCl_3$, 100

MHz) δ 163.1, 152.6, 143.2, 85.1, 65.6, 31.9, 29.6, 29.5, 29.3, 29.2, 28.6, 25.8, 22.7, 14.1. HRMS (DART) calc for $C_{28}H_{46}O_5$ $[M+H]^+$ 463.3418, found 463.3417. FT–IR (ATR, ν/cm^{-1}): 2955 (w), 2925 (s), 2855 (m), 1734 (m), 1707 (s), 1640 (m), 1467 (m), 1391 (w), 1317 (m), 1295 (m), 1269 (s), 1204 (s), 1178 (m), 1111 (s), 1042 (m), 982 (w), 881 (s), 853 (w), 788 (w), 756 (w), 701 (s).

2c. Bis((1*R*,2*S*,5*R*)-2-isopropyl-5-methylcyclohexyl)-7-oxabicyclo[2.2.1]hepta-2,5-diene-2,3-dicarboxylate. Bis((1*R*,2*S*,5*R*)-2-isopropyl-5-methylcyclohexyl) but-2-ynedioate (1.00 g, 2.6 mmol) was dissolved in 10 mL furan, and the solution was allowed to stir at room temperature for six days. The solvent was removed under reduced pressure, and the product was purified by column chromatography (neutralized SiO_2, 0⟶10% $CHCl_3$ in hexanes) to afford a colorless oil (500 mg, 42% yield). ^{1}H NMR ($CDCl_3$) δ 7.21 (m, 2H), 5.65 (m, 2H), 4.81 (m, 2H), 2.04 (m, 2H), 1.86 (m, 2H), 1.69 (m, 4H), 1.57–1.40 (4H), 1.10–0.99 (4H), 0.94–0.82 (14H), 0.75 (d, 6H). ^{13}C NMR ($CDCl_3$) δ 163.5, 163.1, 153.2, 153.1, 144.1, 143.9, 86.0, 85.9, 76.4, 76.2, 47.6, 47.5, 41.5, 41.4, 34.9, 32.1, 26.9, 26.8, 24.1, 24.0, 22.7, 21.6, 21.5, 17.0, 16.9. HRMS (DART) calc for $C_{28}H_{42}O_5$ $[M+H]^+$ 459.3105, found 459.3128. FT–IR (ATR, ν/cm^{-1}): 2955 (s), 2927 (m), 2870 (m), 1733 (s), 1699 (s), 1640 (m), 1572 (m), 1456 (m), 1369 (w), 1314 (m), 1294 (m), 1268 (s), 1253 (s), 1206 (s), 1178 (m), 1110 (s), 1039 (m), 1008 (w), 981 (m), 960 (w), 912 (m), 881 (s), 852 (m), 792 (w), 734 (w), 702 (m).

3b. Didecyl 7-(propan-2-ylidene)bicyclo[2.2.1]hepta-2,5-diene-2,3-dicarboxylate. 6,6-dimethylfulvene (700 mg, 795 μL, 6.6 mmol) and didecyl but-2-ynedioate (3.12 g, 7.9 mmol, 1.2 equiv.) were dissolved in toluene (15 mL), and the reaction mixture was heated to 80°C for two days. The solvent was then removed under reduced pressure, and the product was purified by column chromatography (SiO_2, 0⟶75% CH_2Cl_2 in hexanes) to afford a

colorless oil (3.29 g, 99% yield). ^{1}H NMR ($CDCl_3$) δ 7.00 (m, 2H), 4.40 (m, 2H), 4.17 (t, 4H), 1.67 (p, 4H), 1.49 (t, 6H), 1.40–1.25 (m, 28H), 0.88 (t, 6H). ^{13}C NMR ($CDCl_3$) δ 164.8, 161.8, 151.3, 142.2, 99.9, 65.2, 53.3, 31.9, 29.5, 29.3, 29.2, 28.5, 25.9, 22.6, 18.5, 14.1. HRMS (ESI) calc for $C_{32}H_{52}O_4$ $[M+Na]^+$ 523.3758, found 523.3743. FT–IR (ATR, ν/cm^{-1}): 2955 (m), 2924 (s), 2855 (m), 1709 (s), 1625 (m), 1556 (w), 1467 (m), 1372 (w), 1314 (m), 1250 (s), 1213 (m), 1170 (s), 1101 (s), 1041 (m), 760 (m), 736 (m).

3c. Bis((1*R*,2*S*,5*R*)-2-isopropyl-5-methylcyclohexyl)-7-(propan-2-ylidene) bicyclo[2.2.1]hepta-2,5-diene-2,3-dicarboxylate. 6,6-dimethylfulvene (250 mg, 285 μL, 2.4 mmol) and bis((1*R*,2*S*,5*R*)-2-isopropyl-5-methylcyclohexyl) but-2-ynedioate (1.10 g, 2.83 mmol, 1.2 equiv.) were dissolved in toluene (15 mL), and the reaction mixture was heated to 80°C for 12 hours. The solvent was then removed under reduced pressure, and the product was purified by column chromatography (SiO_2, 20→80% CH_2Cl_2 in hexanes) to afford a colorless oil (0.94 g, 80% yield). ^{1}H NMR ($CDCl_3$) δ 6.96 (m, 2H), 4.75 (m, 2H), 4.32 (m, 2H), 2.07 (m, 2H), 1.86 (m, 2H), 1.66 (m, 4H), 1.54–1.34 (10H), 1.12–0.97 (4H), 0.93–0.80 (14H), 0.77 (d, 3H), 0.74 (d, 3H). ^{13}C NMR ($CDCl_3$) δ 165.2, 164.9, 162.4, 152.1, 151.2, 143.0, 100.3, 75.8, 75.7, 54.2, 53.8, 47.6, 47.5, 41.6, 41.5, 35.0, 32.1, 27.0, 26.9, 24.3, 24.2, 22.8, 21.5, 21.4, 19.2, 19.1, 17.2, 17.1. HRMS (DART) calc for $C_{32}H_{48}O_4$ $[M+H]^+$ 497.3625, found 497.3650. FT–IR (ATR, ν/cm^{-1}): 2954 (m), 2928 (m), 2870 (w), 1730 (m), 1703 (s), 1627 (m), 1556 (w), 1456 (m), 1370 (w), 1310 (w), 1281 (m), 1251 (s), 1212 (m), 1172 (s), 1098 (m), 1034 (m), 982 (w), 957 (w), 914 (w), 735 (s).

3e. 7-(Propan-2-ylidene)bicyclo[2.2.1]hepta-2,5-diene-2,3-dicarbonitrile was prepared according to a modified literature procedure.[48] To a solution of dicyanoacetylene (463 mg, 6.09 mmol) in 6 mL dry toluene at 0°C was added dropwise 6,6-dimethylfulvene

(770 μL, 670 mg, 6.1 mmol, 1.0 equiv.). The reaction mixture was allowed to warm to room temperature over three hours. The solvent was removed under reduced pressure, and the product was purified by column chromatography (SiO_2, 30% CH_2Cl_2 in hexanes) to yield a white solid (705 mg, 64% yield). dec. pt. 123–125 °C. ^{1}H NMR (500 MHz, $CDCl_3$) δ 6.99 (m, 2H), 4.48 (m, 2H), 1.51 (s, 6H). ^{13}C NMR (125 MHz, $CDCl_3$) δ 161.7, 142.2, 141.3, 113.9, 104.5, 55.9, 19.3. HRMS (ESI) calc for $C_{12}H_{10}N_2$ $[M+H]^+$ 183.0917, found 183.0912. FT–IR (ATR, ν/cm^{-1}): 2994 (w), 2924 (m), 2854 (w), 2219 (m), 1722 (w), 1585 (w), 1559 (w), 1444 (m), 1378 (m), 1290 (m), 1271 (w), 1220 (m), 1190 (m), 1141 (w), 1089 (w), 1057 (w), 848 (m), 778 (s), 701 (m).

7. Dicyanoacetylene was prepared according to a modified literature procedure.[44] Briefly, to a vigorously stirring solution of phosphorus pentoxide (13.3 g, 93.7 mmol, 3.5 equiv.) in freshly distilled sulfolane (35 mL) at 110 °C was added dropwise a suspension of acetylene dicarboxamide (**6**) (3.00 g, 26.8 mmol) in sulfolane (25 mL). After the complete addition of compound **6**, the reaction was heated to 120 °C for an hour. Over the course of the reaction, the product was sublimed through a column of glass wool (to prevent collection of sulfolane) at a pressure of ~ 2 Torr and collected at in a U-tube cooled at −78 °C as sublimed white crystals (1.00 g, 49% yield). CAUTION: This compound is known to decompose explosively and likely releases HCN in ambient conditions. Consequently, the compound was stored as a toluene stock solution at −78 °C under argon.

8. Didecyl but-2-ynedioate. A suspension of acetylene dicarboxylic acid (4.00 g, 35.1 mmol), *n*-decanol (13.9 g, 16.7 mL, 87.7 mmol, 2.5 equiv.), and *p*-toluene sulfonic acid (603 mg, 3.5 mmol, 0.1 equiv.) in benzene (70 mL) was heated under reflux with a Dean-Stark apparatus overnight. After cooling to room temperature, the solution was neutralized with

sodium bicarbonate, and the solvent was removed under reduced pressure. The product was purified by column chromatography (SiO_2, 0→30% EtOAc in hexanes) to afford a colorless oil (11.1 g, 80% yield). ^{1}H NMR ($CDCl_3$, 22 °C) δ [ppm] 4.22 (t, 4H), 1.67 (p, 4H), 1.45–1.2 (28H), 0.87 (t, 6H). ^{13}C NMR ($CDCl_3$, 22 °C) δ [ppm] 152.6, 75.4, 67.8, 32.6, 30.2, 30.1, 30.0, 29.8, 29.0, 26.4, 23.3, 14.8. HRMS (DART) calc for $C_{24}H_{42}O_4$ $[M+NH_4]^+$ 412.3421, found 412.3427. FT–IR (ATR, ν/cm^{-1}): 2956 (w), 2925 (m), 2855 (m), 1724 (s), 1467 (w), 1387 (w), 1250 (s), 1034 (m), 920 (w), 748 (m), 723 (w).

9. Bis((1*R*,2*S*,5*R*)-2-isopropyl-5-methylcyclohexyl) but-2-ynedioate. A suspension of acetylene dicarboxylic acid (2.00 g, 17.5 mmol), *l*-menthol (6.85 g, 43.8 mmol, 2.5 equiv.), and *p*-toluenesulfonic acid (300 mg, 1.8 mmol, 0.1 equiv.) in benzene (50 mL) was heated under reflux with a Dean-Stark apparatus overnight. After cooling to room temperature, the solution was washed with twice with water and once with brine. The organic layer was dried over sodium sulfate, and the solvent was removed under reduced pressure. The product was purified by column chromatography (SiO_2, 30–→67% CH_2Cl_2 in hexanes) to afford a white solid (6.30 g, 92% yield). mp 134–135 °C. ^{1}H NMR ($CDCl_3$) δ 4.83 (td, 2H), 2.02 (m, 2H), 1.89 (m, 2H), 1.70 (m, 4H), 1.53–1.40 (m, 4H), 1.12–0.98 (m, 4H), 0.91 (t, 12H), 0.87 (m, 2H), 0.76 (d, 6H). ^{13}C NMR ($CDCl_3$) δ 152.3, 78.36, 75.6, 47.5, 41.1, 34.6, 32.1, 26.7, 23.9, 22.6, 21.4, 16.8. HRMS (DART) calc for $C_{24}H_{38}O_4$ $[M+NH_4]^+$ 408.3108, found 408.3098. FT–IR (ATR, ν/cm^{-1}): 2961 (m), 2923 (w), 2896 (w), 2873 (w), 1708 (s), 1454 (w), 1388 (w), 1370 (w), 1341 (w), 1254 (s), 1181 (w), 1155 (w), 1097 (w), 1080 (w), 1023 (m), 978 (w), 941 (m), 904 (m), 842 (w), 744 (m).

11. 7-(Propan-2-ylidene)bicyclo[2.2.1]hept-5-ene-2,3-dione. To a solution of dimethyl sulfoxide (DMSO, 1.84 mL, 2.03 g, 26.0 mmol, 3.15 equiv.) in 18 mL dry

dichloromethane at −78°C was added trifluoroacetic anhydride (3.30 mL, 4.93 g, 23.5 mmol, 2.85 equiv.) dropwise. A solution of diol **2** (1.37 g, 7.82 mmol) in 10 mL dry dichloromethane was then added dropwise and allowed to stir at −78°C for three hours. Triethylamine (6.10 mL, 4.42 g, 43.7 mmol, 5.3 equiv.) was then added dropwise. The reaction mixture was allowed to warm to room temperature over 12 hours before pouring into 150 mL 2M HCl and extracting with dichloromethane. The organic phase was dried over sodium sulfate, and the solvent was removed under reduced pressure. The product was purified by column chromatography (SiO_2, CH_2Cl_2) and finally recrystallized from dichloromethane and hexanes to afford an orange solid (1.14 g, 90% yield). mp 91–94 °C. ^{1}H NMR (500 MHz, $CDCl_3$) δ 6.57 (m, 2H), 3.86 (m, 2H), 1.75 (s, 6H). ^{13}C NMR (125 MHz, $CDCl_3$) δ 192.3, 138.1, 135.5, 131.2, 56.5, 21.0. HRMS (ESI) calc for $C_{10}H_{10}O_2$ $[M+H]^+$ 163.0754, found 163.0757. FT–IR (ATR, ν/cm^{-1}): 3087 (w), 3034 (w), 2920 (w), 2859 (w), 1750 (s), 1555 (w) 1447 (w), 1383 (w), 1372 (w), 1306 (w), 1248 (w), 1209 (w), 1131 (m), 1060 (w), 1003 (w), 936 (w), 904 (w), 816 (w), 759 (s), 691 (m).

12. 9-(Propan-2-ylidene)-5,8-dihydro-5,8-methanoquinoxaline-2,3-dicarbonitrile. Compound **3** (200 mg, 1.23 mmol) and diaminomaleonitrile (173 mg, 1.60 mmol, 1.3 equiv.) were dissolved in 6 mL dry tetrahydrofuran and allowed to stir at room temperature for three hours. The reaction mixture was then refluxed for two days before removing the solvent under reduced pressure. The product was purified by column chromatography (SiO_2, 50% EtOAc in hexanes) to afford a yellow solid (222 mg, 77% yield). dec pt. 145 °C. ^{1}H NMR (500 MHz, $CDCl_3$) δ 7.03 (m, 2H), 4.53 (m, 2H), 1.66 (s, 6H). ^{13}C NMR (125 MHz, $CDCl_3$) δ 170.8, 155.9, 143.0, 128.2, 117.4, 114.6, 51.9, 20.1. HRMS (ESI) calc for $C_{14}H_{10}N_4$ $[M+H]^+$ 235.0978, found 235.0973. FT–IR (ATR, ν/cm^{-1}): 3093 (w), 3048 (w), 3029 (w), 2997 (w),

2943 (w), 2918 (w), 2859 (w), 2725 (w), 2535 (w), 2239 (w), 1713 (w), 1552 (w), 1446 (m), 1370 (m), 1313 (s), 1286 (m), 1222 (m), 1188 (m), 1168 (w), 1074 (m), 939 (w), 898 (w), 848 (s), 800 (m), 723 (s), 687 (w).

14. [(η^5-$C_5(CH_3)_5$)Ru(η^6-4a)]PF_6. To a solution of monomer **4a** (50 mg, 280 μmol, 1.2 equiv.) in 10 mL dry 1,2-dichloroethane (DCE) under argon was added a solution of [(η^5-$C_5(CH_3)_5$)Ru($CH_3CN)_3$]PF_6 (116 mg, 230 μmol) in 6 mL dry DCE. The reaction mixture was stirred at 55 °C for 4 h. The product was precipitated with pentanes and collected by centrifugation as a mixture of isomers (4:1 ratio, see Scheme 2.6) in 92% yield. ^{1}H NMR (500 MHz, CD_2Cl_2) *major isomer*: δ 6.99 (dd, 2H), 6.07 (m, 2H), 5.35 (m, 2H), 4.30 (m, 2H), 1.85 (s, 15H), 1.44 (s, 6H). *minor isomer*: δ 6.90 (dd, 2H), 5.81 (m, 2H), 5.40 (m, 2H), 4.32 (m, 2H), 1.87 (s, 15H), 1.66 (s, 6H). FT–IR (ATR, ν/cm^{-1}): 3097 (w), 2983 (w), 2914 (w), 1477 (w), 1450 (w), 1419 (w), 1388 (w), 1301 (w), 1269 (w), 1226 (w), 1076 (w), 1034 (w), 876 (m), 835 (s), 794 (w), 736 (w), 713 (m). HRMS (ESI) calc for $C_{24}H_{29}Ru$ M^+ 419.1324, found 419.1318.

18. 6,7-Didodecyl-1,4-dihydro-1,4-epoxynaphthalene. 1,2-didodecyl-4,5-diiodobenzene[81] (575 mg, 0.86 mmol) was dissolved in 10 mL equivolume THF and furan at −50 °C. *n*-Butyllithium (2.35 M, 810 μL, 1.1 equiv.) was then added dropwise, and the reaction mixture was allowed to warm to room temperature over two hours before the reaction was quenched with water and the solvent removed under reduced pressure. The product was extracted in dichloromethane, washed with water, dried over sodium sulfate, and purified by column chromatography (2% Et_3N in hexanes) to yield a colorless oil (415 mg, 83% yield). ^{1}H NMR (500 MHz, $CDCl_3$) δ 7.06 (s, 2H), 7.00 (m, 2H), 5.67 (m, 2H), 2.54 (m, 4H), 1.53 (p, 4H), 1.43–1.20 (36H), 0.90 (t, 6H). ^{13}C NMR (125 MHz, $CDCl_3$) δ 146.3, 143.1, 137.0, 121.7,

82.5, 33.1, 32.2, 31.7, 30.1, 30.0, 30.0, 29.9, 29.9, 29.8, 29.6, 23.0, 14.4. HRMS (ESI) calc for $C_{34}H_{56}O$ $[M+H]^+$ 481.4404, found 481.4393. FT–IR (ATR, ν/cm^{-1}): 3013 (w), 2923 (s), 2853 (s), 1465 (m), 1378 (w), 1281 (w), 1076 (w), 1026 (w), 988 (w), 908 (m), 869 (w), 852 (s), 734 (s), 695 (m).

19. 6,7-Bis(decyloxy)-1,4-dihydro-1,4-epoxynaphthalene. 1,2-bis(decyloxy)-4,5-diiodobenzene[82] (2.51 g, 3.91 mmol) was dissolved in 15 mL of equivolume tetrahydrofuran and furan at −50°C. *n*-Butyllithium (2.50 M in hexanes, 1.72 mL, 1.1 equiv.) was then added dropwise and allowed to slowly warm to room temperature over two hours. The reaction was quenched with water, and the solvent was removed under reduced pressure. The product was extracted in dichloromethane, washed with water, and purified by column chromatography (3% Et_3N, 10→20% CH_2Cl_2 in hexanes) to yield a white solid (841 mg, 48% yield). mp 71–73 °C. ^{1}H NMR (500 MHz, $CDCl_3$) δ 7.03 (s, 2H), 6.95 (s, 2H), 5.65 (s, 2H), 3.95 (m, 4H), 1.76 (p, 4H), 1.45 (p, 4H), 1.38–1.20 (24H), 0.89 (t, 6H). ^{13}C NMR (125 MHz, $CDCl_3$) δ 146.3, 143.5, 142.1, 110.0, 82.8, 70.4, 32.1, 29.9, 29.8, 29.7, 29.7, 29.6, 26.3, 22.9, 14.4. HRMS (ESI) calc for $C_{30}H_{48}O_3$ $[M+H]^+$ 457.3676, found 457.3664. FT–IR (ATR, ν/cm^{-1}): 3088 (w), 3010 (w), 2959 (m), 2922 (s), 2852 (m), 1602 (w), 1489 (w), 1474 (s), 1426 (m), 1376 (w), 1319 (m), 1293 (s), 1209 (s), 1198 (m), 1162 (w), 1079 (s), 1062 (s), 1035 (w), 1000 (w), 979 (w), 968 (w), 936 (w), 863 (m), 852 (w), 842 (s), 830 (m), 801 (m), 745 (m), 722 (m), 702 (s).

20. 6,7-Bis(dodecyloxy)naphthalen-1-ol. Note: the ring-opening of dialkoxyepoxynaphthalenes to naphthols instead of ROMP with catalyst **G2** was observed with both decyloxy and dodecyloxy substituents. The decyloxy is reported above as a result of the successful synthesis of the polymer. The didodecyloxy naphthol is fully characterized here. white solid. mp – 89–90°C. ^{1}H NMR (500 MHz, $CDCl_3$) δ 7.48 (s, 1H), 7.28 (d, 1H), 7.16 (dd,

1H), 7.12 (s, 1H), 6.69 (dd, 1H), 5.23 (s, 1H), 4.14 (m, 4H), 1.92 (p, 4H), 1,52 (p, 4H), 1.45–1.25 (32H), 0.91 (t, 6H). ^{13}C NMR (125 MHz, $CDCl_3$) δ 150.4, 149.8, 149.0, 130.8, 123.9, 119.6, 119.1, 107.8, 107.1, 102.0, 68.9, 68.8, 31.9, 29.7, 29.5, 29.4, 29.1, 26.1, 22.7, 14.1. HRMS (DART) calc for $C_{34}H_{56}O_3$ $[M+H]^+$ 513.4302, found 513.4299. FT–IR (ATR, ν/cm^{-1}): 3431 (br, m), 2954 (m), 2921 (s), 2851 (s), 1631 (w), 1604 (w), 1590 (w), 1520 (w), 1488 (m), 1465 (m), 1406 (w), 1383 (m), 1280 (m), 1256 (s), 1195 (s), 1171 (m), 1154 (w), 1076 (w), 998 (w), 956 (w), 912 (w), 892 (w), 853 (m), 783 (m), 740 (m), 722 (w).

2.4.3 Synthesis of Polymers

*General Procedure for Polymerization with Catalysts **A**–**C** without $B(C_6F_5)_3$*: A solution of catalyst (3.4 μmol) in $CDCl_3$ (1.0 mL) was added to a vigorously stirring solution of monomer (340 μmol, 100 equiv.) in $CDCl_3$ (2 mL), and the solution was stirred until completion. The polymerization was monitored by ^1H NMR spectroscopy. Once the monomer was completely consumed, the polymerization was quenched by precipitating in stirring MeOH (40 mL). The precipitated polymer was isolated by centrifugation and dried overnight.

*General Procedure for Polymerization with Catalysts **A**–**C** with $B(C_6F_5)_3$*: A solution of catalyst (3.4 μmol) and $B(C_6F_5)_3$ (1.9 mg, 3.7 μmol, 1.1 equiv.) in $CDCl_3$ (1.0 mL) was added to a vigorously stirring solution of monomer (340 μmol, 100 equiv.) in $CDCl_3$ (2 mL), and the solution was stirred until completion. The polymerization was monitored by ^1H NMR spectroscopy. Once the monomer was completely consumed, the polymerization was quenched by precipitating in stirring MeOH (40 mL). The precipitated polymer was isolated by centrifugation and dried overnight.

Poly(2a). Catalyst **A**, 22 °C, 10 minutes. ^{1}H NMR (400 MHz, $C_2D_2Cl_4$, 130 °C): δ 5.89 (2H), 5.61 (2H), 3.81 (6H). ^{13}C NMR (100.6 MHz, $C_2D_2Cl_4$, 130 °C): δ 162.1, 138.4, 131.4, 81.7, 51.9. FT–IR (ATR, ν/cm^{-1}): 3010 (w), 2956 (w), 1724 (s), 1674 (m), 1434 (m), 1330 (m), 1270 (s), 1249 (s), 1196 (m), 1157 (m), 1113 (m), 1104 (w), 1046 (w), 1008 (s), 964 (m), 872 (w), 819 (w), 779 (s), 736 (m).

Poly(2b). Catalyst **A**, 22 °C, 5 minutes. ^{1}H NMR (500 MHz, $CDCl_3$): δ 5.86 (2H), 5.51 (2H), 4.15 (4H), 1.63 (4H), 1.25 (32H), 0.87 (6H). ^{13}C NMR (125 MHz, $CDCl_3$): δ 162.2, 137.9, 131.6, 82.0, 66.0, 32.1, 29.7, 29.4, 28.6, 26.1, 22.8, 14.3. FT–IR (ATR, ν/cm^{-1}): 2956 (m), 2921 (s), 2852 (m), 1722 (s), 1665 (m), 1467 (m), 1395 (w), 1377 (w), 1333 (m), 1304 (m), 1266 (s), 1244 (s), 1148 (m), 1107 (m), 1076 (m), 1039 (m), 998 (s), 887 (w), 871 (w), 780 (m), 722 (m).

Poly(2c). Catalyst **A**, 22 °C, 10 minutes. ^{1}H NMR (500 MHz, $CDCl_3$): δ 5.88 (2H), 5.82 (2H), 5.52 (2H), 5.48 (2H), 4.76 (4H), 2.12 (4H), 1.89 (4H), 1.66 (8H), 1.43 (8H), 1.03 (8H), 0.89 (28H), 0.73 (12H). ^{13}C NMR (125 MHz, $CDCl_3$): δ 162.1, 161.6, 138.5, 137.1, 131.4, 131.3, 82.2, 82.0, 76.3, 75.9, 46.8, 46.8, 40.8, 40.7, 34.4, 31.6, 29.9, 25.9, 23.3, 22.3, 21.1, 21.1, 16.5, 16.2. FT–IR (ATR, ν/cm^{-1}): 2955 (m), 2927 (m), 2867 (m), 1716 (s), 1664 (w), 1455 (m), 1387 (w), 1369 (m), 1314 (m), 1261 (s), 1242 (s), 1169 (m), 1138 (m), 1096 (s), 1038 (s), 1010 (s), 997 (s), 955 (m), 914 (m), 834 (m), 796 (s), 763 (m).

Poly(3a). Catalyst **A**, 40 °C, 1 hour. ^{1}H NMR (500 MHz, $CDCl_3$): δ 5.23 (d, 2H), 4.64 (d, 2H), 3.71 (s, 6H), 1.61 (s, 6H). ^{13}C NMR (125 MHz, $CDCl_3$): δ 165.6, 142.0, 134.8, 130.1, 128.6, 52.2, 48.0, 21.3. FT–IR (ATR, ν/cm^{-1}): 3010 (w), 2950 (w), 2914 (w), 1722 (s), 1638 (m), 1435 (m), 1322 (m), 1271 (s), 1204 (s), 1128 (m), 1085 (m), 1019 (w), 959 (m), 916 (w), 836 (w), 812 (w), 759 (m), 755 (m).

Poly(3b). Catalyst **C**, $CDCl_3$, 40 °C, 1 hour. ^{1}H NMR (400 MHz, $CDCl_3$): δ 5.37 (2H), 4.25–4.00 (6H), 1.70–1.55 (10H), 1.40–1.25 (14H), 0.89 (t, 6H). ^{13}C NMR (100 MHz, $CDCl_3$): 164.7, 140.7, 132.2, 131.1, 130.7, 65.1, 53.8, 32.1, 29.8, 29.6, 29.5, 28.8, 28.7, 26.1, 22.8, 20.8, 14.2.

Poly(3c). Catalyst **B**, $B(C_6F_5)_3$, 22 °C, 3 hours. ^{1}H NMR (500 MHz, toluene-d_8, 80 °C): δ 5.58 (1H), 5.48 (1H), 5.36 (1H), 5.13 (1H), 4.92 (2H), 2.71 (1H), 2.58 (1H), 2.42 (1H), 2.22 (1H), 1.88 (2H), 1.67 (2H), 1.63 (6H), 1.44 (2H), 1.26 (2H), 1.07 (6H), 1.01 (12 H), 0.88 (6 H). ^{13}C NMR (125 MHz, toluene-d_8, 80 °C): δ 165.1, 164.0, 146.4, 137.1, 131.9, 131.6, 129.2, 128.3, 127.0, 76.3, 76.3, 50.6, 49.5, 48.0, 47.8, 42.0, 41.6, 35.2, 35.2, 32.2, 32.1, 26.3, 26.0, 24.0, 22.6, 22.6, 22.5, 21.8, 21.4, 17.2, 16.4. FT–IR (ATR, ν/cm^{-1}): 2953 (m), 2928 (m), 2869 (w), 1730 (m), 1709 (s), 1635 (w), 1456 (m), 1386 (w), 1369 (m), 1313 (m), 1280 (m), 1259 (s), 1200 (m), 1182 (m), 1124 (m), 1095 (m), 1082 (m), 1057 (m), 1038 (w), 1008 (w), 982 (m), 955 (m), 913 (m), 848 (m), 818 (w), 780 (w), 749 (m), 653 (m).

Poly(3d). Catalyst **B**, $B(C_6F_5)_3$, 22 °C, 3 hours. ^{1}H NMR (500 MHz, THF-d_8): δ 5.40 (2H), 4.66 (2H), 1.73 (6H). ^{13}C NMR (125 MHz, THF-d_8): δ 140.1, 132.0, 130.7, 130.5, 121.7, 49.0, 22.1. ^{19}F NMR (282 MHz, THF-d_8): δ −59.5 (6F). FT–IR (ATR, ν/cm^{-1}): 3010 (w), 2916 (w), 2857 (w), 1672 (w), 1448 (w), 1347 (m), 1293 (s), 1180 (s), 1144 (s), 1101 (m), 1037 (m), 965 (w), 926 (m), 807 (m), 732 (m), 722 (m).

Poly(3e). Catalyst **A**, 45 °C, 1 hour. ^{1}H NMR (500 MHz, acetone-d_6): δ 5.85 (1H), 5.50 (1H), 4.83 (1H), 4.57 (1H), 1.76 (6H). FT–IR (ATR, ν/cm^{-1}): 3381 (br, w), 2961 (w), 2921 (m), 2850 (w), 2220 (w), 1736 (m), 1609 (br, w), 1454 (m), 1443 (m), 1373 (m), 1260 (s), 1091 (s), 1019 (s), 863 (m), 801 (s), 700 (m).

Poly(4a). Catalyst **A**, 22 °C, 1 hour. ^{1}H NMR (500 MHz, $CDCl_3$): δ 7.29 (2H), 7.22 (2H), 5.30 (2H), 5.11 (2H), 2.07 (6H). ^{13}C NMR (125 MHz, $CDCl_3$): δ 145.4, 138.7, 130.5, 127.6, 127.2, 125.4, 47.3, 22.6. FT–IR (ATR, ν/cm^{-1}): 3066 (w), 3010 (w), 2911 (w), 2854 (w), 1723 (w), 1601 (w), 1586 (w), 1476 (m), 1456 (m), 1379 (w), 1370 (w), 1312 (w), 1189 (w), 1154 (w), 1123 (w), 1097 (w), 1025 (w), 966 (w), 935 (w), 895 (w), 836 (m), 743 (s), 714 (s).

Poly(4b). Catalyst **A**, 22 °C, 10 minutes. ^{1}H NMR (400 MHz, $C_2D_2Cl_4$, 120 °C): δ 7.39 (2H), 7.32 (2H), 6.25 (2H), 5.89 (2H). ^{13}C NMR (100.6 MHz, $C_2D_2Cl_4$, 120 °C): δ 141.6, 133.3, 127.8, 121.9, 79.4. FT–IR (ATR, ν/cm^{-1}): 3072 (w), 3027 (w), 2867 (br, w), 1767 (w), 1724 (w), 1652 (w), 1631 (w), 1605 (w), 1477 (w), 1459 9 (w), 1396 (w), 1323 (w), 1284 (m), 1274 (m), 1243 (w), 1154 (w), 1113 (w), 998 (s), 900 (m), 850 (w), 745 (s), 703 (m), 650 (m).

2.5 References

(1) Anthony, J. E.; Facchetti, A.; Heeney, M.; Marder, S. R.; Zhan, X. *Adv. Mater.* **2010**, *22*, 3876–3892.

(2) Izuhara, D.; Swager, T. M. *J. Am. Chem. Soc.* **2009**, *131*, 17724–17725.

(3) Izuhara, D.; Swager, T. M. *Macromolecules* **2011**, *44*, 2678–2684.

(4) Rochat, S.; Swager, T. M. *J. Am. Chem. Soc.* **2013**, *135*, 17703–17706.

(5) Moslin, R. M.; Andrew, T. L.; Kooi, S. E.; Swager, T. M. *J. Am. Chem. Soc.* **2009**, *131*, 20–21.

(6) Bouffard, J.; Swager, T. M. *Macromolecules* **2008**, *41*, 5559–5562.

(7) Kim, Y.; Swager, T. M. *Chem. Commun.* **2005**, 372–374.

(8) Kim, Y.; Bouffard, J.; Kooi, S. E.; Swager, T. M. *J. Am. Chem. Soc.* **2005**, *127*, 13726–13731.

(9) Lim, J.; Swager, T. M. *Angew. Chem. Int. Ed.* **2010**, *49*, 7486–7488.

(10) Kim, Y.; Whitten, J. E.; Swager, T. M. *J. Am. Chem. Soc.* **2005**, *127*, 12122–12130.

(11) Takeda, Y.; Andrew, T. L.; Lobez, J. M.; Mork, A. J.; Swager, T. M. *Angew. Chem. Int. Ed.* **2012**, *51*, 9042–9046.

(12) Koo, B.; Sletten, E. M.; Swager, T. M. *Macromolecules* **2015**, *48*, 229–235.

(13) Klavetter, F. L.; Grubbs, R. H. *J. Am. Chem. Soc.* **1988**, *110*, 7807–7813.

(14) Jozefiak, T. H.; Ginsburg, E. J.; Gorman, C. B.; Grubbs, R. H.; Lewis, N. S. *J. Am. Chem. Soc.* **1993**, *115*, 1397–1409.

(15) Yu, C.-Y.; Kingsley, J. W.; Lidzey, D. G.; Turner, M. L. *Macromol. Rapid Commun.* **2009**, *30*, 1889–1892.

(16) Porz, M.; Mäker, D.; Brödner, K.; Bunz, U. H. F. *Macromol. Rapid Commun.* **2013**, *34*, 873–878.

(17) Horie, M.; Shen, I. W.; Tuladhar, S. M.; Leventis, H.; Haque, S. A.; Nelson, J.; Saunders, B. R.; Turner, M. L. *Polymer* **2010**, *51*, 1541–1547.

(18) Nomura, K.; Miyamoto, Y.; Morimoto, H.; Geerts, Y. *J. Polym. Sci. Part A Polym. Chem.* **2005**, *43*, 6166–6177.

(19) Mukherjee, N.; Peetz, R. M. *Macromolecules* **2008**, *41*, 6677–6685.

(20) Briziuz, G.; Pschirer, N. G.; Steffen, W.; Stitzer, K.; Zur Loye, H. C.; Bunz, U. H. F. *J. Am. Chem. Soc.* **2000**, *122*, 12435–12440.

(21) Pschirer, N. G.; Bunz, U. H. F. *Macromolecules* **2000**, *33*, 3961–3963.

(22) Kang, E. H.; Yu, S. Y.; Lee, I. S.; Park, S. E.; Choi, T. L. *J. Am Chem. Soc.* **2014**, *136*, 10508–10514.

(23) Kim, J.; Kang, E. H.; Choi, T. L. *ACS Macro Lett.* **2012**, *1*, 1090–1093.

(24) Lee, I. S.; Kang, E.-H.; Park, H.; Choi, T.-L. *Chem. Sci.* **2012**, *3*, 761.

(25) Edwards, J. H.; Feast, W. J. *Polymer* **1980**, *21*, 595–596.

(26) Feast, W. J.; Winter, J. N. *J. Chem. Soc. Chem. Commun.* **1985**, 202–203.

(27) Swager, T. M.; Dougherty, D. A.; Grubbs, R. H. *J. Am. Chem. Soc.* **1988**, *110*, 2973–2974.

(28) Swager, T. M.; Grubbs, R. H. *J. Am. Chem. Soc.* **1987**, *109*, 894–896.

(29) Wagaman, M. W.; Grubbs, R. H. *Macromolecules* **1997**, *30*, 3978.

(30) Pu, L.; Wagaman, M. W.; Grubbs, R. H. *Macromolecules* **1996**, *29*, 1138–1143.

(31) Wagaman, M. W.; Grubbs, R. H. *Synth. Met.* **1997**, *84*, 327–328.

(32) Hong, S. Y.; Kwon, S. J.; Kim, S. C. *Synth. Met.* **1996**, *82*, 183–188.

(33) Bazzi, H. S.; Sleiman, H. F. *Macromolecules* **2002**, *35*, 624–629.

(34) Fischer, W.; Stelzer, F.; Heller, C.; Leising, G. *Synth. Met.* **1993**, *55*, 815–820.

(35) Schimetta, M.; Stelzer, F. *Macromolecules* **1994**, *27*, 3769–3772.

(36) Schimetta, M.; Leising, G.; Stelzer, F. *Synth. Met.* **1995**, *74*, 99–102.

(37) Schimetta, M.; Stelzer, F. *Macromol. Chem. Phys.* **1994**, *195*, 2699–2707.

(38) Hamilton, J. G.; Rooney, J. J. *Macromol. Chem. Phys.* **1995**, *196*, 327–342.

(39) Greenham, N. C.; Moratti, S. C.; Bradley, D. D. C.; Friend, R. H.; Holmes, A. B. *Nature* **1993**, *365*, 628–630.

(40) Barclay, T. M.; Cordes, A. W.; MacKinnon, C. D.; Oakley, R. T.; Reed, R. W. *Chem. Mater.* **1997**, *9*, 981–990.

(41) Andrew, T. L.; Cox, J. R.; Swager, T. M. *Org. Lett.* **2010**, *12*, 5302–5305.

(42) Weis, C. D. *J. Org. Chem.* **1963**, *28*, 74–78.

(43) Helder, R.; Wynberg, H. *Tetrahedron Lett.* **1972**, *13*, 605–608.

(44) Franck-Neumann, M. In *Methoden der Organischen Chemie*; Thieme: Stuttgart, 1977; Vol. 5/2a, p. 677.

(45) Moureu, C.; Bongrand, J. C. *Bull. Soc. Chim. Fr.* **1909**, 846–847.

(46) Moureu, C.; Bongrand, J. C. *Ann. Chim.* **1920**, *14*, 5–46.

(47) Blomquist, A. T.; Winslow, E. C. *J. Org. Chem.* **1945**, *10*, 149–158.

(48) Knothe, L.; Werp, J.; Babsch, H.; Prinzbach, H.; Fritz, H. *Justus Liebigs Ann. Chem.* **1977**, 709–726.

(49) Bazan, G. C.; Khosravi, E.; Schrock, R. R.; Feast, W. J.; Gibson, V. C.; O'Regan, M. B.; Thomas, J. K.; Davis, W. M. *J. Am. Chem. Soc.* **1990**, *112*, 8378–8387.

(50) Flook, M. M.; Jiang, A. J.; Schrock, R. R.; Müller, P.; Hoveyda, A. H. *J. Am. Chem. Soc.* **2009**, *131*, 7962–7963.

(51) Flook, M. M.; Gerber, L. C. H.; Debelouchina, G. T.; Schrock, R. R. *Macromolecules* **2010**, *43*, 7515–7522.

(52) Flook, M. M.; Ng, V. W. L.; Schrock, R. R. *J. Am. Chem. Soc.* **2011**, *133*, 1784–1786.

(53) Schrock, R. R. *Acc. Chem. Res.* **2014**, *47*, 2457–2466.

(54) Peryshkov, D. V.; Schrock, R. R.; Takase, M. K.; Müller, P.; Hoveyda, A. H. *J Am. Chem. Soc.* **2011**, *133*, 20754–20757.

(55) Peryshkov, D. V.; Schrock, R. R. *Organometallics* **2012**, *31*, 7278–7286.

(56) Peryshkov, D. V.; Forrest, W. P.; Schrock, R. R.; Smith, S. J.; Müller, P. *Organometallics* **2013**, *32*, 5256–5259.

(57) Forrest, W. P.; Axtell, J. C.; Schrock, R. R. *Organometallics* **2014**, *33*, 2313–2325.

(58) Feast, W. J.; Millichamp, I. S. *J. Mol. Catal.* **1985**, *28*, 331–336.

(59) Bazan, G. C.; Oskam, J. H.; Cho, H.; Park, L. Y.; Schrock, R. R. *J. Am. Chem. Soc.* **1991**, *113*, 6899–6907.

(60) Schimetta, M.; Stelzer, F. *Macromol. Chem. Phys.* **1994**, *195*, 2699–2707.

(61) Hardy, C. G.; Zhang, J.; Yan, Y.; Ren, L.; Tang, C. *Prog. Polym. Sci.* **2014**, *39*, 1742–1796.

(62) Mcnair, A. M.; Mann, K. R. *Inorg. Chem.* **1986**, *24*, 2519–2527.

(63) Gill, T. P.; Mann, K. R. *Organometallics* **1982**, *1*, 485–488.

(64) Clawson, P.; Lunn, P. M.; Whiting, D. A. *J. Chem. Soc. Perkin Trans 1* **1990**, 159.

(65) Feast, W. J.; Khosravi, E. *J. Fluor. Chem.* **1999**, *100*, 117–125.

(66) Jeong, H.; John, J. M.; Schrock, R. R.; Hoveyda, A. H. *J. Am. Chem. Soc.* **2015**, *137*, 2239–2242.

(67) Samak, B. Al; Carvill, A. G.; Hamilton, J. G.; Rooney, J. J.; Thompson, J. M. *Chem. Commun.* **1997**, 2057–2058.

(68) Wu, Z.; Grubbs, R. H. *Macromolecules* **1995**, *28*, 3502–3508.

(69) Choi, T.-L.; Rutenberg, I. M.; Grubbs, R. H. *Angew. Chem. Int. Ed.* **2002**, *41*, 3839–3841.

(70) Bornand, M.; Torker, S.; Chen, P. *Organometallics* **2007**, *26*, 3585–3596.

(71) Vehlow, K.; Wang, D.; Buchmeiser, M. R.; Blechert, S. *Angew. Chem. Int. Ed.* **2008**, *47*, 2615–2618.

(72) Ilker, M. F.; Coughlin, E. B. *Macromolecules* **2002**, *35*, 54–58.

(73) Amir-Ebrahimi, V.; Rooney, J. J. *J. Mol. Catal. A Chem.* **2004**, *208*, 115–121.

(74) Diels, O.; Alder, K. *Justus Liebigs Ann. Chem.* **1931**, *490*, 236–242.

(75) Prinzbach, H.; Arguëlles, M.; Druckrey, E. *Angew. Chem. Int. Ed.* **1966**, *5*, 1039–1039.

(76) Alder, K.; Rühmann, R. *Justus Liebigs Ann. Chem.* **1950**, *566*, 1–27.

(77) Luo, R.; Liao, J.; Xie, L.; Tang, W.; Chan, A. S. C. *Chem. Commun.* **2013**, *49*, 9959–9961.

(78) Stone, K. J.; Little, R. D. *J. Org. Chem.* **1984**, *49*, 1849–1853.

(79) Haq, M. Z. *J. Org. Chem.* **1972**, *37*, 3015–3019.

(80) Love, J. A.; Morgan, J. P.; Trnka, T. M.; Grubbs, R. H. *Angew. Chem. Int. Ed.* **2002**, *41*, 4035–4037.

(81) Zhou, Q.; Carroll, P. J.; Swager, T. M. *J. Org. Chem.* **1994**, *59*, 1294–1301.

(82) Tahara, K.; Furukawa, S.; Uji-I, H.; Uchino, T.; Ichikawa, T.; Zhang, J.; Mamdouh, W.; Sonoda, M.; De Schryver, F. C.; De Feyter, S.; Tobe, Y. *J. Am. Chem. Soc.* **2006**, *128*, 16613–16625.

2.6 Appendix for Chapter 2

NMR Spectra of Monomers

2b. Didecyl 7-oxabicyclo[2.2.1]hepta-2,5-diene-2,3-dicarboxylate.

^{1}H NMR, $CDCl_3$, 500 MHz

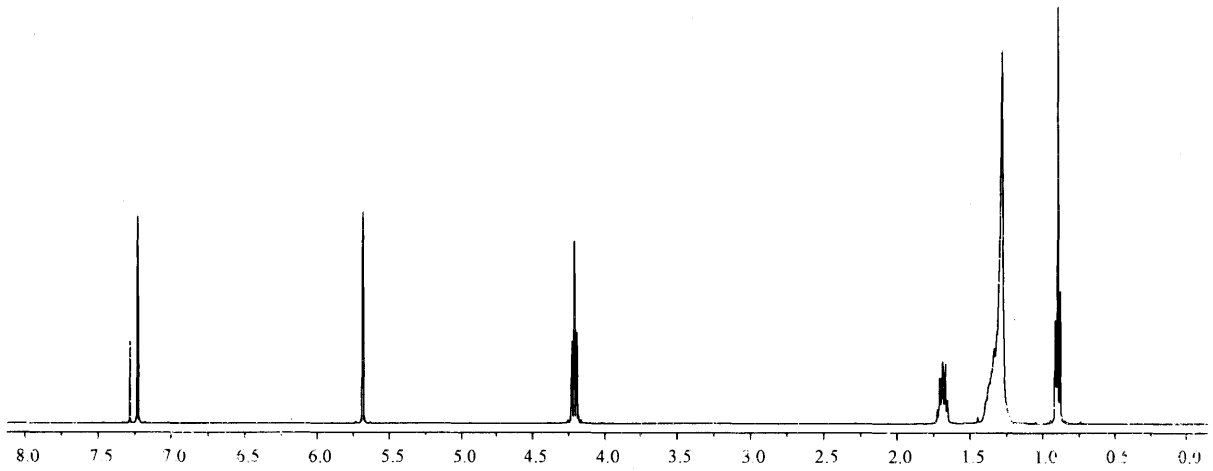

δ (ppm)

^{13}C NMR, $CDCl_3$, 125 MHz

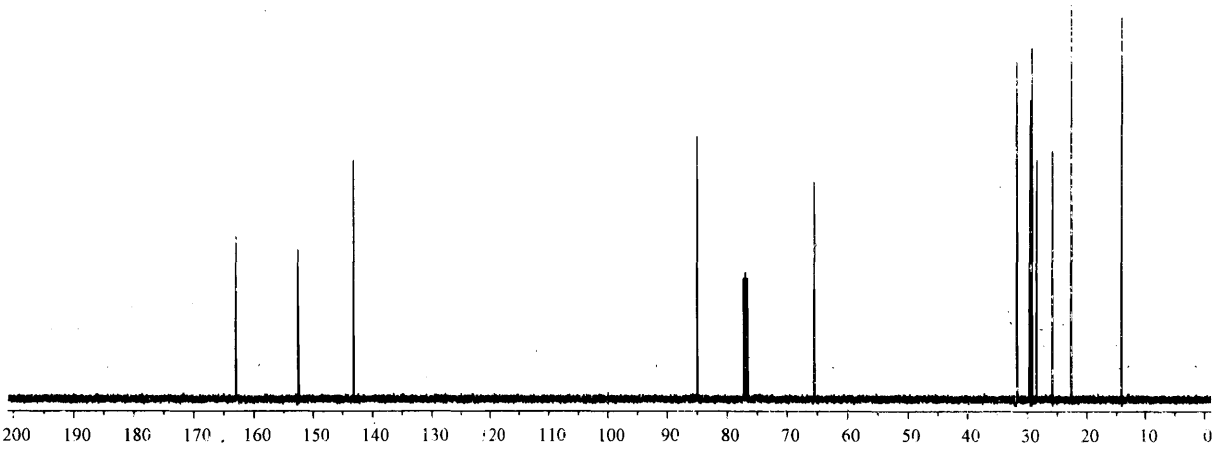

δ (ppm)

2c. Bis((1*R*,2*S*,5*R*)-2-isopropyl-5-methylcyclohexyl)-7-oxabicyclo[2.2.1]hepta-2,5-diene-2,3-dicarboxylate.

^{1}H NMR, $CDCl_3$, 500 MHz

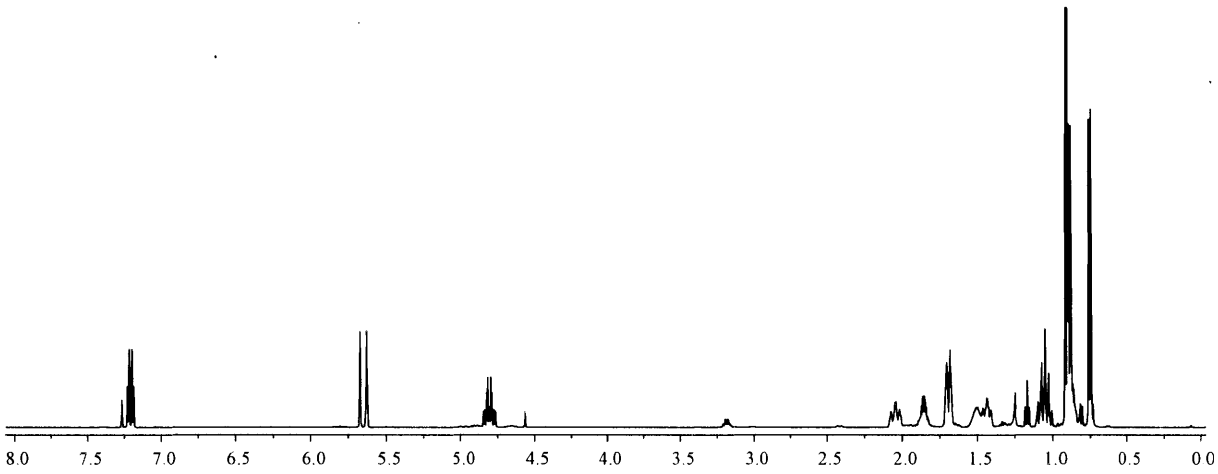

δ (ppm)

^{13}C NMR, $CDCl_3$, 125 MHz

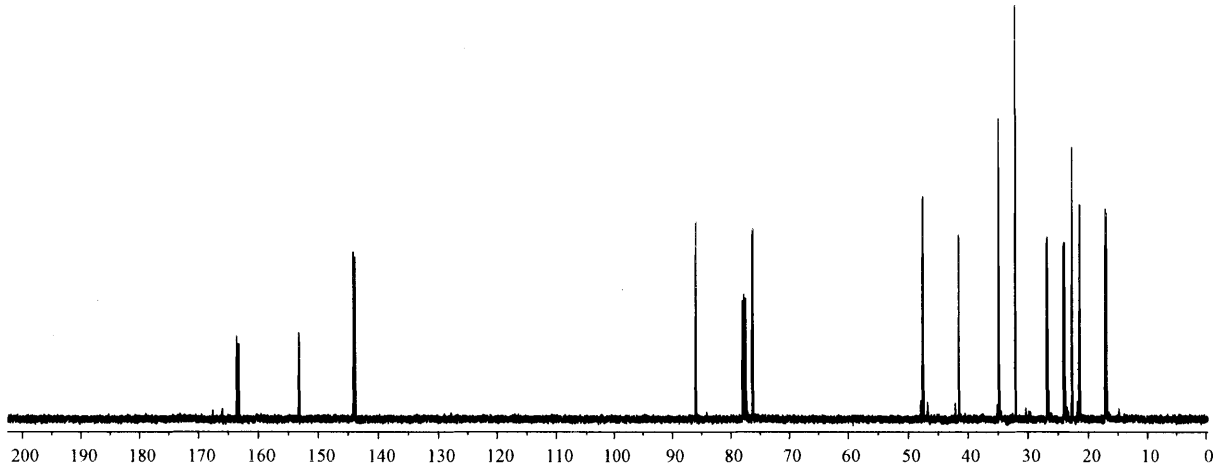

δ (ppm)

3b. Didecyl 7-(propan-2-ylidene)bicyclo[2.2.1]hepta-2,5-diene-2,3-dicarboxylate.

^{1}H NMR, $CDCl_3$, 500 MHz

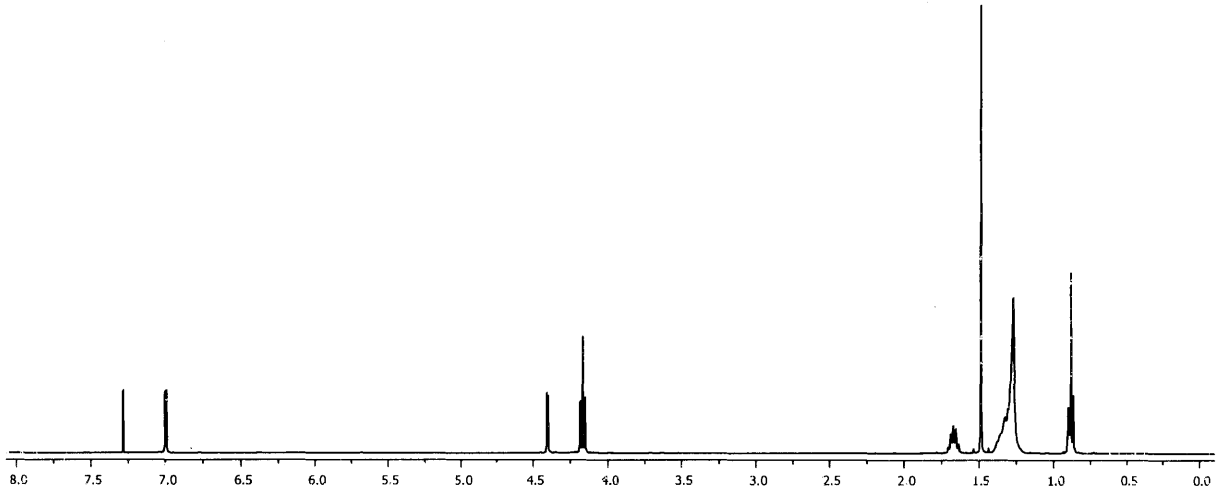

δ (ppm)

^{13}C NMR, $CDCl_3$, 125 MHz

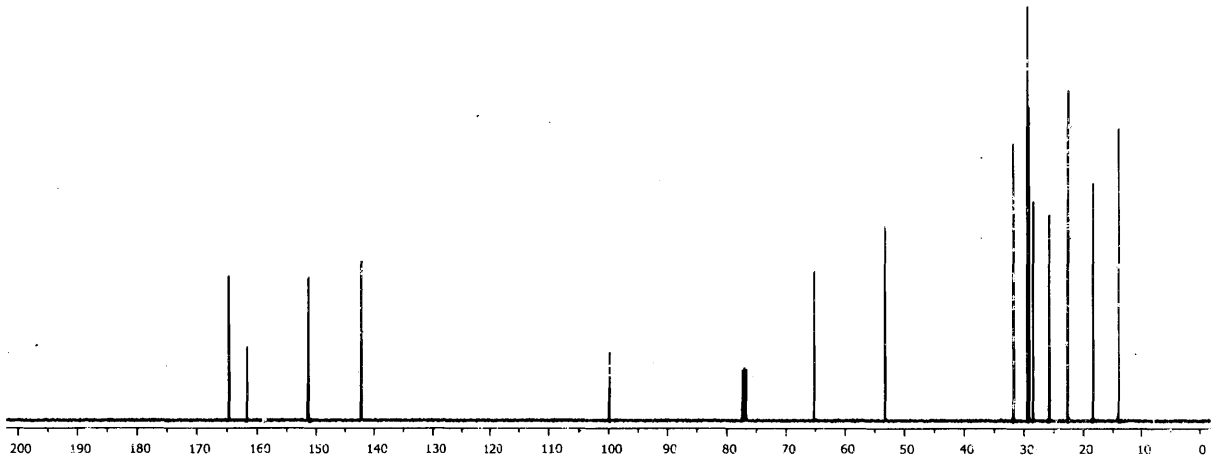

δ (ppm)

3c. Bis((1*R*,2*S*,5*R*)-2-isopropyl-5-methylcyclohexyl)-7-(propan-2-ylidene) bicyclo[2.2.1]hepta-2,5-diene-2,3-dicarboxylate.

^{1}H NMR, $CDCl_3$, 500 MHz

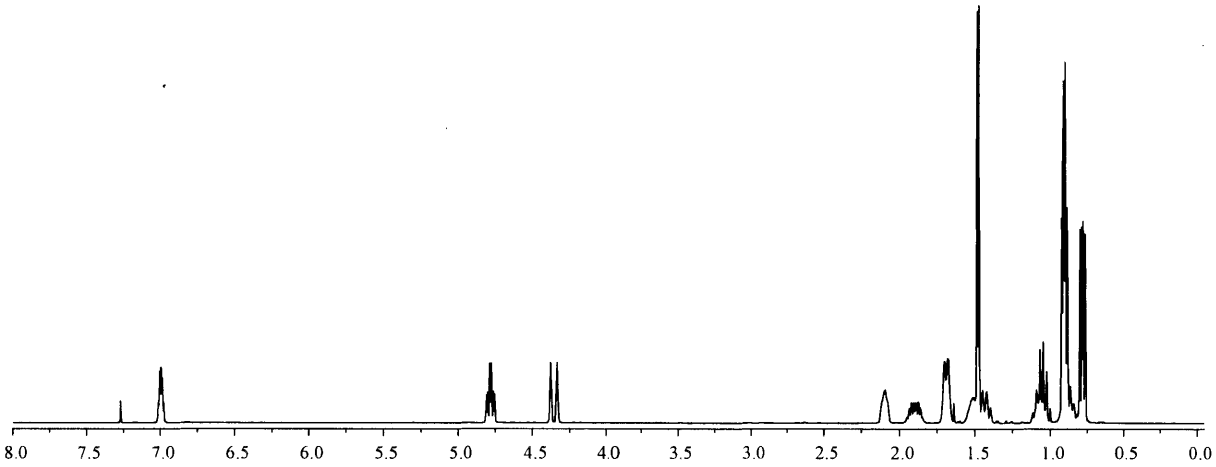

δ (ppm)

^{13}C NMR, $CDCl_3$, 125 MHz

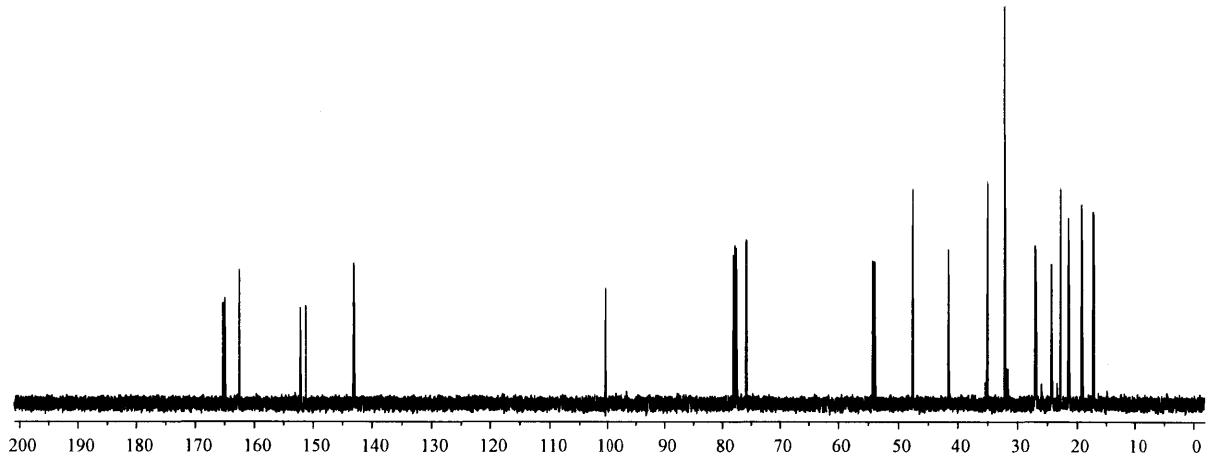

δ (ppm)

3e. 7-(Propan-2-ylidene)bicyclo[2.2.1]hepta-2,5-diene-2,3-dicarbonitrile.

^{1}H NMR, $CDCl_3$, 500 MHz

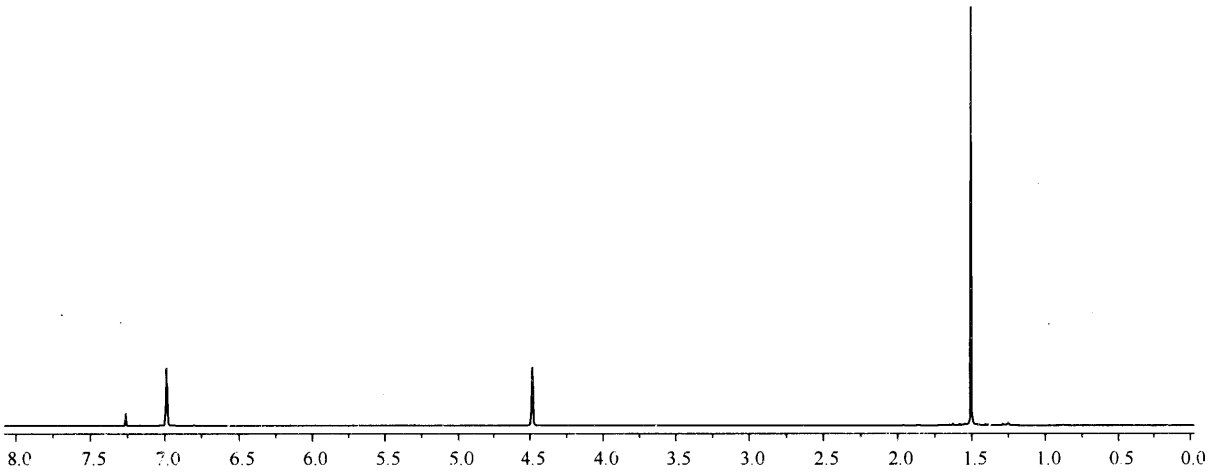

δ (ppm)

^{13}C NMR, $CDCl_3$, 125 MHz

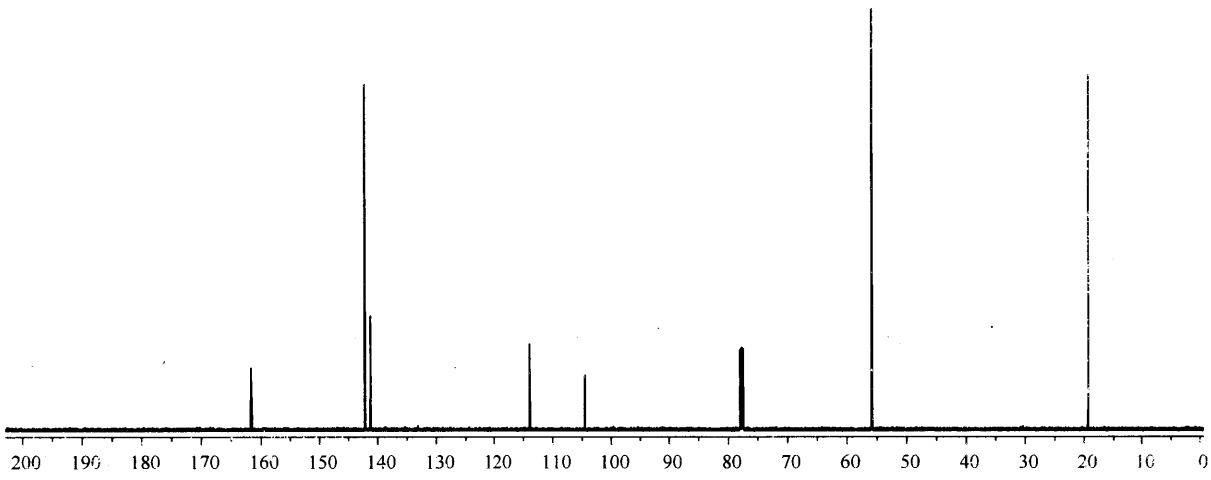

δ (ppm)

8. Didecyl but-2-ynedioate

^{1}H NMR, $CDCl_3$, 500 MHz

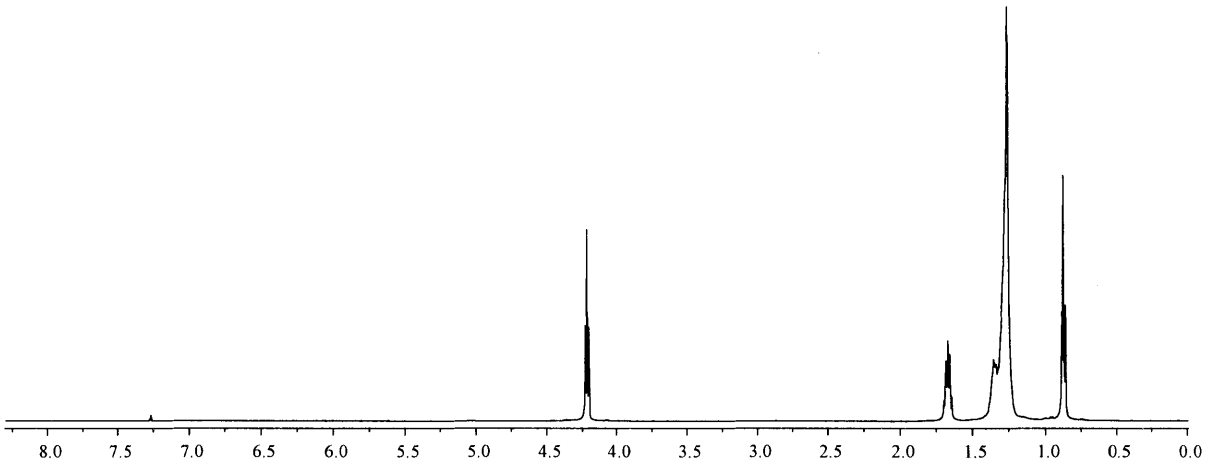

δ (ppm)

^{13}C NMR, $CDCl_3$, 125 MHz

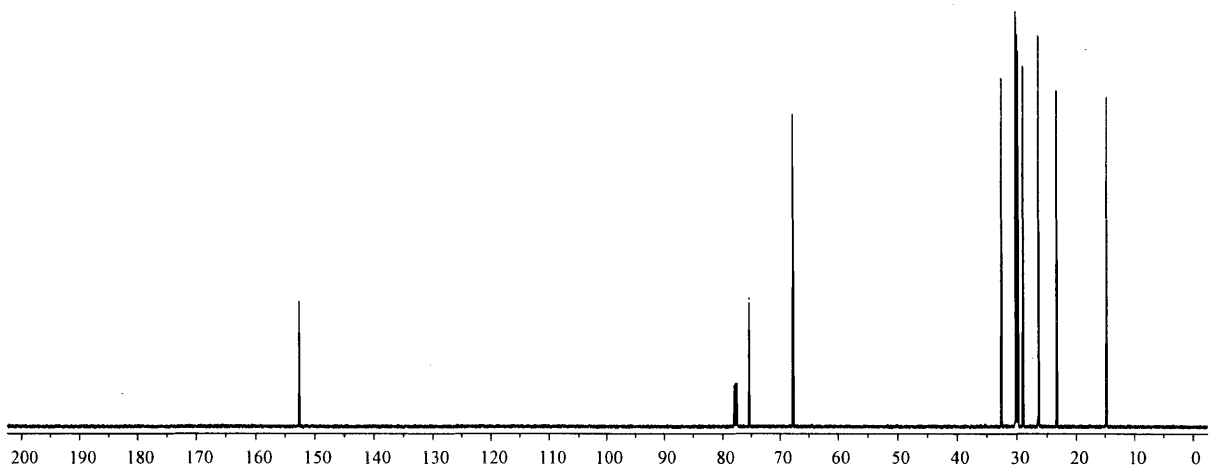

δ (ppm)

9. Bis((1*R*,2*S*,5*R*)-2-isopropyl-5-methylcyclohexyl) but-2-ynedioate.

^{1}H NMR, $CDCl_3$, 500 MHz

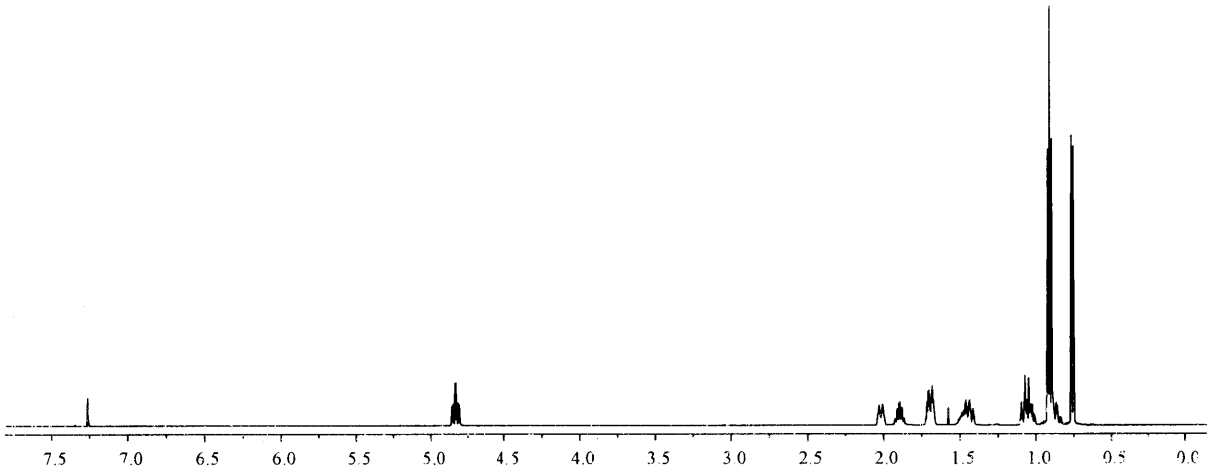

δ (ppm)

^{13}C NMR, $CDCl_3$, 125 MHz

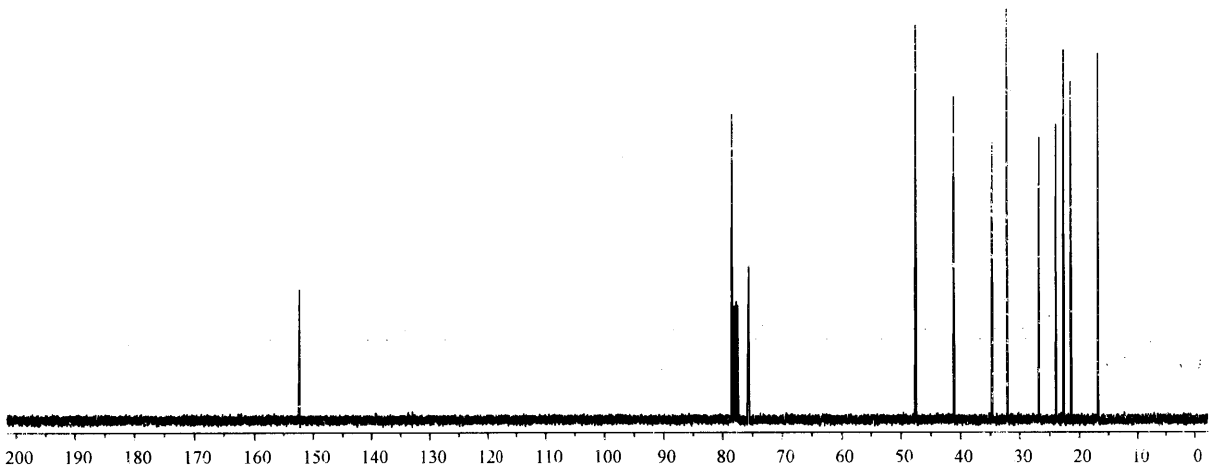

δ (ppm)

11. 7-(Propan-2-ylidene)bicyclo[2.2.1]hept-5-ene-2,3-dione

^{1}H NMR, $CDCl_3$, 500 MHz

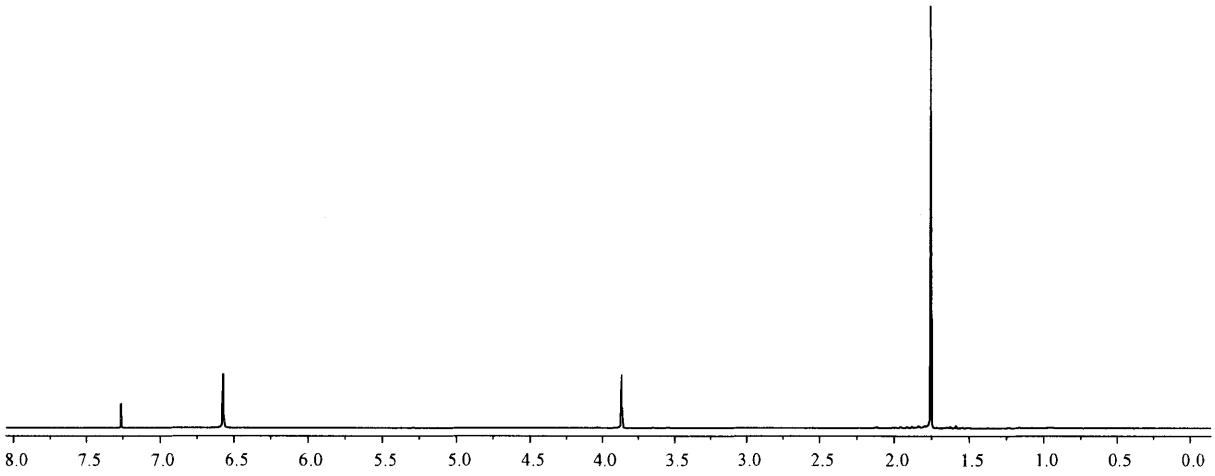

δ (ppm)

^{13}C NMR, $CDCl_3$, 125 MHz

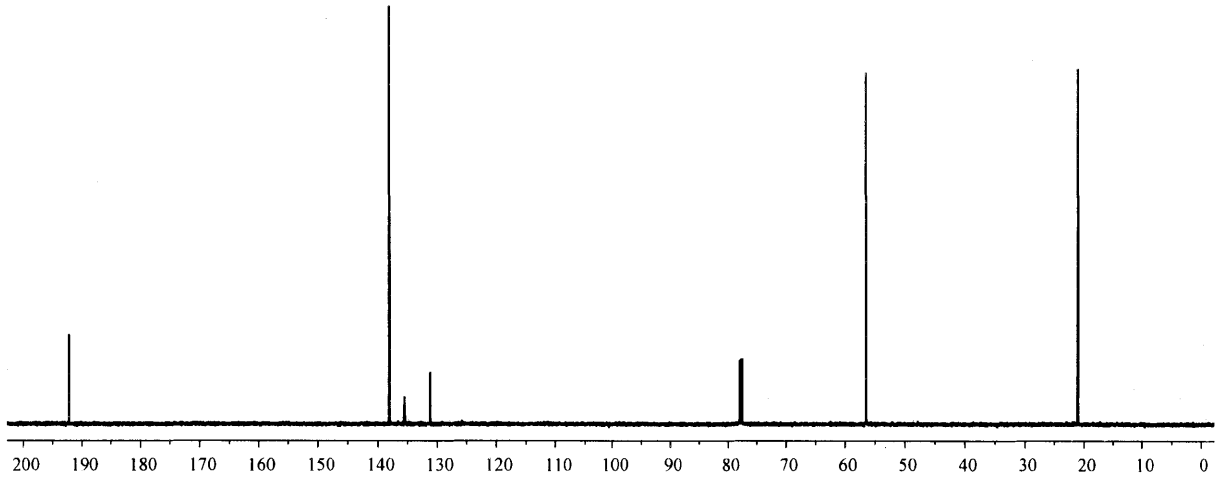

δ (ppm)

12. 9-(Propan-2-ylidene)-5,8-dihydro-5,8-methanoquinoxaline-2,3-dicarbonitrile.

^{1}H NMR, $CDCl_3$, 500 MHz

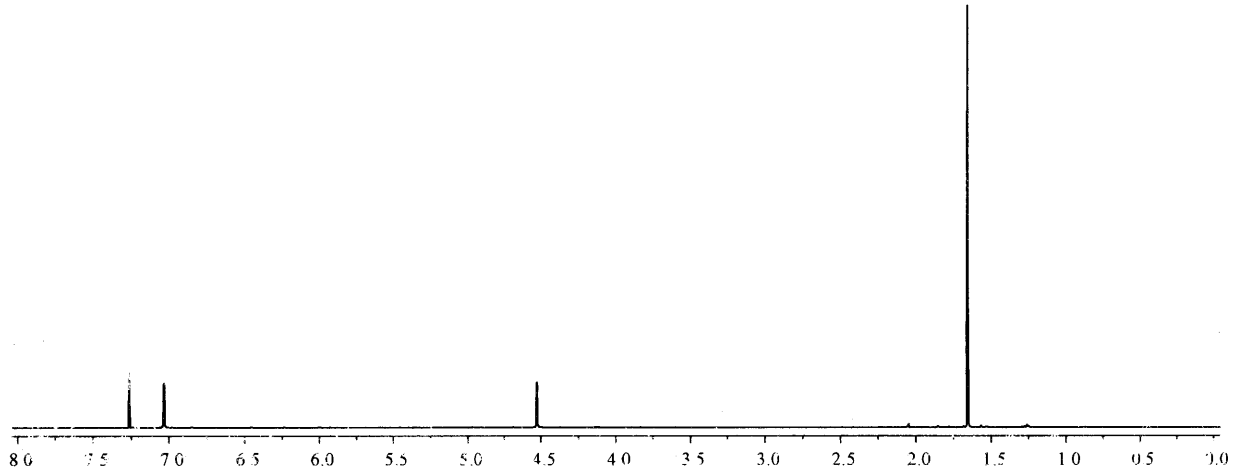

δ (ppm)

^{13}C NMR, $CDCl_3$, 125 MHz

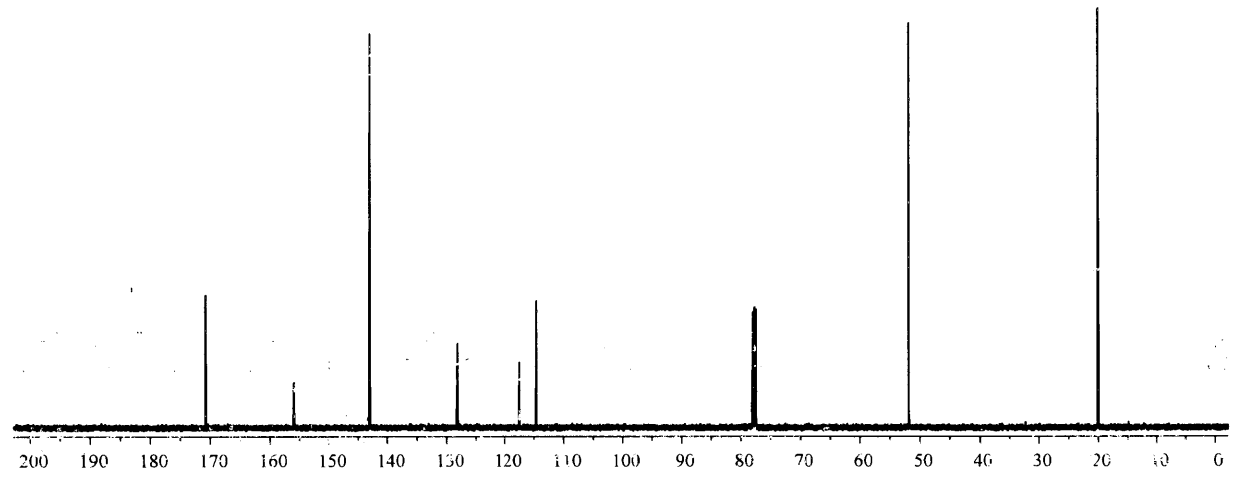

δ (ppm)

14. $[(\eta^5\text{-}C_5(CH_3)_5)Ru(\eta^6\text{-}\mathbf{4a})]PF_6$.

^1H NMR, CD_2Cl_2, 500 MHz

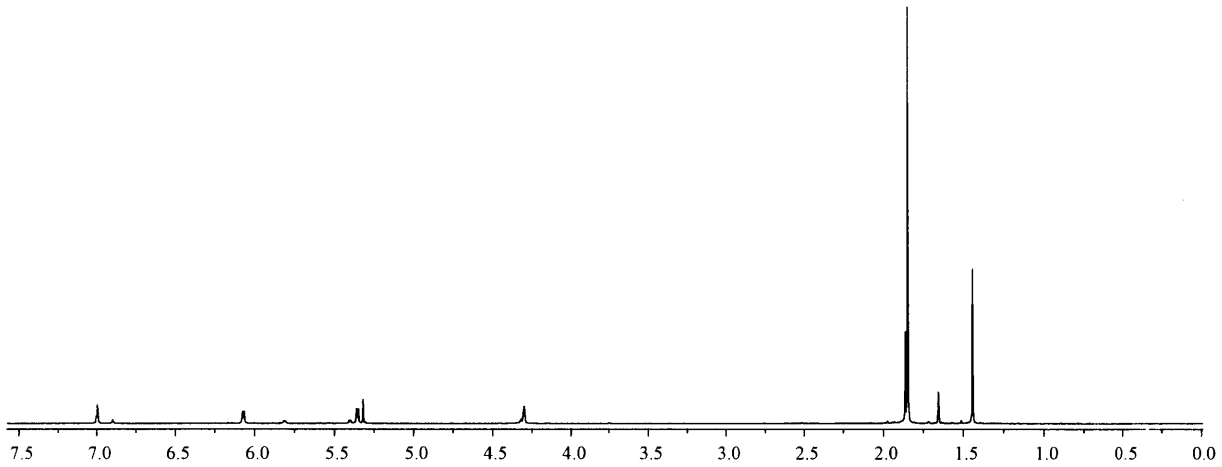

δ (ppm)

^{13}C NMR, CD_2Cl_2, 125 MHz

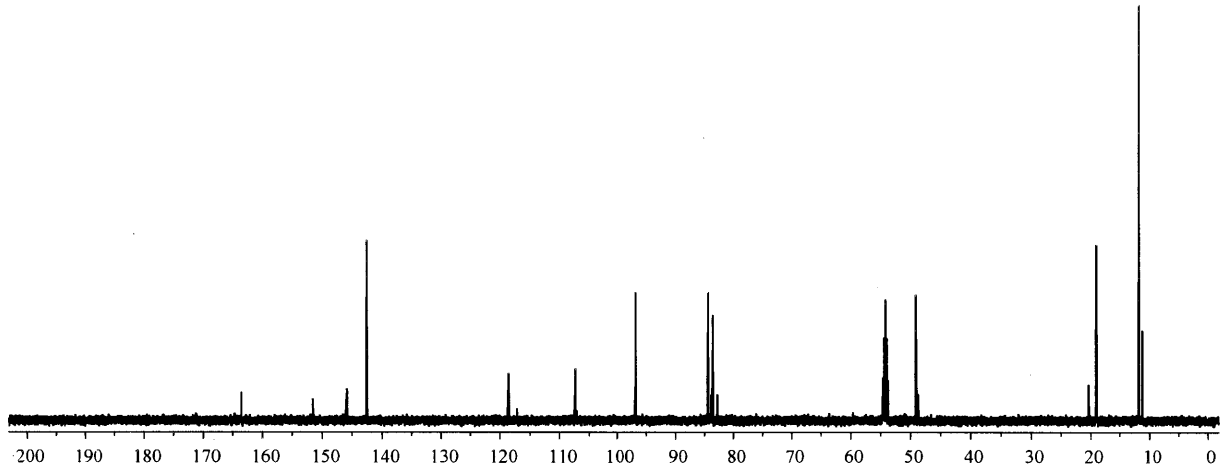

δ (ppm)

14. [(η^5-$C_5(CH_3)_5$)Ru(η^6-**4a**)]PF_6. (cont.)

gCOSY, CD_2Cl_2, 500 MHz

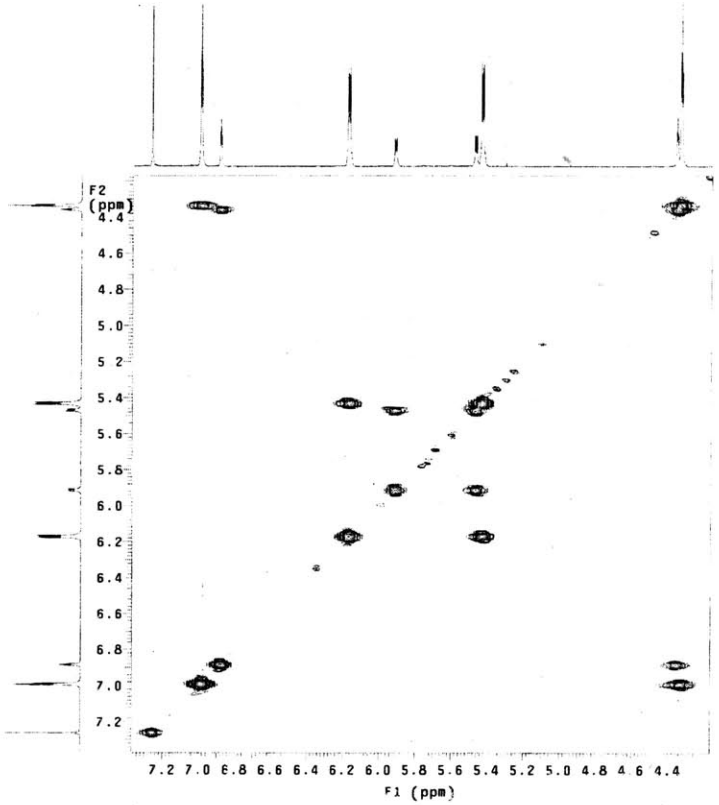

1D NOE Difference Experiment (preirradiation/saturation of Cp* methyl groups at δ 1.85)

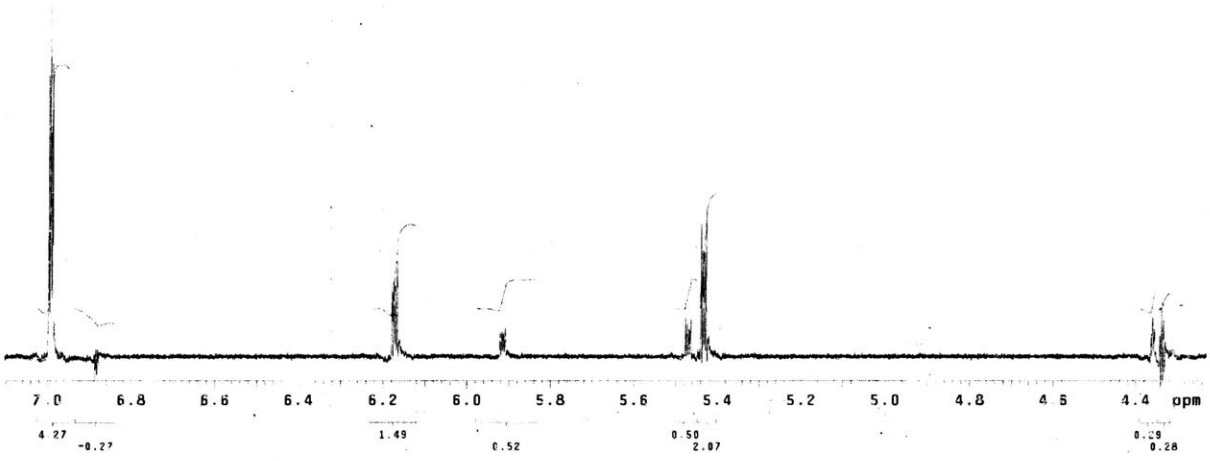

14. $[(\eta^5\text{-}C_5(CH_3)_5)Ru(\eta^6\text{-}\mathbf{4a})]PF_6$. (cont.)

ESI–MS

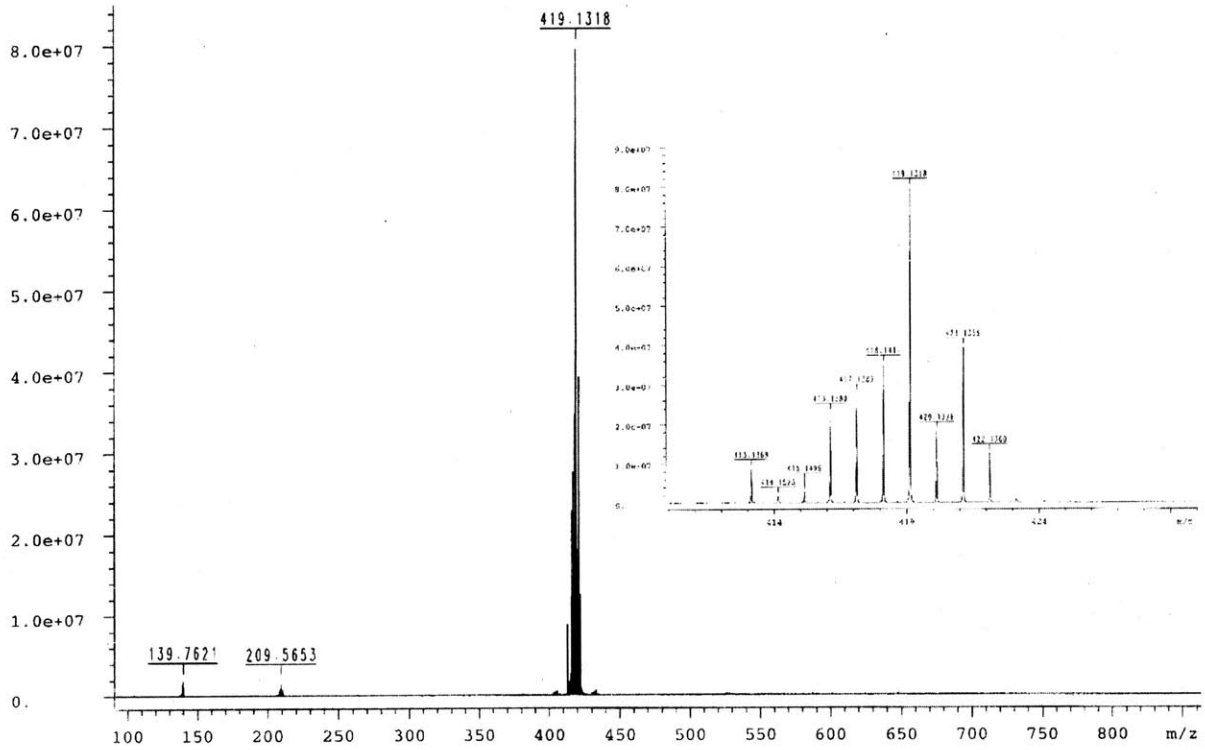

18. 6,7-Didodecyl-1,4-dihydro-1,4-epoxynaphthalene.

^{1}H NMR, $CDCl_3$, 500 MHz

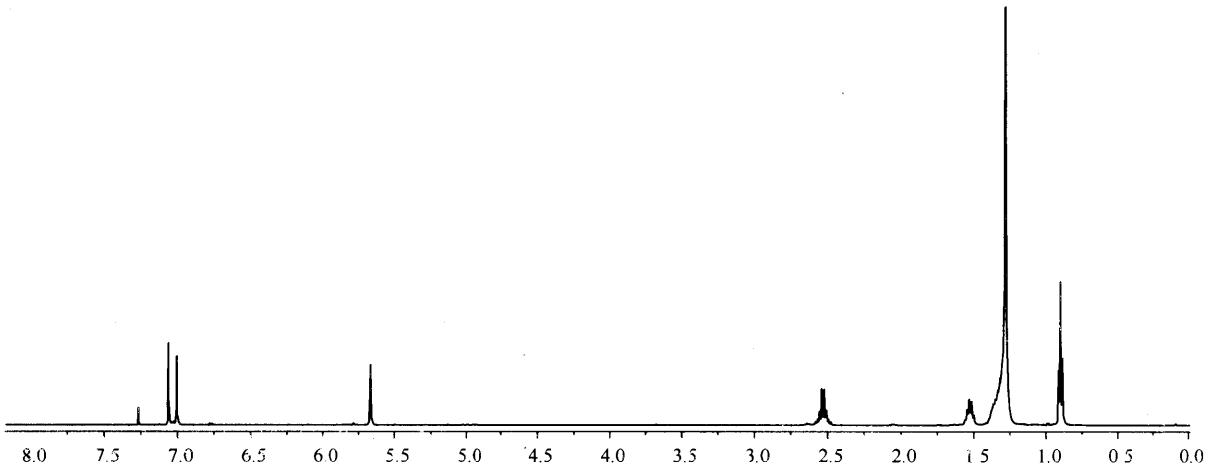

δ (ppm)

^{13}C NMR, $CDCl_3$, 125 MHz

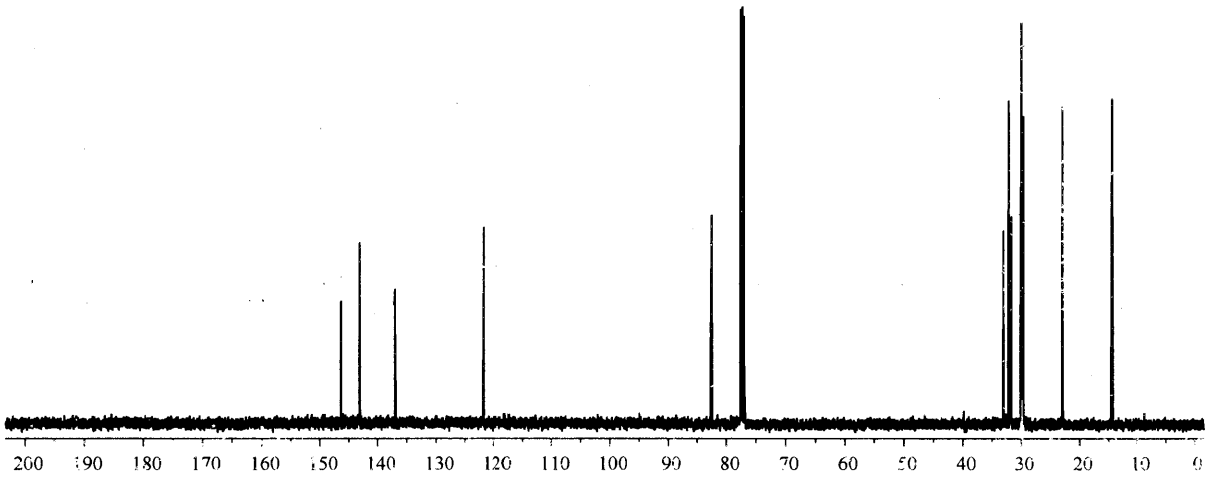

δ (ppm)

19. 6,7-Bis(decyloxy)-1,4-dihydro-1,4-epoxynaphthalene.

^{1}H NMR, $CDCl_3$, 500 MHz

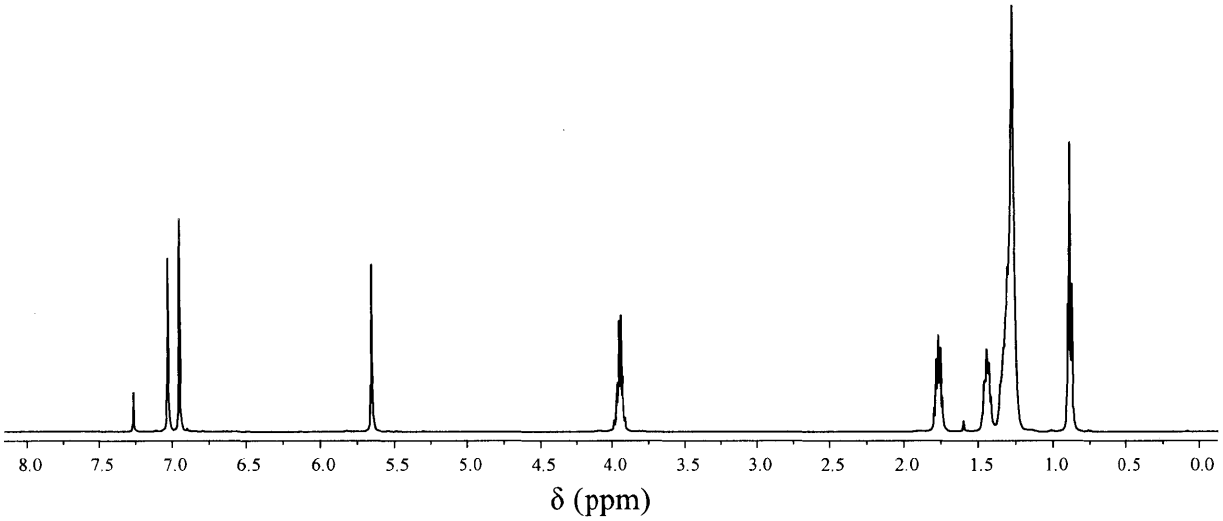

^{13}C NMR, $CDCl_3$, 125 MHz

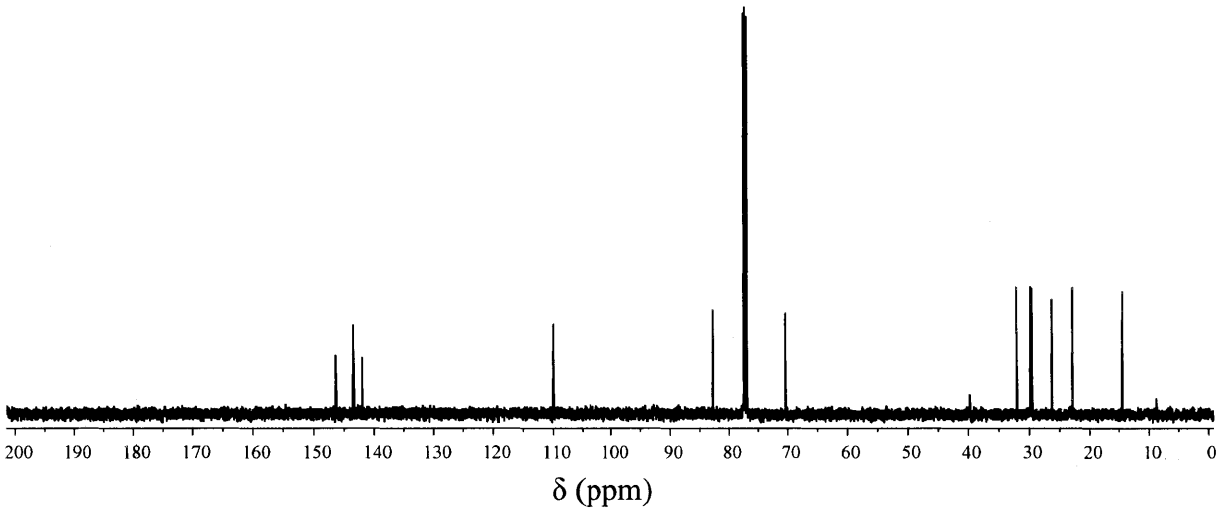

20. 6,7-Bis(dodecyloxy)naphthalen-1-ol.

^{1}H NMR, $CDCl_3$, 400 MHz

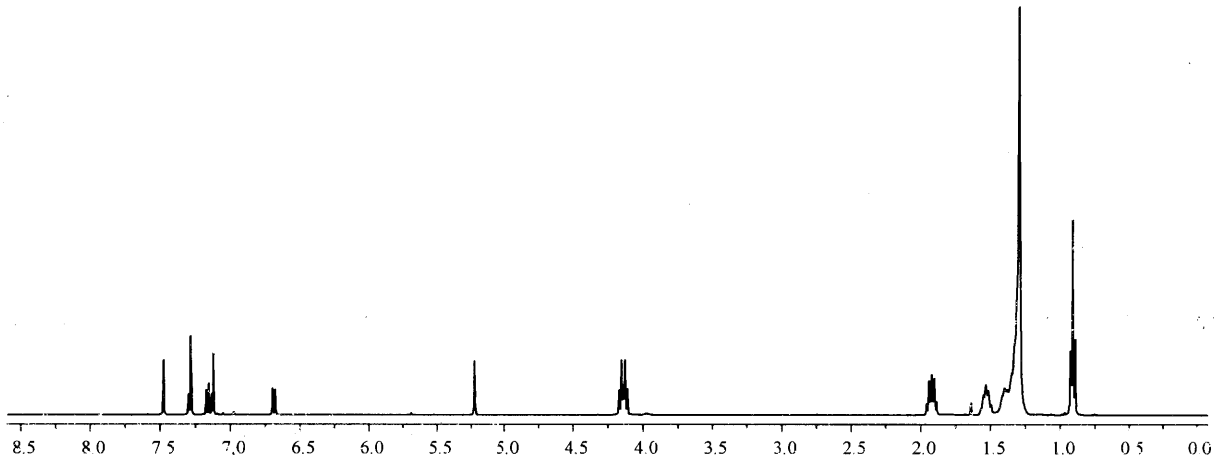

δ (ppm)

^{13}C NMR, $CDCl_3$, 100 MHz

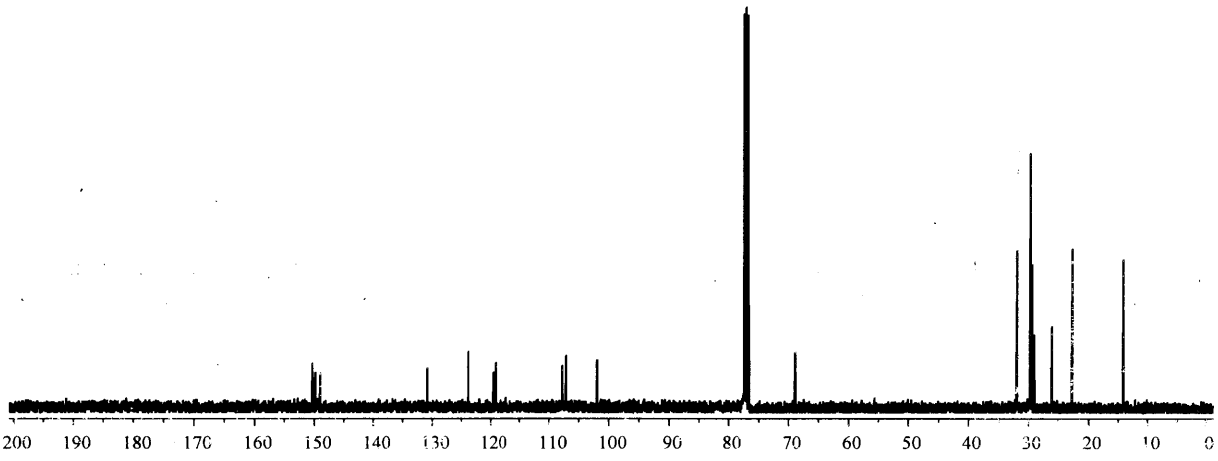

δ (ppm)

NMR Spectra of Polymers

Poly(2a).

^{1}H NMR, $C_2D_2Cl_4$, 400 MHz, 130 °C

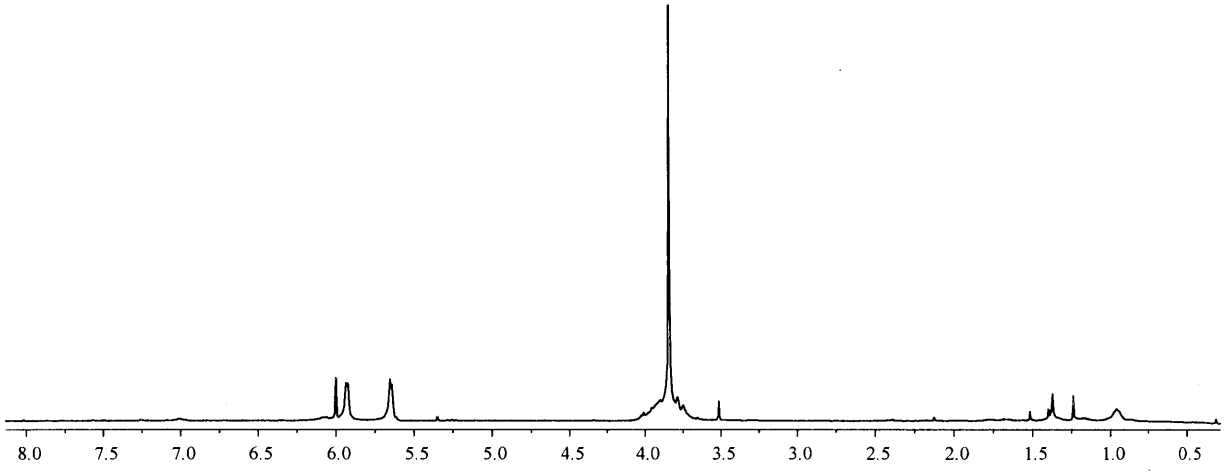

δ (ppm)

^{13}C NMR, $C_2D_2Cl_4$, 100.6 MHz, 130 °C

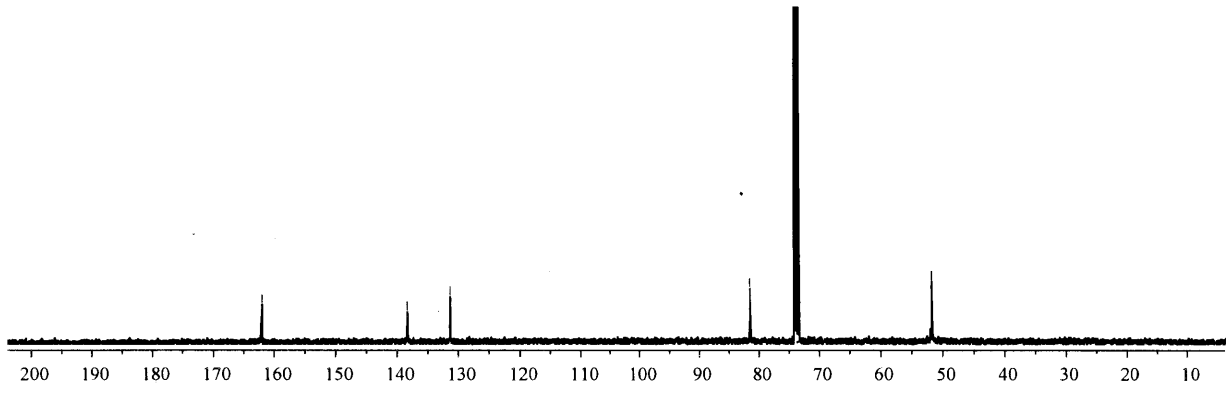

δ (ppm)

Poly(2b).

^{1}H NMR, $CDCl_3$, 500 MHz

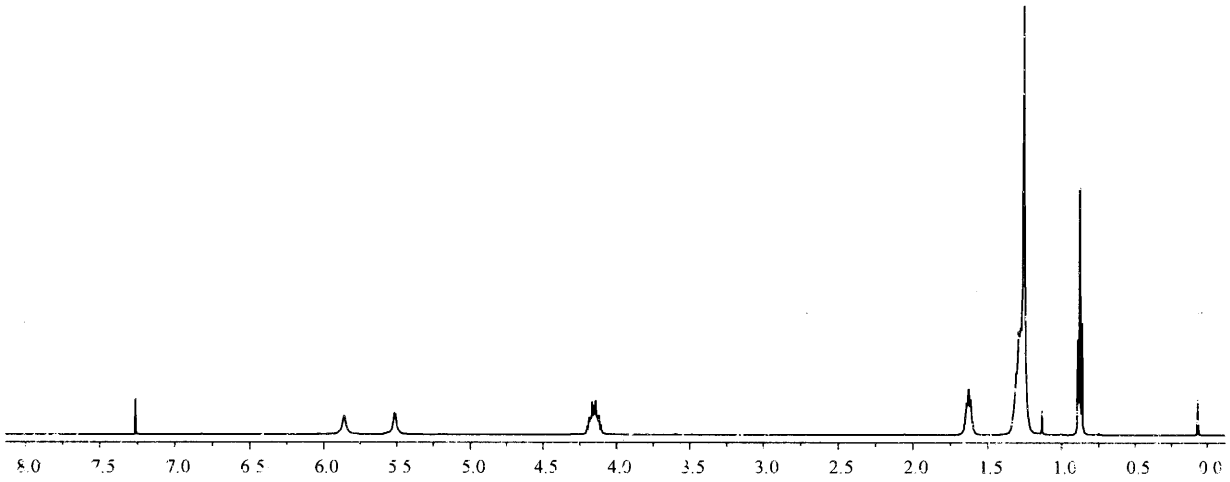

δ (ppm)

^{13}C NMR, $CDCl_3$, 125 MHz

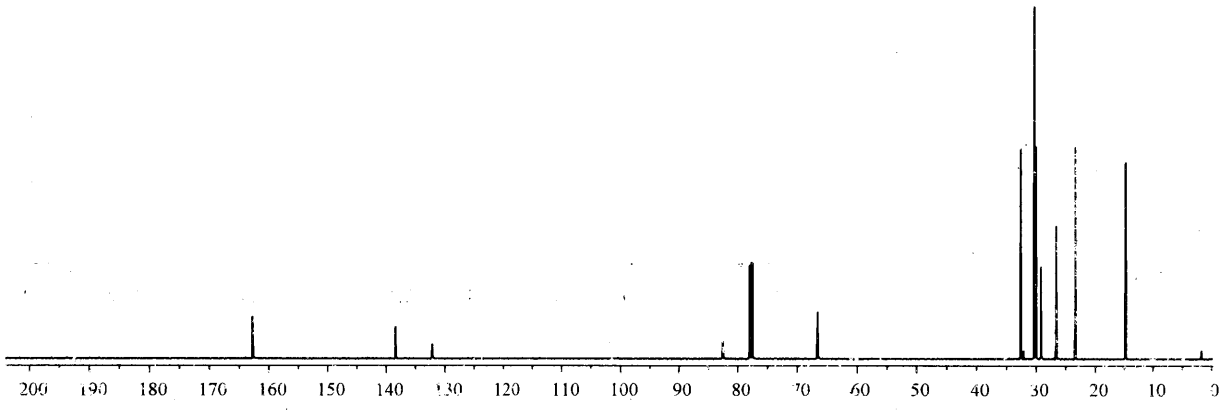

δ (ppm)

Poly(2c).

^{1}H NMR, $CDCl_3$, 500 MHz

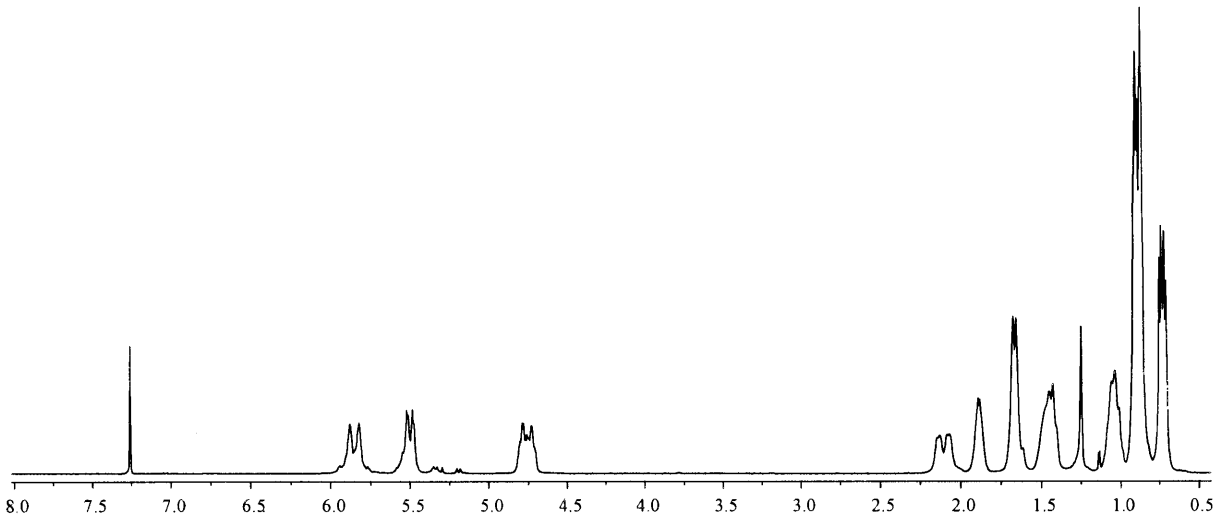

δ (ppm)

^{13}C NMR, $CDCl_3$, 125 MHz

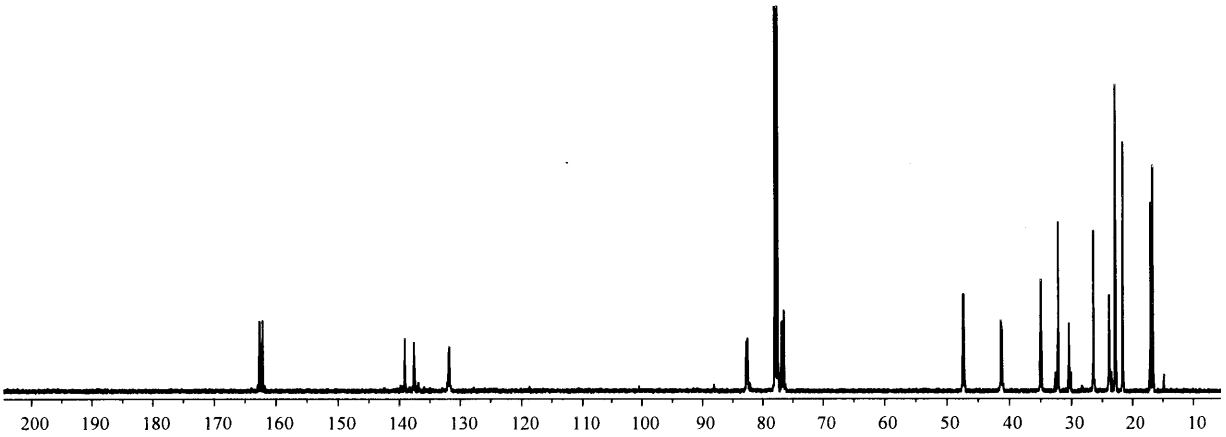

δ (ppm)

Poly(2c). (cont.)

^{1}H–^{1}H gCOSY ($CDCl_3$, 500 MHz) spectrum for *cis,syndiotactic*-**poly(2c)**.

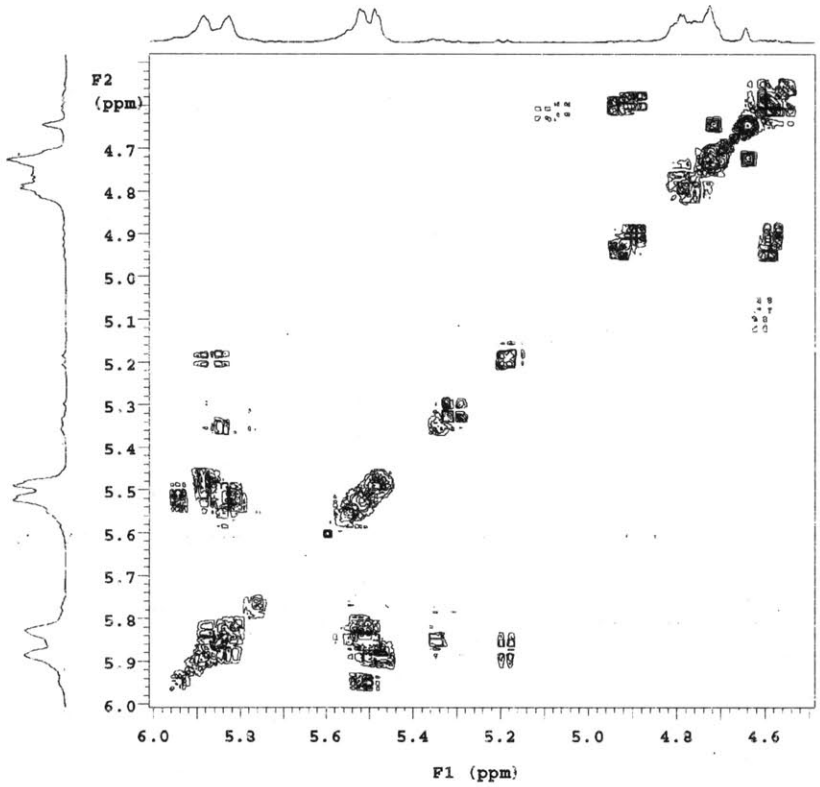

^{1}H–^{13}C HSQC ($CDCl_3$, 500 MHz) spectrum for *cis,syndiotactic*-**poly(2c)**.

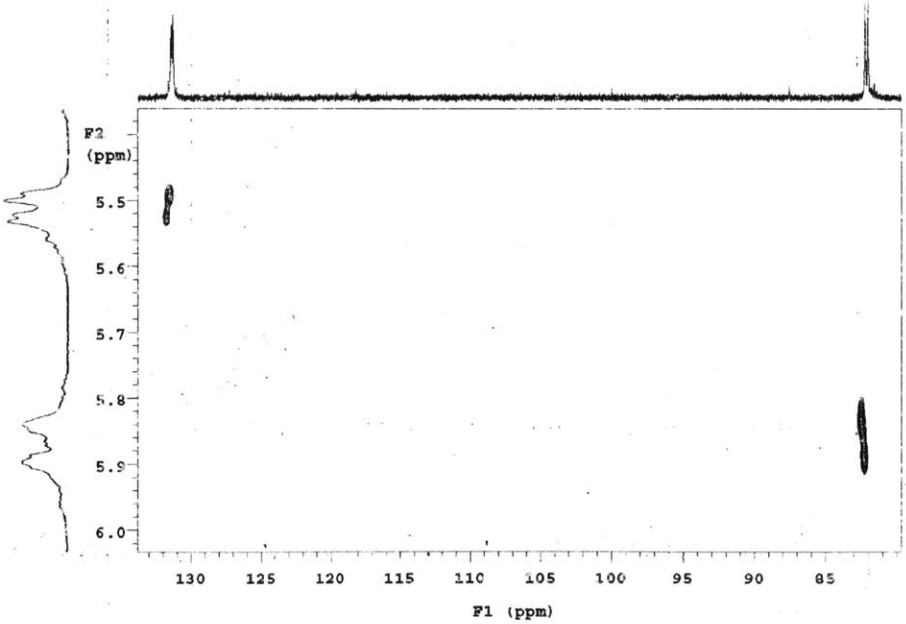

Poly(3a).

^{1}H NMR, $CDCl_3$, 500 MHz

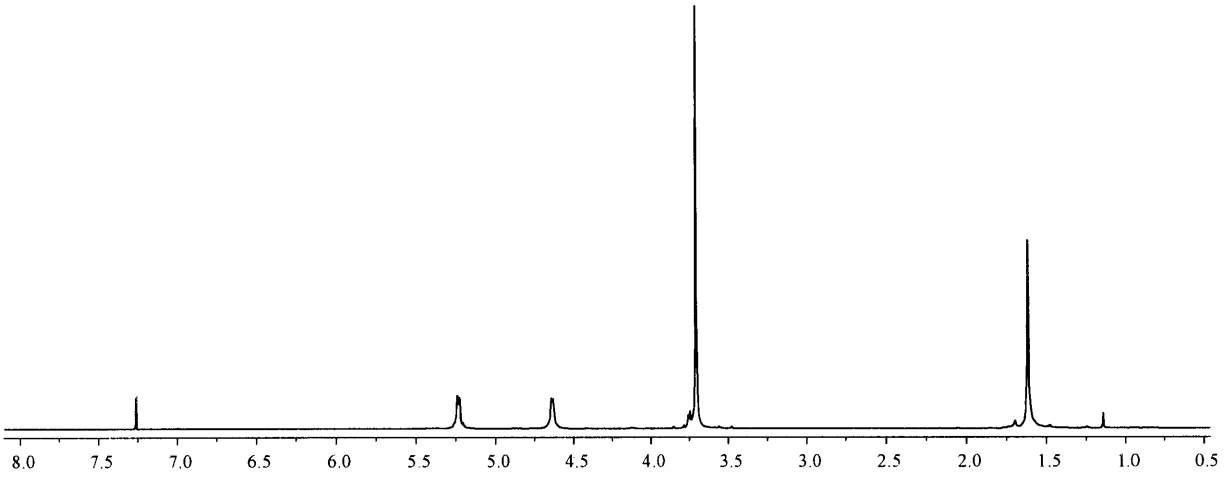

δ (ppm)

^{13}C NMR, $CDCl_3$, 125 MHz

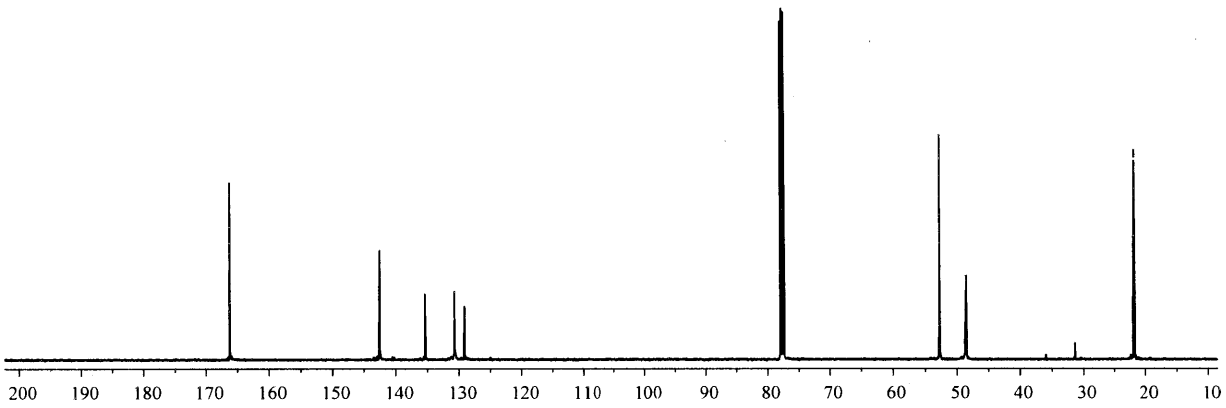

δ (ppm)

Poly(3b).

^{1}H NMR, $CDCl_3$, 400 MHz

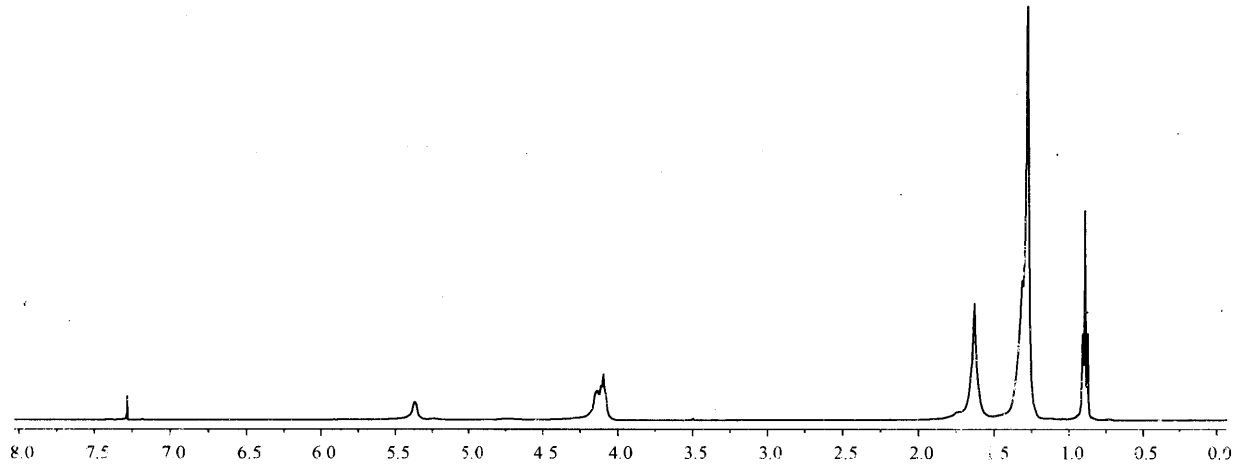

δ (ppm)

^{13}C NMR. $CDCl_3$, 100 MHz

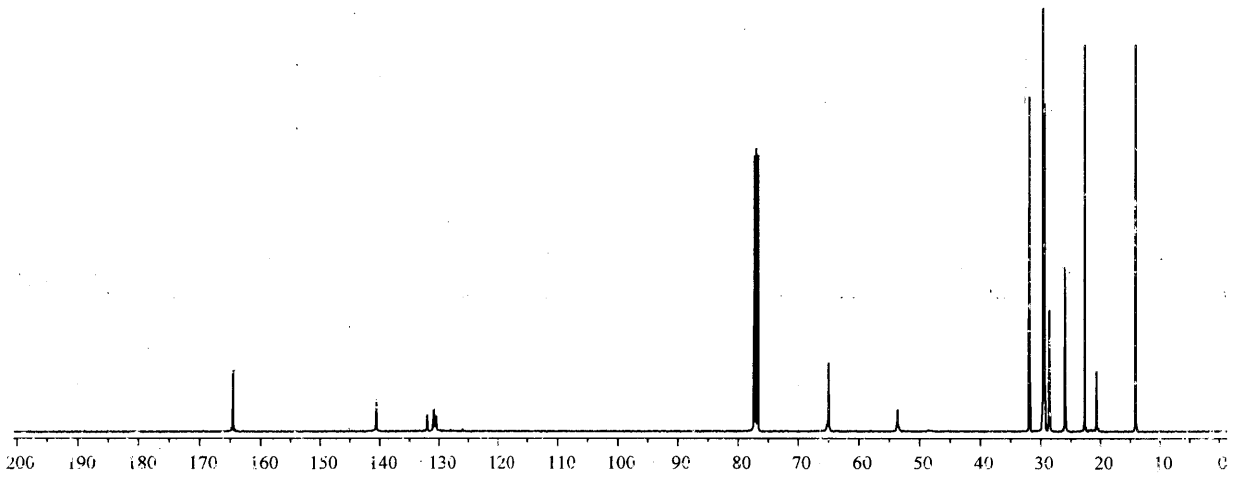

δ (ppm)

Poly(3c).

^{1}H NMR, toluene-d_8, 80 °C, 500 MHz

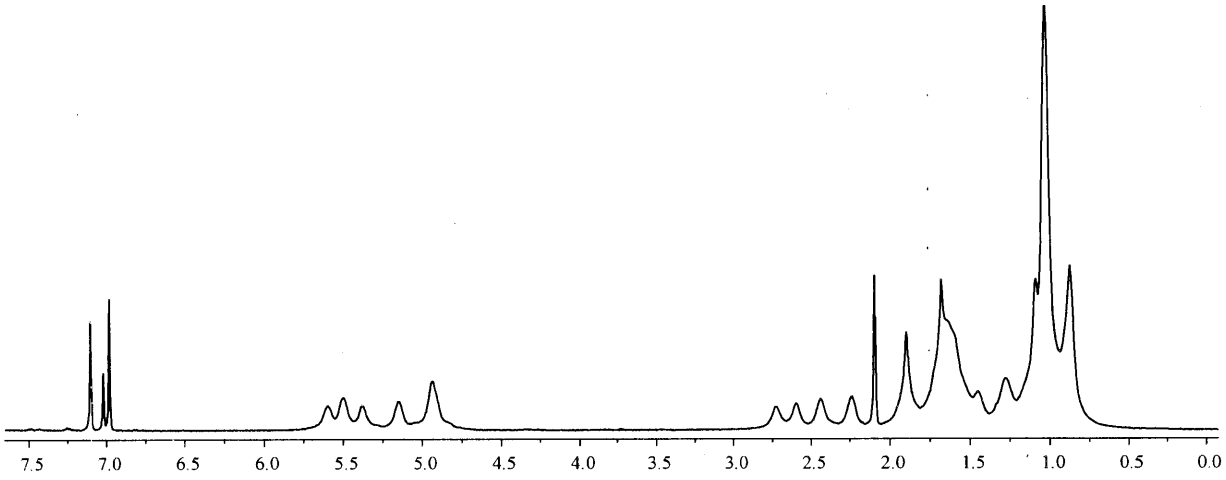

δ (ppm)

^{13}C NMR, toluene-d_8, 80 °C, 125 MHz

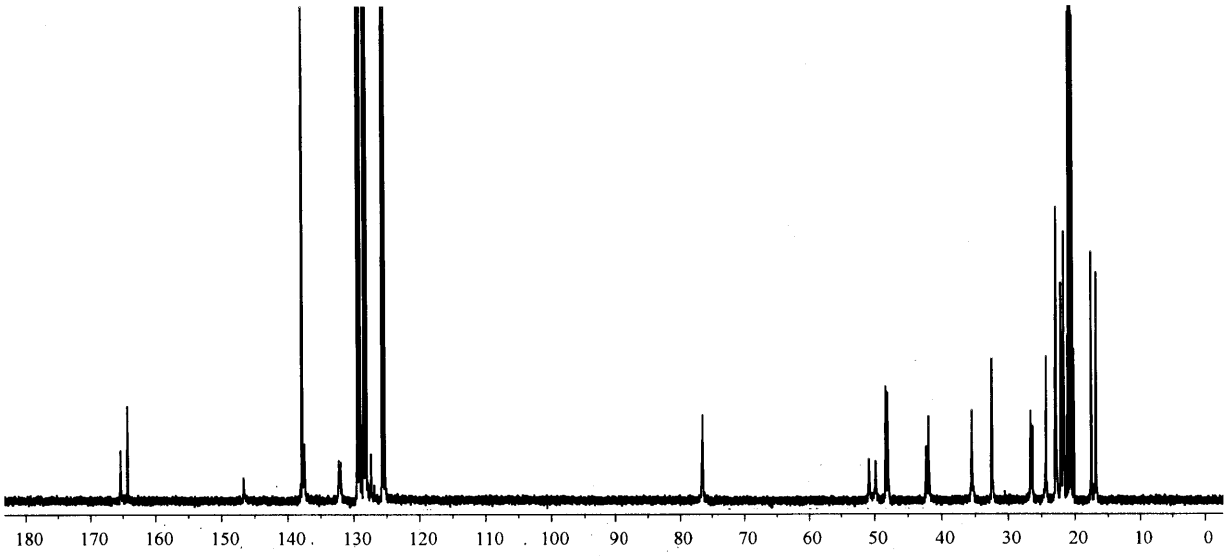

δ (ppm)

Poly(3c). (cont.)

^{1}H–^{1}H COSY (toluene-d_8, 80 °C, 500 MHz) spectrum for *cis,isotactic*-**poly(3c)**.

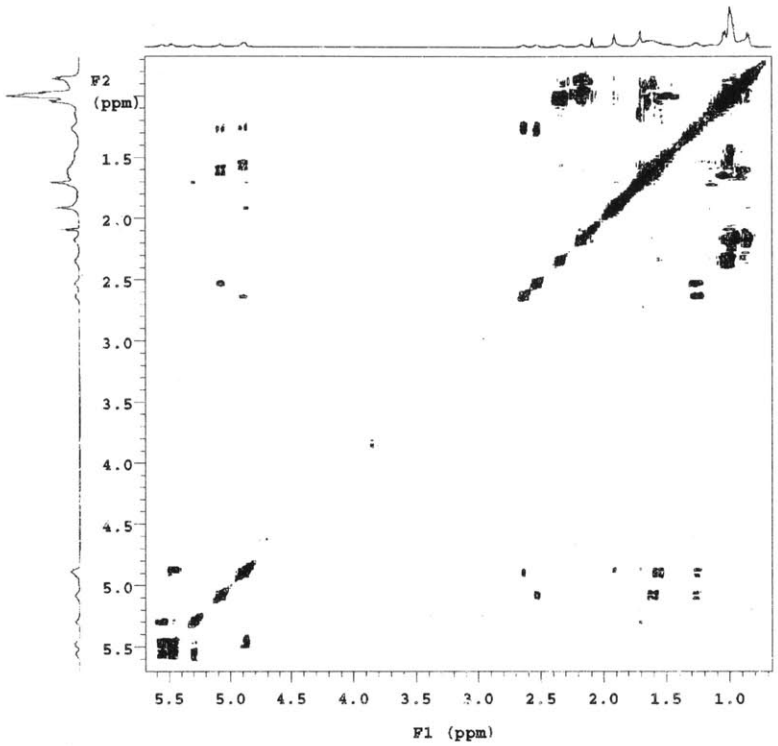

^{1}H–^{13}C HSQC (toluene-d_8, 80 °C, 500 MHz) spectrum for *cis,isotactic*-**poly(3c)** in the olefinic and methine proton region

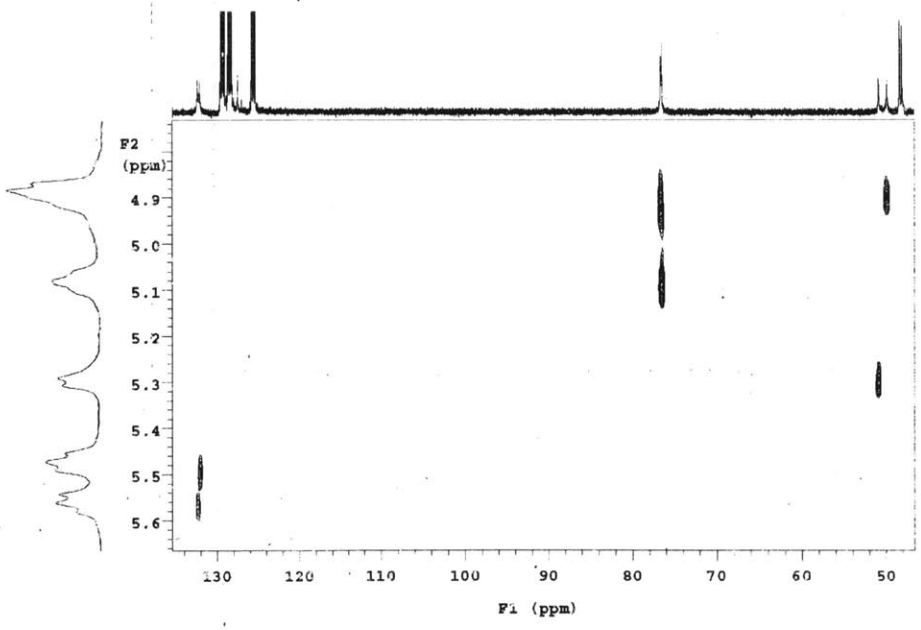

Poly(3d).

^{1}H NMR, THF-d_8, 500 MHz

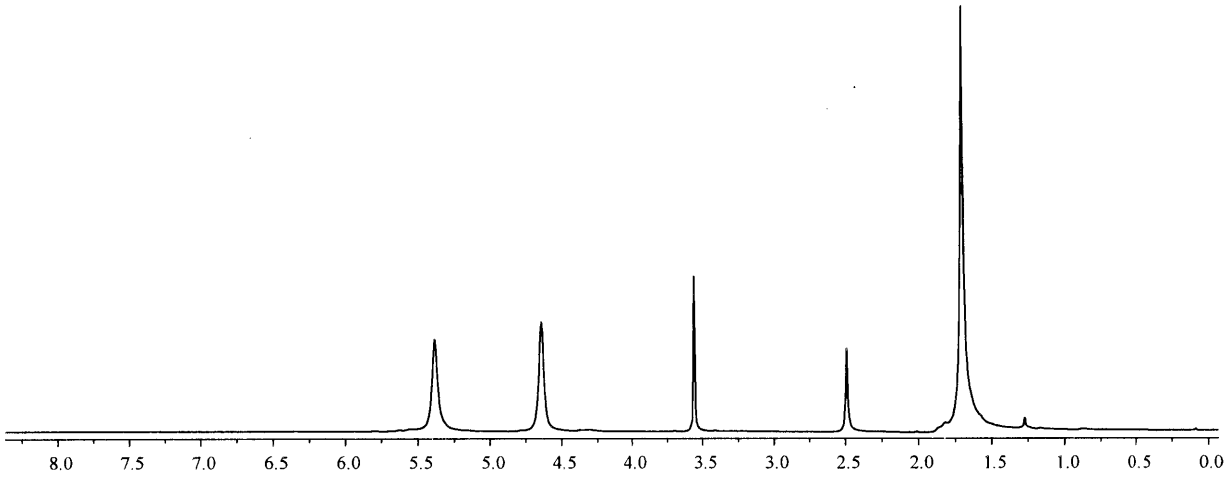

δ (ppm)

^{13}C NMR, THF-d_8, 125 MHz

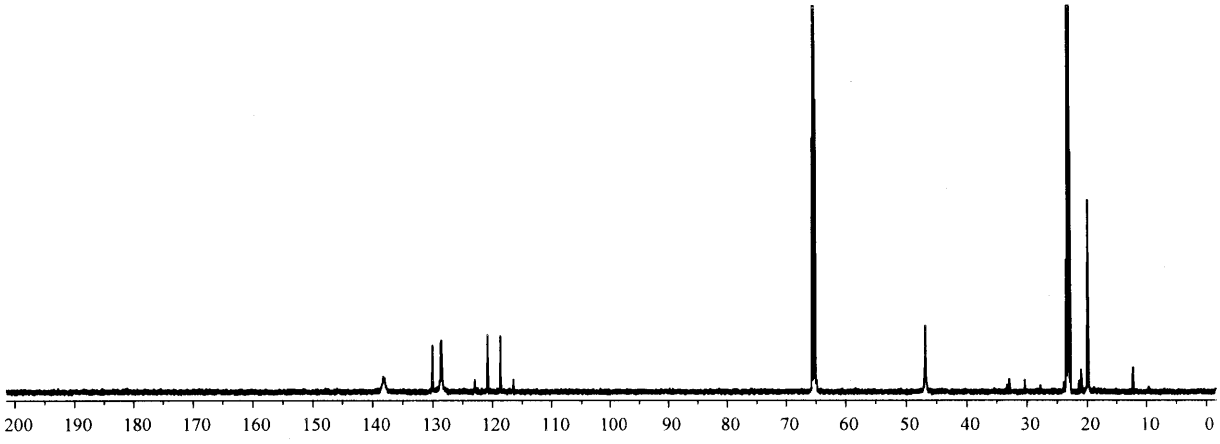

δ (ppm)

Poly(3e).

^{1}H NMR, $(CD_3)_2CO$, 500 MHz

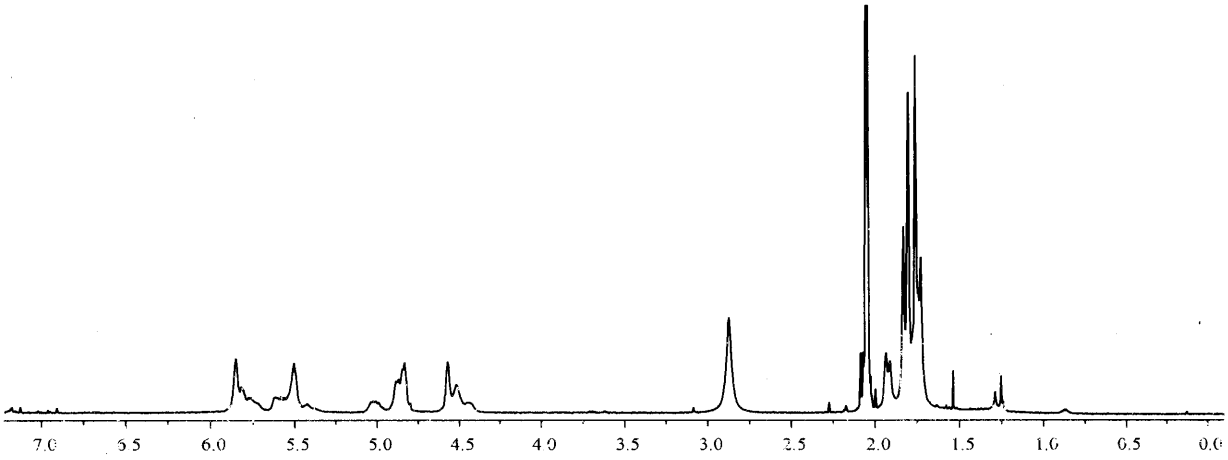

δ (ppm)

Poly(4a).

^{1}H NMR, $CDCl_3$, 500 MHz

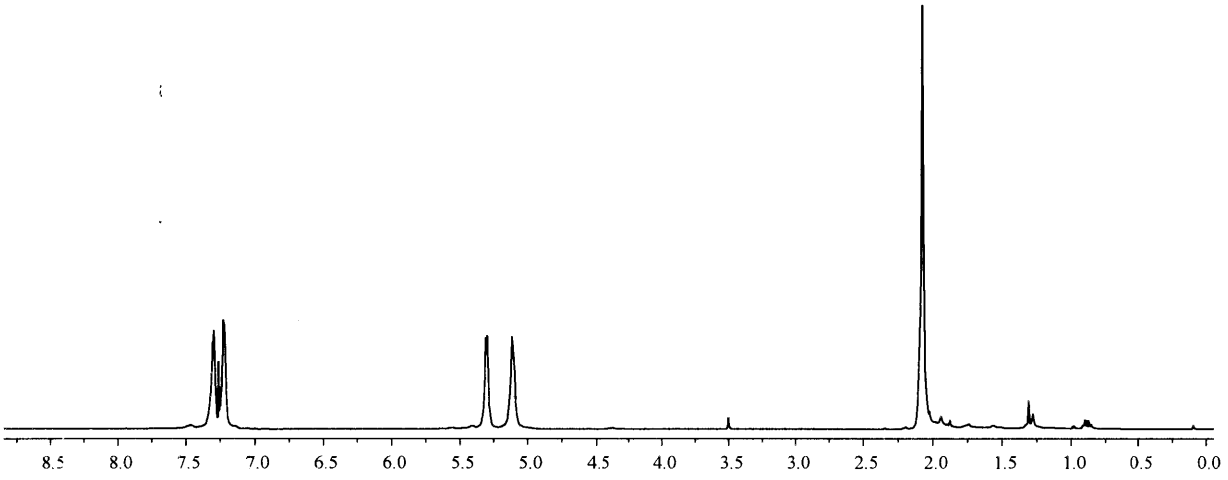

δ (ppm)

^{1}H NMR, $CDCl_3$, 500 MHz

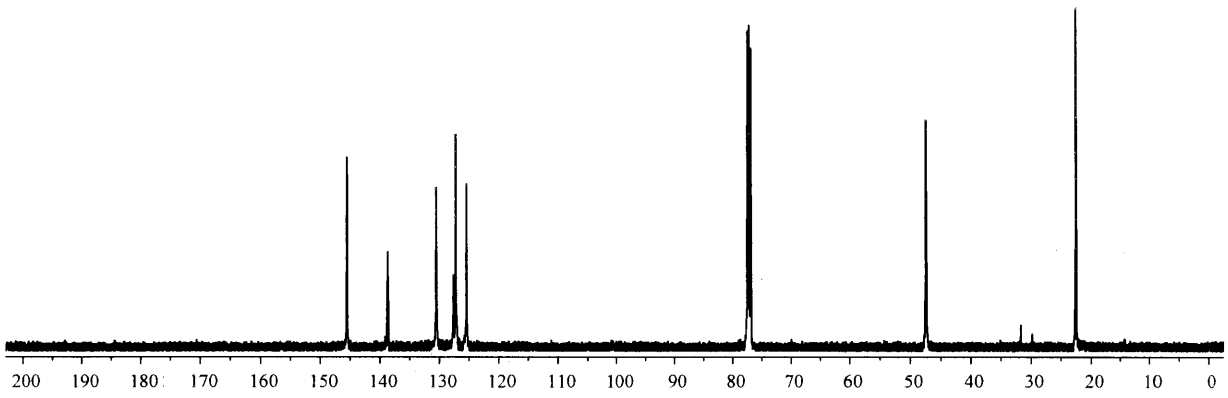

δ (ppm)

Poly(4b).

^{1}H NMR, $C_2D_2Cl_4$, 400 MHz

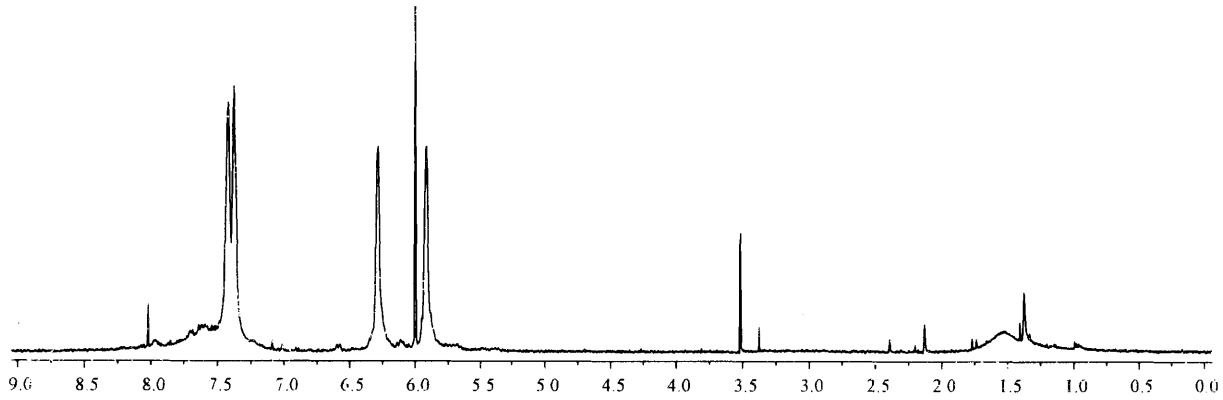

δ (ppm)

^{13}C NMR, $C_2D_2Cl_4$, 100.6 MHz

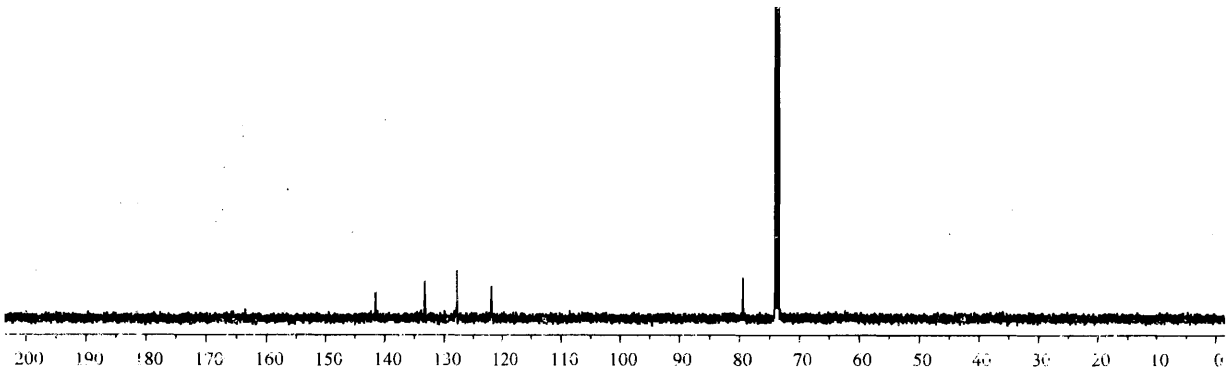

δ (ppm)

CHAPTER 3

Apparent Roughness as an Indicator of Deoxygenation of Graphene Oxide

This chapter was adapted and reprinted with permission from den Boer, D.*; Weis, J. G.; Zuniga, C. A.; Sydlik, S. A.; Swager, T. M.* "Apparent Roughness as Indicator of (Local) Deoxygenation of Graphene Oxide" *Chem. Mater.* **2014**, *26*, 4849–4855.

3.1 Introduction

Over a decade ago, the seminal report on the electronic characterization of single layer graphene[1] initiated a flurry of research activity as a result of graphene's potential applications in electronics, photovoltaics, energy storage, and chemical and biological sensing.[2–5] Graphene has been synthesized numerous ways, including mechanical exfoliation, liquid-phase exfoliation, chemical vapor deposition, SiC-sublimation, and bottom-up molecular assembly.[6,7] An alternative synthesis for applications that can tolerate residual defects is the thermal or chemical reduction of graphene oxide (GO) to generate electronically conductive materials.[8–12] Graphene oxide is synthesized in the reverse manner; graphite is chemically oxidized and subsequently exfoliated to form dispersions of GO. Depending on a variety of parameters, a continuum of degrees of oxygenation and functionalization can be obtained.

The most widely accepted structure of GO is the Lerf–Klinowski model, which consists of two distinct regions. The first is a densely functionalized and oxygenated region possessing predominantly sp^3-hybridized carbon atoms. Smaller graphenic regions with principally sp^2 character comprise the second, as shown in Figure 3.1.[13,14] Although more precise descriptions of the structure of **GO** are still debated in the literature,[8,10,11,14–16] it is undeniably a chemically complex — and probably chemically dynamic — material that possesses a panoply of oxygen-containing functional groups.

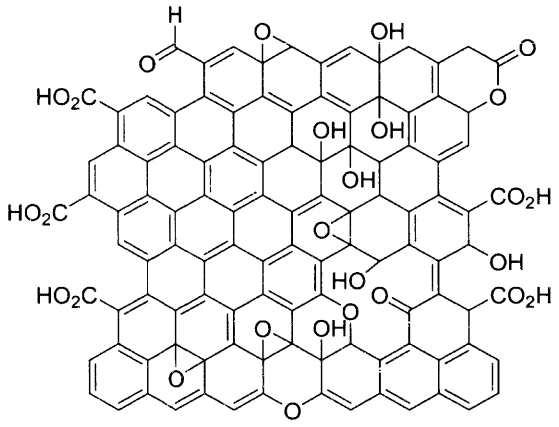

Figure 3.1. Modified Lerf–Klinowski model of GO.[13,14]

On the one hand, these oxygen-containing moieties impart solubility in various solvents[17] and can be exploited for installing functional groups to modulate the electrical and mechanical properties of the GO.[11,18–21] For example, our lab has reported GO's functionalization by carbon nucleophiles,[22] Claisen rearrangement,[23,24] and phosphates.[25] On the other hand, the complex chemistry typically leads to large batch-to-batch variations, resulting in differences even in the macroscopic oxygenation levels.[14] In addition to these difficulties in reproducibility, a key challenge for elucidating the exact structure of GO has been the difficulty of its characterization.[11,26] Therefore, it is important to explore additional tools for the study of this complex material. In this study, we report the use of scanning tunneling microscopy (STM) as a technique to distinguish between GO samples with varying levels of oxygenation or deoxygenation from the synthesis of less oxidized GO (**loGO**) and controlled reductions of conventionally synthesized GO.

The relatively planar nature of graphene oxide and its derivatives makes it suitable for characterization by scanning probe microscopy (SPM). The excellent spatial resolution of SPM techniques provides helpful insight into the nanoscale structure, which is essential for an

in-depth understanding of the process that occurs during (de)oxygenation and functionalization. Atomic force microscopy (AFM) is the most widely employed SPM technique for this type of research. In addition to topographic visualization, AFM allows the determination of the local friction,[27] conductivity,[27,28] and differences in the interaction of the sample with the cantilever, which manifest themselves in the phase image.[29,30] With these methods, AFM can be employed to acquire information on the chemical composition of the material of interest; however, in most cases, AFM analysis is limited to topographic imaging as a result of the difficulty in attaining very high spatial resolution. The limiting factor in these measurements is often the geometry of the tip. For the typical resolution observed with STM images, ultrahigh vacuum and/or tip functionalization (e.g., C≡O) is necessary.

In contrast, STM provides excellent spatial resolution as a result of the exponential dependence of tunneling current on distance. Furthermore, STM has been utilized only sparingly for the analysis of GO and its deoxygenated derivatives. Graphene oxide,[29–34] reduced graphene oxide (rGO),[30,34] and partially reduced graphene oxide (prGO)[35] have been characterized by STM at different levels of detail, in different environments. For example, STM measurements can be performed under ultrahigh vacuum or ambient conditions and with different base surfaces. Generally, these STM measurements vary substantially, and it is difficult to draw conclusions from the often subtle differences in the STM topographic measurements of GO-related materials. In this context, studies with more than one or two different types of GO or (p)rGO must be carried out. Although there has been some effort in this direction,[35] batch-to-batch reproducibility[16,18,36] and the present state of STM topographic characterization falls short of distinguishing different GO derivatives. In order to extract

meaningful and reliable data from the samples, we therefore introduce the analysis of the "apparent roughness" and use STM as a characterization tool for GO and its reduced forms.

Scanning tunneling microscopy has proven a valuable tool for determining the roughness of surfaces.[37–39] In most cases, however, the studied surfaces have been homogenous and exhibited uniform characteristics. For surfaces with electronic heterogeneity (e.g., GO), it is important to note that the topographic STM images are a convolution of the geometric features on the surface and their local electronic properties.[40,41] As a result, we measure the "apparent roughness" for heterogeneous surfaces and emphasize its dependence on both the local topographic and electronic properties. To quantify the apparent roughness, we apply the root-mean-square (RMS) roughness, R_q, as defined in Equation 1. R_q represents the standard deviation of the distribution of surface heights.[42] Consequently, the R_q is more sensitive to large deviations from the RMS mean line than the arithmetic average height (R_a), which is defined as the average absolute deviation of irregularities from the mean line (Equation 2).

$$R_q = \sqrt{\frac{1}{l}\int_0^l \{y(x)\}^2 dx} \quad (1)$$

$$R_a = \frac{1}{l}\int_0^l |y(x)| dx \quad (2)$$

Recent calculations, along with chemical intuition, suggest that graphene becomes less planar with increasing oxidation, as a result of the conversion from sp^2 to sp^3 carbon atoms.[43–45] This roughening of the surface upon oxidation, in comparison to a pristine graphene layer, has been observed experimentally in a qualitative manner.[17,30,46,47] Calculations[45] and experiments[47] further suggest that this roughening is reversible; upon deoxygenation of GO to rGO, the surface roughness should be reduced.

Graphene oxide in its highly oxidized form is an insulating material. Upon reduction to rGO, it partially recovers graphene-like conductive properties.[8] Differences in the planarity and conductivity of GO, prGO, and rGO will have an effect on the apparent roughness, which suggests that apparent roughness can provide valuable information about the material including its level of deoxygenation.

In addition to characterization, SPM techniques enable the manipulation of GO and rGO at the nanoscale by inducing a change in the local chemical structure of the material. These local manipulations open up applications in graphene nanoelectronics.[27] In recent years, AFM has been employed to locally reduce GO by using a heated tip,[27] an applied bias voltage,[28,48] or a Pt-covered tip in a hydrogen atmosphere.[49] In the reverse manner, pristine graphene has been locally oxidized with an applied bias voltage on the AFM tip.[50] AFM has also been employed for local lithography by removing sections of flakes.[51] Although STM has been applied for the local lithography of graphene[52,53] and GO,[34] it has not been used for the study of the local reduction of GO to rGO or prGO.

We analyze the apparent roughness of macroscopically chemically reduced GO flakes, with different levels of deoxygenation. Comparisons can then be made with locally manipulated GO flakes obtained by direct reduction from GO to prGO or rGO by STM. We determined that inducing the reduction by applying a negative bias voltage leads to a partial return to planarity of the GO, the extent of which is controlled by the bias voltage. This demonstration illustrates the possibility of using STM for local manipulation and analysis of a GO surface.

3.2 Results and Discussion

3.2.1 Synthesis of Materials

Graphene oxide (**GO**) was synthesized using a modified Hummer's method.[54] In order to examine the effect of deoxygenation on GO by AFM and STM, two partially reduced GOs (**prGO2h** and **prGO4h**) and a heavily reduced GO (**rGO**) were prepared by reduction of **GO** with *l*-ascorbic acid.[55] We also examined a less oxidized graphene oxide (**loGO**) made from 1:1 ratio of oxidant to graphite, in contrast to the conventional 3:1 ratio. The prepared materials were examined by X-ray photoelectron spectroscopy (XPS) to determine the relative atomic percentages of carbon and oxygen. These differences are summarized in Table 3.1. Conventionally prepared **GO** possesses the highest oxygen content (29.0%) while **loGO** displays moderately lower oxygen content (23.9%). The partial reductions of **GO** at 2 and 4 h lowered the oxygen content by 5 and 7 %, respectively, relative to **GO**. The fully reduced GO possessed the lowest oxygen content with a 12.3% reduction, resulting in more than a 50% decrease in the O/C value.

	O 1s (atomic %)	C 1s (atomic %)	O/C
loGO	23.9	76.1	0.31
GO	29.0	71.0	0.41
prGO2h	24.0	76.0	0.32
prGO4h	22.0	77.9	0.28
rGO	16.7	83.3	0.20

Table 3.1. Relative atomic percentages of O 1s and C 1s, determined by X-ray photoelectron spectroscopy (XPS). Spectra are displayed in Figure 3.7 in the appendix of this chapter.

3.2.2 AFM Studies

A drop of a solution containing the graphitic material was applied to a freshly cleaved highly oriented pyrolytic graphite (HOPG) surface, which exhibits a very low roughness, as expected. The high affinity of the GO π–π stacking to the graphite affixes the samples adequately for imaging by SPM. Regardless of how well surface roughness can be correlated to (de)oxygenation by AFM alone, AFM measurements were necessary to determine the density of the flakes on the surface prior to STM measurements, as shown in Figure 3.2.

A sufficiently high surface coverage of graphene flakes is necessary as a result of the limited working scanning range of the STM. In this context the insolubility of **rGO** in water proved problematic and required prolonged sonication times to generate dispersions of **rGO** in NMP that were sufficiently concentrated for STM imaging. Attempts to solubilize **rGO** with water, DMF, or other common organic solvents were unsuccessful. The average flake size of **rGO** samples was also smaller than the less reduced compounds, as measured by AFM. It is important to note that this generalization is complicated by a large variation in flake sizes with a standard deviation of approximately 100%. For **rGO**, the average flake size was ~1.0×10^4 nm^2; for **prGO2h** ~1.6×10^4 nm^2; for **prGO4h** ~2.0×10^4 nm^2; for **loGO** ~4.0×10^4 nm^2; and for **GO** ~1.5×10^5 nm^2, based on analysis of at least 100 flakes per compound. This trend suggests reductive fragmentation of the flakes. An interesting observation is the significant difference in the size of the **GO** and **loGO** flakes. Increasing oxygenation of the graphite should result in smaller platelets; however, the observation that the **GO** flakes are larger is likely a matter of solubility. Considering that **loGO** has fewer solubilizing groups than **GO**, only the smaller flakes of **loGO** would be soluble enough in water for sample preparation.

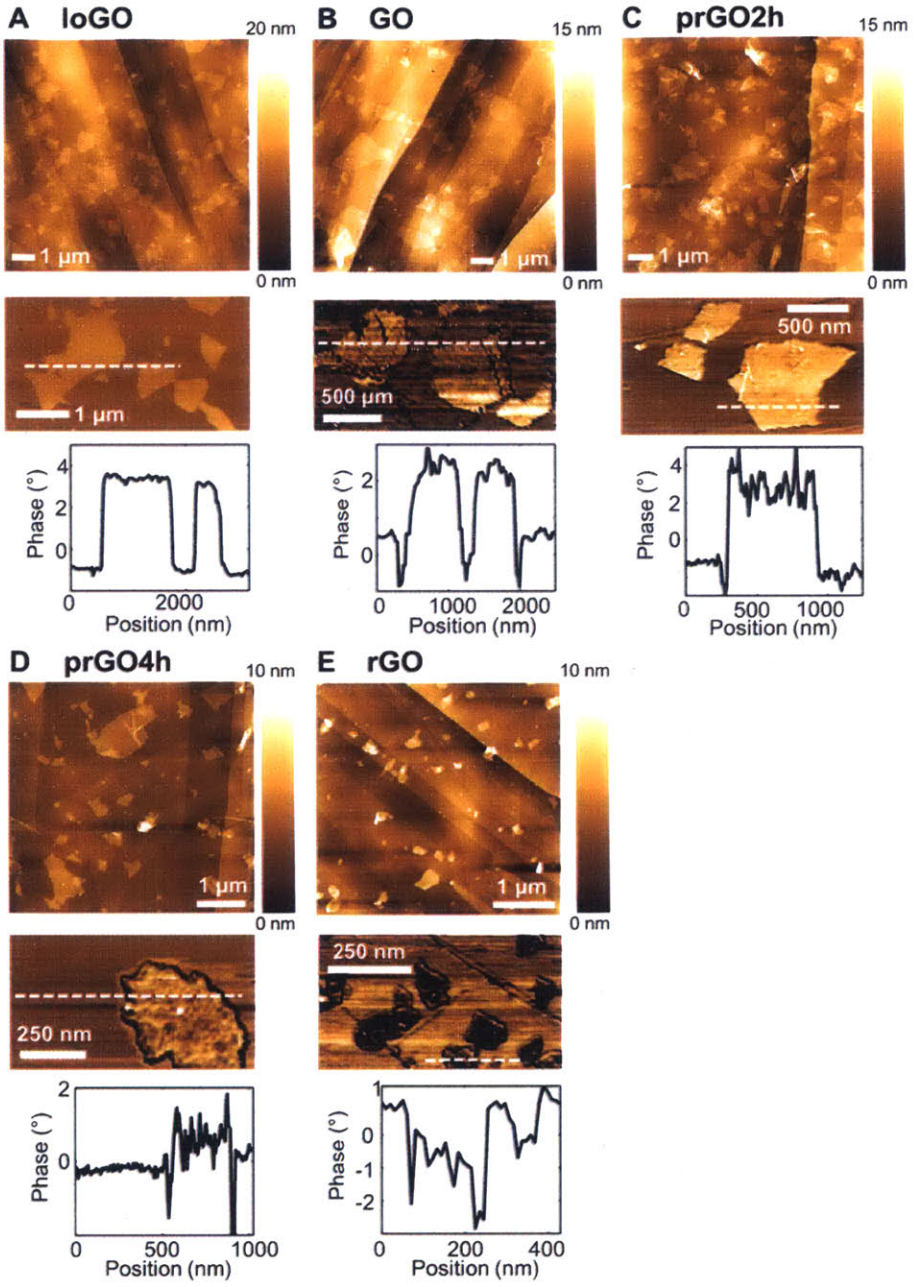

Figure 3.2. AFM images of graphene oxide flakes at varying degrees of (de)oxygenation at the HOPG / air interface after dropcasting. Top: AFM topographic images; center: AFM phase images; bottom: line profiles of the corresponding phase image. a) Less oxidized graphene oxide (**loGO**) deposited from H_2O. b) Graphene oxide (**GO**) deposited from H_2O. c) Partially reduced graphene oxide, after 2 h of reduction (**prGO2h**), deposited from H_2O. d) Partially reduced graphene oxide, after 4 h of reduction (**prGO4h**), deposited from H_2O. e) Fully reduced graphene oxide (**rGO**) deposited from NMP.

Attempts to determine the roughness R_q by AFM were unsuccessful, as the analysis yielded an $R_q = 0.10 - 0.15$ nm, implying that there is no difference between the different types of flakes. This lack of sensitivity to roughness can most likely be ascribed to the large AFM tip radius (>5 nm).[56,57] STM has an advantage over AFM with respect to spatial resolution as a result of the exponential dependence of tunneling current on distance.

In AFM imaging, phase-contrast images typically produce greater detail about rough surfaces than topographic imaging. In tapping mode, the phase-contrast image is generated by measuring the phase difference between the AFM cantilever's oscillations and the standard signal.[58] The mechanical and chemical properties of the surface influence the interaction between the tip and sample, and these interactions ultimately dictate the phase contrast. It has been shown that GO displays a larger phase contrast with the underlying graphite in AFM measurements,[17,29] relative to that observed for rGO. We also have observed this effect, and the **GO** flakes were easily distinguished from the HOPG background in phase measurements. For **loGO**, **GO**, and **prGO2h**, the phase difference is about 3–4° with respect to the underlying graphite (Figure 3.2a,b,c), consistent with values of 2.5° and 5.5° previously observed for **GO** on graphite,[17,29] and ±1° for **prGO4h** and **rGO** (Figure 3.2d,e). We were, however, unable to use these values to reproducibly distinguish between gradations of deoxygenation.

3.2.3 STM Studies and Apparent Roughness

After we verified a sufficient density of flakes on the surface with AFM, the isolated flakes were studied by STM, as shown in Figure 3.3. The measurements were acquired at V_{bias} = +1 V (of the surface with respect to the tip) and an I_{set} of several pA. With these scanning

parameters, all of the different flake types were stable, and it was possible to monitor individual flakes for more than 48 hours.

Scanning at negative voltages typically led to unstable measurements. A **GO** flake that had been monitored for over 20 h at +1 V fragmented into smaller pieces within several minutes after the V_{bias} was shifted to −1 V. For larger flakes, it was possible to scan at −1 V without flake fragmentation, as long as the scan range was smaller than the flake (see local manipulation section below). It is possible that the distance between the tip and graphitic material is too small at these settings, and the flakes are pushed aside and broken apart. As previously observed with pristine graphene,[59] the various flakes in this study are all flexible and conform to the underlying HOPG surface, as can be seen in Figure 3.3a,c,f, where the flakes lie on a step-edge on the HOPG surface. In line with this flexibility, flakes are also observed to possess folds (Figure 3.3d, bottom) and partly overlap with neighboring flakes (Figure 3.3a bottom and c bottom).

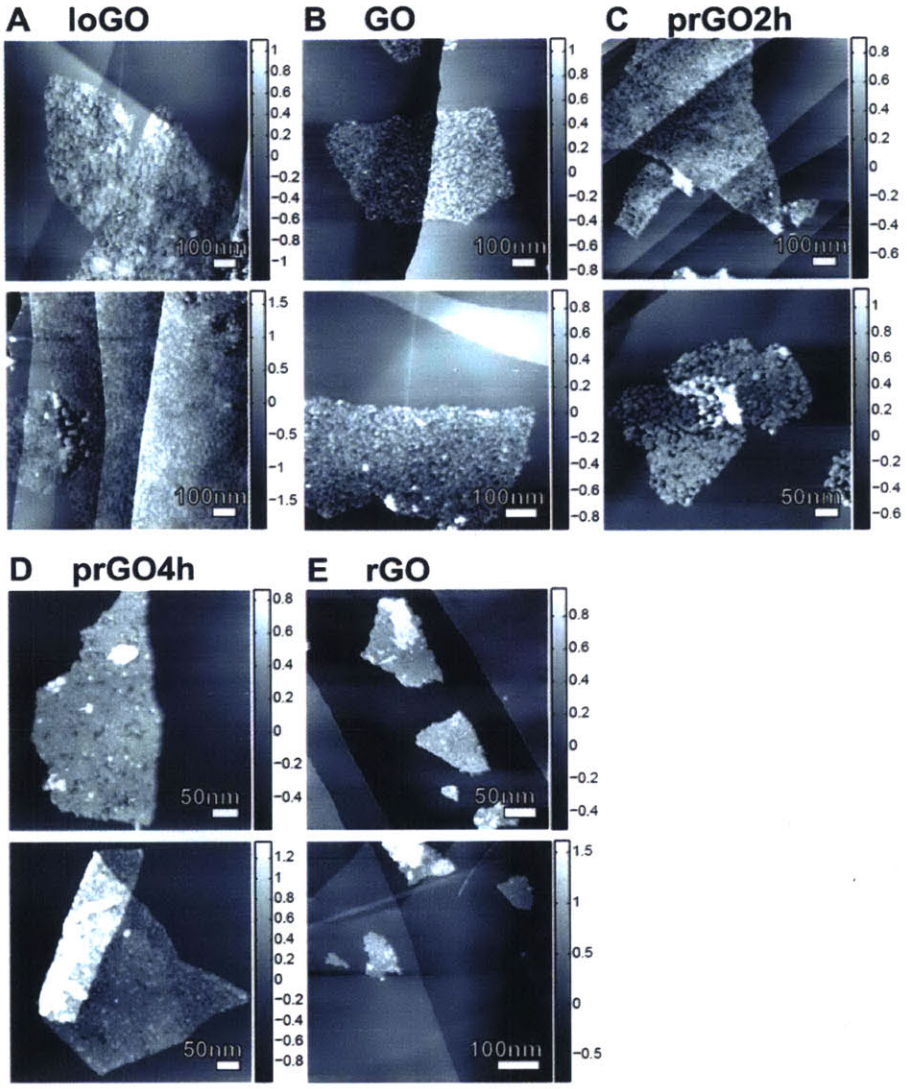

Figure 3.3. STM topographic images of graphene oxide flakes at varying degrees of (de)oxygenation at the HOPG / air interface. The depicted z scale bars are in nm. V_{bias} = +1 V, I_{set} = 2–5 pA. a) **loGO** deposited from H_2O. b) **GO** deposited from H_2O. c) **prGO2h** deposited from H_2O. d) **prGO4h** deposited from H_2O. e) **rGO** deposited from NMP.

The measurements of **GO** (Figure 3.3b) show a surface with small granular domains, different than what was found in some reports,[29,32] but similar to other observations in the literature.[30,34,35] The granular domains are consistent with a clustering of the oxygen functional groups. Previous studies suggest that defects in graphene — e.g., oxygen-containing functional

groups — increase the local reactivity of the basal plane, driving the formation of domains.[44] This model is also consistent with the apparent topographic signature of **loGO** (Figure 3.3a), wherein domains are present, but do not cover the entirety of the flake.

These differences between the different types of GO materials in the STM topographic images are small. Consequently, it is challenging to distinguish the results of **loGO** (Figure 3.3a), **GO** (Figure 3.3b), and **prGO2h** (Figure 3.3). The more reduced materials, **prGO4h** (Figure 3.3d) and **rGO** (Figure 3.3e), appear different from the more heavily oxidized flakes and have similarly smooth surfaces. The observed difference between **prGO2h** and **prGO4h** is surprising, as there is only a small diffference in the O/C ratio (0.31 vs. 0.28), as determined by XPS. STM images of **prGO2h** are similar to the moderately reduced flakes observed in the literature,[35] but images of the more fully reduced **prGO4h** and **rGO** appear (by qualitative visual examination) to be smoother than the published heavily reduced materials.[30,35] To establish a quantitative correlation between planarity and deoxygenation, we analyzed the apparent roughness of the different types of flakes (Figure 3.4). The apparent roughness was determined at the same bias voltage for all flakes, +1 V, at a current of several pA, for $n > 9$ flakes. To check against artifacts introduced by the tip, each sample was measured with at least two different STM tips, and there were no differences observed between the different tips. To further mitigate the introduction of artifacts, all measurements were subjected to idential image processing. Areas were selected from STM images with the same pixels/nm^2. To decouple the long-range waviness from the short-range roughness,[60] we subjected the measurements to an ISO 16610-61 L-Filter.

We measured several GO flakes for long periods of time (n = 3, for 3, 16, and 20 h) and compared the apparent roughness of the same area before and after this time interval. We

found that the difference remained below 5%, which is well within the observed flake-to-flake variation of ~10%. Within a flake, this difference remained below 6%, as determined by comparing four different sections of three flakes. We observed that the roughness has a dependance on bias voltage, with negative voltages (<−1 V) typically exhibiting slightly lower (~8%) roughness over the same area measured with a positive voltage (+1 V). This difference is probably related to the apparent roughness' dependence on the local electronic properties of the surface.

The values of the apparent R_q for **GO** (0.28 ± 0.03 nm) is considerably higher than for **rGO** (0.12 ± 0.03 nm), and decreasing apparent roughness correlates with increasing deoxygenation, as was previously predicted by theory.[45] A surprising result is the value of **loGO** compared to **GO**. At first, it would seem that with increasing oxygenation, the graphene should become less planar (increased roughness),[43–45] which contradicts this experimental observation. This effect can be rationalized after considering that the clustering or the oxygen functionality creates what may be better understood as defined hills and valleys. In the case of a more completely covered **GO** surface, the valleys are narrowed sufficiently to a point wherein they are not contributing to the roughness. In **loGO**, however, they are readily imaged and therefore contribute more to the roughness. Also, it is important to remember that the STM measures apparent roughness (a convolution of topographic and electronic properties). Completely oxygenated **GO** is probably less heterogeneous in its electronic properties than loGO.

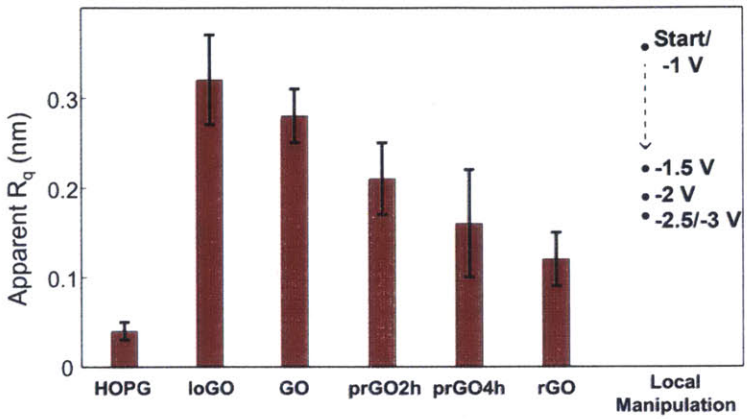

Figure 3.4. Apparent RMS roughness, R_q, of graphene oxide flakes at different degrees of oxygenation and deoxygenation on HOPG, as determined by topographic STM measurements. For every bar, n = 9–11 flakes, and error bars represent the standard deviation. All measurements were obtained with at least 2 different STM tips. V_{bias} = +1 V, I_{set} = 2–5 pA. Indicated on the right is the apparent roughness that was found for experiments with local manipulation (see Figure 3.5), in which areas of the surface of **loGO** were scanned at the indicated voltage.

Another striking difference is between **loGO** and **prGO2h**. While these compounds have nearly identical O:C ratios, the roughness of **prGO2h** is considerably lower. This observation illustrates the differences present between samples that may have similar oxygenation levels but are prepared by direct partial oxygenation of graphite or by the reductive deoxygenation of heavily oxidized graphene oxide.

Figure 3.4 shows the apparent R_q, the RMS roughness, which is more sensitive to peaks and valleys than the average roughness, R_a.[42] The average roughness — defined as the average absolute deviation of the roughness irregularities from the mean (Equation 2) — does, however, display the same trends with more deoxygenated materials having lower apparent R_a (Figure 3.9).

3.2.4 Local Manipulation Induced by STM

There are examples of oxygenated graphene being locally reduced by AFM; however, previous attempts at local reduction of GO by STM led to etching and degradation of the GO. Furthermore, STM has not been successful at visualizing the locally deoxygenated GO prior to this work. With respect to their electrochemical behavior, graphene oxide typically begins to exhibit cathodic reduction at approximately 700 mV (vs. Ag/AgCl), which has been attributed to oxygen-bearing functional groups.[61–63] Recently, a theoretical study suggested reduction of oxygenated graphene with negative voltages, wherein the electric field perpendicular to the surface dramatically weakened the oxygen–carbon bonds in epoxides.[64] These findings suggest that strong localized electric fields underneath the STM tip will facilitate cleavage of C–O bonds and consequently deoxygenate the oxygenated graphene.

Figure 3.5 shows a **loGO** flake that we used for the local manipulation. The measurements were performed at V_{bias} = +1 V and I_{set} = 2 pA. Under these conditions, **loGO** flakes are stable, as they can be monitored without any changes for over 10 hours. To locally reduce the material, the scan size was made smaller, and a negative voltage is applied for both an up and down scan with the STM, taking a period of approximately eight minutes. The scan size is subsequently increased, and the flake can be reimaged under the normal conditions with a positive bias voltage. Figure 3.5a and Figure 3.5b depict the result of scanning with V_{bias} = −2V. A clear, bright square has appeared on the flake where the negative voltage was applied. This increased brightness reflects the expected higher conductivity upon reduction. This procedure was performed for V_{bias} = −1 V, −1.5 V, −2 V, −2.5 V, and −3 V and reveals that for extensive reduction, bias voltages more negative than −1.5 V are required. Specifically, for V_{bias} = −1 V, no effect is observed, as seen in Figure 3.5f. For V_{bias} = −1.5 V, a subtle, bright

square is observed, whereas for $V_{bias} = -2$ V and more negative values, the bright conductive squares are prominent. Such experiments were not possible with smaller flakes, as they disintegrated at these negative voltages. Instability is also observed in the experiments performed on this large flake: the yellow, dotted lines in Figure 3.5a–e denote the edge of the flake before the square is scanned at −3 V (between Figure 3.5d and Figure 3.5e). A large section of the flake breaks off during this step, likely as a result of the large negative bias voltage applied.

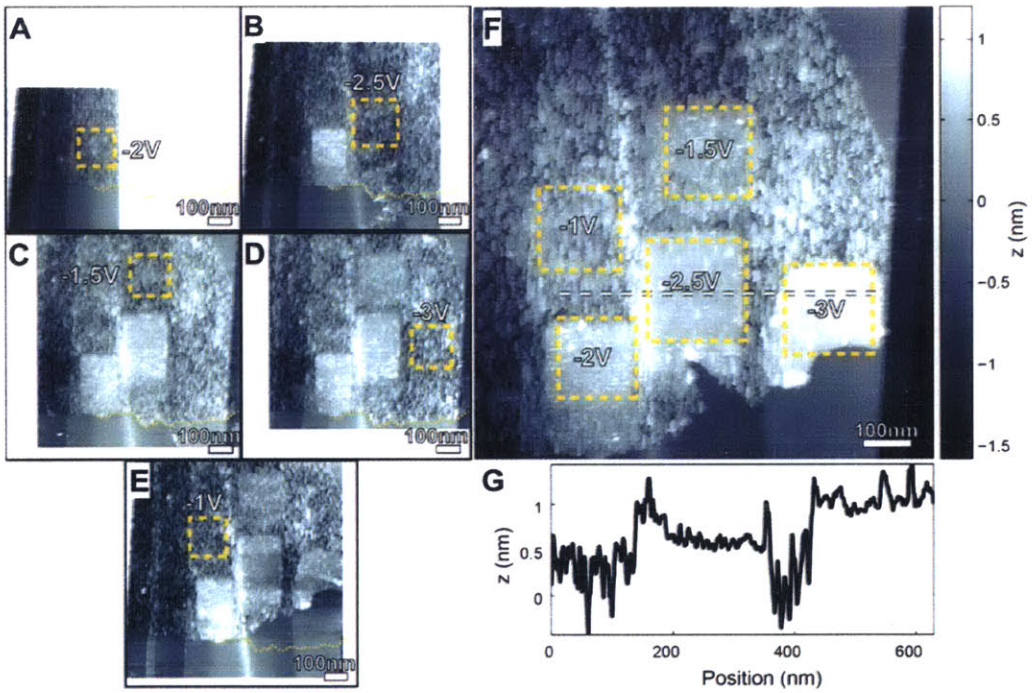

Figure 3.5. Local manipulation of **loGO** at the HOPG / air interface by STM. $V_{bias} = +1$ V, $I_{set} = 2$ pA. a–e) The yellow squares indicate the area that is scanned twice (once up and once down) at the specified negative voltage, with each scan taking ~ 4 min, for a total of ~ 8 min between the STM images that are shown. The yellow, dotted line in the lower right in images a–e is drawn as a guide for the edge of the flake, displaying the flake degrades during the local manipulation. f) The resulting flake after the local manipulation, with the yellow squares indicating the different voltages applied. g) Line profile corresponding to the dotted white line displayed in (f).

The apparent roughness of the areas reduced by STM scanning at negative voltages decreases significantly. Scanning at +1 V, we measure an apparent R_q of 0.36 nm. This value remains constant after scanning at −1 V but decreases by greater than 50% to 0.17 nm after scanning with a bias voltage of −2 V. After scanning with bias voltages of −2.5 V and −3 V, the apparent R_q drops to 0.13 nm. These values are indicated in the apparent R_q graph of the various GO materials in Figure 3.4. The final value of 0.13 nm strongly suggests a heavily deoxygenated graphene oxide material. An additional example of local manipulation of loGO can be found in Figure 3.10 in the appendix of this chapter.

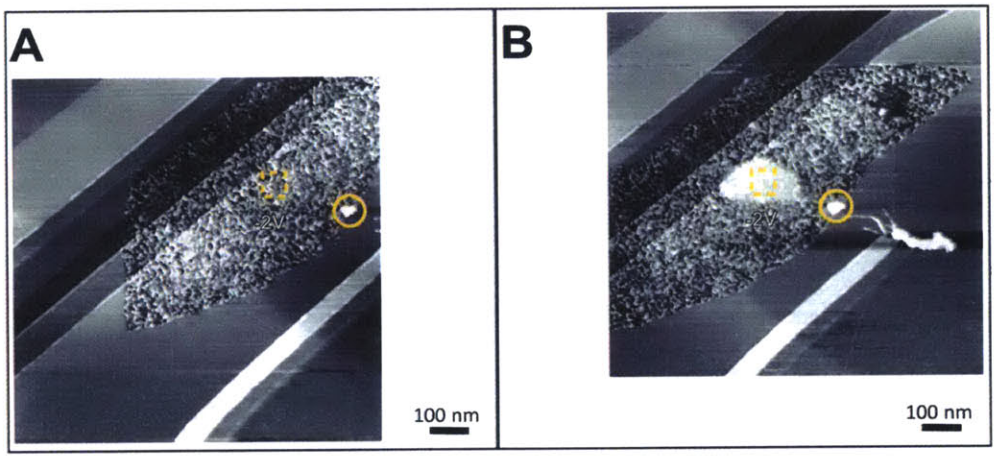

Figure 3.6. Local manipulation of **GO** by STM at the HOPG / air interface. V_{bias} = +1 V, I_{set} = 2 pA. The yellow squares indicate the area that has been scanned twice (up and down) at a V_{bias} = −2 V. Δt ~ 12 minutes. The yellow circle indicates a high feature that was used as a reference point. STM measurements are taken before (a) and after (b) the local manipulation.

The reduction was also successfully executed on **GO** (Figure 3.6), but similar experiments on **rGO** and **prGO4h** showed no modification of the graphene flakes. This finding is consistent with our hypothesis that the chemical change is the result of significant local reduction of the surface.

Consistent with theoretical predictions[64] and observations by conductive AFM,[28] applying a negative bias voltage induces the reduction of the GO surface. At higher positive voltages, no changes were observed. From our measurements, it is unclear if such a reduction occurs on one or both sides of the oxygenated graphene flakes. The applications of heterobifunctionalized, "two-faced" graphene are numerous, and the topic has received considerable attention.[21,65] As measurements were performed under ambient conditions, water is certainly present — as it can be difficult to remove even under more extreme conditions[66] — and expected to play a role in the reaction.

3.3 Conclusions

The exact structure of graphene oxide remains elusive as a result of the difficulty in characterizing it as a material. We have explored the use of the scanning tunneling microscope as an addition tool for the quantitative study of graphene oxide and measured this material at varying degrees of (de)oxygenation. Analyzing the apparent RMS roughness — "apparent" to emphasize that it is based on the apparent height in STM measurements, and therefore it is dependent on both electronic and geometrical properties of the surface — reveals the trend that with increasing deoxygenation, the apparent roughness is reduced. This correlation suggests that STM can also be used for the quantitative characterization of similar nanomaterials.

We demonstrated that STM can also be used for the local manipulation of GO. Applying a negative bias voltage creates locally deoxygenated, conductive areas with a concomitant reduction in apparent R_q. A sufficiently large, negative voltage was required: for positive voltages and with $V_{bias} = -1$V, no effect was observed, experimentally confirming what was theoretically predicted.

Although this analytical technique that employs the analysis of roughness cannot supplant other common characterization techniques, it can serve as a useful supplement to the techniques currently available for the study of GO and related materials. Our findings are not limited to the deoxygenation of GO, as covalent functionalization also affects the roughness and electronic homogeneity of graphene and other planar nanomaterials.

3.4 Acknowledgements

The authors would like to thank Dr. Elizabeth Shaw of the Surface and Scanning Probe Microscopy Laboratories at the MIT Center for Materials Science and Engineering (CMSE) for useful discussions on the XPS analyses.

3.5 Experimental Details

3.5.1 General

All reagents were purchased from Sigma–Aldrich unless otherwise noted.

X-ray photoelectron spectroscopy (XPS) was performed on a Versaprobe II X-ray photoelectron spectrometer from Physical Electronics with a monochromated Al Kα X-ray source (1486.6 eV) and operated at a base pressure of 1×10^{-9} Torr during the XPS analysis. The scans were made with a 200 μm size beam with a take-off angle of 45° and a total power of 45.7 W. The XPS spectra were analyzed using CasaXPS software to determine the relative atomic percentages of carbon and oxygen present in the samples.

3.5.2 Synthesis of loGO, GO, prGO2h, prGO4h, and rGO

Graphene oxide (**GO**) and less oxidized graphene oxide (**loGO**) were synthesized via a modified Hummer's method.[54] Briefly, graphite powder (325 mesh, Alfa Aesar) was added to concentrated sulfuric acid cooled to < 5 °C. Potassium permanganate (in a 3:1 weight ratio to graphite for **GO** or in a 1:1 weight ratio to graphite for **loGO**) was added slowly to the

cooled mixture. After stirring for four hours, chilled deionized water (500 mL) was added slowly producing an exothermic reaction. 30% hydrogen peroxide (in 3:1 volume to weight ratio of peroxide to permanganate) and additional deionized water (500 mL) were added. After several hours of stirring, the solids were isolated by centrifugation and washed with 10% hydrochloric acid followed by neutralization with copious washings with deionized water. The solids were dialyzed against deionized water for one week and subsequently lyophilized to obtain graphite oxide (golden brown colored) and less oxidized graphite oxide (dark brown colored). The resulting graphite oxides were exfoliated with sonication and dispersed into deionized water to produce dispersions of **GO** or **loGO**.

Partial reductions of GO (**prGO2h** and **prGO4h**) were carried out by addition of *l*-ascorbic acid to a 1 mg/mL dispersion of GO in water at 50 °C in 3:4 weight ratio of acid to **GO**. After two hours, half of the solution was removed and washed with copious amounts of deionized water. To the remaining half of the solution, an additional and equal portion of *l*-ascorbic acid was added. After an additional two hours the remaining solution was washed with copious amounts of deionized water. The **prGO2h** and **prGO4h** solids were dried by lyophilization.

Fully reduced **rGO** was produced by the addition of l-ascorbic acid to a 1 mg/mL dispersion of GO in water in a 10:1 weight ratio of acid to **GO**. The resulting flocculated black solids were washed with copious amounts of deionized water and dried by lyophilization.

3.5.3 AFM and STM Measurements

AFM and STM images were obtained with an Agilent 5100. Vibration isolation was provided by a bungee system enclosed in a chamber with multiple layers of sound-damping materials for acoustic isolation. AFM was performed in ACAFM tapping mode using silicon

tips with a force constant of 20 – 80 N/m. STM was performed in the constant current mode with mechanically cut tips from Pt/Ir wires (80:20) with a diameter of 0.25 mm. The graphite used as the sample surface was HOPG ZYB (NT-MDT) and was freshly cleaved with tape before each experiment. Measurements were performed at the HOPG / air interface under ambient conditions (22 ± 1 °C, 50 ± 8% relative humidity). V_{bias} values mentioned in the manuscript refer to the surface, with respect to the STM tip.

Graphitic samples were suspended in water (**loGO**, **GO**, **prGO2h**, **prGO4h**) or *N*-methyl-2-pyrrolidone (NMP) (**rGO**) at a concentration of 0.1 mg/mL and sonicated for 1–10 min using a bath sonicator. A volume of 40–100 µL of the resulting dispersion was then dropcasted onto a freshly cleaved HOPG surface, and the solvent was evaporated in a vacuum desiccator before imaging with AFM and then STM. A piece of HOPG was never used for more than one type of graphene oxide material in order to prevent cross-contamination.

The topographic measurements depicted in the manuscript were subjected to background correction (plane : flatten), and a 3 × 3 median filter was applied.

3.5.4 Apparent Roughness Analysis

For the analysis of the apparent roughness, we used Scanning Probe Image Processor (SPIP) software (Image Metrology ApS). The topographic images were all background corrected and the same filters were applied for all measurements, in the same order. All these procedures are built in the software. The applied procedures (in order) were as follows: Plane Correct: Global leveling; Filter: Spikes – medium; Filter: Streaks – thin bright; Plane Correct Linewise Leveling; Filter 1.0 µm: ISO 16610-61 L-Filter; Filter: Median 3 × 3 weak.

For the analysis, parts of the flakes were selected that did not cross a step and were not part of a double layer. Such areas were chosen as large as possible (from larger STM images

with approximately 1 pixel/nm^2). As there were different flake sizes, this method led to more area being used for some of the flakes compared to others. The average sizes of the areas used for the analyses were 5×10^4 nm^2 for **GO**, 5×10^4 nm^2 for **loGO**, 2×10^4 nm^2 for **prGO2h**, 1×10^4 nm^2 for **prGO4h** and 2.5×10^3 nm^2 for **rGO**. As **rGO** had the smallest flake sizes, it therefore also had the smallest areas usable for the apparent roughness analysis. The analysis was repeated by selecting areas of this smaller area (2.5×10^3 nm^2) for all the materials to exclude the possibility that our observations were due to this difference in areas. These smaller areas were selected by a square box as much in the center of the flake as possible, not crossing a step and on a single layer of the flake. The results of this analysis are depicted in Figure 3.9b and c. These graphs show the same trend (decreasing apparent roughness as a function of deoxygenation) as the graph for the apparent R_q (Figure 3.4).

3.6 References

(1) Novoselov, K. S.; Geim, A. K.; Morozov, S. V; Jiang, D.; Zhang, Y.; Dubonos, S. V; Grigorieva, I. V; Firsov, A. A. *Science* **2004**, *306*, 666–669.

(2) Biswas, C.; Lee, Y. H. *Adv. Funct. Mater.* **2011**, *21*, 3806–3826.

(3) Jariwala, D.; Sangwan, V. K.; Lauhon, L. J.; Marks, T. J.; Hersam, M. C. *Chem. Soc. Rev.* **2013**, *42*, 2824–2860.

(4) Du, J.; Pei, S.; Ma, L.; Cheng, H. M. *Adv. Mater.* **2014**, *26*, 1958–1991.

(5) Savage, N. *Nature* **2012**, *483*, S30–S31.

(6) Novoselov, K. S.; Fal'ko, V. I.; Colombo, L.; Gellert, P. R.; Schwab, M. G.; Kim, K. *Nature* **2012**, *490*, 192–200.

(7) Avouris, P.; Dimitrakopoulos, C. *Mater. Today* **2012**, *15*, 86–97.

(8) Park, S.; Ruoff, R. S. *Nat. Nanotechnol.* **2009**, *4*, 217–224.

(9) Paredes, J. I.; Villar-Rodil, S.; Solís-Fernández, P.; Fernández-Merino, M. J.; Guardia, L.; Martínez-Alonso, A.; Tascón, J. M. D. *J. Alloys Compd.* **2012**, *536*, S450–S455.

(10) Pei, S.; Cheng, H. M. *Carbon* **2012**, *50*, 3210–3228.

(11) Chen, D.; Feng, H.; Li, J. *Chem. Rev.* **2012**, *112*, 6027–6053.

(12) Ha, D. H.; Jung, S.; Kim, H.-J.; Kim, D.; Kim, W.-J.; Yi, S. N.; Jun, Y.; Yun, Y. J. *Synth. Met.* **2015**, *204*, 90–94.

(13) Lerf, A.; He, H.; Forster, M.; Klinowski, J. *J. Phys. Chem. B* **1998**, *102*, 4477–4482.

(14) Dreyer, D. R.; Todd, A. D.; Bielawski, C. W. *Chem. Soc. Rev.* **2014**, *43*, 5288–5301.

(15) Compton, O. C.; Nguyen, S. T. *Small* **2010**, *6*, 711–723.

(16) Dimiev, A.; Kosynkin, D. V.; Alemany, L. B.; Chaguine, P.; Tour, J. M. *J. Am. Chem. Soc.* **2012**, *134*, 2815–2822.

(17) Parades, J. I.; Villar-Rodil, S.; Martínez-Alonso, A.; Tascón, J. M. D. *Langmuir* **2008**, *24*, 10560–10564.

(18) Dreyer, D. R.; Park, S.; Bielawski, C. W.; Ruoff, R. S. *Chem. Soc. Rev.* **2010**, *39*, 228–240.

(19) Zhu, Y.; Murali, S.; Cai, W.; Li, X.; Suk, J. W.; Potts, J. R.; Ruoff, R. S. *Adv. Mater.* **2010**, *22*, 3906–3924.

(20) *Graphene Nanoelectronics*; Raza, H., Ed.; Springer, 2012.

(21) Swager, T. M. *ACS Macro Lett.* **2011**, 3–5.

(22) Collins, W. R.; Schmois, E.; Swager, T. M. *Chem. Commun.* **2011**, *47*, 8790–8792.

(23) Collins, W. R.; Lewandowski, W.; Schmois, E.; Walish, J.; Swager, T. M. *Angew. Chem. Int. Ed.* **2011**, *50*, 8848–8852.

(24) Sydlik, S. A.; Swager, T. M. *Adv. Funct. Mater.* **2013**, *23*, 1873–1882.

(25) Goods, J. B.; Sydlik, S. A.; Walish, J. J.; Swager, T. M. *Adv. Mater.* **2014**, *26*, 718–723.

(26) Allen, M. J.; Tung, V. C.; Kaner, R. B. *Chem. Rev.* **2010**, *110*, 132–145.

(27) Wei, Z.; Wang, D.; Kim, S.; Kim, S.; Hu, Y.; Yakes, M. K.; Laracuente, A. R.; Dai, Z.; Marder, S. R.; Berger, C.; King, W. P.; de Heer, W. A.; Sheehan, P. E.; Riedo, E. *Science* **2010**, *328*, 1373–1376.

(28) Mativetsky, J. M.; Treossi, E.; Orgiu, E.; Melucci, M.; Veronese, G. P.; Samorì, P.; Palermo, V. *J. Am. Chem. Soc.* **2010**, *132*, 14130–14136.

(29) Pandey, D. K., Chung, T. F.; Prakash, G.; Piner, R.; Chen, Y. P.; Reifenberger, R. *Surf. Sci.* **2011**, *605*, 1669–1675.

(30) Paredes, J. I.; Villar-Rodil, S.; Solís-Fernández, P.; Martínez-Alonso, A.; Tascón, J. M. D. *Langmuir* **2009**, *25*, 5957–5968.

(31) Gómez-Navarro, C.; Weitz, R. T.; Bittner, A. M.; Scolari, M.; Mews, A.; Burghard, M.; Kern, K. *Nano Lett.* **2007**, *7*, 3499–3503.

(32) Pandey, D.; Reifenberger, R.; Piner, R. *Surf Sci.* **2008**, *602*, 1607–1613.

(33) Kudin, K. N.; Ozbas, B.; Schniepp, H. C.; Prud'homme, R. K.; Aksay, I. A.; Car, R. *Nano Lett.* **2008**, *8*, 36–41.

(34) Solís-Fernández, P.; Paredes, J. I.; Villar-Rodil, S.; Guardia, L.; Fernández-Merino, M. J.; Dobrik, G.; Biró, L. P.; Martínez-Alonso, A.; Tascón, J. M. D.; Solís-

Fernández, P.; Paredes, J. I.; Villar-Rodil, S.; Guardia, L.; Fernández-Merino, M. J.; Dobrik, G.; Biró, L. P.; Martínez-Alonso, A.; Tascón, J. M. D. *J. Phys. Chem. C* **2011**, *115*, 7956–7966.

(35) Solís-Fernández, P.; Rozada, R.; Paredes, J. I.; Villar-Rodil, S.; Fernández-Merino, M. J.; Guardia, L.; Martínez-Alonso, A.; Tascón, J. M. D. *J. Alloys Compd.* **2012**, *536*, S532–S537.

(36) Jones, C. P.; Jurkschat, K.; Crossley, a.; Banks, C. E. *J. Iran. Chem. Soc.* **2008**, *5*, 279–285.

(37) Files-Sesler, L. A.; Randall, J. N.; Harkness, D. J. *J. Vac. Sci. Technol. B* **1991**, *9*, 659–662.

(38) Reiss, G.; Brückl, H.; Vancea, J.; Lecheler, R.; Hastreiter, E. *J. Appl. Phys.* **1991**, *70*, 523–525.

(39) Deng, J.; He, Y. F.; Ye, F.; Long, Q. Y.; Lung, C. W. *J. Phys. D. Appl. Phys.* **1999**, *32*, 45–48.

(40) Bai, C. *Scanning Tunneling Microscopy and Its Application*; Springer, 2000.

(41) Chen., C. J. *Introduction to Scanning Tunneling Microscopy*; Oxford University Press, 2008.

(42) Gadelmawla, E. S.; Koura, M. M.; Maksoud, T. M. A.; Elewa, I. M.; Soliman, H. H. *J. Mater. Process. Technol.* **2002**, *123*, 133–145.

(43) Liu, L.; Wang, L.; Gao, J.; Zhao, J.; Gao, X.; Chen, Z. *Carbon* **2012**, *50*, 1690–1698.

(44) Mehmood, F.; Pachter, R.; Lu, W.; Boeckl, J. J. *J. Phys. Chem. C* **2013**, *117*, 10366–10374.

(45) Sheka, E. F.; Popova, N. A. *Phys. Chem. Chem. Phys.* **2013**, *15*, 13304–13322.

(46) Mkhoyan, K. A.; Contryman, A. W.; Silcox, J.; Stewart, D. A.; Eda, G.; Mattevi, C.; Miller, S.; Chhowalla, M. *Nano Lett.* **2009**, *9*, 1058–1063.

(47) Gómez-Navarro, C.; Meyer, J. C.; Sundaram, R. S.; Chuvilin, A.; Kurasch, S.; Burghard, M.; Kern, K.; Kaiser, U. *Nano Lett.* **2010**, *10*, 1144–1148.

(48) Ekiz, O. O.; Ürel, M.; Güner, H.; Mizrak, A. K.; Dâna, A. *ACS Nano* **2011**, *5*, 2475–2482.

(49) Zhang, K.; Fu, Q.; Pan, N.; Yu, X.; Liu, J.; Luo, Y.; Wang, X.; Yang, J.; Hou, J. *Nat. Commun.* **2012**, *3*, 1194.

(50) Masubuchi, S.; Arai, M.; MacHida, T. *Nano Lett.* **2011**, *11*, 4542–4546.

(51) Vasić, B.; Kratzer, M.; Matković, A.; Nevosad, A.; Ralević, U.; Jovanović, D.; Ganser, C.; Teichert, C.; Gajić, R. *Nanotechnology* **2013**, *24*, 015303.

(52) Tapasztó, L.; Dobrik, G.; Lambin, P.; Biró, L. P. *Nat. Nanotechnol.* **2008**, *3*, 397–401.

(53) Biró, L. P.; Lambin, P. *Carbon* **2010**, *48*, 2677–2689.

(54) William S. Hummers, J.; Offeman, R. E. *J. Am. Chem. Soc* **1958**, *80*, 1339.

(55) Zhang, J.; Yang, H.; Shen, G.; Cheng, P.; Zhang, J.; Guo, S. *Chem. Commun.* **2010**, *46*, 1112–1114.

(56) Mannelquist, A.; Almqvist, N.; Fredriksson, S. *Appl. Phys. A Mater. Sci. Process.* **1998**, *66*, S891–S895.

(57) Méndez-Vilas, A.; Nuevo, M. J.; González-Martín, M. L.; Labajos-Broncano, L. *Mater. Sci. Forum* **2002**, *408-412*, 239–244.

(58) Pang, G. K. H.; Baba-Kishi, K. Z.; Patel, A. *Ultramicroscopy* **2000**, *81*, 35–40.

(59) Vallés, C.; Drummond, C.; Saadaoui, H.; Furtado, C. A.; He, M.; Roubeau, O.; Ortolani, L.; Monthioux, M.; Pénicaud, A. *J. Am. Chem. Soc.* **2008**, *130*, 15802–15804.

(60) De Oliveira, R. R. L.; Albuquerque, D. A. C.; Cruz, T. G. S.; Yamaji, F. M.; Leite, F. L. In *Atomic Force Microscopy - Imaging, Measuring and Manipulating Surfaces at the Atomic Scale*; Bellitto, V., Ed.; InTech, 2012; pp. 147–174.

(61) Zhou, M.; Wang, Y.; Zhai, Y.; Zhai, J.; Ren, W.; Wang, F.; Dong, S. *Chem. Eur. J.* **2009**, *15*, 6116–6120.

(62) Pumera, M. *Electrochem. Commun.* **2013**, *36*, 14–18.

(63) Toh, H. S.; Ambrosi, A.; Chua, C. K.; Pumera, M. *J. Phys. Chem. C* **2011**, *115*, 17647–17650.

(64) Topsakal, M.; Gürel, H. H.; Ciraci, S. *J. Phys. Chem. C* **2013**, *117*, 5943–5952.

(65) Toth, P. S.; Velický, M.; Ramasse, Q. M.; Kepaptsoglou, D. M.; Dryfe, R. A. W. *Adv. Funct. Mater.* doi: 10.1002/adfm.201500277.

(66) Temmen, M.; Ochedowski, O.; Schleberger, M.; Reichling, M.; Bollmann, T. R. J. *New J. Phys.* **2014**, *16*, 053039.

3.7 Appendix for Chapter 3

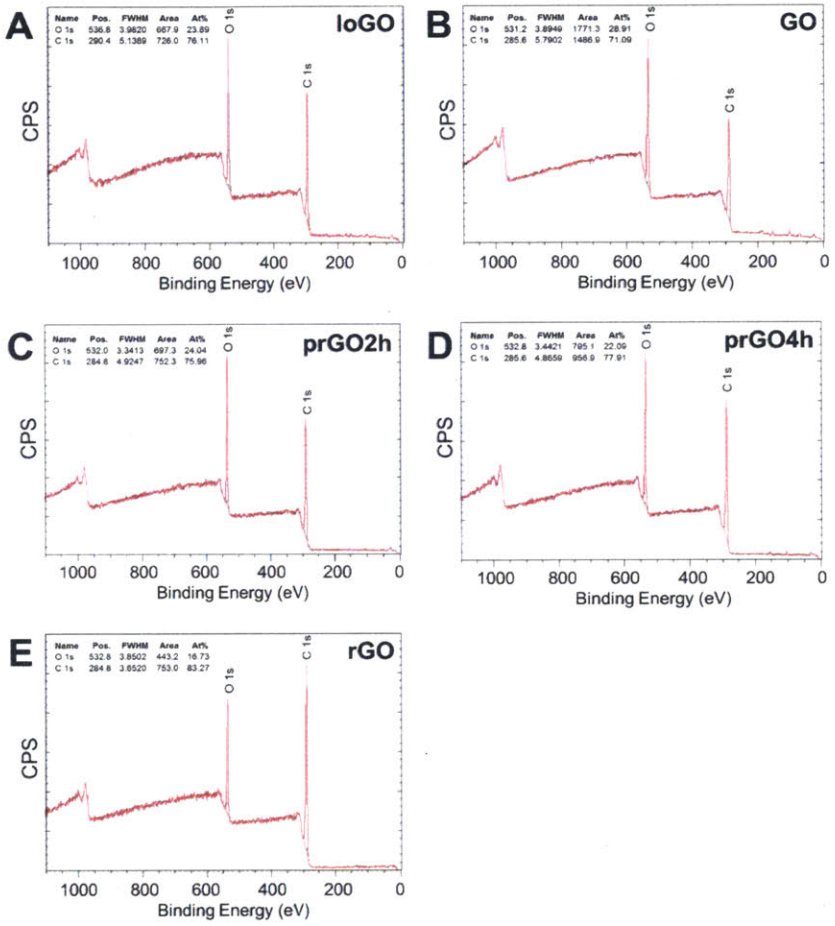

Figure 3.7. a–e) X-ray photoelectron spectra of **loGO**, **GO**, **prGO2h**, **prGO4h**, and **rGO**, respectively.

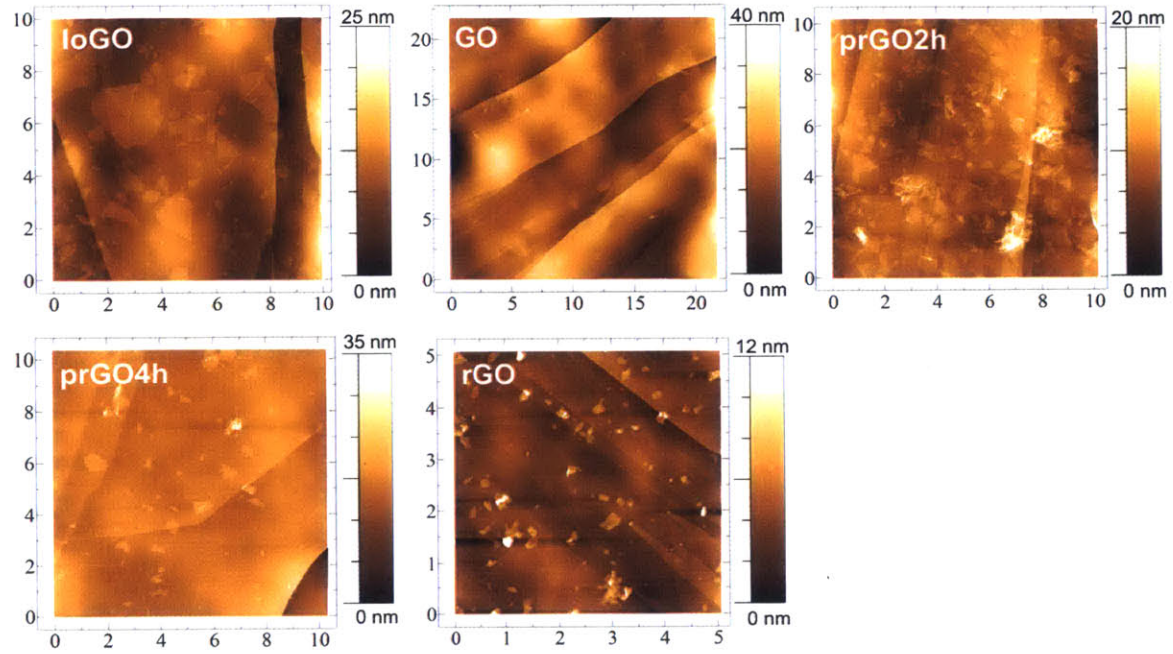

Figure 3.8. Additional AFM topographic images of graphene oxide flakes at varying degrees of (de)oxygenation at the HOPG / air interface after deposition from solution. Depicted x,y scale bars are in μm.

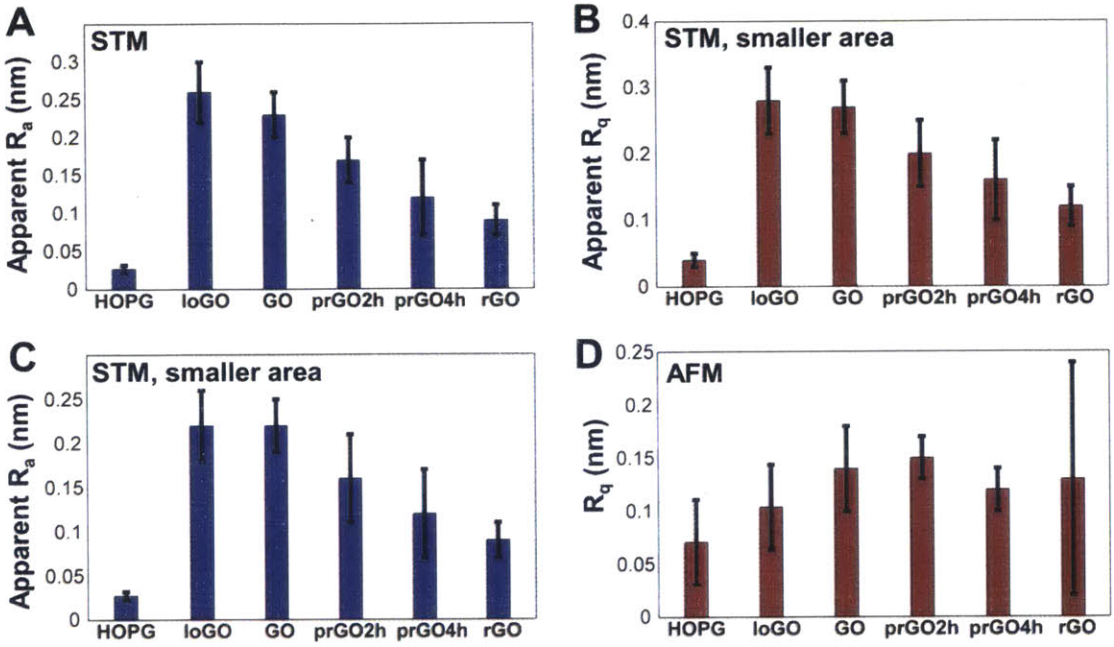

Figure 3.9. a–c) Apparent roughness graphs, determined from the same STM topography measurements as in Figure 3.4. a) Apparent average roughness, R_a, showing the same trend that more deoxygenation corresponds to lower apparent roughness. b) Apparent R_q determined with all areas ~2500 nm^2. c) Same as (b) but for the apparent R_a. d) R_q obtained from AFM measurements. For every bar, n = 9–11 flakes.

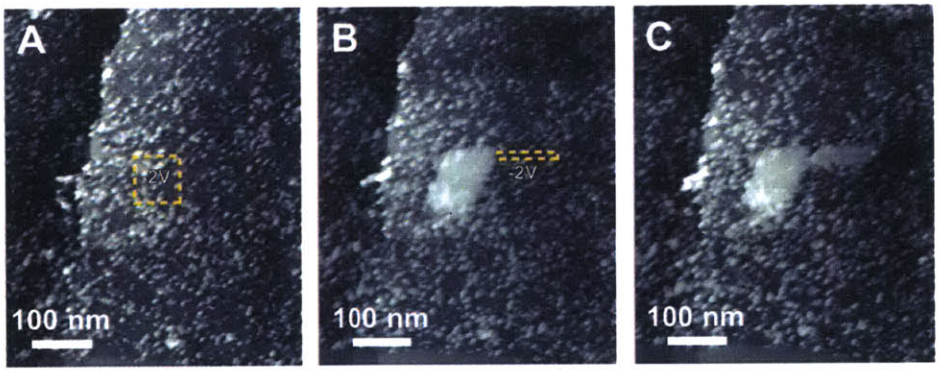

Figure 3.10. An additional example of local manipulation of **loGO** by STM at the HOPG / air interface. V_{bias} = +1 V, I_{set} = 2 pA. The yellow squares indicate the areas that have been scanned at a V_{bias} = −2 V between the shown images. Δt ~ 9 minutes.

CHAPTER 4

DNA-Mediated Self-Assembly of Carbon Nanotubes

Weis, J. G.; Weizmann, Y.; Swager, T. M.* "Self-Assembly of SWCNT Networks Mediated by a DNA Trilinker" *in preparation.*

4.1 Introduction

Since their discovery and initial characterization in 1991 by Iijima,[1] carbon nanotubes (CNTs) have captivated scientists of numerous fields due to the unique electrical, optical, and mechanical properties that render them ideal candidates for field-effect transistors,[2–5] single-electron transistors,[6–8] energy generation and storage,[9–14] transparent conducting films,[15–18] high performance composites,[16,19,20] and sensors.[21–24] For applications in electronics, it is important to recognize that a carbon nanotube's electronic structure is derived from graphene's, as the structure of carbon nanotubes can be considered by rolling a sheet of graphene into a cylinder. The resulting electronic properties of the CNTs are dependent on the chiral angle or indices, denoted as a pair of integers (n,m). Nanotubes with a chiral vector where $n = m$ are described as armchair CNTs while those where $m = 0$ are known as zigzag CNTs. A general description of their electronic character can be made. Nanotubes with $n - m = 3k$, where k is an integer are metallic, and CNTs with $n - m \neq 3k$ are semiconducting.[25] These diverse electronic properties enable CNTs to be employed as nanoscale electrical components.

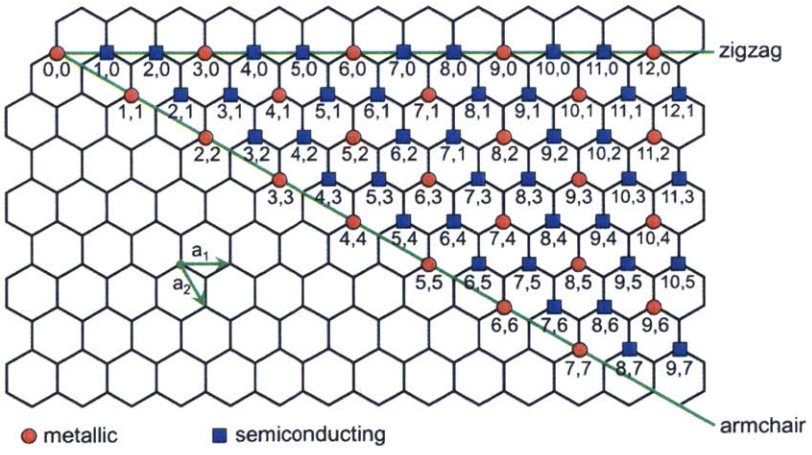

Figure 4.1. Chiral vectors in CNTs. $na_1+ma_2 \equiv (n,m)$. n and m are integers where $0 \leq |m| \leq n$. For $n - m = 3k$, CNTs are metallic if k is an integer and semiconducting if not.

Nanoscale devices based on CNTs necessitate the controlled formation of junctions between different types of carbon nanotubes as well as between carbon nanotubes and other nanomaterials.[26,27] Various electronically important junctions can be constructed. Schottky junctions occur between metallic and semiconducting materials, p-n junctions exist between p-type and n-type materials, and heterojunctions form between two semiconducting materials with dissimilar band structures.[28] For example, intramolecular (fused)[29–32] or intermolecular (crossed)[33] heterojunctions of metallic and semiconducting carbon nanotubes can form two-terminal nanodiodes, which have applications in rectification, solar cells, and switching.[34] A more complex structure, the intramolecular Y-junction, has also been observed and experimentally demonstrated to exhibit diode-like behavior[35] or even sharp electrical switching for logic applications.[36,37] Similar rectifying behavior has also been shown in intermolecular T-junctions.[38,39]

Intramolecular carbon nanotube junctions can be confirmed by transmission electron microscopy (TEM),[36,40–42] scanning tunneling microscopy (STM),[30,43,44] or even scanning electron microscopy (SEM) and Raman spectroscopy.[45] In fact, CNTs have been observed to coalesce under an electron beam.[46,47] Although these CNT intramolecular junctions exhibit excellent electrical properties and robustness, the difficulty in obtaining predictable junctions with the desired nanotube chiralities and organizing these junctions into a useful nanoscale circuit remains a key challenge in their commercialization.[28] For this reason, the bottom-up assembly of intermolecular three-way junctions (3WJs) is an attractive alternative.

Despite their appealing dimensions and properties, the implementation of CNTs in commercial nanocircuitry has experienced little success, mainly due to the challenges in positioning and orienting the CNTs into desired configurations. Covalent or noncovalent

modification of CNTs is often required to manipulate them in an intramolecular or intermolecular manner. Intramolecular covalent[48,49] and noncovalent[50] methods have been demonstrated to successfully form CNT rings. Intermolecularly, CNTs have also been connected by simple amide bond formation,[51–53] although all these methods suffer from the lack of regiomeric control (tube end vs. sidewall). Palma, Wind, and coworkers have recently reported the construction of end-selective, multi-terminal nanotube junctions through the use of small-molecule homomultifunctional linkers in solution.[54] Unfortunately, this method lacks a handle for the selective placement on a device or surface.

Deoxyribonucleic acid (DNA) possesses extraordinary self-assembly capabilities by predictable Watson–Crick base pairing. In 1982, Nadrian Seeman proposed that DNA itself could be used as a building block for geometrically complex nanomaterials.[55] Over the past 30 years, that dream has been realized, and "structural DNA nanotechnology" is now an established field of its own.[56–59] DNA has been shown to interact with and assemble CNTs; however, these attempts controlled neither regioselectivity nor valence, greatly hindering efficient formation of functional junctions.[60–65] These deficiencies likely arise from the noncovalent and nonregioselective (or sidewall-selective[66–68]) attachment to the CNTs. For biosensing applications, DNA allows the facile incorporation of aptamers to the junctions.[69–72]

Our group has reported a strategy for the regioselective functionalization of SWCNTs that relies on shielding the sidewalls of CNTs with a polymer mixture of Triton X-100 and PEG-10,000. By protecting the sidewalls from further functionalization, we have demonstrated the regioselective attachment of amino-functionalized gold nanoparticles to the ends of carbon nanotubes through EDC–NHS amidation chemistry.[73] This chemistry was elaborated to form

linear, terminally linked DNA–CNT nanowires with the DNA-junctions labeled by binding gold nanoparticles.[74] Furthermore, these networks could be designed for the horse radish peroxidase-assisted, junction-specific silver deposition that resulted in the selective detection of DNA sequences.[75] In addition to biodetection schemes, we envision that this local, DNA-directed deposition of silver could also be exploited as "molecular solder" to construct robust electronic junctions of CNTs.

Specifically, we hypothesized that this selective covalent functionalization of CNT ends would facilitate the DNA-mediated assembly of end-functionalized CNTs, extending our methodology to create higher order architectures. The first architecture we targeted was the three-way junction (3WJ), as shown in Figure 4.2. With modern advances in the separation of carbon nanotubes by chirality[76–83] and length,[84–88] the controlled growth of carbon nanotubes with specific helicities,[89] and asymmetric carbon nanotube end-functionalization,[90–93] these structures will greatly expand the scope of applications for the DNA-directed assembly of CNTs for controlled nanocircuitry and lead to more sensitive biosensors.

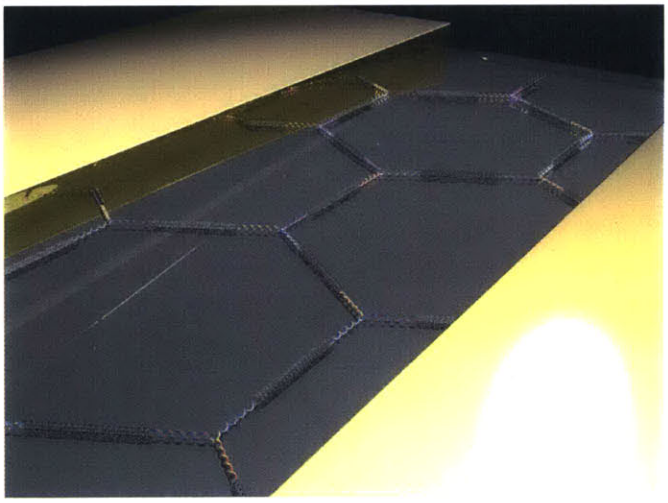

Figure 4.2. Schematic of an ideal DNA–CNT network deposited between gold electrodes.

4.2 Results and Discussion

4.2.1 Solution-based Assembly Methods

Our first strategy was to construct individual 3WJs in solution by forming a DNA trilinker with primary amines on each 5′-terminus (Figure 4.3), which could subsequently be coupled with carbon nanotubes bearing carboxylic acids on their ends.

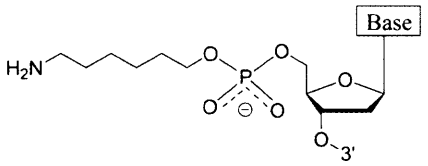

Figure 4.3. Structure of 5′-6-aminohexyl terminus of DNA that allows bioconjugation to oxidized SWCNTs.

Oxidized single-walled CNTs (oCNTs) were prepared by sonicating HiPCO CNTs in a 3:1 H_2SO_4/HNO_3 solution, followed by 30 minutes in 4:1 H_2SO_4/30% aqueous H_2O_2 to remove extraneous carbonaceous particles.[94–96] We determined by atomic force microscopy (AFM) that the oxidized tubes are significantly shortened to an average length of 195 ± 78 nm. Literature reports also confirm that the oxidation introduces defects to the sidewalls of the nanotubes.[94,97] It is important to note that the reactivity of the carbon nanotubes is predominantly dependent on their diameter, with small diameter tubes being the most susceptible to oxidation.[98] This observation is readily understood considering the effective "ring strain" in the carbon nanotubes possessing high curvature.

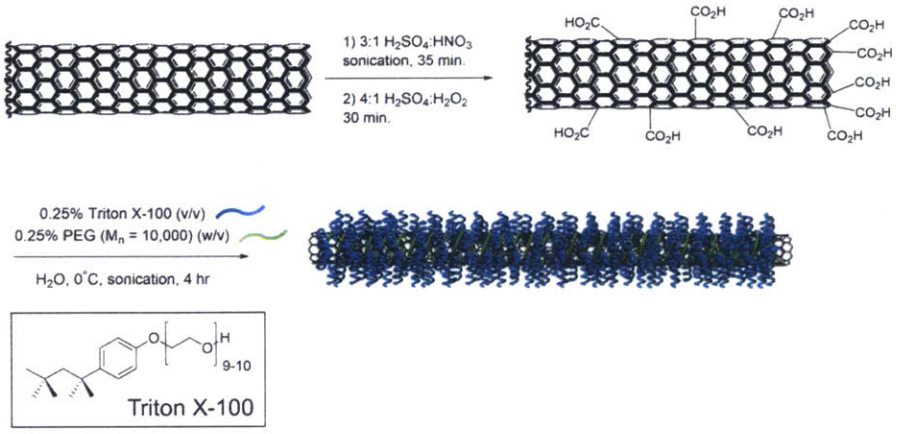

Scheme 4.1. Oxidation and subsequent shielding of SWCNTs.

To prevent sidewall functionalization in subsequent modification steps and greatly improve solubility, the oCNTs were sonicated in an aqueous solution of 0.25% Triton X-100 (v/v) and 0.25% PEG 10,000 (w/v),[99,100] as depicted in Scheme 4.1. It is important to note that it is possible that further defects are introduced to the carbon nanotubes in this step through the degradation of the solvent and subsequent radical reactions with the nanotubes.[101,102] After the shielding reaction, the nanotubes are centrifuged to remove any aggregates or undispersed tubes. The concentration of the resulting shielded CNT solution can be monitored by UV–Vis spectroscopy (Figure 4.4a), with which we determined ε_{808nm} = 0.0078 L mg^{-1} cm^{-1}. Transmission electron micrographs confirm the prevalence of individual CNTs rather than bundles (Figure 4.4b).

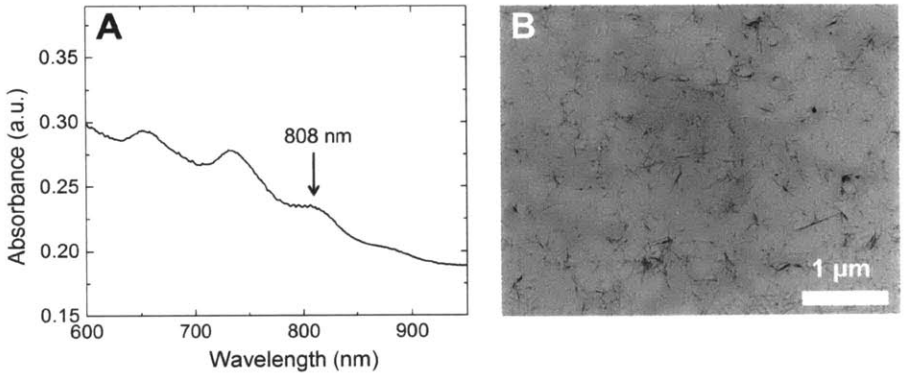

Figure 4.4. a) UV–Vis absorption spectrum of shielded SWCNTs dispersed in H_2O. To calculate the concentration of SWCNTs, an extinction coefficient of 0.0078 L mg^{-1} cm^{-1} at 808 nm was used. b) Transmission electron micrograph of shielded SWCNTs.

In order to form uniform networks of carbon nanotubes (as shown in Figure 4.2), it is necessary to begin with SWCNTs with relatively monodisperse lengths. Therefore, the oCNTs were subsequently sorted by length by size exclusion chromatography (SEC) with consecutive columns of 1000Å and 3000Å controlled pore glass, according to literature procedure.[85] Improved length distributions were obtained (Figure 4.5), although more narrow distributions have been achieved with DNA-wrapped SWCNTs.[84,103,104] For this application, however, it is possible that the excess DNA dispersant would interfere with our amide bond formation and/or the DNA-directed self-assembly.

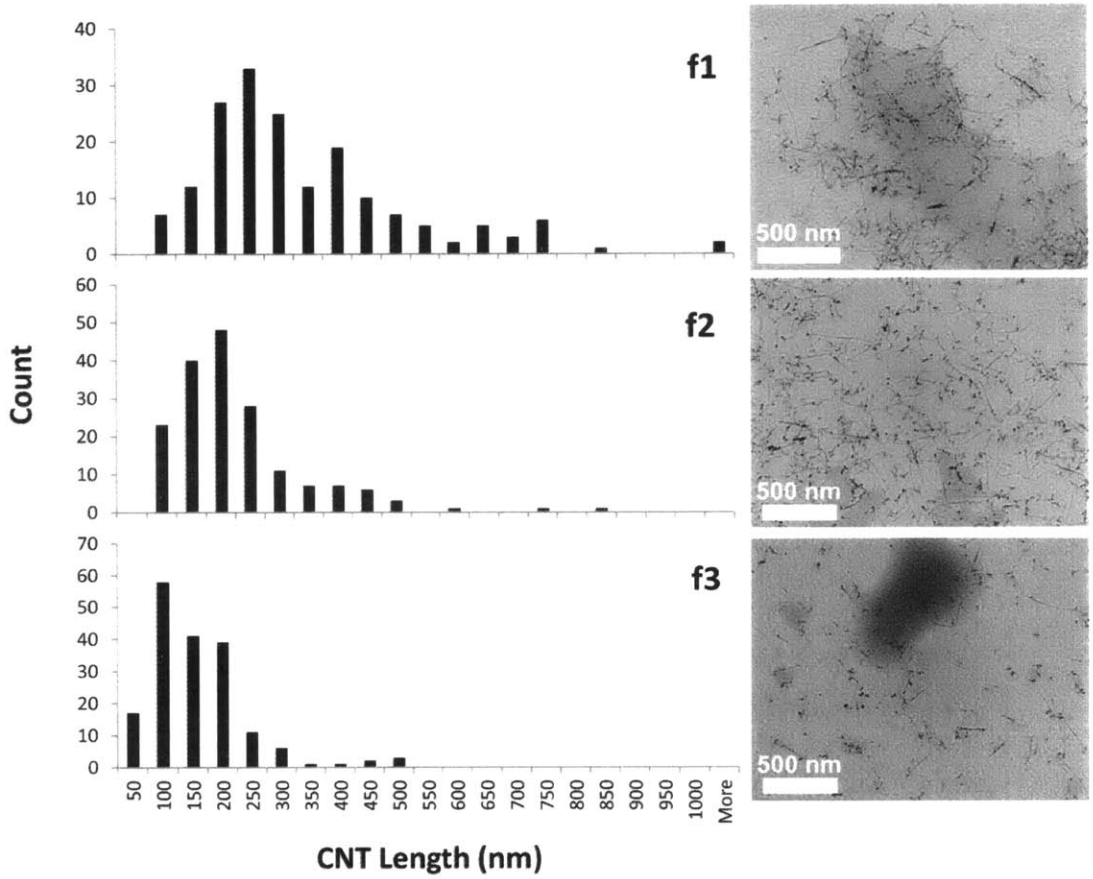

Figure 4.5. Length separation of carbon nanotubes by SEC with 1000Å controlled pore glass. Histograms and corresponding TEM image of fractions 1–3.

The DNA sequences were designed to form 3WJs using the program UNAFold,[105] minimizing intrastrand hybridizations to enable efficient junction formation at lower temperatures. All sequences were designed with 100 nucleotides per strand with intrastrand melting temperatures of less than 40 °C. The resulting DNA 3WJ contains three arms of approximately 17 nm. Because double-stranded DNA has a persistence length of approximately 45 nm at room temperature,[106] we expect these arms to be relatively rigid. All sequences were purchased with 5′-6-aminohexyl (6AH) modifications (Figure 4.3) to allow for bioconjugation to the oCNTs using 1-ethyl-3-(3-dimethylaminopropyl)carbodiimide

(EDC) / N-hydroxysulfosuccinimide (sulfo-NHS)-mediated amide bond formation[107] on the CNT termini. Bioconjugation to the sidewalls of the CNTs was prevented by wrapping the CNTs with Triton X-100 and PEG–10,000 surfactants.

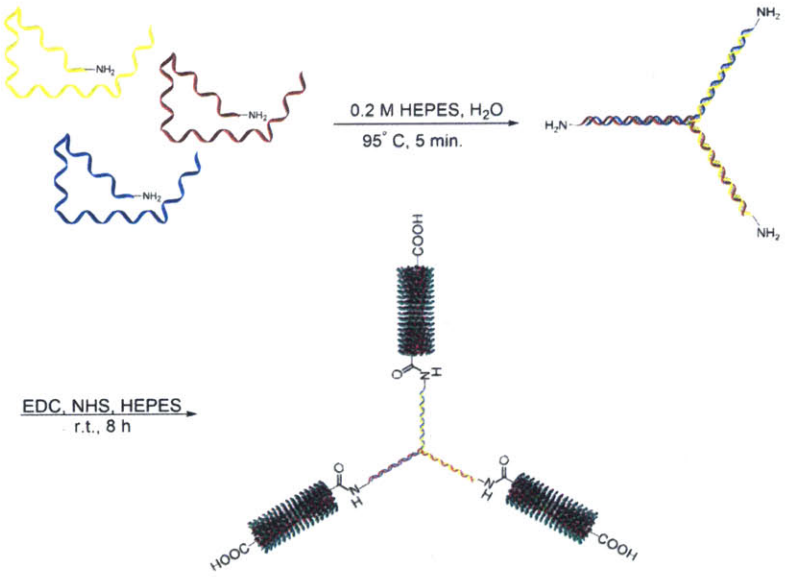

Scheme 4.2. Assembly method A for forming CNT–DNA 3WJs in solution.

Solution Assembly Method A. The DNA sequences were first hybridized to form the desired 3WJs and then bioconjugated to the shielded oCNTs (~200 nm length) through EDC–sulfo-NHS-facilitated amide bond formation, as depicted in Scheme 4.2. The formation of 3WJs was analyzed by AFM and TEM, which indicated significant junction formation. AFM line profiles exhibited the anticipated shielded-CNT and DNA heights of ~8 nm and 2 nm, respectively (Figure 4.6c). We attempted to label the junctions by using stains for electron microscopy (e.g., uranyl acetate); however, TEM images were complicated by nonspecific staining of the surfactant and CNTs, preventing clear labeling of the DNA junctions. TEM and thermogravimetric analysis (TGA) also revealed significant residual iron catalyst from the

HiPco® process, indicating that higher purity CNTs (<5% metal content) were necessary for our experiments. Excess catalyst located at the end of the tubes could prevent any end-functionalization from occurring, ultimately resulting in a "dead end." Alternatively, CNTs formed by the CoMoCat® process can be used, as it has been found that CoMoCat® CNTs are less susceptible to drastic shortening upon oxidation.[108]

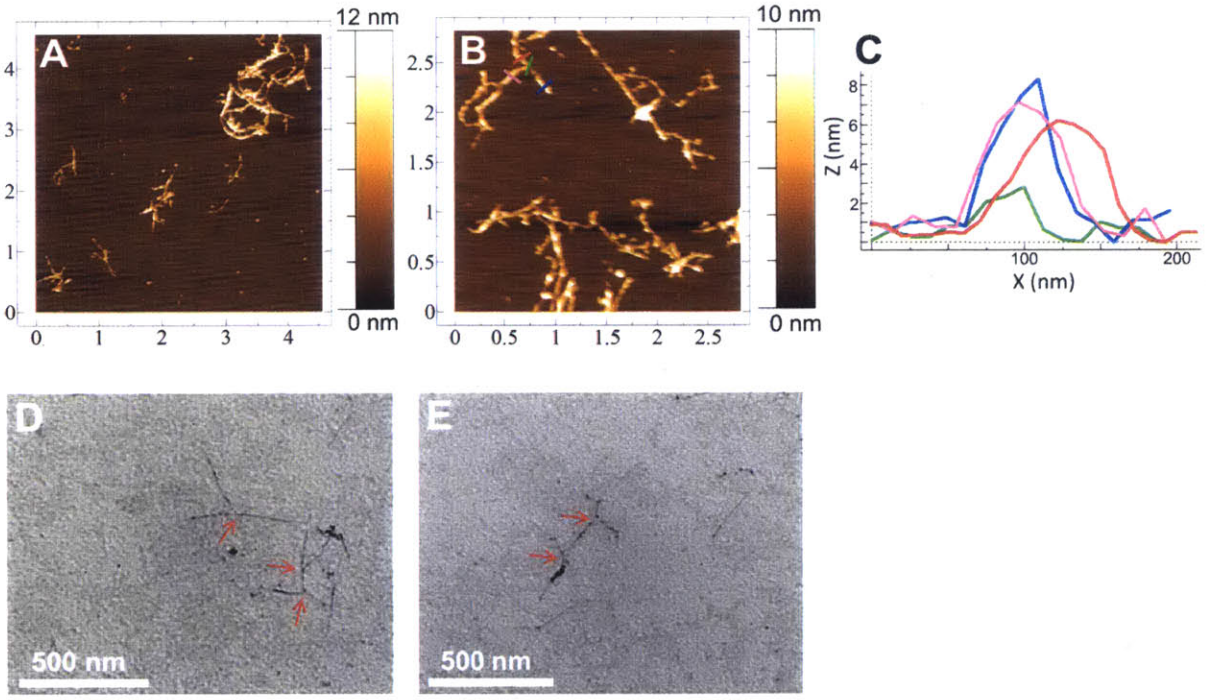

Figure 4.6. Characterization of 3WJs formed by solution assembly method A (Scheme 4.2). a, b) AFM images. The x and y scale bars are in μm. c) Line profiles indicating shielded CNTs and DNA as marked in (d). d, e) TEM images. The red arrows indicate the locations of 3WJs.

Solution Assembly Method B: With successful formation of 3WJs, we looked to better demonstrate self-assembly through the construction of a CNT–DNA network. In this approach, the CNTs were homobifunctionalized with DNA. After bioconjugation, approximate concentrations could be determined by UV–Vis spectroscopy (ε_{808nm} = 0.0078 L mg^{-1} cm^{-1}), reasonably assuming similar reactivity of DNA strands **A**, **B**, and **C**. To prevent termination

of "active" CNT–DNA ends, excess free DNA was removed using multiple washes via centrifugal filtration. The **A**-, **B**-, and **C**-DNA-functionalized SWCNTs were then combined stoichiometrically in solution to form 3WJs, as shown in Scheme 4.3.

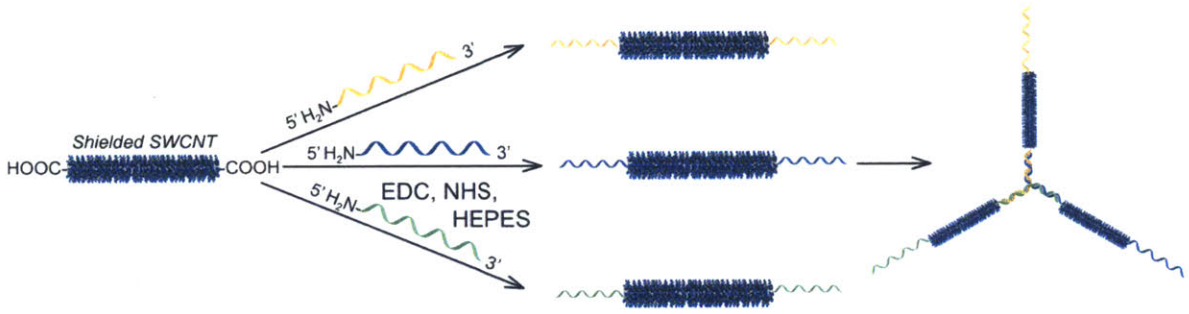

Scheme 4.3. Assembly method B for formation of CNT–DNA 3WJs in solution.

TEM revealed successful network formation, as shown in Figure 4.7; however, the large size of many of the CNT–DNA networks made imaging with AFM very difficult.

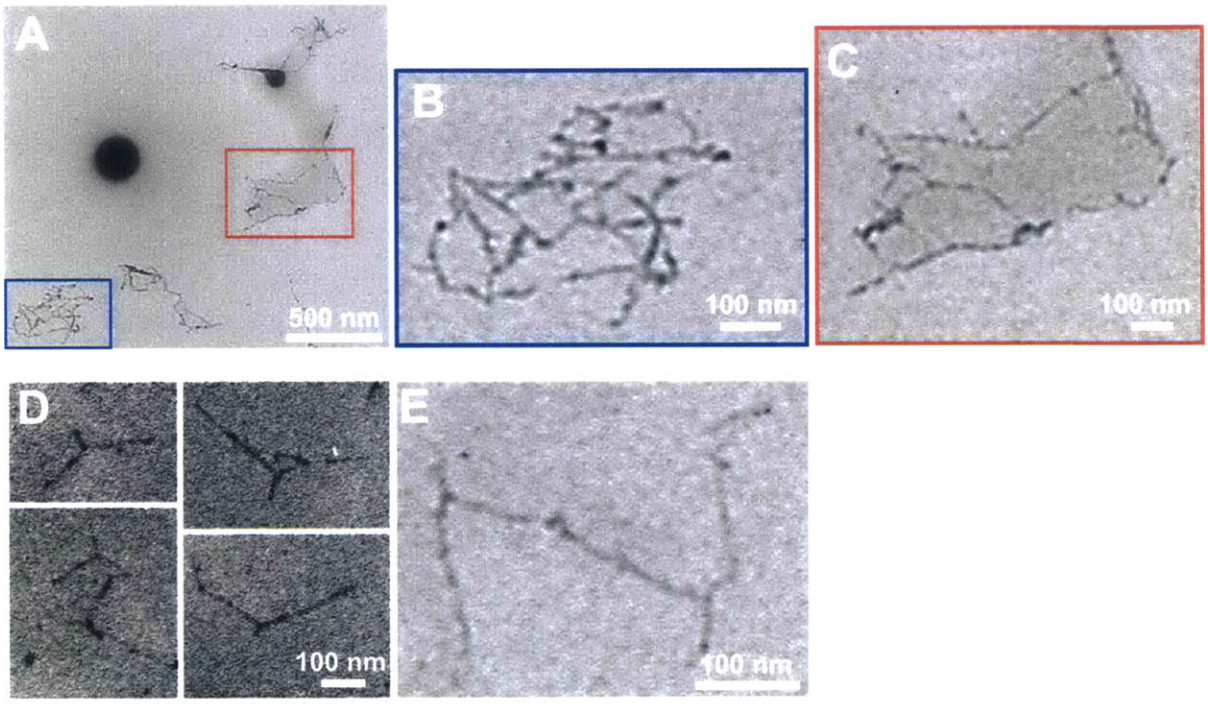

Figure 4.7. Characterization by TEM of 3WJs formed by Solution Assembly Method B.

Control experiments with 3-(perfluorooctyl)propylamine-conjugated oCNTs and DNA designed for linear architectures provided evidence against simple aggregation caused by deshielding of the CNTs and the resulting CNT–CNT interactions. Carbon nanotubes were functionalized with 3-(perfluorooctyl)propylamine following the same procedure as the CNT–DNA conjugates. TEM images confirmed the formation of aggregates significantly different in structure to those obtained with the programmed DNA trilinker, as expected (Figure 4.8a–c). In this case, the aggregation can be ascribed to the fluorous effect.[109] Linear CNT–DNA nanowires were also constructed by functionalizing carbon nanotubes with DNA strand **C** and **C**-complementary. TEM images show significantly fewer multi-terminal junctions and many isolated wires of two or three tubes joined linearly, as shown in Figure 4.8d–g.

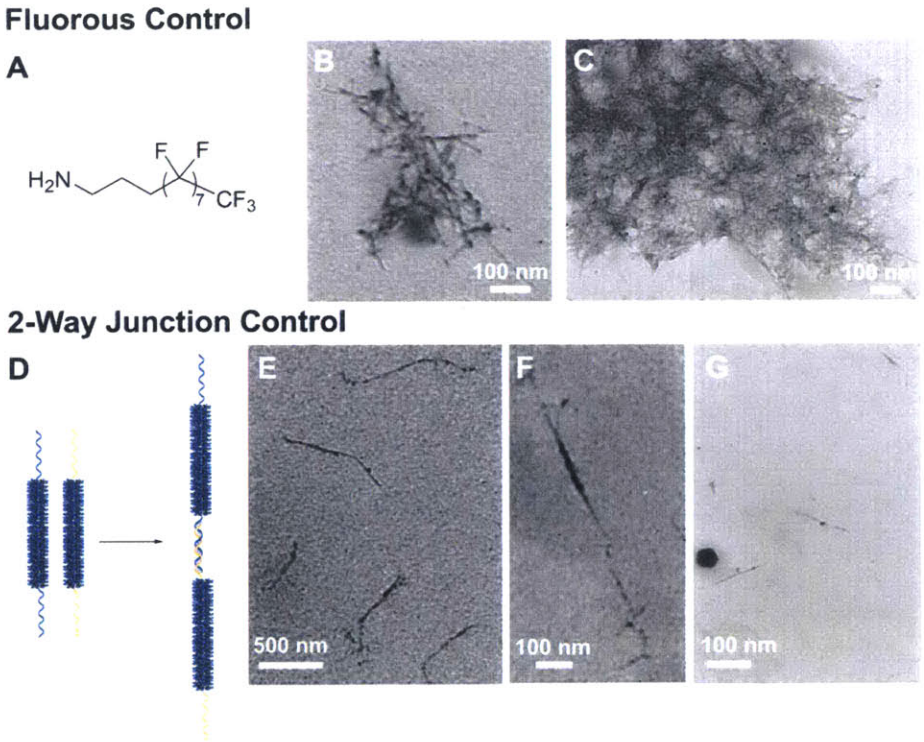

Figure 4.8. a) Structure of fluorous amine used to cause aggregation b,c) TEM images displaying aggregates. d) Scheme for formation of linear DNA–CNT nanowires. e–g) TEM images of linear DNA–CNT nanowires.

A number of parameters were optimized to obtain clean networks of CNT–DNA conjugates. For the bioconjugation of DNA to the CNTs, reaction concentrations of approximately 50–500 nM were ideal, resulting in CNT:DNA strand ratios between 1:1 and 1:10. Alternative surfactants (e.g., Tween 20) were attempted to prevent non-specific binding and sidewall functionalization, but these often resulted in greater difficult in imaging with AFM or TEM due to the formation of micelles. The one parameter that did result in a drastic change was changing the hybridization buffer from HEPES to PBS (10 mM). After ten minutes, large aggregates could be seen crashing out of solution once CNT–DNA conjugates functionalized with DNA **A**, **B**, and **C** were mixed stoichiometrically, as shown in Figure 4.9. Control experiments with shielded carbon nanotubes without DNA did not form visible aggregates, suggesting that this aggregation was not a result of the increased ionic strength of PBS compared to HEPES but rather of complete network formation. Although this result was encouraging, characterization of the individual junctions was greatly complicated, leading us to pursue alternative routes.

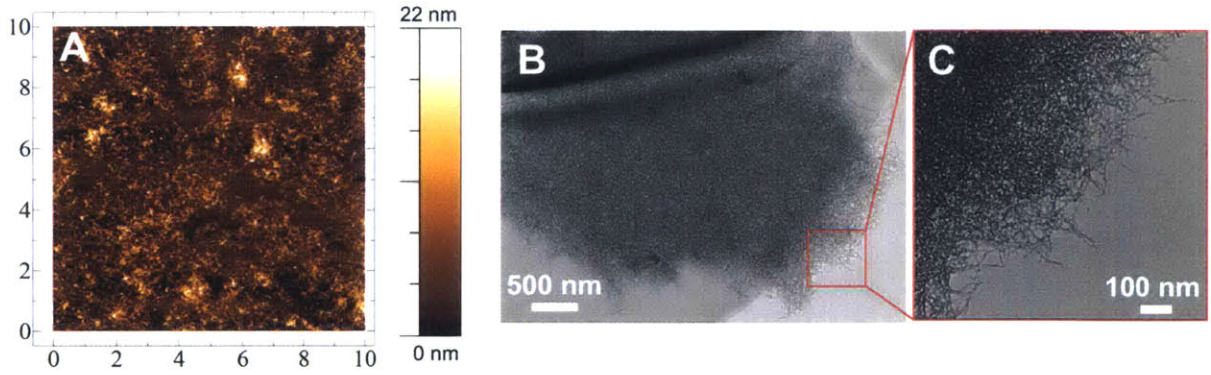

Figure 4.9. a) AFM topographic image of aggregates formed during DNA–CNT network construction in PBS buffer. The x- and y-axes are in μm. b) TEM image of DNA hybridization-induced aggregation. c) Zoom in on region labeled in (b).

4.2.2 Surface-based Assembly Methods

Surface Assembly Method A: To circumvent the problem of aggregation and enable more facile surface characterization, we devised a surface assembly route, as depicted in Scheme 4.4. Silanol-covered surfaces were prepared by plasma treating silicon(100) wafers followed by treatment with (3-aminopropyl)trimethoxysilane (APTMS) to yield an amino-functionalized surface.[110] The wafer was subsequently treated with homobifunctional cross-linker bis(sulfosuccinimidyl)suberate (BS^3) in phosphate buffer (PB) to yield a covalently functionalized sulfo-NHS surface. After covalently anchoring 6AH-modified complementary DNA to the surface, CNT 3WJs could then be constructed in a stepwise fashion.

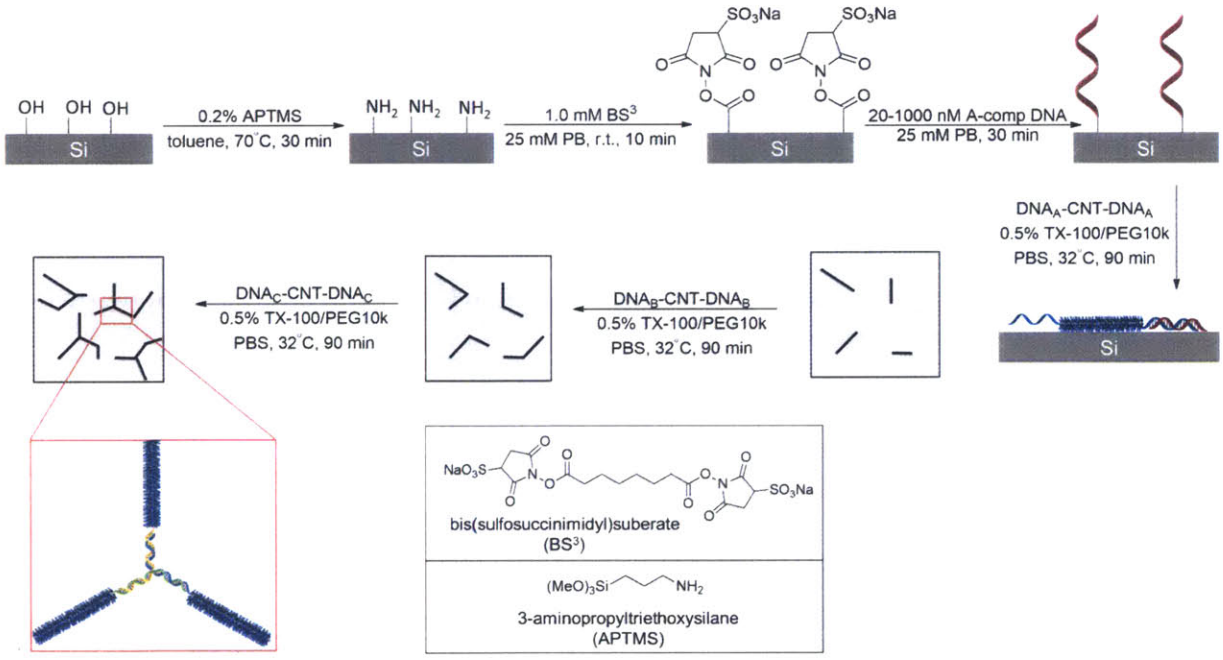

Scheme 4.4. Surface assembly method A for the bottom-up construction of CNT–DNA 3WJs on silicon surfaces.

AFM imaging confirmed the formation of 3WJs on the surface; however, single carbon nanotubes were still observed, as seen in Figure 4.10. These lone nanotubes could arise from

nonspecific binding of carbon nanotubes to the surface or carbon nanotubes with "dead ends" — i.e., they were unable to hybridize with other DNA ends due to lack of DNA at one end or duplex formation with free DNA. Control experiments without the surface bound DNA anchors displayed approximately 90% fewer CNTs on the surface, as shown in Figure 4.11; however, nonspecific binding (NSB) was problematic nonetheless. In collaboration with Prof. Klavs Jensen's group, we used microfluidics in an attempt to shear unbound CNTs away from the surface and possibly induce CNT alignment; however, the NSB proved persistent.

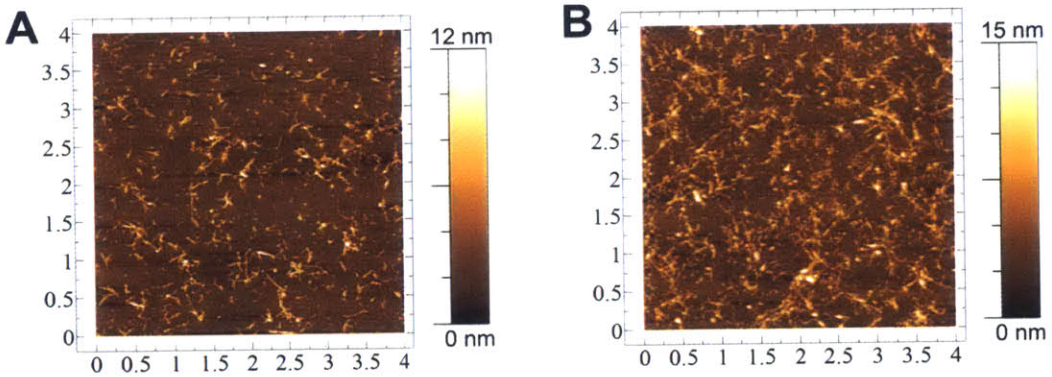

Figure 4.10. AFM topographic measurements of DNA–CNT networks assembled by surface method A. The x- and y- axes are in μm.

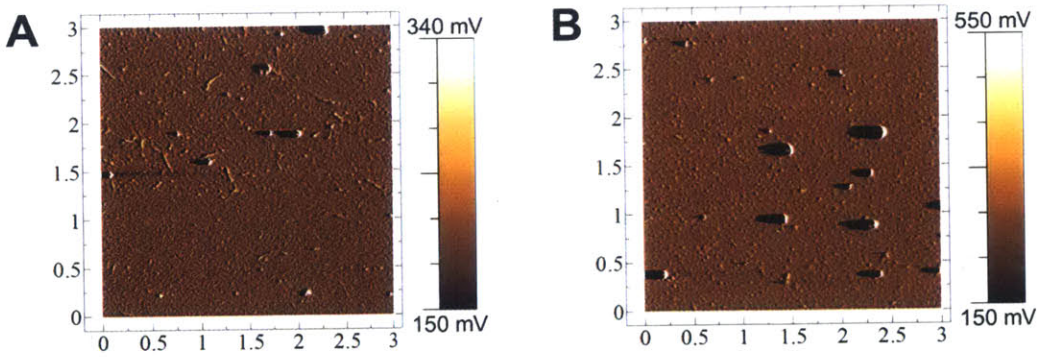

Figure 4.11. AFM amplitude images of control measurements (a) with and (b) without the presence of DNA anchors. The x- and y- axes are in μm.

Surface Assembly Method B: We hypothesized the NSB could be decreased by a more uniformly functionalized surface. An alternative approach to forming an NHS-functionalized surface is through sonochemically activated hydrosilation.[111] To obtain a hydrogen-passivated surface, silicon(111) was first treated with 40% aqueous ammonium fluoride and directly followed by an ω-NHS-functionalized-α-alkene. The presence of the functionalized monolayer was confirmed by ATR–FTIR spectroscopy. A similar step-by-step procedure as in surface assembly method A could then be pursued to build up CNT 3WJs.

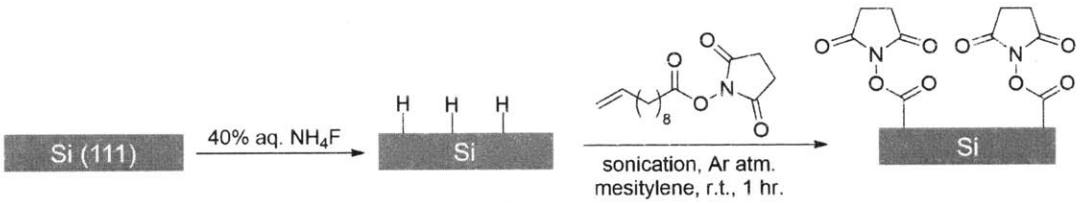

Scheme 4.5. Surface assembly method B. Alternative functionalization of silicon surfaces with NHS esters by sonochemical hydrosilation.

Using these DNA-modified surfaces, a number of parameters were optimized in an effort to obtain ordered DNA–CNT networks. First, the initial surface-bound anchor strand concentration was varied. Concentrations between 5 nM and 5 μM were investigated, and 50 nM appeared to give the optimal amount of CNTs on the surface. The surfactant concentration also played a key role. We found that Triton X-100/PEG–10,000 concentrations of less than 0.25% resulted in increased NSB whereas concentrations greater than 1% led to diminished CNT–DNA hybridization to the anchor strand. In an effort to improve the homogeneity of the 3WJ formation and further decrease NSB, the hybridization temperature was optimized. Higher temperatures are needed to fully overcome the T_m of the DNA single strands prior to annealing; however, hybridization temperatures above 35°C greatly increased non-specific

binding, most likely due to the dissociation of the surfactant from the CNTs. We determined that 32°C kept nonspecific binding minimal while still enabling moderately high 3WJ formations.

The DNA:CNT bioconjugation ratio was also critical. DNA:CNT ratios less than 3.5:1 resulted in many isolated CNTs on the surface, as observed by AFM, presumably due to significant monofunctionalization of the CNTs. Ratios greater than 5:1 resulted in overfunctionalized CNTs, existing as cross-linked networks in AFM images. The intermediate ratio of 4:1 proved successful at forming 3WJs on DNA-functionalized surfaces, although additional optimization is expected to increase the yield of 3WJs.

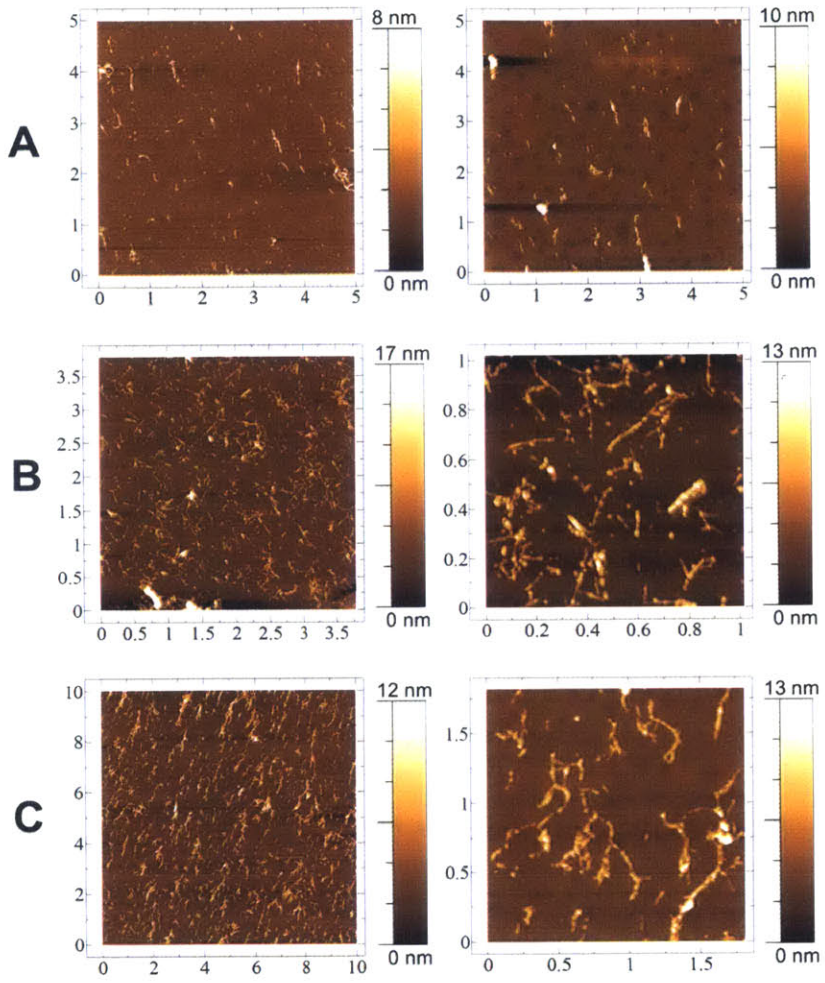

Figure 4.12. AFM topographic measurements of CNT–DNA 3WJs prepared by Solution Method B with DNA:CNT bioconjugation ratios of a) 3:1, b) 4:1, and c) 5:1.

4.3 Conclusions

In summary, we report a controllable method for constructing three-way SWCNT junctions in a predictable manner in solution or stepwise on a surface by exploiting the self-assembly properties of DNA. By selectively functionalizing singular types of carbon nanotubes or other nanoparticles, we envision the controlled bottom-up synthesis of molecular circuits.

A number of electronic junctions analogous to their macroscale counterparts can be prepared. For example, selective metallization of the DNA junction can result in more sensitive biosensors as a result of the increased rate at which conductive pathways are formed. Localized metallization could also serve as a nanoscale "solder" to create mechanically robust junctions. With the scalable synthesis of end-functionalized CNTs with minimal sidewall defects, DNA could serve as a nanoscale "wire nut" to lock the nanotubes together in a controlled formation. DNA's ability to mediate charge transport[112–114] could enable DNA itself to be employed as an electrical component in nanoscale devices. Ultimately, advances in controlling the chirality and length of CNTs will be critical to realizing predictable and precise nanocircuits.

4.4 Experimental Details

4.4.1 General

Purified single-walled carbon nanotubes (HiPCO) were purchased from Unidym, Inc. Oligonucleotides were purchased from Integrated DNA Technologies and stored as a frozen 50 μm solution in water. *N*-Hydroxysulfosuccinimide sodium salt (Sulfo-NHS), *N*-(3-dimethylaminopropyl)-*N'*-ethylcarbodiimide hydrochloride (EDC), Tween® 20, Triton™ X-100, and polyethylene glycol with average molecular weight 10 kDa were purchased from Sigma–Aldrich. HEPES (free acid) and hydrogen peroxide (30%) were purchased from EMD Biosciences, Inc. Centrifugation was performed with an Eppendorf MiniSpin® plus or a Beckman Coulter Allegra X-22R centrifuge. Amicon® Ultra centrifugal filters (10,000 molecular weight cut-off) were purchased from Millipore. Ultrapure water from a NANOpure™ Analytical Ultrapure Water System was used for all experiments. Sonication was performed in a Branson 3510 bath sonicator.

Transmission electron microscopy (TEM) images were obtained on a JEOL 2000 FX instrument (acceleration voltage 200 kV) using a 200- or 400-mesh copper grid with or without amorphous carbon film (Ted Pella). Atomic force microscopy (AFM) measurements were performed at room temperature (22 ± 1°C) with a relative humidity of 50 ± 8% using an Agilent 5100 or Veeco Nanoscope V in ACAFM tapping mode using silicon tips with a force constant of 20 – 80 N/m. Vibration isolation was provided by a bungee system enclosed in a chamber with multiple layers of sound-damping materials for acoustic isolation.

4.4.2 Design of DNA Sequences

Strand A (T_M = 35.7 °C)

5′(6AH) –

CGGGCGAAATACACTGTGACAGTAACATGCAGCAACAAACAACAATTATT

CTCGCGCAGTAGGAACTATTAACACTGACTAAGAAGTCTATGCTCCAGAC

– 3′

Strand B (T_M = 34.3 °C)

3′ –

GCCCGCTTTATGTGACACTGTCATTGTACGTCGTTGTTTGTTGTTAATAA

ACTTAGAGACTTGTCTATATCGAAGATGACTGTTGTATCGTGGCATTGCT

– 5′(6AH)

Strand C (T_M = 37.1 °C)

5′(6AH) –

GTCTGGAGCATAGACTTCTTAGTCAGTGTTAATAGTTCCTACTGCGCGAG

TGAATCTCTGAACAGATATAGCTTCTACTGACAACATAGCACCGTAACGA

– 3′

Strand C Complement (T_M = 36.9 °C)

5′(6AH) –

TCGTTACGGTGCTATGTTGTCAGTAGAAGCTATATCTGTTCAGAGATTCA

CTCGCGCAGTAGGAACTATTAACACTGACTAAGAAGTCTATGCTCCAGAC

– 3′

4.4.3 Oxidation, Shielding, and Length Separation of SWCNTs

Oxidation of CNTs

SWCNTs were oxidized according to a modified literature procedure.[94] Pure HiPco SWCNTs (Unidym, 150 mg) were placed in a solution of concentrated sulfuric acid (18 mL) and 70% nitric acid (6 mL) (3:1, 24 mL) at room temperature and sonicated (bath) for 35 minutes. The solution was added to 200 mL water and filtered using a 0.6 μm polycarbonate membrane. The nanotubes were then etched for 30 minutes with a solution of concentrated sulfuric acid (16 ml) and 30% hydrogen peroxide (4 mL) (4:1, 20 mL) to remove all carbonaceous particles produced by the first oxidation. The mixture was then added to 200 mL water, and the resulting nanotube mixture was filtered with a 0.6 μm polycarbonate membrane. The resulting SWCNT filter cake was then washed with 100 mL water followed by 100 mL ethanol. The final material was dried in a vacuum desiccator overnight (131 mg recovered).

Shielding of Oxidized CNTs

A solution of oxidized SWCNTs (0.1% w/v) was prepared with 0.25% (v/v) Triton X-100 and 0.25% (w/v) PEG–10,000 and sonicated (bath) for four hours in an ice bath. The dispersed CNTs were then subjected to centrifugation at 14,000 rpm for one hour. The

supernatant was then collected, and the concentration of SWCNTs was analyzed by UV–Vis spectroscopy (ε_{808nm} = 0.0078 L mg^{-1} cm^{-1}). This extinction coefficient was determined by sequentially diluting a solution of fully dispersed oxidized CNTs in triplicate.

Length Separation of Shielded CNTs

A shielded SWCNT solution was added to an SEC column packed with controlled pore glass (1000Å or 3000Å, Millipore) and eluted with an aqueous 0.125% Triton X-100 / 0.125% PEG--10,000 solution at 9.6 mL/h. Fractions were collected in 0.5 mL increments. Subsequent surfactant exchanges or dilutions could be performed with Amicon® Ultra centrifugal filters (10,000 molecular weight cut-off).

4.4.4 Self-Assembly of CNT–DNA Conjugates

DNA was stored as a 50 μM stock solution in water at −30 °C.

Solution Assembly Method A

DNA Trilinker. To a 0.5 mL Eppendorf tube was added 0.2 M HEPES (100 μL) and water (88 μL) and homogenized with a vortexer. A solution of 50 μM DNA strand A (4 μL) was added and vortexed. A solution of 50 μM DNA strand B (4 μL) was added and vortexed. A solution of 50 μM DNA strand C (4 μL) was added and vortexed. The solution was then warmed to 90 °C in a large water bath and allowed to slowly cool to room temperature overnight.

In a 0.5 mL Eppendorf tube, the following were added sequentially: CNT solution, water (amount necessary to make final solution 100 μL), 1M stock HEPES solution (2 μL, 20 mM final), 1 μM stock DNA Trilinker solution, 66.7 mM stock EDC solution (3 μL, 2 mM final), and 167 mM stock NHS solution (3 μL, 5 mM final). CNT and DNA concentrations

were varied. The solution was then vortexed at room temperature for 8 hours and stored at +4 °C.

AFM samples were prepared on freshly cleaved mica. A 5 mM solution of $MgCl_2$ was spincoated on the mica, followed by spincoating water three times. A solution of the CNT–DNA conjugates were allowed to rest on the surface for 60 s before spincoating. The samples was finally washed by spincoating water once.

TEM samples were prepared by allowing 5 μL of a sample of CNT–DNA conjugates to rest on the amorphous carbon film side of a Cu TEM grid for 5 minutes. The excess solution was wicked away with a Kimwipe™. The samples were washed in the same manner with water.

Solution Assembly Method B

In a 0.5 mL Eppendorf vial, the following were added sequentially to form a total volume of 110 μL: CNT stock solution, water (volume to ensure final volume of 110 μL), 1M stock HEPES solution (2.2 μL, 20 mM final), 50 μM stock solution of 5′-6-aminohexyl-functionalized DNA strand, 66.7 mM stock EDC solution (3.3 μL, 2 mM final), and 167 mM stock NHS solution (3.3 μL, 5 mM final). CNT and DNA concentrations were varied. The solutions were then vortexed at room temperature for 12 hours. Excess DNA was removed by centrifugal filtration (three times) and collected with a phosphate buffer solution (50 μM PB, 0.1% Triton X-100, 0.1% PEG–10,000). The bioconjugates were stored at +4 °C.

Water (34.8 μL) and 0.2 M HEPES solution (5.0 μL) were added to a 0.5 mL Eppendorf vial. CNT–DNA conjugates **A**, **B**, and **C** (~ 3.4 μL each) were then added and briefly vortexed. Approximate concentrations of **A**-, **B**-, and **C**-DNA-functionalized CNTs were determined by UV–Vis spectroscopy (ε_{808nm} = 0.0078 L mg^{-1} cm^{-1}), and the volumes were adjusted

accordingly. The vial was sealed with parafilm and placed in a large water bath and heated to 60 °C before allowing to cool to room temperature slowly overnight. The bioconjugates were stored at +4 °C.

AFM and TEM samples were prepared as described for Solution Assembly Method A.

Surface Assembly Method A and B

A silicon wafer was treated with oxygen plasma for 30 seconds and then submerged in 0.2 % (3-aminopropyl)trimethoxysilane (APTMS) in toluene for 30 minutes at 70 °C. The wafer was washed with excess toluene and dried under a stream of nitrogen. The sample was then submerged in a 1.0 mM solution of bis(sulfosuccinimidyl)suberate (BS^3) for twenty minutes at room temperature and subsequently washed with 25 mM phosphate buffer to yield the NHS-functionalized surface. Alternatively, the NHS-functionalized surface was prepared by sonochemical hydrosilation with silicon(111) according to literature procedure.[111] (*Surface Assembly Method B*)

The DNA-functionalized surface was prepared by reacting 15 μL of 5 μM C-comp DNA for 45 minutes. The remaining NHS esters were quenched by exposing to 50 mM Tris buffer for 15 minutes and then washing with excess PBS with 0.1% Triton X-100 and 0.1% PEG–10,000. The surface was then treated sequentially with **C**-, **B**-, and **A**-functionalized CNTs as described below. The surface was coated with a solution of 15 μL DNA-functionalized CNTs and 1.5 μL 10X PBS and allowed to hybridize for 90 minutes at 30 °C before washing with excess PBS with 0.1% Triton X-100 and 0.1% PEG–10,000. The surface was dried under a gentle stream of nitrogen before the next treatment. After the final hybridization (with **A**-functionalized CNTs), the surface was washed with copious amounts of PBS and then water prior to imaging with AFM.

4.5 References

(1) Iijima, S. *Nature* **1991**, *354*, 56–58.

(2) Tans, S. J.; Verschueren, A. R. M.; Dekker, C. *Nature* **1998**, *393*, 49–52.

(3) Martel, R.; Schmidt, T.; Shea, H. R.; Hertel, T.; Avouris, P. *Appl. Phys. Lett.* **1998**, *73*, 2447–2449.

(4) Bachtold, A.; Hadley, P.; Nakanishi, T.; Dekker, C. *Science* **2001**, *294*, 1317–1320.

(5) LeMieux, M. C.; Roberts, M.; Barman, S.; Jin, Y. W.; Kim, J. M.; Bao, Z. *Science* **2008**, *321*, 101–104.

(6) Tans, S. J.; Devoret, M. H.; Dai, H.; Thess, A.; Smalley, R. E.; Geerligs, L. J.; Dekker, C. *Nature* **1997**, *386*, 474–477.

(7) Bockrath, M.; Cobden, D. H.; McEuen, P. L.; Chopra, N. G.; Zettl, A.; Thess, A.; Smalley, R. E. *Science* **1997**, *275*, 1922–1925.

(8) Postma, H. W. C.; Teepen, T.; Yao, Z.; Grifoni, M.; Dekker, C. *Science* **2001**, *293*, 76–79.

(9) Gogotsi, Y.; Simon, P. *Science* **2011**, *334*, 917–918.

(10) Le Goff, A.; Artero, V.; Jousselme, B.; Tran, P. D.; Guillet, N.; Métayé, R.; Fihri, A.; Palacin, S.; Fontecave, M. *Science* **2009**, *326*, 1384–1387.

(11) Gabor, N. M.; Zhong, Z.; Bosnick, K.; Park, J.; McEuen, P. L. *Science* **2009**, *325*, 1367–1371.

(12) Dominko, R.; Arčon, D.; Mrzel, A.; Zorko, A.; Cevc, P.; Venturini, P.; Gaberscek, M.; Remskar, M.; Mihailovic, D. *Adv. Mater.* **2002**, *14*, 1531–1534.

(13) An, K. H.; Kim, W. S.; Park, Y. S.; Choi, Y. C.; Lee, S. M.; Chung, D. C.; Bae, D. J.; Lim, S. C.; Lee, Y. H. *Adv. Mater.* **2001**, *13*, 497–500.

(14) Hu, L.; Hecht, D. S.; Grüner, G. *Chem. Rev.* **2010**, *110*, 5790–5844.

(15) Wu, Z.; Chen, Z.; Du, X.; Logan, J. M.; Sippel, J.; Nikolou, M.; Kamaras, K.; Reynolds, J. R.; Tanner, D. B.; Hebard, A. F.; Rinzler, A. G. *Science* **2004**, *305*, 1273–1276.

(16) De Volder, M. F. L.; Tawfick, S. H.; Baughman, R. H.; Hart, A. J. *Science* **2013**, *339*, 535–539.

(17) Gu, H.; Swager, T. M. *Adv. Mater.* **2008**, *20*, 4433–4437.

(18) Ng, S. H.; Wang, J.; Guo, Z. P.; Chen, J.; Wang, G. X.; Liu, H. K. *Electrochim. Acta* **2005**, *51*, 23–28.

(19) Chou, T. W.; Gao, L.; Thostenson, E. T.; Zhang, Z.; Byun, J. H. *Compos. Sci. Technol.* **2010**, *70*, 1–19.

(20) Endo, M.; Strano, M.; Ajayan, P. Topics in Applied Physics; Springer: Berlin / Heidelberg, 2008; Vol. 111, pp. 13–61.

(21) Kauffman, D. R.; Star, A. *Angew. Chem. Int. Ed.* **2008**, *47*, 6550–6570.

(22) Schnorr, J. M.; Swager, T. M. *Chem. Mater.* **2011**, *23*, 646–657.

(23) Zhang, T.; Mubeen, S.; Myung, N. V; Deshusses, M. A. *Nanotechnology* **2008**, *19*, 332001.

(24) Mahar, B.; Laslau, C.; Yip, R.; Sun, Y. *Sensors Journal, IEEE* **2007**, *7*, 266–284.

(25) Charlier, J. C.; Blase, X.; Roche, S. *Rev. Mod. Phys.* **2007**, *79*, 677–732.

(26) Zhang, Y.; Ichihashi, T.; Landree, E.; Nihey, F.; Iijima, S. *Science* **1999**, *285*, 1719–1722.

(27) Hu, J.; Ouyang, M.; Yang, P.; Lieber, C. M. *Nature* **1999**, *399*, 48–51.

(28) Wei, D.; Liu, Y. *Adv. Mater.* **2008**, *20*, 2815–2841.

(29) Yao, Z.; Postma, H. W. C.; Balents, L.; Dekker, C. *Nature* **1999**, *402*, 273–276.

(30) Ouyang, M., Huang, J. L.; Cheung, C. L.; Lieber, C. M. *Science* **2001**, *291*, 97–100.

(31) Yao, Y.; Li, Q.; Zhang, J.; Liu, R.; Jiao, L.; Zhu, Y. T.; Liu, Z. *Nat. Mater.* **2007**, *6*, 283–286.

(32) Collins, P. G.; Zettl, A.; Bando, H.; Thess, A.; Smalley, R. E. *Science* **1997**, *278*, 100–102.

(33) Fuhrer, M. S.; Nygard, J.; Shih, L.; Forero, M.; Yoon, Y.-G.; Mazzoni, M. S. C.; Choi, H. J.; Ihm, J.; Louie, S. G.; Zettl, A.; McEuen, P. L. *Science* **2000**, *288*, 494–497.

(34) Saito, S. *Science* **1997**, *278*, 77–78.

(35) Satishkumar, B. C.; Thomas, P. J.; Govindaraj, A.; Rao, C. N. R. *Appl. Phys. Lett.* **2000**, *77*, 2530–2532.

(36) Bandaru, P. R.; Daraio, C.; Jin, S.; Rao, A. M. *Nat. Mater.* **2005**, *4*, 663–666.

(37) Xu, H. Q. *Appl. Phys. Lett.* **2001**, *78*, 2064–2066.

(38) Liu, L. W.; Fang, J. H.; Lu, L.; Zhou, F.; Yang, H. F.; Jin, A. Z.; Gu, C. Z. *Phys. Rev. B* **2005**, *71*, 2–5.

(39) Chiu, P.-W.; Roth, S. *Appl. Phys. Lett.* **2007**, *91*, 102109.

(40) Han, J.; Anantram, M. P.; Jaffe, R. L.; Kong, J.; Dai, H. *Phys. Rev. B* **1998**, *57*, 14983–14989.

(41) Jin, C.; Suenaga, K.; Iijima, S. *Nat. Nanotechnol.* **2008**, *3*, 17–21.

(42) Grimm, D.; Venezuela, P.; Banhart, F.; Grobert, N.; Terrones, H.; Ajayan, P. M.; Terrones, M.; Latgé, A. *Small* **2007**, *3*, 1900–1905.

(43) Ruppalt, L. B.; Lyding, J. W. *Small* **2007**, *3*, 280–284.

(44) Osváth, Z.; Koós, A. A.; Horváth, Z. E.; Gyulai, J.; Benito, A. M.; Martínez, M. T.; Maser, W. K.; Biro, L. P. *Chem. Phys. Lett.* **2002**, *365*, 338–342.

(45) Doorn, S. K.; O'Connell, M. J.; Zheng, L.; Zhu, Y. T.; Huang, S.; Liu, J. *Phys. Rev. Lett.* **2005**, *94*, 1–4.

(46) Terrones, M.; Banhart, F.; Grobert, N.; Charlier, J.-C.; Terrones, H.; Ajayan, P. M. *Phys. Rev. Lett.* **2002**, *89*, 075505.

(47) Terrones, M.; Terrones, H.; Banhart, F.; Charlier, J.-C.; Ajayan, P. M. *Science* **2000**, *288*, 1226–1230.

(48) Sano, M.; Kamino, A.; Okamura, J.; Shinkai, S. *Science* **2001**, *293*, 1299–1301.

(49) Singh, P.; Toma, F. M.; Kumar, J.; Venkatesh, V.; Raya, J.; Prato, M.; Verma, S.; Bianco, A. *Chem. Eur. J.* **2011**, *17*, 6772–6780.

(50) Geng, J.; Ko, Y. K.; Youn, S. C.; Kim, Y. H.; Kim, S. a.; Jung, D. H.; Jung, H. T. *J. Phys. Chem. C* **2008**, *112*, 12264–12271.

(51) Chiu, P. W.; Duesberg, G. S.; Dettlaff-Weglikowska, U.; Roth, S. *Appl. Phys. Lett.* **2002**, *80*, 3811–3813.

(52) Chiu, P. W.; Kaempgen, M.; Roth, S. *Phys. Rev. Lett.* **2004**, *92*, 246802–1.

(53) Frehill, F.; Vos, J. G.; Benrezzak, S.; Koós, A. A.; Kónya, Z.; Rüther, M. G.; Blau, W. J.; Fonseca, A.; Nagy, J. B.; Biró, L. P.; Minett, A. I.; in het Panhuis, M. *J. Am. Chem. Soc.* **2002**, *124*, 13694–13695.

(54) Palma, M.; Wang, W.; Penzo, E.; Brathwaite, J.; Zheng, M.; Hone, J.; Nuckolls, C.; Wind, S. J. *J. Am. Chem. Soc.* **2013**, *135*, 8440–8443.

(55) Seeman, N. C. *J. Theor. Biol.* **1982**, *99*, 237–247.

(56) Rothemund, P. W. K. *Nature* **2006**, *440*, 297–302.

(57) Saccà, B.; Niemeyer, C. M. *Angew. Chem. Int. Ed.* **2012**, *51*, 58–66.

(58) Pinheiro, A. V.; Han, D.; Shih, W. M.; Yan, H. *Nat. Nanotechnol.* **2011**, *6*, 763–772.

(59) Tørring, T.; Voigt, N. V.; Nangreave, J.; Yan, H.; Gothelf, K. V. *Chem. Soc. Rev.* **2011**, *40*, 5636–5646.

(60) Lyonnais, S.; Chung, C.-L.; Goux-Capes, L.; Escudé, C.; Piétrement, O.; Baconnais, S.; Le Cam, E.; Bourgoin, J.-P.; Filoramo, A. *Chem. Commun.* **2009**, 683–685.

(61) Eskelinen, A. P.; Kuzyk, A.; Kaltiaisenaho, T. K.; Timmermans, M. Y.; Nasibulin, A. G.; Kauppinen, E. I.; Törmä, P. *Small* **2011**, *7*, 746–750.

(62) Li, S.; He, P.; Dong, J.; Guo, Z.; Dai, L. *J. Am. Chem. Soc.* **2005**, *127*, 14–15.

(63) Kwak, M.; Gao, J.; Prusty, D. K.; Musser, A. J.; Markov, V. A.; Tombros, N.; Stuart, M. C. A.; Browne, W. R.; Boekema, E. J.; ten Brinke, G.; Jonkman, H. T.; van Wees, B. J.; Loi, M. A.; Herrmann, A. *Angew. Chem. Int. Ed.* **2011**, *50*, 3206–3210.

(64) Xin, H.; Woolley, A. T. *Nanotechnology* **2005**, *16*, 2238–2241.

(65) Keren, K.; Berman, R. S.; Buchstab, E.; Sivan, U.; Braun, E. *Science* **2003**, *302*, 1380–1382.

(66) Mangalum, A.; Rahman, M.; Norton, M. L. *J. Am. Chem. Soc.* **2013**, *135*, 2451–2454.

(67) Maune, H. T.; Han, S.; Barish, R. D.; Bockrath, M.; Goddard III, W. A.; Rothemund, P. W. K.; Winfree, E. *Nat. Nanotech.* **2010**, *5*, 61–66.

(68) Han, S. P.; Maune, H. T.; Barish, R. D.; Bockrath, M.; Goddard, W. A. *Nano Lett.* **2012**, *12*, 1129–1135.

(69) Kong, R. M.; Zhang, X. B.; Chen, Z.; Tan, W. *Small* **2011**, *7*, 2428–2436.

(70) So, H.-M.; Won, K.; Kim, Y. H.; Kim, B.-K.; Ryu, B. H.; Na, P. S.; Kim, H.; Lee, J.-O. *J. Am. Chem. Soc.* **2005**, *127*, 11906–11907.

(71) Degefa, T. H.; Hwang, S.; Kwon, D.; Park, J. H.; Kwak, J. *Electrochim. Acta* **2009**, *54*, 6788–6791.

(72) Famulok, M.; Mayer, G. *Acc. Chem. Res.* **2011**, *44*, 1349–1358.

(73) Weizmann, Y.; Lim, J.; Chenoweth, D. M.; Swager, T. M. *Nano Lett.* **2010**, *10*, 2466–2469.

(74) Weizmann, Y.; Chenoweth, D. M.; Swager, T. M. *J. Am. Chem. Soc.* **2010**, *132*, 14009–14011.

(75) Weizmann, Y.; Chenoweth, D. M.; Swager, T. M. *J. Am. Chem. Soc.* **2011**, *133*, 3238–3241.

(76) Tu, X.; Manohar, S.; Jagota, A.; Zheng, M. *Nature* **2009**, *460*, 250–253.

(77) Liu, H.; Nishide, D.; Tanaka, T.; Kataura, H. *Nat. Commun.* **2011**, *2*, 309.

(78) Cambré, S.; Wenseleers, W. *Angew. Chem. Int. Ed.* **2011**, *50*, 2764–2768.

(79) Hong, G.; Zhou, M.; Zhang, R.; Hou, S.; Choi, W.; Woo, Y. S.; Choi, J. Y.; Liu, Z.; Zhang, J. *Angew. Chem. Int. Ed.* **2011**, *50*, 6819–6823.

(80) Zheng, M.; Jagota, A.; Strano, M. S.; Santos, A. P.; Barone, P.; Chou, S. G.; Diner, B. A.; Dresselhaus, M. S.; McLean, R. S.; Onoa, G. B.; Samsonidze, G. G.; Semke, E. D.; Usrey, M.; Walls, D. J. *Science* **2003**, *302*, 1545–1548.

(81) Maeda, Y.; Kimura, S.; Kanda, M.; Hirashima, Y.; Hasegawa, T.; Wakahara, T.; Lian, Y.; Nakahodo, T.; Tsuchiya, T.; Akasaka, T.; Lu, J.; Zhang, X.; Yu, Y.; Nagase, S.; Kazaoui, S.; Minami, N.; Shimizu, T.; Tokumoto, H.; Saito, R. *J. Am. Chem. Soc.* **2005**, *127*, 10287–10290.

(82) Chattopadhyay, D.; Galeska, I.; Papadimitrakopoulos, F. *J. Am. Chem. Soc.* **2003**, *125*, 3370–3375.

(83) Tulevski, G. S.; Franklin, A. D.; Afzali, A. *ACS Nano* **2013**, *7*, 2971–2976.

(84) Huang, X.; Mclean, R. S.; Zheng, M. *Anal. Chem.* **2005**, *77*, 6225–6228.

(85) Duesberg, G. S.; Muster, J.; Krstic, V.; Burghard, M.; Roth, S. *Appl. Phys. A Mater. Sci. Process.* **1998**, *67*, 117–119.

(86) Fagan, J. A.; Becker, M. L.; Chun, J.; Nie, P.; Bauer, B. J.; Simpson, J. R.; Hight-Walker, A.; Hobbie, E. K. *Langmuir* **2008**, *24*, 13880–13889.

(87) Fagan, J. A.; Becker, M. L.; Chun, J.; Hobbie, E. K. *Adv. Mater.* **2008**, *20*, 1609–1613.

(88) Fagan, J. A.; Bauer, B. J.; Hobbie, E. K.; Becker, M. L.; Hight Walker, A. R.; Simpson, J. R.; Chun, J.; Obrzut, J.; Bajpai, V.; Phelan, F. R.; Simien, D.; Huh, J. Y.; Migler, K. B. *Adv. Mater.* **2011**, *23*, 338–348.

(89) Zhou, X.; Boey, F.; Zhang, H. *Chem. Soc. Rev.* **2011**, *40*, 5221.

(90) Lee, K. M.; Li, L.; Dai, L. *J Am. Chem. Soc.* **2005**, *127*, 4122–4123.

(91) Burghard, M. *Small* **2005**, *1*, 1148–1150.

(92) Peng, Q.; Qu, L.; Dai, L.; Park, K.; Vaia, R. A. *ACS Nano* **2008**, *2*, 1833–1840.

(93) Chopra, N.; Majumder, M.; Hinds, B. J. *Adv. Funct. Mater.* **2005**, *15*, 858–864.

(94) Liu, J.; Rinzler, A. G.; Dai, H.; Hafner, J. H.; Bradley, R. K.; Boul, P. J.; Lu, A.; Iverson, T.; Shelimov, K.; Huffman, C. B.; Rodriguez-Macias, F.; Shon, Y.-S.; Lee, T. R.; Colbert, D. T.; Smalley, R. E. *Science* **1998**, *280*, 1253–1256.

(95) D'Este, M.; De Nardi, M.; Menna, E. *Eur. J. Org. Chem.* **2006**, *2006*, 2517–2522.

(96) Hu, H.; Zhao, B.; Itkis, M. E.; Haddon, R. C. *J. Phys. Chem. B* **2003**, *107*, 13838–13842.

(97) Hamon, M. A.; Hu, H.; Bhowmik, P.; Niyogi, S.; Zhao, B.; Itkis, M. E.; Haddon, R. C. *Chem. Phys. Lett.* **2001**, *347*, 8–12.

(98) Menna, E ; Della Negra, F.; Dalla Fontana, M.; Meneghetti, M. *Phys. Rev. B* **2003**, *68*, 193412.

(99) Rastogi, R.; Kaushal, R.; Tripathi, S. K.; Sharma, A. L.; Kaur, I.; Bharadwaj, L. M. *J. Colloid Interface Sci.* **2008**, *328*, 421–428.

(100) Chen, R. J.; Bangsaruntip, S.; Drouvalakis, K. A.; Wong Shi Kam, N.; Shim, M.; Li, Y.; Kim, W.; Utz, P. J.; Dai, H. *Proc. Natl. Acad. Sci.* **2003**, *100*, 4984–4989.

(101) Lu, K. L.; Lago, R. M.; Chen, Y. K.; Green, M. L. H.; Harris, P. J. F.; Tsang, S. C. *Carbon* **1996**, *34*, 814–816.

(102) Riesz, P.; Kondo, T. *Free Radic. Biol. Med.* **1992**, *13*, 247–270.

(103) Zheng, M.; Jagota, A.; Semke, E. D.; Diner, B. A.; Mclean, R. S.; Lustig, S. R.; Richardson, R. E.; Tassi, N. G. *Nat. Mater.* **2003**, *2*, 338–342.

(104) Asada, Y.; Miyata, Y.; Shiozawa, K.; Ohno, Y.; Kitaura, R.; Mizutani, T.; Shinohara, H. *J. Phys. Chem. C* **2011**, *115*, 270–273.

(105) Markham, N. R.; Zuker, M. In *Bioinformatics Vol. II*; 2008; pp. 3–31.

(106) Geggier, S.; Kotlyar, A.; Vologodskii, A. *Nucleic Acids Res.* **2011**, *39*, 1419–1426.

(107) Dwyer, C.; Guthold, M.; Falvo, M.; Washburn, S.; Superfine, R.; Erie, D. *Nanotechnology* **2002**, *13*, 601.

(108) Tchoul, M. N.; Ford, W. T.; Lolli, G.; Resasco, D. E.; Arepalli, S. *Chem. Mater.* **2007**, *19*, 5765–5772.

(109) Gladysz, J. A.; Jurisch, M. *Top. Curr. Chem.* **2012**, *308*, 1–24.

(110) Caravajal, G. S.; Leyden, D. E.; Quinting, G. R.; Maciel, G. E. *Anal. Chem.* **1988**, *60*, 1776–1786.

(111) Zhong, Y. L.; Bernaṣek, S. L. *J. Am. Chem. Soc.* **2011**, *133*, 8118–8121.

(112) Slinker, J. D.; Muren, N. B.; Renfrew, S. E.; Barton, J. K. *Nat. Chem.* **2011**, *3*, 230–235.

(113) Genereux, J. C.; Wuerth, S. M.; Barton, J. K. *J. Am. Chem. Soc.* **2011**, *133*, 3863–3868.

(114) Guo, X.; Gorodetsky, A. A.; Hone, J.; Barton, J. K.; Nuckolls, C. *Nat. Nanotechnol.* **2008**, *3*, 163–167.

CHAPTER 5

Halogen Bonding in Carbon Nanotube-Based Chemiresistive Sensors

Weis, J. G.; Ravnsbæk, J. B.; Mirica, K. A.; Swager, T. M.* "Halogen Bonding in SWCNT-based Chemiresistive Sensors" *in preparation.*

5.1 A Primer on CNT-based Chemiresistors

An ideal chemical sensor rapidly communicates small changes in chemical environment with selectivity and predictability. Currently, the most common methods rely on high-performance liquid chromatography (HPLC) or gas chromatography (GC),[1,2] both of which demand considerable resources — time, power, money, and physical space. Thus, the development of sensors that are quick, low-power, inexpensive, robust, and portable are highly desired. The resulting technology would have tremendous impact in environmental monitoring, diagnostic medicine, agriculture, food processing, and homeland security.

Carbon nanotubes (CNTs) are promising materials for chemical sensors as a result of an electronic structure that is sensitive to slight changes in local chemical environment.[3] Additional advantages of CNTs for their application in chemical sensors are their nanoscale physical size, high electrical conductivity, remarkable strength, and extraordinary specific surface area.[4] Furthermore, the chemistry for covalently and noncovalently functionalizing CNTs is well established.[5,6] These methods can enable the facile introduction of selectivity to the sensors.

A number of device architectures are available to exploit the high electronic sensitivity of CNTs, including resistors, field-effect transistors, and capacitors. The simple nature of a direct current measurement with only two electrical contacts (source and drain) makes the chemiresistor an attractive architecture for sensors (Figure 5.1). The advantages of this simplicity include portability, ease of use, low cost, and suitability for operation at room temperature. When located between two electrodes, single carbon nanotubes or networks of carbon nanotubes can be considered a variable resistor whose resistance is modulated by changes in the chemical composition of the CNTs' surrounding environment. The biggest

disadvantage of chemiresistors is that they often require meticulous calibration with a wide variety of interferents in order to achieve sufficiently high selectivity to be commercially viable.[7]

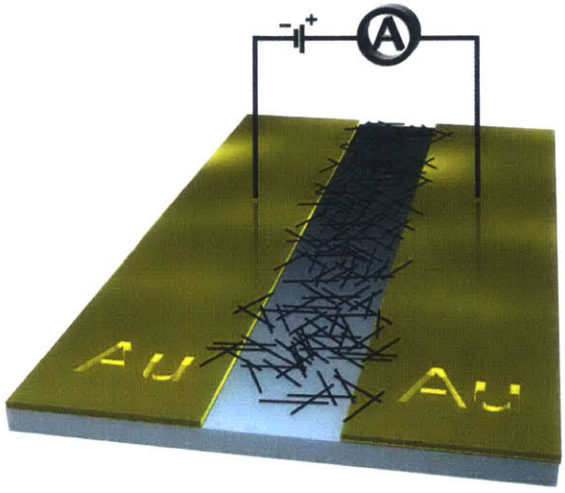

Figure 5.1. Schematic of a chemiresistor based on a randomly oriented network of CNTs deposited between two gold electrodes.

Chemiresistors can be constructed using different arrangements of carbon nanotubes. Single nanowires, aligned networks, or randomly oriented networks have all been successfully employed as chemiresistors. Although sensors based on single nanotubes and aligned nanotubes have the advantages of excellent sensitivity and low resistivity, respectively, our lab favors randomly oriented networks as a result of their simplicity and consequent reproducibility and scalability. These randomly oriented networks can be constructed with either multi-walled carbon nanotubes (MWCNTs) or single-walled carbon nanotubes (SWCNTs), each with their own advantages. For example, MWCNTs can be covalently functionalized and retain the bulk of their electronic properties; however, most covalent functionalization of SWCNTs results in a significant loss of conductivity. SWCNTs can be

synthesized or separated with a high percentage of semiconducting carbon nanotubes which are ideal for sensors. MWCNTs are almost always metallic as a result of their increased diameters which begin to resemble graphene electronically.[8]

The networks can be deposited a number of ways, including direct growth on substrates, deposition of dispersions, Langmuir–Blodgett, dip coating, and electrophoresis.[9] However, there are a number of drawbacks to these methods, including the dependence on expensive, specialized equipment for growing CNTs directly on substrates. For solution-based methods, the main obstacles are the need for solution processing, the poor solubility of CNTs in most solvents, and the limited stability of dispersions of CNTs. Our group has reported the mechanical abrasion of compressed CNT composites on various substrates to overcome these difficulties.[10–12]

The precise signal transduction mechanism is still debated, and a number of mechanisms are likely at play. Ultimately, the analyte alters the number and mobility of charge carriers through these nanowires. These modulations can result from varying contributions from intertube or intratube changes, particularly in networks and bundles of CNTs. Regarding the direct interaction between the analyte and CNTs in a network, there are four possible sites for adsorption of the analyte: (i) the sidewalls of the outermost nanotubes of the bundle, (ii) the groove between adjacent tubes on the external surface, (iii) the interior pores of the nanotubes (endohedral), and (iv) interstitial channels formed between adjacent tubes within the bundle.[13] It is important to note that it is also possible for the analyte to change the conductance by interacting with the electrodes or other compounds in a composite material.

Charge transfer between the analyte and carbon nanotubes is a common explanation for the alteration of current. In the presence of oxygen, carbon nanotubes are p-doped, resulting in

an excess of holes.[14] Thus, sensing responses in ambient conditions typically result from the modulation of the available number of charge carriers (i.e., holes). For charge transfer mechanisms, exposure to strongly electron-withdrawing molecules — e.g., NO_2 — increases the number of holes and consequently produces a decreased resistance, or increased conductance.[15] It has been calculated that NO_2 and O_2 are both charge acceptors that undergo considerable charge transfer with CNTs.[16] These calculations are consistent with experimental results.[14,17] Conversely, electron-rich analytes — e.g., NH_3 — de-dope the CNTs, rendering them less conductive.[18]

The adsorption of analytes including water, carbon dioxide, methane, hydrogen, and argon to CNTs has been identified as physisorption with small charge transfer character and very weak binding.[16] Surprisingly, these analytes have been shown to elicit sensing responses, suggesting that other mechanisms contribute substantially. Even neon and nitrogen gases have been shown to modulate the resistance of a degassed CNT mat.[19] An alternative (or parallel) sensing mechanism is the effect of physically adsorbed molecules on the electron hopping effects or intertube conductivity.[20] In the absence of charge transfer, decreases in carrier mobility can be attributed to increased carrier scattering caused by the transient adsorption of gas molecules on the CNT sidewalls.

In addition to scattering effects, there has been increasing evidence for the importance of the barriers formed at the CNT–electrode interfaces.[21] Salehi-Khojin *et al.* found that the prevailing mechanism is highly dependent on the innate conductance of the carbon nanotubes.[22] In CNTs with few defects, the modulation of the junctions between adjacent tubes and between the CNTs and the electrode dominates the sensing response. For highly defective tubes, the resistance of the individual nanotubes is the key contributor.

Barbara and coworkers determined that the density of CNT junctions — defined as the ratio between crossed junctions and CNTs — affects the degree to which each mechanism contributes. In the case of high densities (junctions : CNTs > 4), the CNT–CNT junctions dominate the device conductance and consequently the sensing response. For junctions : CNTs < 2, the electrode–CNT interface plays a larger role. [23] The extreme case is a sensor based on an individual CNT, where the electrode–CNT interface accounts for nearly all of the sensing response.[24,25]

With networks of CNTs, particularly composites, a likely origin of the sensing response is the swelling of the network upon exposure to the analyte.[26–28] In composite networks with insulating matrices, the CNTs provide an electrical path whose conductance rises and falls with the swelling and collapsing of the polymer network, respectively. This dependence is a result of the average CNT–CNT distance at crossed junctions.

Careful design of CNT-based sensors can overcome or mitigate common limitations in sensitivity, reversibility, stability, and selectivity. To improve the sensitivity, a key sensing parameter is the signal to noise ratio, which can be maximized by operating the device with the optimized current of 0.1–10 μA.[29] Signal amplification techniques can also be employed. For example, our lab has reported the DNA sequence-selective deposition of silver at CNT–DNA–CNT junctions to detect DNA. Deposition makes conductive pathways more conductive by simultaneously bridging the CNT–DNA–CNT gap and doping the nanotubes, rendering them more conductive.[30]

One common problem in CNT-based chemiresistors is the relatively slow recovery time or irreversibility,[31] particularly if that irreversibility is not exploited as a dosimeter. The rapid reversibility of carbon nanotubes sensors can be effected by the photodesorption of

analytes by exposure to UV light.[20] This decreased recovery time has been demonstrated in individual CNT sensors with analytes like NO_2.[32] An alternative is intermittent thermal treatment of the carbon nanotubes or operating the sensor at an elevated temperature.[18,33]

In practice, carbon nanotube devices that operate under ambient conditions typically have short lifetimes that result from structural or chemical changes over time. Our lab has created trifunctional selectors that address the former.[34] In addition to a moiety that selectively enhances the response to a desired analyte, pyrene and triethoxysilane moieties can tether the carbon nanotubes and glass substrate, respectively, to generate a robust sensing platform.

Covalent or noncovalent functionalization can introduce high degrees of selectivity in CNT-based sensors. Our group has reported gas sensing of volatile organic compounds at part-per-million and part-per-billion concentrations using chemiresistors based on randomly oriented networks of CNTs. MWCNTs can be covalently functionalized by treatment with zwitterionic intermediates to construct an array of cyclopentenone-fused CNTs[35] that possess moieties to selectively enhance the conductometric sensing responses to various analytes.[36] SWCNTs can be wrapped by polythiophenes bearing calixarenes that distinguish between xylene isomers[37] or with hexafluoroisopropanol groups to enhance the signal for organophosphorus chemical warfare agents.[38] Nonpolar compounds such as ethylene can also be detected with excellent sensitivity by noncovalently functionalizing SWCNTs with a tris(pyrazolyl)borate copper complex.[39] SWCNTs covalently functionalized with thioureas or squaramides greatly enhanced the response for nitroaromatics in explosives or the cyclohexanone used to recrystallize RDX.[34,40] Recently, the detection of biogenic amines to detect meat spoilage was accomplished by noncovalently functionalizing CNTs with metalloporphyrins.[41] Exploiting the effects of insulating matrices, ionizing radiation can also

be detected in a "turn-on" fashion with a poly(olefin sulfone)/MWCNT composite that becomes conductive upon radiation-induced degradation of the poly(olefin sulfone).[42] Our lab has also demonstrated that these techniques can work in aqueous solution. Covalently functionalized SWCNTs possessing tetraphosphonate cavitands give a selectively enhanced response to *N*-methylammonium species.[43]

Although a variety of chemical strategies can be employed to overcome the inherent limitations of CNT-based sensors, sensing parameters such as sensitivity and reproducibility will greatly improve along with advances in fundamental CNT research. For example, better control of the defects, diameter, chirality, and length in as-synthesized CNTs will have a profound influence on the entire field of organic electronics. Furthermore, there are particular knowledge gaps that need to be addressed. For example, the association constants are critical values in host–guest chemistry and are well characterized in solution; however, solution-based trends may not accurately reflect the molecular interactions of a heterogeneous sensing platform. Even if these events occur as predicted, the signal transduction components for each sensor seem to be unique, and no universal sensing mechanism for these devices has been established. Better understanding of these signal transduction events will lead to the rational design of sensitive and selective sensors that can serve in cross-reactive arrays to ultimately realize the "electronic nose."

5.2 Introduction

Chemical sensors have important applications in industrial and environmental monitoring, biomedicine, and homeland security. Latest developments in nanotechnology have enabled the fabrication of sensors that are highly sensitive, inexpensive, and portable with low power consumption. Single-walled carbon nanotubes (SWCNTs) are promising materials for

chemical sensors, as a result of their exceptionally high surface-to-volume ratio and electrical properties that render them particularly sensitive to electronic changes in their local chemical environment. An important advantage of CNT-based chemiresistive sensors is that they can be operated at room temperature, in comparison to the high temperatures needed for sensors based on semiconducting metal oxides (200–600 °C).

Although highly sensitive, SWCNT-based sensors often suffer from a lack of selectivity. A strategy to address this concern utilizes covalent or noncovalent functionalization of SWCNTs with small molecules, polymers, or biomolecules. Hydrogen bonding motifs are often employed to introduce selective signal enhancement of sensors towards target analytes. This approach, however, has limited selectivity, as many potential interferents can compete with target analytes through hydrogen bonding. Thus, expansion of strategies for molecular recognition of analytes with SWCNT-based sensors would enable the improved design of selective and sensitive gas sensors.

We introduce halogen bonding moieties into our chemiresistive sensors prepared by mechanical abrasion to complement traditional hydrogen bonding motifs. Halogen bonds (XBs) are generally described as electrostatic interactions between an electrophilic halogen atom (XB donor) and a Lewis base (XB acceptor). The nature of halogen bonding is rooted in the σ-hole of the halogen, a positive potential along the R–X bond axis enclosed by a belt of negative potential on the sides of the halogen. The σ-hole becomes more positive — and the electrostatically-driven[44] halogen bonding interaction becomes stronger — as i) X is less electronegative, ii) X is more polarizable, and iii) R is more electron-withdrawing.[45] In diatomic fluorine, the σ-hole is essentially nonexistent, whereas electrostatic potential maps for CF_3Cl, CF_3Br, and CF_3I clearly exhibit increasingly positive potentials along the

C–X (X = Cl→I) bond axis.[46] It is important to note that the σ-hole forces halogen bonding interactions to be highly directional: the R–X···Y bond angle is approximately 180°. This restriction is in stark contrast to traditional hydrogen bonds and halogen···halogen bonds.[47]

The application of halogen bonding in CNT-based sensors remains largely unexplored and provides an additional dimension of selectivity in cross-reactive sensing arrays. Now celebrating its sesquicentennial,[48] the discovery of XB adducts has led to modern advances in crystal engineering,[49–51] liquid crystals,[52] and anion sensing.[53] Indeed, halogen bonds have been demonstrated to outcompete hydrogen bonding in self-assembly processes.[54] Exploiting these strong N···X halogen bonding interactions, we envisioned the detection of nitrogen-containing heterocycles (e.g., pyridines) using rationally designed CNT-based sensors incorporating aryl iodides as "selectors."

5.3 Results and Discussion

5.3.1 Selection and Fabrication of Sensors

We fabricated the sensors employed in this study using our previously reported fabrication techniques PENCIL (Process Enhanced NanoCarbon for Integrated Logic) and DRAFT (Deposition of Resistors with Abrasion Fabrication Technique).[10,11] Briefly, selectors and pristine SWCNTs were combined in a 2:1 mass ratio, respectively, ball-milled for five minutes at 30 Hz, and compressed into a pellet at 10 MPa for one minute. The pellet was then mechanically abraded between thermally evaporated gold electrodes (120 nm thick with a 1 mm gap between the electrodes) on weighing paper (i.e., highly compressed cellulose) to attain resistances between 30 and 100 kΩ. It is important to note that the values of the resistance did not affect the relative sensing response, as long as the measured resistances were within the same order of magnitude. We characterized the abraded CNT composites using

optical microscopy, scanning electron microscopy (SEM), energy-dispersive X-ray (EDX) spectroscopy, and Raman spectroscopy. As we have previously reported,[11] there are no significant changes in the ratio of intensities between the D and G bands, suggesting that no degradation or radical functionalization occurs during the ball milling process. Furthermore, SEM and EDX images illustrate the uniform distribution of CNTs and selectors throughout the aryl halide matrix.

We chose the aryl halides in the preliminary study based on their relative ambient stability, their commercial availability, and our following hypotheses: 1) the sensing response of the selectors follows Cl < Br < I, consistent with solution-phase studies and corresponding to the size of the sigma hole that is proportional to the polarizability of the XB donor; 2) electron-deficient aryl halides are stronger XB donors than electron-rich aryl halides; and 3) longer alkyl chains increase the interaction between the nanotubes and the selector material, due to the geometrical fit between alternating methylene groups on the alkyl chain and the centers of the CNTs' hexagonal rings.[55,56]

In order to investigate the role of halogen bonding in CNT-based chemiresistors, we investigated a variety of known halogen bonding trends using the compounds displayed in Figure 5.2 as selectors.

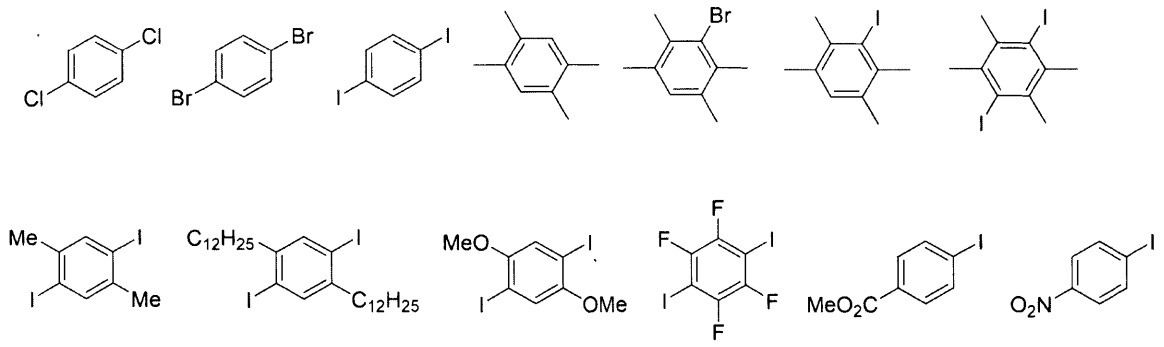

Figure 5.2. "Selectors" employed in this study.

5.3.2 Sensing Responses to Pyridine

We first investigated the *p*-dihalobenzene series, as shown in Figure 5.3. *p*-Dichlorobenzene, *p*-dibromobenzene, and *p*-diiodobenzene were chosen over the *ortho* and *meta* isomers because all *para* isomers exist as solids at room temperature and exhibit lower volatility. This property is necessary to produce mechanically robust pellets for mechanically abrading a film on paper. As predicted, the sensing response intensifies as the polarizability of the halogen increases. This observation is consistent with solution-phase studies.[57] For the *p*-diiodobenzene composite, a maximum response is obtained upon exposure to only 3 ppm pyridine ($-\Delta G/G_0$ = 5.1 ± 0.9 %). The response to pyridine for the chloro- and bromo-derivatives rises as the concentration of pyridine is increased to 25 ppm. In all cases, the response to pyridine is significantly greater than the control sensors fabricated with pristine CNTs in the absence of a selector (p-CNTs), where the response was only 1.5 ± 0.3 % at 25 ppm. We calculated the theoretical limits of detection for pyridine of *p*-diiodobenzene, *p*-dibromobenzene, and *p*-dichlorobenzene to be 16, 37, and 92 ppm, respectively.

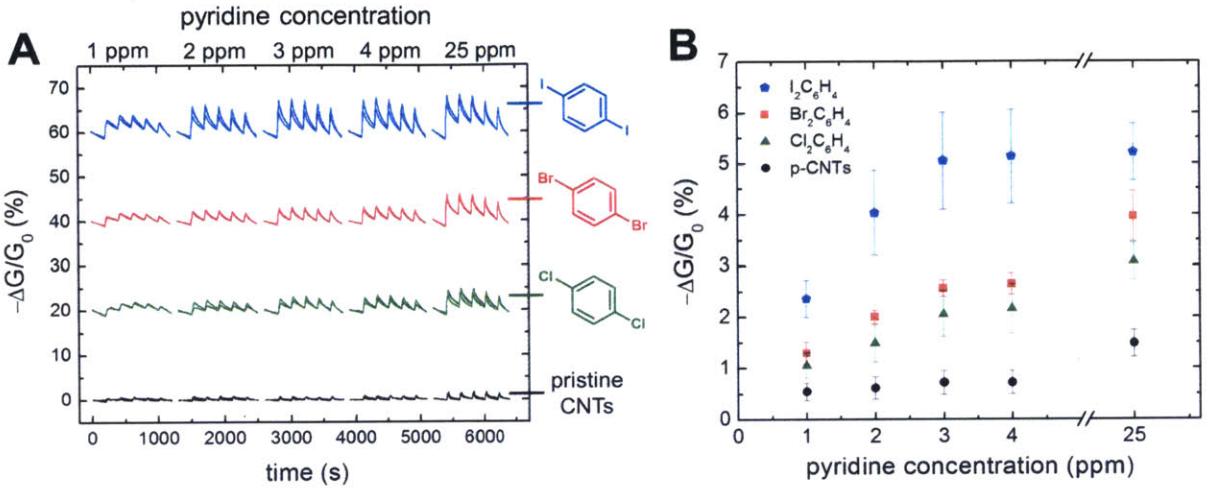

Figure 5.3. Sensing response of *p*-dihalobenzene series to varying concentrations of pyridine in N_2 carrier gas at room temperature. Each type of sensor was examined in triplicate. The three traces for each type of sensor are overlaid to show reproducibility.

To further investigate consistency with the effect of halogen bonding, sensing experiments were performed with bromodurene and iododurene, as shown in Figure 5.4. A composite material with unsubstituted durene and the pristine CNT pellet were used as controls. These controls exhibited similar behavior with $-\Delta G/G_0 = 0.7 \pm 0.2$ % at 4 ppm whereas the bromodurene and iododurene produced responses of 2.2 ± 0.1 % and 3.2 ± 0.1 %, respectively.

Sensing measurements were also carried out using 4-picoline as an analyte. As a result of the electron-rich character relative to pyridine, an enhanced sensing response is predicted by previous solution phase studies on halogen bonding.[57] Indeed, the sensing responses are significantly enhanced upon exposure to 25 ppm 4-picoline in comparison to 25 ppm pyridine; however, the pristine CNT and durene composite controls also exhibited an increase in the sensing response. This increase is likely attributed to the better ability of 4-picoline to de-dope the carbon nanotubes relative to pyridine, resulting in an attenuated conductance. Thus, the

inability to decouple this de-doping in the absence of selectors from effects caused by halogen bonding precludes further conclusions. Furthermore, attempts with other commercially available electron-rich or electron-poor pyridines were unsuccessful as a result of technical difficulties associated with the controlled generation of vapors from the selected compounds.

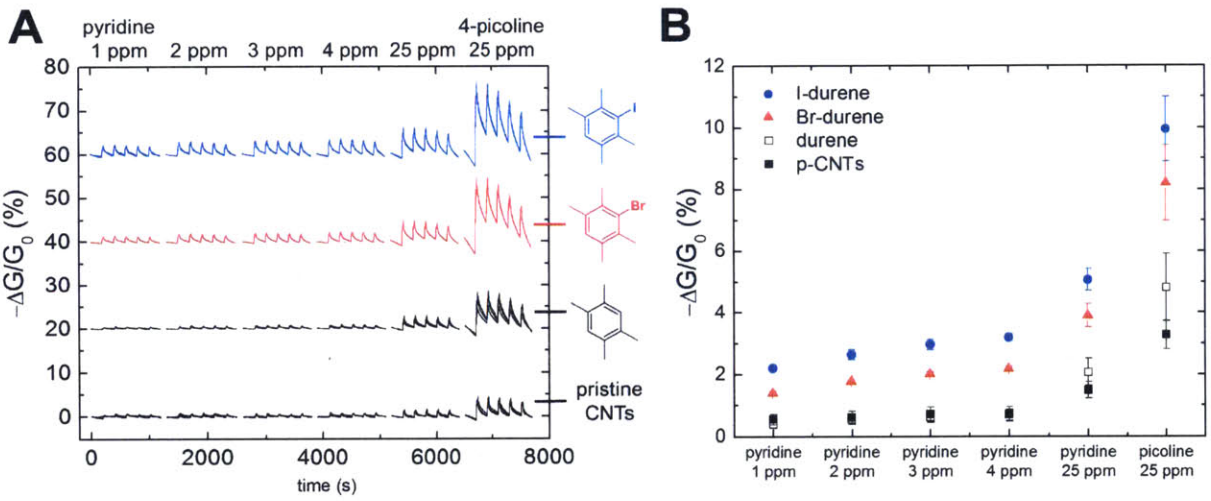

Figure 5.4. Sensing response of halodurene series to varying concentrations of pyridine. A composite with unsubstituted durene and pristine CNTs were used as controls. Each type of sensor was examined in triplicate. The three traces for each type of sensor are overlaid to show reproducibility.

Interestingly, when comparing 3-iododurene and 3,6-diiododurene, the monosubstituted durene leads to drastically greater responses to ppm concentrations of pyridine, as shown in Figure 5.5. In fact, no enhancement with the 3,6-diiododurene is observed, as it exhibited responses similar to the controls with pristine carbon nanotubes and the unsubstituted durene composite. This observation could be ascribed to increased halogen···halogen bonding within the matrix, leading to stronger competitive binding, phase separation, and/or decreased analyte permeability into the CNT composite film. It is important to note that halogen···halogen bonding is distinctly different than standard halogen bonding.

There are no critical bond angles, and the halogen atoms' σ-holes are not utilized. Rather, the character of the halogen···halogen bond reflects an unusually strong van der Waals-type interaction.[58]

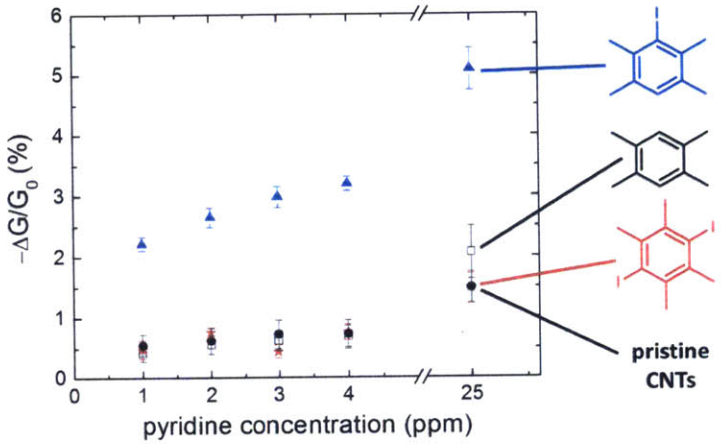

Figure 5.5. Sensing response of durene-based selectors to varying concentrations of pyridine.

To supplement comparisons within the dihalobenzene and halodurene series, we investigated the effect of arenes' electronics on the sensing response to pyridine, as shown in Figure 5.6. In addition to *p*-diiodobenzene, 1,4-diiodotetrafluorobenzene and 1,4-diiodo-2,5-dimethoxybenzene were investigated as electron-deficient and electron-rich analogues, respectively. As the group attached to the halogen atom becomes more electron-withdrawing, the σ-hole of the halogen atom becomes more positive, creating a better XB donor. Indeed, 1,4-diiodotetrafluorobenzene has been used as an ideal XB donor in solution phase assembly.[59] The N···I interaction of 4,4′ dipyridyl and 1,4-diiodobenzene in an infinite chain is 13.2 kJ/mol but is strengthened to 24.3 kJ/mol when 1,4-diiodotetrafluorobenzene is used as the XB donor.[60,61] Conversely, the introduction of electron-donating groups results in a worse XB donor.[45] As expected, the methoxy-bearing selector resulted in an attenuated signal relative to

p-diiodobenzene, although the response was significantly greater than that of pristine carbon nanotubes. Surprisingly, the electron-withdrawing tetrafluoro-containing selector behaved similarly to the selector possessing the electron-donating methoxy groups. This unexpected behavior could be ascribed to a number of factors. The perhalogenated XB-donor could produce a coating repulsive to most organic analytes of interest, similar to the interactive orthogonality of the fluorous effect.[62] The result would be diminished swelling effects and consequently weakened sensing response in the CNT composite. Alternatively, the introduction of four fluorine atoms changes the quadrupole moment of the benzene ring resulting in a different interaction with the carbon nanotubes. This interaction could alter the susceptibility of the CNTs to changes in local dipole moment or impose geometrical limitations on the halogen bonding near the nanotubes — i.e., the pyridine analyte is unable to comply with the strongly directional nature inherent to halogen bonding.

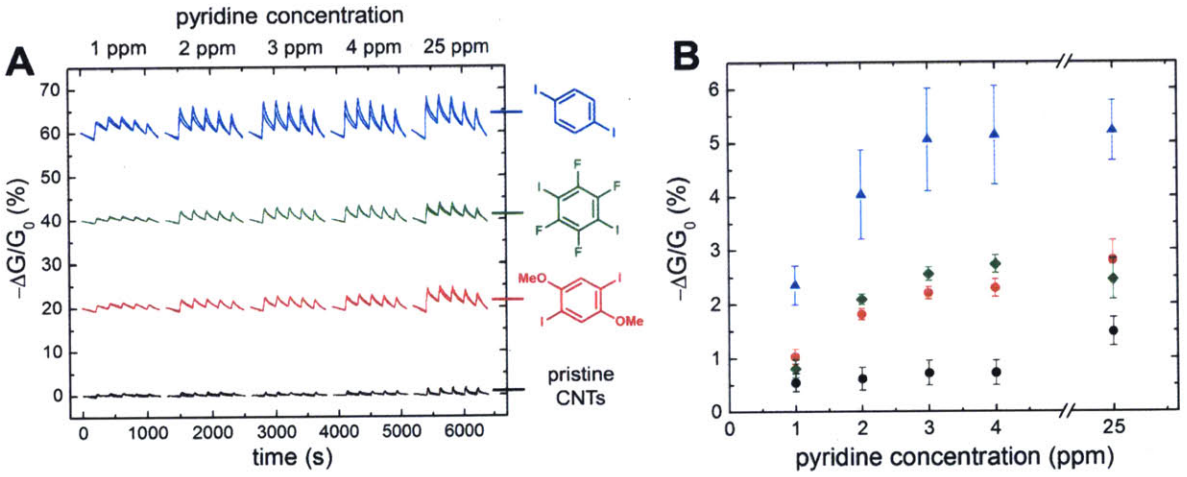

Figure 5.6. Electronic effects on sensing response to varying concentrations of pyridine. Sensing responses ($-\Delta G/G_0$, %) of sensors to varying concentrations of pyridine. Each type of sensor was examined in triplicate. The three traces for each type of sensor are overlaid to show reproducibility.

We also investigated the effect of alkyl chain length on the sensing response to pyridine, as shown in Figure 5.7. Longer alkyl chains could increase the interaction parameter between the carbon nanotubes and the selector, due to the geometrical fit between alternating methylene groups on the alkyl chain and the centers of the CNTs' hexagonal rings.[55,56] Using 1,4-didodecyl-2,5-diiodobenzene as a selector produced a slightly greater response to pyridine than the xylene analogue. In addition to the greater interaction with the nanotubes, the dodecyl derivative is likely to exhibit greater swelling effects, which we expect to produce an increased sensing response. An additional benefit of the longer alkyl chain is the mechanical properties of the composite pellet. The pellet is robust enough to be easily manipulated by hand and abrades similar to a crayon when abraded onto the weighing paper. The ease with which uniform films are deposited likely explain the excellent reproducibility of this CNT composite sensor.

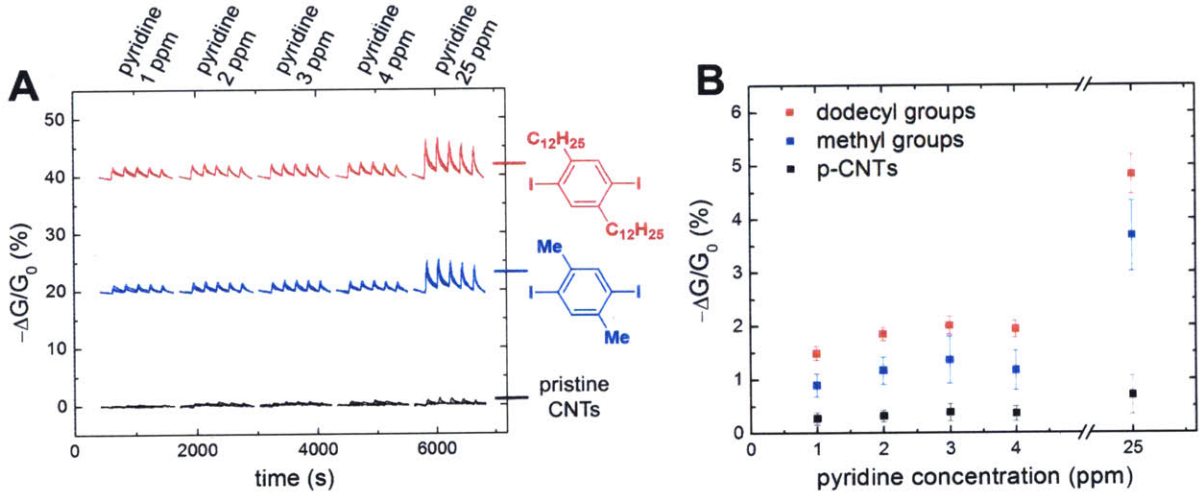

Figure 5.7. Effect on alkyl chain length on enhancement by dialkyldiiodobenzenes.

After assessing the trends associated with halogen bonding and carbon nanotube interactions, we investigated the response of our top selectors, 3-iododurene and 1,4-

didodecyl-2,5-diiodobenzene, to elevated concentrations (> 1000 ppm) of hexanes, benzene, isopropanol, and acetonitrile in addition to varying low concentrations of pyridine (≤ 25 ppm). As displayed in Figure 5.8, both sensing composites responded more strongly to pyridine at a concentration of 1 ppm than to higher concentrations (> 1000 ppm) of the interferents. Interestingly, the composite with 3-iododurene produced a perceptible signal to hexanes and benzene. This result can almost certainly be attributed to swelling effects rather than local electronic changes near the carbon nanotubes. Exposure to acetonitrile resulted in no response, consistent with its significantly weaker interaction in halogen bonding in comparison to amines and pyridine as a result of the nitrogen's *sp* hybridization. In fact, acetonitrile can be used as a solvent in halogen bonding-mediated self-assembly.[57]

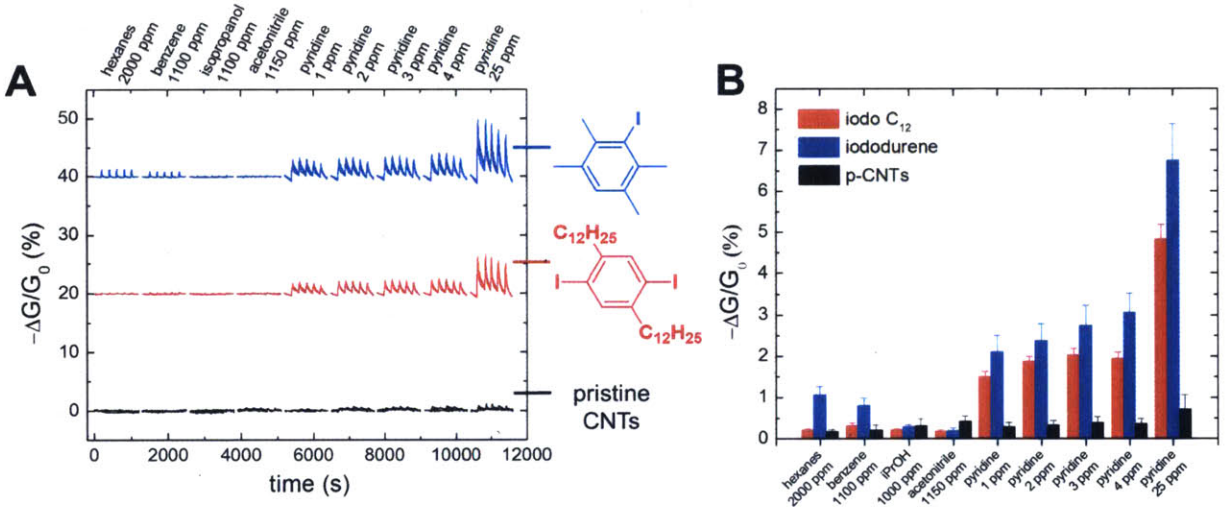

Figure 5.8. Screening for XB-specific signal enhancement. Pyridine was tested as an analyte in comparison to hexanes, benzene, isopropanol, and acetonitrile.

With these design principles in hand, we sought to create an ideal selector that possesses one iodine and an alkynyl group. The *sp*-hybridized alkyne should result in a slightly more electron-deficient ring that increases the electrophilicity of the halogen atom, and the

long alkyl chains should increase the interaction parameter with the CNTs or promote a larger swelling effect. The structures of the examined selectors are shown in Figure 5.9. Upon exposure to pyridine (4 ppm), the selectors with an octyl and dodecyl chain produced the highest response of $-\Delta G/G_0 = 1.3 \pm 0.1$ % and 1.2 ± 0.1 %, respectively. The trimethylsilyl-substituted selector produced pellets with poor mechanical properties for abrading on weighing paper. Only one of three devices were measurable by the potentiostat. It is important to note these responses are minor in comparison to the top two selectors, 3-iododurene and 1,4-didodecyl-2,5-diiodobenzene which give responses greater than 5%.

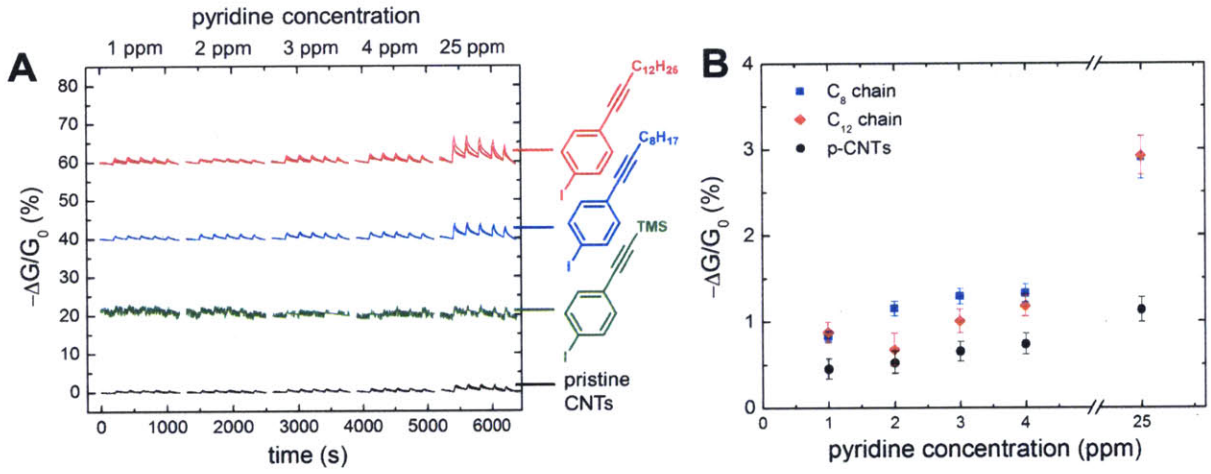

Figure 5.9. Sensing response ($-\Delta G/G_0$, %) of alkynyl aryl iodides to varying concentrations of pyridine.

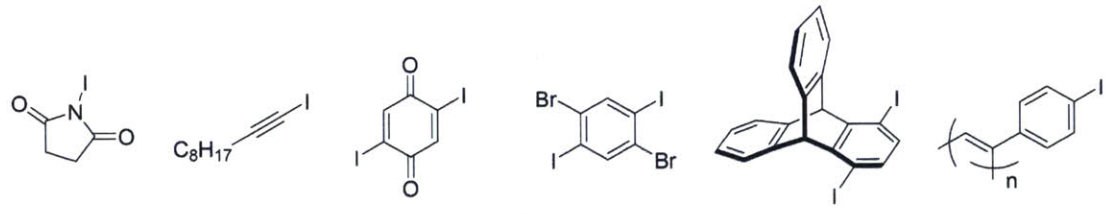

Figure 5.10. Other selectors employed for the selective enhancement of signal upon exposure to pyridine vapor.

As displayed in Figure 5.10, we investigated other selectors that could possibly result in stronger responses by halogen bonding, but none resulted in sensing responses of $-\Delta G/G_0 > 4\%$. *N*-iodosuccinimide has been demonstrated to behave as an excellent XB donor,[63] and 1-iodoalkynes are reported to be among the best XB-donors;[57,59] however, both of these are known to slowly decompose under ambient conditions. Investigation by NMR spectroscopy showed that neither compound decomposed significantly after subjecting them to ball milling with CNTs, so other factors likely limit the performance of these composite sensors. We also investigated 2,5-diiodo-*p*-benzoquinone as a result of its electron-deficient character expected to increase the ability of iodine to serve as an XB donor. It is possible that charge transfer with CNTs by the selector decreased the sensitivity of the composite material to the analyte. We tried 1,4-dibromo-2,5-diiodobenzene as a result of its high halogen content. An impermeable network resulting from halogen···halogen interactions could prevent percolation of the analyte, as the compound is known to have very poor solubility in most solvents. We hypothesized that diiodotriptycene could facilitate permeation of the analyte as a result of triptycene's high internal free volume.[64–66] Finally, poly(*p*-iodophenylacetylene) was prepared by Rh-catalyzed polymerization with potential to introduce a polymeric selector for added device stability. Poly(phenylacetylene)s prepared by rhodium-catalyzed polymerizations are known to give *cis-cisoidal* polymers that are highly crystalline and insoluble,[67] potentially preventing the polymer network from swelling.

5.3.3 Fabrication of Covalently-functionalized CNT-based Sensors

After performing stress tests and studies on device stability on our noncovalent CNT composites, we observed that the responses of our sensors weaken over a period of days. This problem could be attributed to the nontrivial volatility of the smaller selectors — e.g.,

dihalobenzenes and halodurenes. For all selectors, phase segregation between the carbon nanotubes and selectors over time could result in attenuated responses. To overcome these limitations, we sought to covalently functionalize the carbon nanotubes with *p*-halobenzenes.

A straightforward route to introducing halobenzenes to the sidewalls of the carbon nanotubes is by reaction with thermally generated diazonium compounds.[68,69] As shown in Scheme 5.1, carbon nanotubes were combined with 4-haloanilines in DMF, and then isoamyl nitrite was added dropwise. After reacting at 60 °C for ten minutes, the reaction was filtered through a PTFE membrane (0.60 μm) and washed with excess DMF. To ensure the complete removal of reagents, the nanotubes were collected, redispersed by sonication in DMF, filtered, and washed. This procedure was carried out four times before washing with diethyl ether to remove the DMF. To create an array of functionalized nanotubes, we functionalized the CNTs with 4-chloro-, 4-bromo-, and 4-iodophenyl groups and altered the equivalents of aniline to control the degree of functionalization.

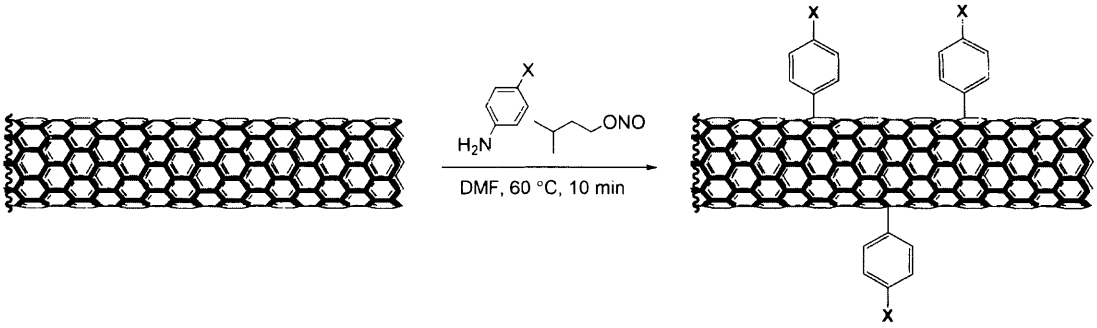

Scheme 5.1. Covalent functionalization of carbon nanotubes with aryl iodides through diazonium chemistry.

The functionalized CNTs were initially characterized by UV–Vis spectroscopy, X-ray photoelectron spectroscopy (XPS), and conductance measurements. The UV–Vis spectrum of the functionalized tubes shows a disappearance of the peaks that can be attributed to low-defect

tubes with distinct chiralities. XPS spectra indicated the functionalization of the nanotubes, as summarized in Table 5.1. Increasing the equivalents of aniline (1 equiv. aniline = 6 CNT carbons) in the reaction increased the density in all derivatives, and the effectiveness of the functionalization by diazonium salts followed the trend I < Br < Cl. When one equivalent of the aniline was used, the tubes became nonconductive, as determined by dropcasting 20 drops of concentrated functionalized CNT solution between gold electrodes (gap = 1.0 mm) on a glass slide (resistance < 500 kΩ).

X	equiv.[1]	conductivity[2]	X/C (XPS)[3]
Cl	0.1	✓	0.0064
Cl	0.2	✓	0.0120
Br	0.1	✓	0.0042
Br	0.2	✓	0.0074
Br	1	X	--
I	0.1	✓	0.0011
I	0.2	✓	0.0032
I	1	X	0.0066

Table 5.1. Characterization of covalently functionalized CNTs. [1]1 equiv. = 6 CNT carbons. [2]Sufficiently low resistance (R < 500 kΩ) determined by dropcasting 20 drops of concentrated CNT solution in DMF between 1 mm gold electrodes on glass. [3]X:C ratio, as determined by X-ray photoelectron spectroscopy (XPS).

To test the effect of functionalization on the CNTs' response to pyridine, we fabricated devices with a 1 mm gap between gold electrodes and deposited a solution of functionalized CNTs in the gap and removed the solvent under reduced pressure. The target resistance for each device was 80 – 120 kΩ. We then monitored the current ($V_{applied}$ = 0.1 V) over five exposures to pyridine at concentrations of 1, 4, and 25 ppm. The response to pyridine vapor at

25 ppm was approximately 0.3% for all devices, including the unfunctionalized CNT control. The functionalization resulted in no signal enhancement, and these values are well below those obtained for the noncovalent CNT composites. One possible explanation is that the dominant sensing mechanism relies on the swelling of the CNT network and opening greater gaps at CNT–CNT junctions. As a result of the absence of an insulating selector matrix, the spacing between the CNT–CNT contacts remains relatively unchanged. Thus, the signal would rely on the interaction of pyridine with functionalized CNTs, predominantly modulating the intratube transport. In this context, a key difference would be the orientation of the selector relative to the carbon nanotube. Whereas haloarenes likely have some degree of cofacial interaction with CNTs in the noncovalent platform, covalent functionalization results in an orthogonal orientation. The resulting change in distance[70] or orientation of the change in dipole moment may result in an attenuated response relative to the noncovalent platform.

Furthermore, in CNT chemiresistors based on CNTs, networks with highly defective nanotubes, the chemiresistive response is dictated by the modulation of the resistance of the nanotubes, rather than the CNT–electron or $CNT_{metallic}$–$CNT_{metallic}$ junctions in networks with nanotubes with few defects.[22] The UV–Vis and conductance measurements support the finding that the functionalized nanotubes are highly defective; thus, this lack of enhancement supports our hypothesis that the signal transduction mechanism for our sensors is largely based on the swelling of the insulating haloarene matrix.

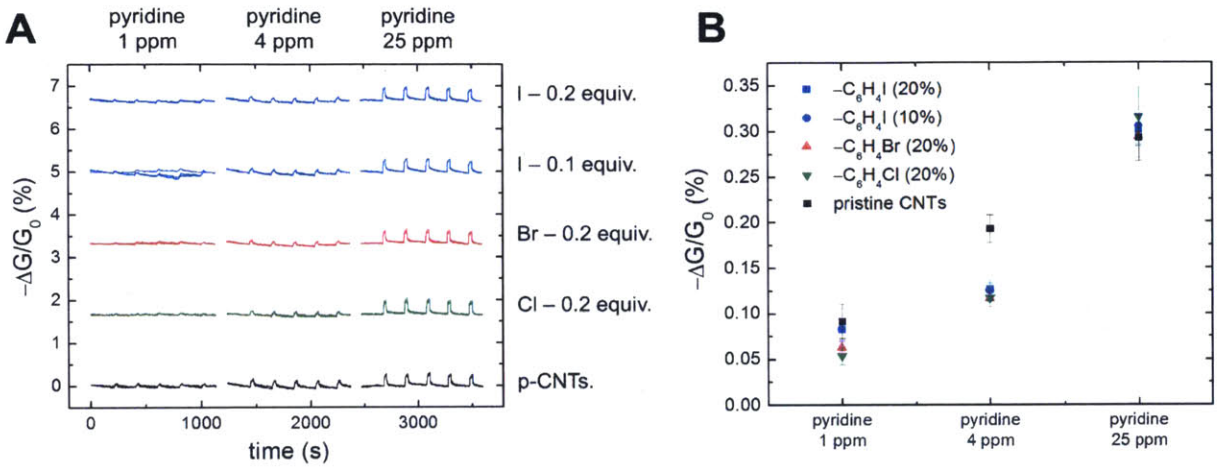

Figure 5.11. Sensing response of covalently functionalized CNTs to pyridine vapor at 1, 4, and 25 ppm.

5.4 Conclusions

In conclusion, we utilized halogen bonding in carbon nanotube-based chemiresistive sensors to selectively enhance the response to the Lewis base pyridine. The chemiresistors were prepared by ball milling of SWCNTs and selectors, compression into a pellet, and mechanical abrasion between gold electrodes onto paper. *p*-Dihalobenzene and 3-halodurene derivatives were investigated and exhibited sensing responses consistent with halogen bonding. The fundamental transduction mechanism of these sensors is likely based on swelling of the CNT composite, which is dictated by the affinity of the insulating selector matrix for the analyte.

We believe that these sensors can offer halogen bonding as an additional dimension in CNT-based cross-reactive sensing arrays. The development of more complex selectors — those with multiple halogen bonding sites at calculated spacings — could facilitate the specific detection of biologically relevant *N*-heterocyclic compounds in solution.

5.5 Experimental Details

5.5.1 General

All chemicals were commercially available and used without additional purification, unless noted otherwise. Single-walled carbon nanotubes (purified ≥95% as SWCNT) were generously provided by Nano-C, Inc. Weighing paper — the substrate used for fabricating the sensors by mechanical abrasion — was purchased from VWR International. 1-Ethynyl-4-iodobenzene,[71] 1,4-didodecyl-2,5-diiodobenzene,[72] ((4-iodophenyl)ethynyl)trimethylsilane,[73] 1-iodo-1-decyne,[74] 2,5-diiodo-1,4-benzoquinone,[75] and 1,4-diiodotriptycene[76] were prepared according to literature procedure.

5.5.2 Fabrication of Sensors

Evaporation of Gold onto Paper: Gold electrodes (120 nm thickness) were deposited on weighing paper through a stainless steel shadow mask (Stencils Unlimited) using a thermal evaporator (Angstrom Engineering) under a pressure of 0.5–5 × 10^{-5} Torr at a rate of 1–3 Å/s.

Mixing of "Selector" and SWCNTs. Selective sensing materials were generated by solvent-free ball milling of SWCNTs with small molecules "selectors" using an oscillating mixer mill (MM400, Retsch GmbH) within a stainless steel milling vial (5 mL) equipped with a single stainless steel ball (7 mm diameter). All mixtures in this study were prepared by ball-milling 40 mg SWCNTs and 80 mg "selector" for 5 minutes at 30 Hz.

Fabrication of PENCILs. PENCILs were fabricated by loading powdered material into a pressing die set with an internal diameter of 6 mm (Across International, Item #SDS6), or a pressing die set with an internal diameter of 13 mm (Sigma-Aldrich). The powdered mixture was then compressed by applying a constant pressure of 10 MPa for one minute using a hydraulic press (Carver, Model #3912 or Across International Item #MP24A).

Fabrication of Sensors by DRAFT. Sensing materials were deposited on paper between gold electrodes by manual abrasion of the PENCIL. This process involves holding the pellet with a gloved hand between the index finger and thumb, or with a pair of tweezers, and then manually rubbing the pellet on the surface of the paper between gold electrodes at rate of approximately 5 cm/s for approximately 20 times to obtain the desired resistance of each device (typically 30–100 kΩ). Caution: Dust from carbon nanotubes and selectors may be harmful upon inhalation. To prevent potential inhalation of dust particles generated by the abrasion of PENCIL on paper, fabrication of devices was carried on in a fume hood.

Fabrication of Sensors with Covalently Modified CNTs: Microscope glass slides (purchased from VWR) were cleaned by sonication in acetone and isopropanol. Using a thermal evaporator and stainless steel shadow mask, a 10 nm layer of chromium (99.99%, R. D. Mathis) was deposited onto the glass slide. A 100 nm layer of gold (99.99%, R. D. Mathis) was subsequently deposited. The resulting device is shown in Figure 5.12.

Figure 5.12. Structure of device used for drop-casting covalently functionalized CNTs between electrodes.

A suspension of covalently functionalized CNTs in DMF (~0.25 mg/mL) was treated with ultrasonication briefly at room temperature before dropcasting 1μL in the electrode gap. The solvent was then removed under reduced pressure. This process was repeated until a desired resistance between 80 – 120 kΩ was obtained, as measured by a multimeter.

5.5.3 Sensing Measurements

The array of devices on weighing paper was mounted onto a 25 mm x 75 mm x 1 mm glass slide using double-sided Scotch tape. The array was then inserted into a 2 x 30 pin edge connector (DigiKey) to make electrical contacts with each of the gold electrodes within the array. The edge connector was the connected to the potentiostat via a breadboard (DigiKey). For sensing measurements, the devices were enclosed within a custom-made gas-tight Teflon chamber containing an inlet and outlet port for gas flow, as shown in Figure 5.13.

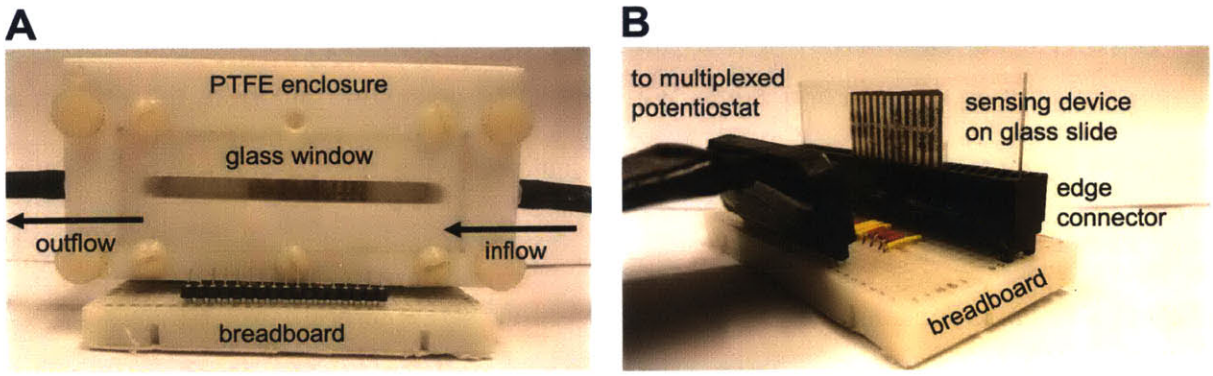

Figure 5.13. Layout of sensing device a) with and b) without the PTFE enclosure.

Before sensing measurements, the device was equilibrated by applying a voltage of 0.1 V under a flow of nitrogen (500 sccm) for two hours. The device was then exposed to varying concentrations of analyte for 30 s and allowed to recover under nitrogen for 70 s between successive exposures. Measurements of conductance were performed under a constant applied voltage of 0.1 V using PalmSense EmStat-MUX equipped with a 16-channel multiplexer (Palm Instruments BV). Data acquisition was performed using PSTrace 3.0 or 4.2 software provided by Palm Instruments. Matlab (R2014a) and Microsoft Excel were used to perform baseline correction and calculate relative sensing responses. Because some sensors showed partially irreversible response towards certain analytes, where the magnitude of the first

response is significantly larger than the response from subsequent exposures, the sensing response of all first exposures was excluded from calculating the average sensing response and the standard deviation.

Dilution of Vapors: Delivery of controlled concentrations of vapors to devices was carried out using a KIN-TEK gas generator system. Calibration (mass loss rates) for each compound was performed by monitoring the mass loss over three trials of two hours. Alternatively, a pyridine permeation tube was used. All vapors were diluted with N_2 at total flow rates of 250–1000 mL/minute.

Calculation of Detection Limit. We derived the detection limit from the sensors as described below. The sensor noise can be calculated using the variation in the relative conductance change in the baseline using the root-mean-square deviation.[77] According to IUPAC, a signal is considered an actual signal when the signal-to-noise ratio equals 3.[78]

$$V_{\chi^2} = \sum (y_i - y)^2$$

$$rms_{noise} = \sqrt{\frac{V_{\chi^2}}{N}}$$

$$DL\ (\text{ppm}) = 3\frac{rms}{slope}$$

5.5.4 Characterization of Devices

Scanning electron microscopy (SEM) was carried out using a JEOL JSM-6060 or JEOL JSM-6700F field emission SEM (FESEM) with energy-dispersive X-ray spectroscopy (EDX). Typical accelerating voltages were 1.5–5.0 kV. UV–Vis spectra were recorded on a Cary 4000 spectrophotometer.

5.5.5 Synthesis of Selectors

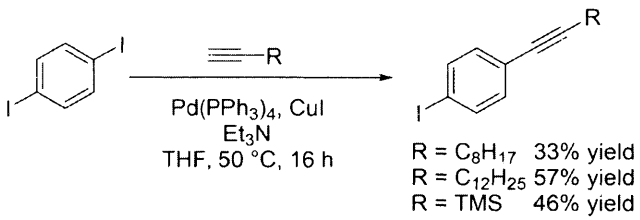

1-(Dec-1-yn-1-yl)-4-iodobenzene. To a solution of 1,4-diiodobenzene (10.0 g, 30.3 mmol, 3 equiv.), $Pd(PPh_3)_4$ (350 mg, 300 μmol, 3%), and CuI (173 mg, 900 μmol, 9%) in THF (140 mL) was added a mixture of trimethylamine (10 mL) and 1-decyne (1.82 mL, 1.40 g, 10.1 mmol). The mixture was the stirred at 60 °C for 9 hours. After allowing the reaction mixture to cool to room temperature, the solvent was removed under reduced pressure. The crude mixture was dissolved in hexanes and passed through a pad of Celite. The product was purified by column chromatography (SiO_2, hexanes) to yield a pale yellow oil (1.10 g, 33% yield). ^1H NMR (400 MHz, $CDCl_3$) δ 7.61 (m, 2H), 7.12 (m, 2H), 2.39 (t, 2H), 1.60 (p, 2H), 1.44 (m, 2H), 1.37–1.22 (8H), 0.90 (t, 3H). ^{13}C NMR (100 MHz, $CDCl_3$) δ 137.4, 133.3, 123.8, 93.2, 92.2, 79.9, 32.0, 29.3, 29.2, 29.1, 28.8, 22.8, 19.6, 14.3. HRMS (ESI) calc for $C_{16}H_{21}I$ $[M+H]^+$ 341.0761, found 341.0747. FT–IR (ATR, ν/cm^{-1}): 2953 (m), 2925 (m), 2854 (m), 2237 (w), 1708 (w), 1645 (w), 1583 (w), 1483 (s), 1464 (m), 1390 (w), 1329 (w), 1257 (w), 1059 (m), 1006 (s), 819 (s), 722 (w).

1-Iodo-4-(tetradec-1-yn-1-yl)benzene was synthesized and purified in a similar manner using 1-tetradecyne to afford a pale yellow oil (57% yield). ^1H NMR (400 MHz, $CDCl_3$) δ 7.61 (m, 2H), 7.12 (m, 2H), 2.39 (t, 2H), 1.60 (p, 2H), 1.44 (m, 2H), 1.28 (m, 16H), 0.90 (t, 3H). ^{13}C NMR (100 MHz, $CDCl_3$) δ 137.4, 133.3, 123.8, 93.2, 92.2, 79.9, 32.1, 29.8 (x3), 29.7, 29.5, 29.3, 29.1, 28.8, 22.8, 19.6, 14.3. HRMS (ESI) calc for $C_{20}H_{29}I$ $[M+H]^+$

397.1387, found 397.1384. FT–IR (ATR, ν/cm^{-1}): 2923 (s), 2853 (s), 2204 (w), 1709 (m), 1676 (m), 1582 (w), 1483 (m), 1466 (w), 1391 (w), 1268 (w), 1178 (m), 1059 (w), 1007 (s), 820 (s), 722 (w).

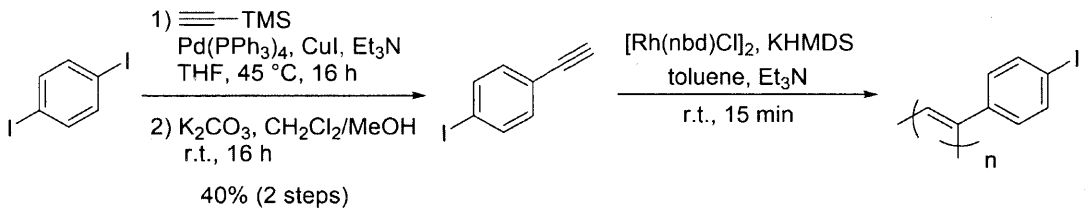

Poly(1-ethynyl-4-iodoacetylene). To a solution of 1-ethynyl-4-iodoacetylene (100 mg, 434 μmol) in 1 mL dry toluene was added a solution of bicyclo[2.2.1]hepta-2,5-diene-rhodium(I) chloride dimer (2.0 mg, 4.3 μmol, 1%) and KHMDS (8.7 μL, 0.5 M, 4.3 μmol, 1%) in 1 mL dry toluene at room temperature. The reaction mixture was stirred vigorously for 20 minutes, during which time a dark red precipitate formed. The polymer was isolated as an insoluble, bright red powder by filtration and washing with methanol (96 mg, 96% yield).

5.5.6 References

(1) Sparkman, O. D.; Penton, Z. E.; Kitson, F. G. *Gas Chromatography and Mass Spectroscopy: A Practical Guide*; Academic Press: Oxford, 2011.

(2) Zhou, X.; Lee, S.; Xu, Z.; Yoon, J. *Chem. Rev.* **2015**, doi: 10.1021/cr500567r.

(3) Kong, J.; Franklin, N. R.; Zhou, C.; Chapline, M. G.; Peng, S.; Cho, K.; Dai, H. *Science* **2000**, *287*, 622–625.

(4) Fam, D. W. H.; Palaniappan, A.; Tok, A. I. Y.; Liedberg, B.; Moochhala, S. M. *Sensors Actuators, B Chem.* **2011**, *157*, 1–7.

(5) Tasis, D.; Tagmatarchis, N.; Bianco, A.; Prato, M. *Chem. Rev.* **2006**, *106*, 1105–1136.

(6) Karousis, N.; Tagmatarchis, N.; Tasis, D. *Chem. Rev.* **2010**, *110*, 5366–5397.

(7) Pedersen, H.; Muguruma, H.; DeLa Cruz, E. Chemical Sensors. *Wiley Encyclopedia of Electrical and Electronics Engineering*, 1999, 284–299.

(8) Dresselhaus, M. S.; Dresselhaus, G.; Avouris, P. *Carbon Nanotubes: Synthesis, Structure, Properties, and Applications*; 2001.

(9) Hu, L.; Hecht, D. S.; Grüner, G. *Chem. Rev.* **2010**, *110*, 5790–5844.

(10) Mirica, K. A.; Weis, J. G.; Schnorr, J. M.; Esser, B.; Swager, T. M. *Angew. Chem. Int. Ed.* **2012**, *51*, 10740–10745.

(11) Mirica, K. A.; Azzarelli, J. M.; Weis, J. G.; Schnorr, J. M.; Swager, T. M. *Proc. Natl. Acad. Sci.* **2013**, *110*, E3265–E3270.

(12) Frazier, K. M.; Mirica, K. A; Walish, J. J.; Swager, T. M. *Lab Chip* **2014**, *14*, 4059–4066.

(13) Williams, K. A.; Eklund, P. C. *Chem. Phys. Lett.* **2000**, *320*, 352–358.

(14) Collins, P. G.; Bradley, K.; Ishigami, M.; Zettl, A. *Science* **2000**, *287*, 1801–1804.

(15) Peng, S.; Cho, K. *Nanotechnology* **2000**, *11*, 57–60.

(16) Zhao, J.; Buldum, A.; Han, J.; Lu, J. P. *Nanotechnology* **2002**, *13*, 195–200.

(17) Cantalini, C.; Valentini, L.; Lozzi, L.; Armentano, I.; Kenny, J. M.; Santucci, S. *Sensors Actuators, B Chem.* **2003**, *93*, 333–337.

(18) Valentini, L.; Cantalini, C.; Armentano, I.; Kenny, J. M.; Lozzi, L.; Santucci, S. *Diam. Relat. Mater.* **2004**, *13*, 1301–1305.

(19) Sumanasekera, G. U.; Adu, C. K. W.; Fang, S.; Eklund, P. C. *Phys. Rev. Lett.* **2000**, *85*, 1096–1099.

(20) Li, J.; Lu, Y.; Ye, Q.; Cinke, M.; Han, J.; Meyyappan, M. *Nano Lett.* **2003**, *3*, 929–933.

(21) Varghese, O. K.; Kichambre, P. D.; Gong, D.; Ong, K. G.; Dickey, E. C.; Grimes, C. A. *Sensors Actuators B Chem.* **2001**, *81*, 32–41.

(22) Salehi-Khojin, A.; Khalili-Araghi, F.; Kuroda, M. A.; Lin, K. Y.; Leburton, J.-P.; Masel, R. I. *ACS Nano* **2010**, *5*, 153–158.

(23) Boyd, A.; Dube, I.; Fedorov, G.; Paranjape, M.; Barbara, P. *Carbon* **2014**, *69*, 417–423.

(24) Zhang, J.; Boyd, A.; Tselev, A.; Paranjape, M.; Barbara, P. *Appl. Phys. Lett.* **2006**, *88*, 123112.

(25) Peng, N.; Zhang, Q.; Chow, C. L.; Tan, O. K.; Marzari, N. *Nano Lett.* **2009**, *9*, 1626–1630.

(26) Petty, M. C.; Casalini, R. *Eng. Sci. Educ. J.* **2001**, *10*, 99–105.

(27) Yeow, J. T. W.; Wang, Y.; Yeow, J. T. W. *J. Sensors* **2009**, *2009*, 493904.

(28) Cho, S. M.; Kim, Y. J.; Kim, Y. S.; Yang, Y.; Ha, S.-C. *Proc. IEEE Sensors* **2004**, *2*, 701–704.

(29) Li, W. J.; Ouyang, M.; Zhang, Y. In *IEEE Nanotechnology Materials and Devices Conference*; 2010; pp. 207–211.

(30) Weizmann, Y.; Chenoweth, D. M.; Swager, T. M. *J. Am. Chem. Soc.* **2011**, *133*, 3238–3241.

(31) Saaman, A. A.; Bergveld, P. *Sensors and Actuators* **1985**, *7*, 69–71.

(32) Chen, R. J.; Franklin, N. R.; Kong, J.; Cao, J.; Tombler, T. W.; Zhang, Y.; Dai, H. *Appl. Phys. Lett.* **2001**, *79*, 2258–2260.

(33) Cho, W.-S.; Moon, S.-I.; Lee, Y.-H. Y.-D.; Park, J.; Ju, B.-K. *IEEE Electron Device Lett.* **2005**, *26*, 498–500.

(34) Frazier, K. M.; Swager, T. M. *Anal. Chem.* **2013**, *85*, 7154–7158.

(35) Zhang, W.; Sprafke, J. K.; Ma, M.; Tsui, E. Y.; Sydlik, S. A.; Rutledge, G. C.; Swager, T. M. *J. Am. Chem. Soc.* **2009**, *131*, 8446–8454.

(36) Wang, F.; Swager, T. M. *J. Am. Chem. Soc.* **2011**, *133*, 11181–11193.

(37) Wang, F.; Yang, Y.; Swager, T. M. *Angew. Chem. Int. Ed.* **2008**, *47*, 8394–8396.

(38) Wang, F.; Gu, H.; Swager, T. M. *J. Am. Chem. Soc.* **2008**, *130*, 5392–5393.

(39) Esser, B.; Schnorr, J. M.; Swager, T. M. *Angew. Chem. Int. Ed.* **2012**, *51*, 5752–5756.

(40) Schnorr, J. M.; van der Zwaag, D.; Walish, J. J.; Weizmann, Y.; Swager, T. M. *Adv. Funct. Mater.* **2013**, *23*, 5285–5291.

(41) Liu, S. F.; Petty, A. R.; Sazama, G. T.; Swager, T. M. *Angew. Chem. Int. Ed.* **2015**, doi: 10.1002/anie.201501434.

(42) Lobez, J. M.; Swager, T. M. *Angew. Chem. Int. Ed.* **2010**, *49*, 95–98.

(43) Dionisio, M.; Schnorr, J. M.; Michaelis, V. K.; Griffin, R. G.; Swager, T. M.; Dalcanale, E. *J. Am. Chem. Soc.* **2012**, *134*, 6540–6543.

(44) Stone, A. J. *J. Am. Chem. Soc.* **2013**, *135*, 7005–7009.

(45) Politzer, P.; Murray, J. S.; Clark, T. *Phys. Chem. Chem. Phys.* **2010**, *12*, 7748–7757.

(46) Metrangolo, P.; Meyer, F.; Pilati, T.; Resnati, G.; Terraneo, G. *Angew. Chem. Int. Ed.* **2008**, *47*, 6114–6127.

(47) Metrangolo, P.; Pilati, T.; Resnati, G. *CrystEngComm* **2006**, *8*, 946–947.

(48) Guthrie, F. *J. Chem. Soc.* **1863**, *16*, 239–244.

(49) Priimagi, A.; Cavallo, G.; Metrangolo, P.; Resnati, G. *Acc. Chem. Res.* **2013**, *46*, 2686–2695.

(50) Erdelyi, M. *Nat. Chem.* **2014**, *6*, 762–764.

(51) Mukherjee, A.; Tothadi, S.; Desiraju, G. R. *Acc. Chem. Res.* **2014**, *47*, 2514–2524.

(52) Houbenov, N.; Milani, R.; Poutanen, M.; Haataja, J.; Dichiarante, V.; Sainio, J.; Ruokolainen, J.; Resnati, G.; Metrangolo, P.; Ikkala, O. *Nat. Commun.* **2014**, *5*, 4043.

(53) Zapata, F.; Caballero, A.; White, N. G.; Claridge, T. D. W.; Costa, P. J.; Félix, V.; Beer, P. D. *J. Am. Chem. Soc.* **2012**, *134*, 11533–11541.

(54) Corradi, E.; Meille, S. V.; Messina, M. T.; Metrangolo, P.; Resnati, G. *Angew. Chem. Int. Ed.* **2000**, *39*, 1782–1786.

(55) Groszek, A. J. *Proc. Roy. Soc. Lond. A* **1970**, *314*, 473–498.

(56) Schymura, S.; Kühnast, M.; Lutz, V.; Jagiella, S.; Dettlaff-Weglikowska, U.; Roth, S.; Giesselmann, F.; Tschierske, C.; Scalia, G.; Lagerwall, J. *Adv. Funct. Mater.* **2010**, *20*, 3350–3357.

(57) Beale, T. M.; Chudzinski, M. G.; Sarwar, M. G.; Taylor, M. S. *Chem. Soc. Rev.* **2013**, *42*, 1667–1680.

(58) Johansson, M. P.; Swart, M. *Phys. Chem. Chem. Phys.* **2013**, *15*, 11543–11553.

(59) Rissanen, K. *CrystEngComm* **2008**, *10*, 1107–1113.

(60) Walsh, R. B.; Padgett, C. W.; Metrangolo, P.; Resnati, G.; Hanks, T. W.; Pennington, W. T. *Cryst. Growth Des.* **2001**, *1*, 165–175.

(61) Metrangolo, P.; Neukirch, H.; Pilati, T.; Resnati, G. *Acc. Chem. Res.* **2005**, *38*, 386–395.

(62) Gladysz, J. A.; Jurisch, M. *Top. Curr. Chem.* **2012**, *308*, 1–24.

(63) Raatikainen, K.; Rissanen, K. *Chem. Sci.* **2012**, *3*, 1235.

(64) Swager, T. M. *Acc. Chem. Res.* **2008**, *41*, 1181–1189.

(65) Yang, J. S.; Swager, T. M. *J. Am. Chem. Soc.* **1998**, *120*, 5321–5322.

(66) Long, T. M.; Swager, T. M. *J. Am. Chem. Soc.* **2003**, *125*, 14113–14119.

(67) Liu, J.; Lam, J. W. Y.; Tang, B. Z. *Chem. Rev.* **2009**, *109*, 5799–5867.

(68) Bahr, J. L.; Tour, J. M. *Chem. Mater.* **2001**, *13*, 3823–3824.

(69) Dyke, C. A.; Tour, J. M. *J. Am. Chem. Soc.* **2003**, *125*, 1156–1157.

(70) Lerner, M. B.; Resczenski, J. M.; Amin, A.; Johnson, R. R.; Goldsmith, J. I.; Johnson, A. T. C. *J. Am. Chem. Soc.* **2012**, *134*, 14318–14321.

(71) Aakeröy, C. B.; Baldrighi, M.; Desper, J.; Metrangolo, P.; Resnati, G. *Chem. Eur. J.* **2013**, *19*, 16240–16247.

(72) Huang, S.; Tour, J. M. *J. Am. Chem. Soc.* **1999**, *121*, 4908–4909.

(73) Yao, Y.; Tour, J. M. *J. Org. Chem.* **1999**, *64*, 1968–1971.

(74) Rossi, R.; Carpita, A.; Quirici, M. G.; Gaudenzi, M. L. *Tetrahedron* **1982**, *38*, 631–637.

(75) López-Alvarado, P.; Avendaño, C.; Carlos Menéndez, J. *Synth. Commun.* **2002**, *32*, 3233–3239.

(76) Williams, V. E.; Swager, T. M. *Macromolecules* **2000**, *33*, 4069–4073.

(77) Martens, H.; Naes, T. *Multivariate Calibration*; Wiley & Sons: New York, NY, 1998.

(78) Currie, L. A. *Pure Appl. Chem.* **1995**, *67*, 1699–1723.

5.6 Appendix for Chapter 5

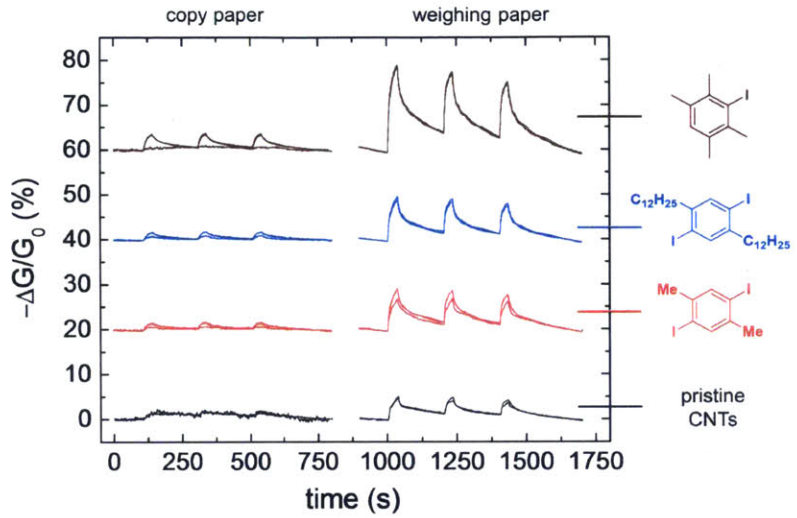

Figure 5.14. Sensing response ($-\Delta G/G_0$, %) of CNT-based to 25 ppm pyridine on copy paper (high roughness) and weighing paper (low roughness). Each type of sensor was examined in triplicate. The three traces for each type of sensor are overlaid to show reproducibility.

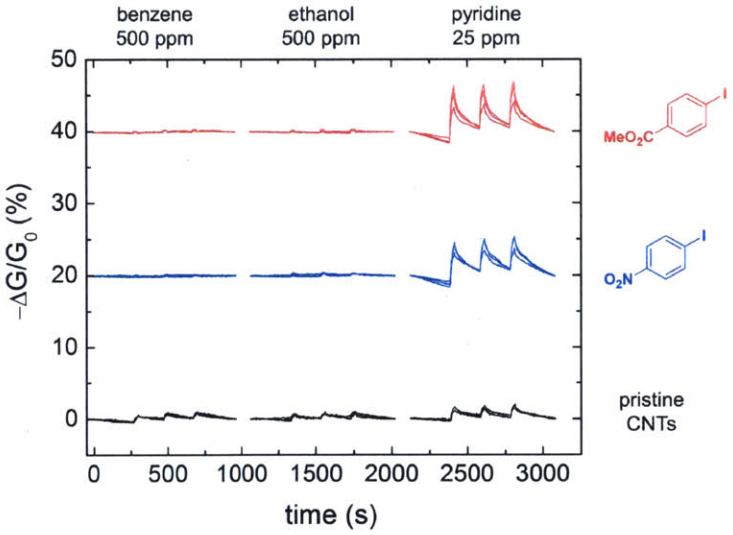

Figure 5.15. Sensing response of electron-deficient selector / SWCNT composites to benzene, ethanol, and pyridine.

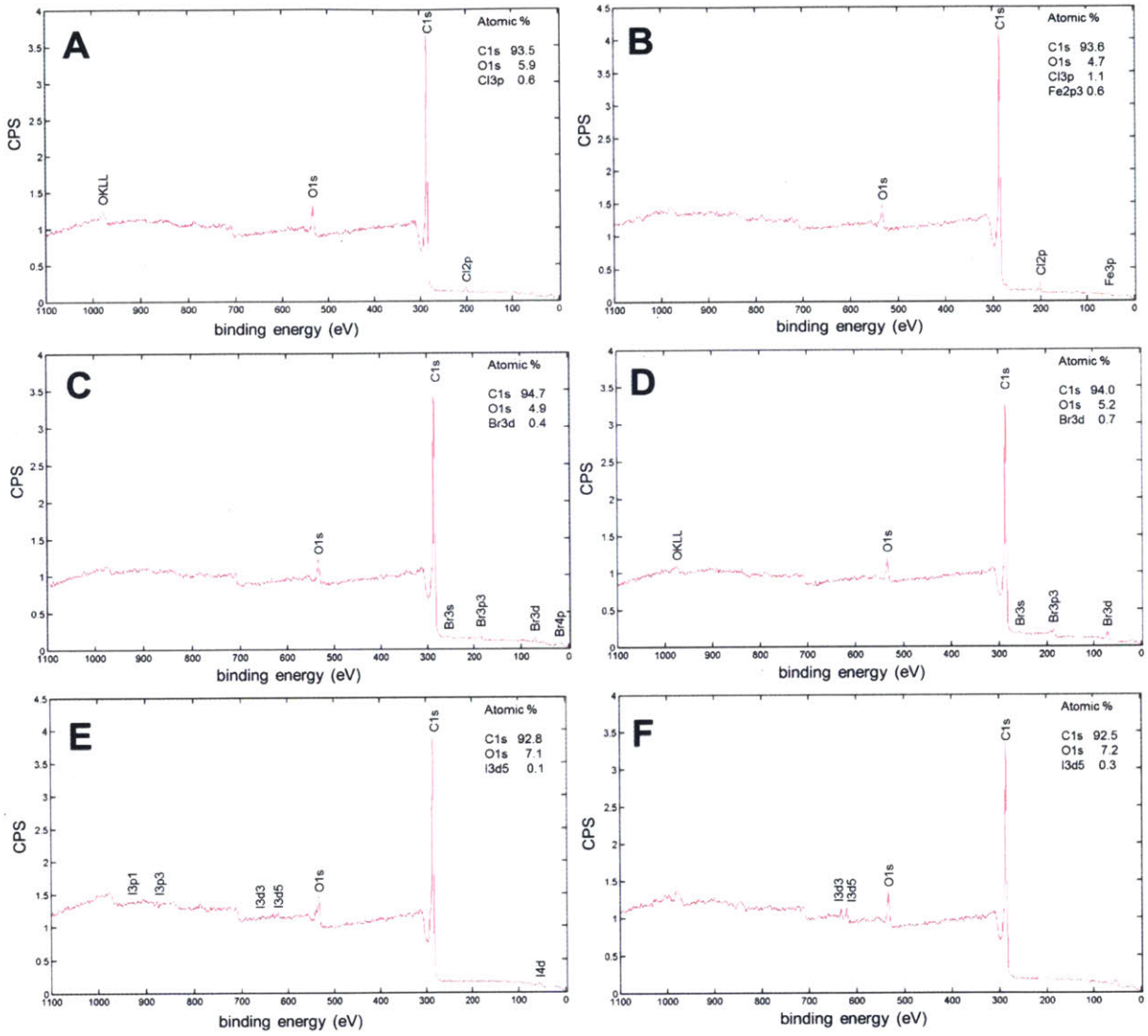

Figure 5.16. X-ray photoelectron spectra of covalently functionalized CNTS. a) Cl, 0.1 equiv.; b) Cl, 0.2 equiv.; c) Br, 0.1 equiv.; d) Br, 0.2 equiv.; e) I, 0.1 equiv.; f) I, 0.2 equiv.

1-(Dec-1-yn-1-yl)-4-iodobenzene.

^{1}H NMR, $CDCl_3$, 400 MHz

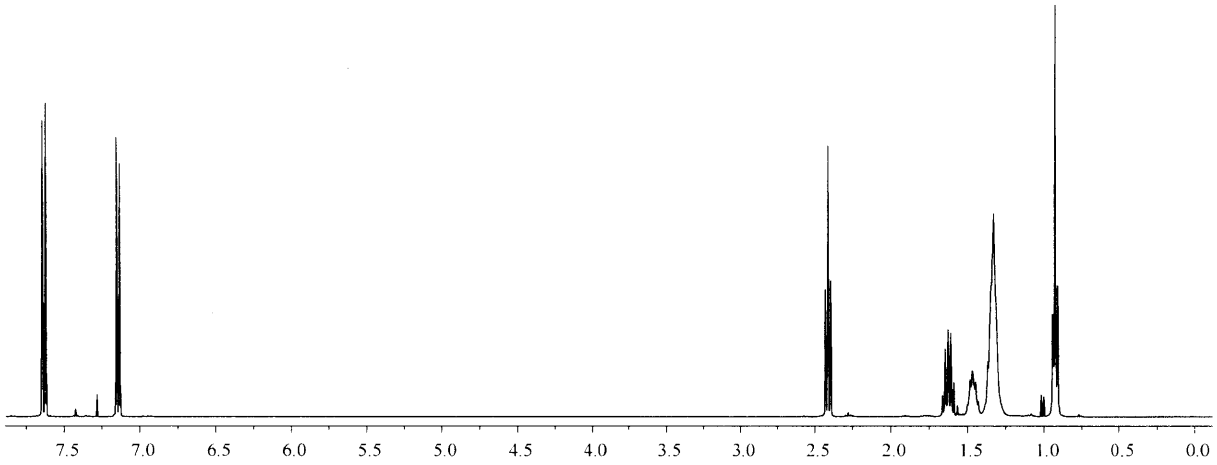

δ (ppm)

^{13}C NMR, $CDCl_3$, 100 MHz

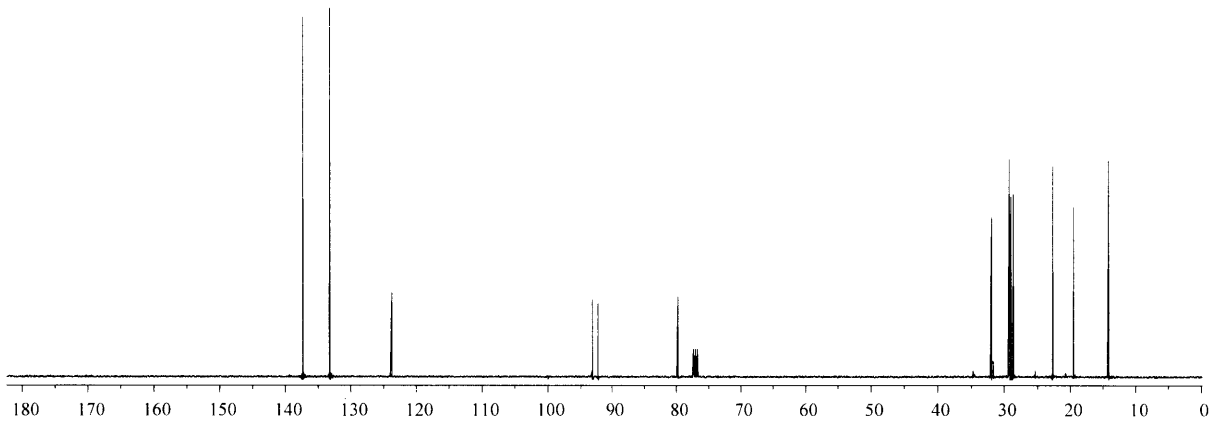

δ (ppm)

1-Iodo-4-(tetradec-1-yn-1-yl)benzene.

^{1}H NMR, $CDCl_3$, 400 MHz

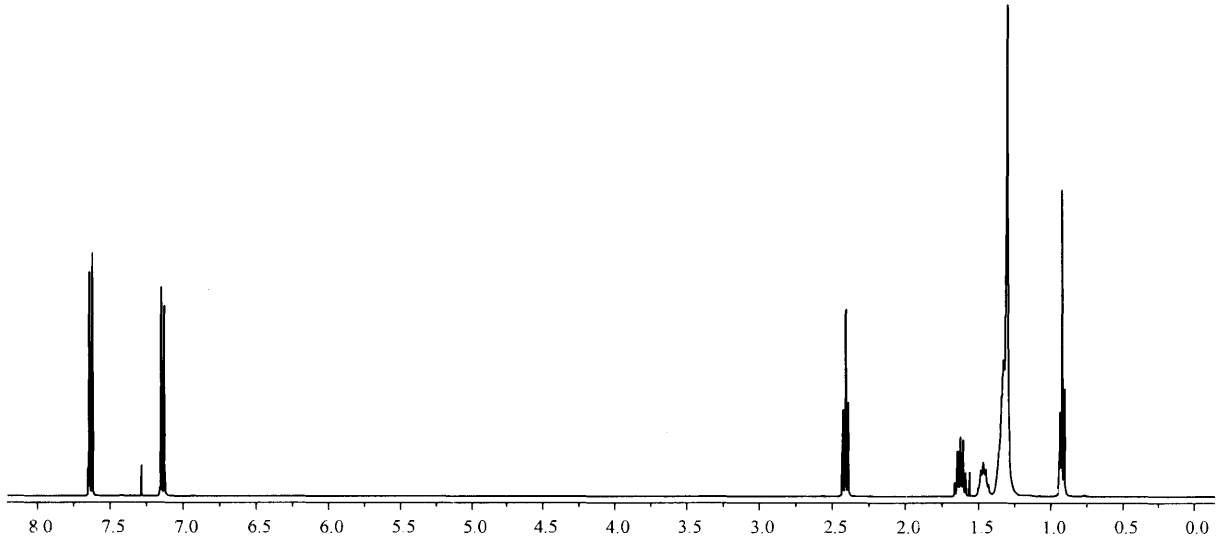

δ (ppm)

^{13}C NMR, $CDCl_3$, 100 MHz

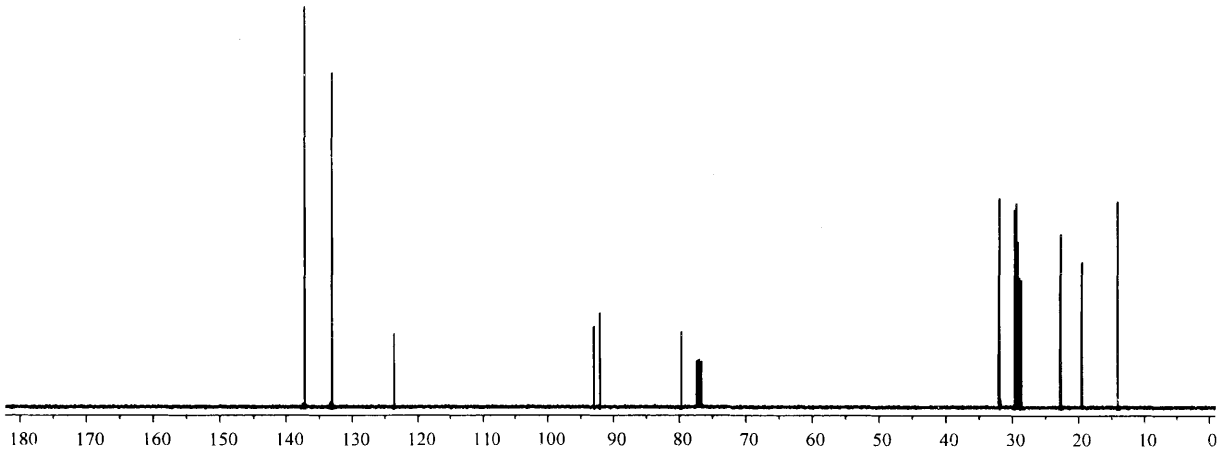

δ (ppm)

CURRICULUM VITAE

Jonathan G. Weis
Graduate Student, Swager Group
Massachusetts Institute of Technology
Department of Chemistry, Building 18–053
77 Massachusetts Avenue
Cambridge, MA 02139
jgweis@mit.edu

EDUCATION

Massachusetts Institute of Technology (Aug 2010 – June 2015)
Department of Chemistry, Organic Chemistry Division
Research Advisor: Professor Timothy M. Swager

Case Western Reserve University (Aug 2006 – May 2010)
B.S.E., Polymer Science and Engineering, *summa cum laude*
B.A., German, *summa cum laude*

RESEARCH EXPERIENCE

MIT, Department of Chemistry
Advisor: Professor Timothy M. Swager
Graduate Researcher (Nov 2010 – present)

CWRU, Department of Macromolecular Science and Engineering
Advisor: Professor Stuart J. Rowan
Undergraduate Researcher (Jan 2007 – May 2010)

Carnegie Mellon University, Department of Chemistry
Advisor: Professor Krzysztof Matyjaszewski
Undergraduate Researcher (May 2008 – Aug 2008)

Carnegie Mellon University, Institute for Complex Engineered Systems
Advisor: Professor Phil G. Campbell
Undergraduate Researcher (May 2007 – Aug 2007)

TEACHING EXPERIENCE

MIT, Department of Chemistry
Teaching Assistant, Organic Chemistry I (fall 2010, spring 2011)

CWRU, Educational Services for Students
Supplemental Instructor, Organic Chemistry I (fall 2009)
Supplemental Instructor, Organic Chemistry II (spring 2009, 2010)
Peer Tutor, chemistry and engineering courses, (spring 2007 – spring 2009)

AWARDS

2015 Excellence in Graduate Polymer Research – MIT Chemistry
ACS Division of Polymer Chemistry
2011 Award for Outstanding Teaching, Department of Chemistry, MIT
2010 Lester Wolfe Fellowship, MIT
2010 Outstanding Senior in Polymer Science and Engineering, CWRU
2009 Beta Theta Pi Founders' Scholarship
2009 Order of Omega, Greek Life Leadership Honor Society, CWRU
2009 Gamma Sigma Alpha, Greek Life Academic Honor Society, CWRU
2008 Tau Beta Pi, Engineering Honor Society, CWRU
2008 The Outstanding Sophomore Award of Case School of Engineering
2008 Phi Beta Kappa Prize, CWRU

PUBLICATIONS

9. **Weis, J. G.**; Ravnsbæk, J. B.; Mirica, K. A.; Swager, T. M.* Halogen Bonding in SWCNT-based Chemiresistive Sensors. *in preparation.*

8. **Weis, J. G.**; Weizmann, Y.; Swager, T. M.* Self-Assembly of SWCNT Networks Mediated by a DNA Trilinker. *in preparation.*

7. Belger, C.; **Weis, J. G.**; Ahmed, E.; Swager, T. M.* Colorimetric Stimuli-Responsive Hydrogel Polymers for the Detection of Nerve Agents. *in preparation.*

6. Chang, S.; Han, G. D.; **Weis, J. G.**; Park, H.; Swager, T. M.*; Gradečak, S.* Ambient-processed Transition Metal Oxide-Free Perovskite Solar Cells Enabled by a New Organic Charge Transport Layer. *under review.*

5. **Weis, J. G.**; Swager, T. M.* Thiophene-Fused Tropones as Chemical Warfare Agent-Responsive Building Blocks. *ACS Macro Lett.* **2015**, *4* (1), 138–142.

4. den Boer, D.*; **Weis, J. G.**; Zuniga, C. A.; Sydlik, S. A.; Swager, T. M.* Apparent Roughness as Indicator of (Local) Deoxygenation of Graphene Oxide. *Chem. Mater.* **2014**, *26* (16), 4849–4855.

3. Forrest, W. P.; **Weis, J. G.**; John, J. M.; Axtell, J. C.; Simpson, J. H.; Swager, T. M.; Schrock, R. R.* Stereospecific Ring-Opening Metathesis Polymerization of Norbornadienes Employing Tungsten Oxo Alkylidene Initiators. *J. Am. Chem. Soc.* **2014**, *136* (31), 10910–10913.

2. Mirica, K. A.; Azzarelli, J. M.; **Weis, J. G.**; Schnorr, J. M.; Swager, T. M.* Rapid Prototyping of Carbon-Based Chemiresistive Gas Sensors on Paper. *Proc. Natl. Acad. Sci. USA* **2013**, *110*, E3265–E3270.

1. Mirica, K. A.; **Weis, J. G.**; Schnorr, J. M.; Esser, B.; Swager, T. M.* Mechanical Drawing of Gas Sensors on Paper. *Angew. Chem. Int. Ed.* **2012**, *51*, 10740–10745.

PATENT

1. Swager, T. M., Mirica, K. A., Azzarelli, J. M., **Weis, J. G.**, Schnorr, J. M., Esser, B. Methods for Deposition of Materials Including Mechanical Abrasion. US 20130330231, December 12, 2013.

PRESENTATIONS

7. Weis, J. G.; Swager, T. M. Manipulating Conjugation in Electronic Polymers: Chemical Sensors and Precursor Routes. 249th ACS National Meeting & Exhibition, Denver, CO, USA, March 22–26, 2015. (oral presentation)

6. Weis, J. G.; Swager, T. M. Dithienobenzotropone: A Chemical Warfare Agent-Responsive Building Block. 248th ACS National Meeting & Exhibition, San Francisco, CA, USA, August 10–14, 2014. (oral)

5. Weis, J. G.; Swager, T. M. Thiophene-fused Tropones as Chemical Warfare Agent-Responsive Building Blocks. MIT Graduate Research Symposium in Organic and Bioorganic Chemistry, Cambridge, MA, USA, May 27, 2014. (oral)

4. Han, G. D.; Maurano, A.; Weis, J. G.; Bulović, V.; Swager, T. M. Efficiency Enhancement of Polymer Solar Cells by Diels–Alder Fullerene Modification. 2014 MRS Spring Meeting & Exhibit, San Francisco, CA, USA, April 21–25, 2014.

3. Weis, J. G.; Swager, T. M. Chemical Warfare Agent-Responsive Polymers by Direct Arylation or Ring-Opening Metathesis Polymerization. MIT Polymer Day, Cambridge, MA, USA, March 12, 2014. (poster)

2. Mirica, K. A.; Azzarelli, J. M.; Weis, J. G.; Schnorr, J. M.; Swager, T. M. Rapid prototyping of selective carbon-based gas sensors by mechanical drawing on paper. 246th ACS National Meeting & Exposition, Indianapolis, IN, USA, September 8–12, 2013.

1. Weis, J. G.; Shatova, T. A.; Shimizu, S.; Strano, M. S.; Jensen, M. S.; Swager, T. M. Resistivity-Based Microfluidic Sensing. Institute for Soldier Nanotechnology, Cambridge, MA, USA, June 20, 2012. (poster)

LEADERSHIP AND SERVICE

Jan 2012 – Dec 2013	Contributor, *Synfacts*
Dec 2011 – Oct 2013	Synthesis Subgroup Captain, Swager Lab, MIT
Jan – Dec 2011	Sensing Subgroup Captain, Swager Lab, MIT
June 2014 – present	MIT Materials Science and Engineering Outreach Program
Sep 2010 – present	MIT Chemistry Outreach Program

ACKNOWLEDGEMENTS

"I am a success today because I had a friend who believed in me,
and I didn't have the heart to let him down."
– Abraham Lincoln

First, I would like to express my gratitude to my research advisor, Prof. Tim Swager, for his support, guidance, and inspiration. He has been an exceptional advisor whom I admire greatly for his chemical instincts, limitless creativity, indefatigable work ethic, and perpetual positivity. It is clear that he not only genuinely cares deeply about his group, but also about the individual well-being and success of those in it. I thank him for the tremendous academic freedom to explore exciting interdisciplinary research and supporting me in sharing my work at conferences. I am grateful for his belief and trust in me, and I could not have asked for a more supportive mentor. It has been a true honor to be a member of his research group.

I would like to thank Prof. Rick Danheiser, the chair of my thesis committee, for his advice over the past five years and his patience with my engineering background in Tutorial. Having been both a student and TA in his classes, his passion for and dedication to teaching is unmistakable. I would also like to thank Prof. Jeremiah Johnson for his assistance in guiding my academic progress at MIT and serving on my thesis committee.

In the Swager Lab, we are spoiled to have the support of hard-working and talented lab managers. Dr. Joseph Walish, Brian Pretti, and Caitlin McDowell have all made my time at MIT immeasurably easier. I also thank Kathy Sweeney for her prompt and thorough assistance with all administrative issues.

The Institute for Soldier Nanotechnologies (ISN) was a second base on campus for me during my first few years. I thank Dr. Steven Kooi for his assistance with Raman spectroscopy and helpful advice on patterning films by lithography. I appreciate Bill DiNatale's assistance with AFM, SEM, TEM, and contact angle measurements. I also thank the DCIF team in Building 18: Jeff Simpson, Li Li, and Anne Rachupka, who have been quick to assist me many times over the years.

I am fortunate that Tim has a keen eye for selecting outstanding postdocs who are not only knowledgeable and creative scientists, but also fantastic mentors. In my first year and a half, Dr. Yossi Weizmann served as a tremendous research and career mentor to me, and his advice contributed significantly to Chapter 4 of this thesis. I am lucky to have shared an office with Dr. Jens Ravnsbæk, a mentor and friend. Our scientific and not-so-scientific discussions were always enjoyable, and the levity you brought to daily lab life was greatly appreciated. I am grateful for Dr. Katherine Mirica for going out of her way to mentor me in my third year and assisting with Chapter 5 of this thesis. Dr. Duncan den Boer helped me become a better and more thorough scientist, and I enjoyed our early morning conversations. I also thank Dr. Derik Frantz, Dr. Matthew Kiesewetter, Dr. Baltosar Bonillo, Dr. Silvia Rocha, Dr. Yanchuan Zhao, Dr. Derek Schipper, Dr. Ellen Sletten, Dr. Julia Kalow, Dr. Myles Herbert, Dr. Graham Sazama and Dr. Elizabeth Sterner for their support throughout my time at MIT.

When I joined the Swager Lab, there were several graduate students who provided unofficial mentorship and to whom I am grateful. Thank you to Dr. Jan Schnorr for sharing his advances in CNT-based chemiresistors as well as for his willingness help younger students even when swamped. I also greatly appreciated Dr. Jason Cox for his daily mechanism problems that I caught at the ISN during my first year. These sessions helped me immensely with cumes. I thank Dr. Joel Batson for his attempts at teaching me how to relax in lab and Dr. Stefanie Sydlik for her guidance and assistance on advancing my projects.

Thank you to several key collaborators outside of the Swager lab: Jon Axtell for helping me to initiate our continuing collaboration that is presented in Chapter 2; Dr. William Forrest and Dr. Jeremy John for setting up polymerizations with Mo and W catalysts; Tanya Shatova from the Jensen lab for collaborating on a number of microfluidic-based CNT-based detection schemes.

I would like to acknowledge and thank the excellent fellow graduate students who have made me a better scientist: John Goods, Grace Han, Kelvin Frazier, Joseph Azzarelli, Greg Gutierrez, Sophie Liu, Byungjin Koo, Markrete Krikorian, and Sarah Luppino. I particularly would like to thank Lionel Moh for his selflessness with instrument stewardship and John Fennell for being a mentor and friend. Furthermore, my appreciation goes out to the outstanding undergraduates that have worked with me. Thank you, Lily Chen, for your hard work and keeping me honest with excellent questions over the past two years. Chapter 2 would have been embarrassingly weak without your long hours in lab. Sam Heilbroner assisted in TEM imaging and 3ds Max images for Chapter 4. Warren Kay, an industrious summer student, contributed towards the covalent functionalization of CNTs in Chapter 5.

I also would like to thank the people who have paved my path to MIT, intentionally or not. I thank Prof. Stuart Rowan, my undergraduate research advisor at CWRU for allowing me to acquire hands-on experiences in organic and polymer chemistry in his lab and encouraging my application to MIT. I would not have earned a Ph.D. in organic chemistry if I did not have the fortune of being a student of two passionate and talented chemistry teachers: Matthew Davis and Robert Wienand of North Allegheny Senior High School in my hometown of Pittsburgh, PA.

Immeasurable thanks to my family: Mark, Michele, and Josh Weis. Thank you for everything. From an early age, my parents have instilled in me the value of a strong work ethic. I have carried this with me throughout my education and am receiving this Ph.D. because of their lesson. Thank you, Mom and Dad. To my brother Josh, I have unending appreciation for reminding me there is a lot of fun to be had outside of work. From the days when I was still "big brudder," he has motivated me to be the best version of myself and has given me a lifetime of memories worth sharing with my own children.

I have saved the most important acknowledgement for the end. I am grateful for my beautiful wife, Sarah, for making the difference when it mattered most. Her unwavering love, understanding, patience, and support pushed me through slumps and made good times all the better. The last five years have been a terrific chapter of our lives. Our relationship has strengthened as we've forged innumerable unforgettable memories, the greatest of which are our marriage and the recent birth of our son, Charles James, now only 5 months old. Sarah, thank you for getting me through. Now, I'm excited to see what our family makes of the future.